Shadow

Understanding the impact of shadows in satellite remote sensing of aerosols and clouds

Trees, V.J.H.

DOI
10.4233/uuid:cded831c-c9dc-4ac0-90c0-c2f19bb291e5

Publication date
2025

Document Version
Final published version

Citation (APA)
Trees, V. J. H. (2025). *Shadow: Understanding the impact of shadows in satellite remote sensing of aerosols and clouds.* [Dissertation (TU Delft), Delft University of Technology].
https://doi.org/10.4233/uuid:cded831c-c9dc-4ac0-90c0-c2f19bb291e5

Important note
To cite this publication, please use the final published version (if applicable).
Please check the document version above.

SHADOW

UNDERSTANDING THE IMPACT OF SHADOWS IN SATELLITE REMOTE SENSING OF AEROSOLS AND CLOUDS

Victor Jacq Hugo TREES

SHADOW

UNDERSTANDING THE IMPACT OF SHADOWS IN SATELLITE REMOTE SENSING OF AEROSOLS AND CLOUDS

Dissertation

for the purpose of obtaining the degree of doctor
at Delft University of Technology
by the authority of the Rector Magnificus, prof. dr. ir. T.H.J.J. van der Hagen,
chair of the Board for Doctorates
to be defended publicly on
Wednesday 2, July 2025 at 15:00 o'clock

by

Victor Jacq Hugo TREES

Master of Science in Aerospace Engineering,
Delft University of Technology, Delft, the Netherlands

This Dissertation has been approved by the promotors.

Composition of the doctoral committee:

Rector Magnificus,	TU Delft, *chair*
Prof. dr. A.P. Siebesma,	TU Delft, *promotor*
Dr. S.R. de Roode,	TU Delft, *copromotor*
Dr. P. Wang,	KNMI, *external advisor and daily supervisor*
Dr. K.F. Boersma,	KNMI/WUR, *external advisor*
Dr. ir. C.C. van Heerwaarden,	WUR, *external advisor*
Prof. dr. ir. H.W.J. Russchenberg,	TU Delft, *external advisor*
Dr. D.M. Stam,	Leiden University, *external advisor*

This work has been supported by the Dutch Research Council (NWO) and is part of the User Support Programme Space Research (GO), project number ALWGO.2018.016.

Keywords: Clouds, shadows, radiative transfer, solar eclipses, remote sensing

Front & Back: Annular solar eclipse behind clouds. Image generated by deepai.org.

ISBN 978-90-835486-7-8

An electronic version of this dissertation is available at
http://repository.tudelft.nl/.

Worry less about what you want to be,
and think more about what you want to do.

Barack Obama

CONTENTS

Summary ix

Samenvatting xiii

1 Introduction 1
- 1.1 Shadows in satellite measurements . . . 2
  - 1.1.1 Shadow types . . . 2
  - 1.1.2 Solar eclipses in satellite measurements . . . 3
  - 1.1.3 Cloud shadows in satellite measurements . . . 5
- 1.2 Research questions . . . 5
- 1.3 Thesis structure . . . 6

2 Restoring the top-of-atmosphere reflectance during solar eclipses 7
- 2.1 Introduction . . . 9
- 2.2 Method . . . 11
  - 2.2.1 Solar irradiance correction . . . 11
  - 2.2.2 Moon shadow types . . . 13
  - 2.2.3 Obscuration fraction . . . 14
  - 2.2.4 Eclipse geometry . . . 18
- 2.3 Results . . . 19
  - 2.3.1 Annular solar eclipse on 26 December 2019 . . . 19
  - 2.3.2 Annular solar eclipse on 21 June 2020 . . . 30
- 2.4 Discussion . . . 31
- 2.5 Summary and conclusions . . . 33

3 Clouds dissipate quickly during solar eclipses as the land surface cools 35
- 3.1 Introduction . . . 36
- 3.2 Results . . . 37
- 3.3 Discussion . . . 42
- 3.4 Methods . . . 42
  - 3.4.1 Cloud measurements . . . 42
  - 3.4.2 Solar eclipse correction . . . 43
  - 3.4.3 Surface temperature measurements . . . 44
  - 3.4.4 Selection of comparable days . . . 44
  - 3.4.5 Cloud simulations . . . 45
- 3.5 Supplementary material . . . 48

4 DARCLOS: a cloud shadow detection algorithm for TROPOMI **55**
4.1 Introduction . . . 56
4.2 Method . . . 59
4.2.1 Potential cloud shadow flag (PCSF) . . . 59
4.2.2 Actual cloud shadow flag (ACSF) . . . 62
4.3 Results . . . 67
4.3.1 Southern Chile and Argentina, 3 August 2019 . . . 67
4.3.2 The Netherlands and Germany, 18 November 2018 . . . 68
4.3.3 Sahara desert, 18 January 2021 . . . 69
4.4 Validation . . . 71
4.5 Discussion . . . 74
4.5.1 Limitations of the ACSF and PCSF . . . 74
4.5.2 Spectral cloud shadow flag (SCSF) . . . 75
4.6 Summary and conclusions . . . 76

5 Cancellation of cloud shadow effects in the absorbing aerosol index retrieval algorithm of TROPOMI **79**
5.1 Introduction . . . 81
5.2 Method . . . 82
5.2.1 Description of TROPOMI . . . 82
5.2.2 Absorbing Aerosol Index (AAI) . . . 82
5.2.3 Selected data set . . . 83
5.2.4 Cloud shadow detection . . . 84
5.2.5 Selecting cloud- and shadow-free neighbours . . . 85
5.2.6 Simulating the cloud shadow effect . . . 86
5.3 Results . . . 87
5.3.1 Cloud shadow fraction . . . 87
5.3.2 Measured cloud shadow effects on the AAI . . . 87
5.3.3 Simulated cloud shadow effects on the AAI . . . 91
5.4 MONKI simulations of a shadow cast on a reflecting surface produced by a high cloud . . . 98
5.5 Discussion and conclusion . . . 98

6 Conclusion and outlook **101**
6.1 Conclusion . . . 101
6.2 Outlook . . . 103

Acknowledgements **107**

A Appendix of Chapter 2 **109**
A.1 Eclipse geometry at the ground pixel . . . 109
A.2 Error propagation . . . 112

Curriculum Vitæ **133**

List of Publications **137**

SUMMARY

Earth observation satellites which monitor air quality and clouds retrieve their information about the atmosphere from the reflected sunlight by the Earth. An estimation of, for example, the amount of aerosols, trace gas concentrations, or cloud optical thickness, are based on measurements of the reflected sunlight compared with model computations of this reflected sunlight. The model atmosphere and surfaces in those 'radiative transfer models' are based on assumptions, and any deviation from reality could introduce biases in the measurements of the atmospheric constituent of interest. One of the phenomena that has not yet been included in the radiative transfer models of the satellite algorithms are shadows. In this thesis, the shadows of clouds and the shadow of the Moon are addressed, the latter also often referred to as a solar eclipse. Besides the measurement biases that they could introduce, they also provide the opportunity to study the real sensitivity of the Earth's atmosphere to variations in sunlight other than the diurnal cycle, but only if reliable measurements are available.

During a solar eclipse the solar irradiance reaching the top-of-atmosphere (TOA) is reduced in the Moon shadow. The solar irradiance is commonly measured by Earth observation satellites before the start of the solar eclipse and is not corrected for this reduction, which results in a decrease of the computed TOA reflectances. Consequently, air quality and cloud products that are derived from TOA reflectance spectra, such as the ultraviolet (UV) Absorbing Aerosol Index (AAI), the cloud optical thickness (COT) and the cloud fraction, are distorted or undefined in the shadow of the Moon. The availability of air quality and cloud satellite data in the shadow during solar eclipses, however, is of particular interest to users studying the atmospheric response to solar eclipses. Given the time and location of a point on the Earth's surface, we explain in this thesis how to compute the obscuration during a solar eclipse taking into account wavelength-dependent solar limb darkening. With the calculated obscuration fractions, we restore the TOA reflectances and subsequently the measurements of air quality and clouds.

The first application of our eclipse correction method is to the AAI. We study the penumbral shadow (i.e. partial eclipse region) during the annular solar eclipses on 26 December 2019 and 21 June 2020 measured by the TROPOMI/S5P instrument. We compare the calculated obscuration to the estimated obscuration using an uneclipsed orbit. In the corrected products, the signature of the Moon shadow disappeared, but only if wavelength-dependent solar limb darkening is taken into account. We find that the Moon shadow anomaly in the uncorrected AAI is caused by a reduction of the measured reflectance at 380 nm, rather than a color change of the measured light. We restore common AAI features such as the sunglint and desert dust, and we confirm the restored AAI feature on 21 June 2020 at the Taklamakan desert by measurements of the GOME-2C satellite instrument on the same day but outside the Moon shadow. No indication of local absorbing aerosol changes caused by the eclipses was found.

The second application of our eclipse correction method is to the measurements of

cloud fraction and COT. Clouds affected by solar eclipses could influence the reflection of sunlight back into space and might change local precipitation patterns. Satellite cloud retrievals have so far not taken into account the lunar shadow, hindering a reliable spaceborne assessment of the eclipse-induced cloud evolution. In this thesis we use satellite cloud measurements during three solar eclipses between 2005 and 2016 that have been corrected for the partial lunar shadow together with large-eddy simulations to analyze the eclipse-induced cloud evolution. Our corrected data reveal that, over cooling land surfaces, shallow cumulus clouds start to disappear at very small solar obscurations (~15%). Our simulations explain that the cloud response was delayed and was initiated at even smaller solar obscurations. We demonstrate that neglecting the disappearance of clouds during a solar eclipse could lead to a considerable overestimation of the eclipse-related reduction of net incoming solar radiation. These findings should spur cloud model simulations of the direct consequences of sunlight-intercepting geoengineering proposals, for which our results serve as a unique benchmark.

The other type of shadows in this thesis are the shadows of clouds. Cloud shadows can be detected in the radiance measurements of the TROPOMI instrument on board the Sentinel-5P satellite due to its high spatial resolution, and could possibly affect its air quality products. The cloud shadow induced signatures are, however, not always apparent and may depend on various cloud and scene parameters. Hence, the quantification of the cloud shadow impact requires the analysis of large data sets. If the shadows are to be removed from the data, or if shadows are to be studied, an automatic detection of the shadow pixels is needed.

In this thesis, we present the Detection AlgoRithm for CLOud Shadows (DARCLOS) for TROPOMI, which is the first cloud shadow detection algorithm for a spaceborne spectrometer. DARCLOS raises potential cloud shadow flags (PCSFs), actual cloud shadow flags (ACSFs) and spectral cloud shadow flags (SCSFs). The PCSFs indicate the TROPOMI ground pixels that are potentially affected by cloud shadows based on a geometric consideration with safety margins. The ACSFs are a refinement of the PCSFs using spectral reflectance information of the PCSF pixels, and identify the TROPOMI ground pixels that are confidently affected by cloud shadows. Because we find indications of the wavelength dependence of cloud shadow extents in the UV, the SCSF is a wavelength dependent alternative for the ACSF at the wavelengths of TROPOMI's air quality retrievals. We validate the PCSF and ACSF with true color images made by the VIIRS instrument on board of Suomi NPP orbiting in close proximity to TROPOMI on board of Sentinel-5P. We find that the cloud evolution during the overpass time difference between TROPOMI and VIIRS complicates this validation strategy, implicating that an alternative cloud shadow detection approach using co-located VIIRS observations could be problematic. We conclude that the PCSF can be used to exclude cloud shadow contamination from TROPOMI data, while the ACSF and SCSF can be used to select pixels for the scientific analysis of cloud shadow effects.

We applied DARCLOS to detect cloud shadow pixels in the TROPOMI absorbing aerosol index (AAI) product over Europe during 8 months. For every shadow pixel, we automatically select cloud- and shadow-free neighbour pixels, in order to estimate the cloud shadow induced signature. In addition, we simulate the measured cloud shadow impact on the AAI with our newly developed 3D radiative transfer algorithm MONKI. Both the

measurements and simulations show that the average cloud shadow impact on the AAI is close to zero (0.06 and 0.16, respectively). However, the top-of-atmosphere reflectance ratio between 340 and 380 nm, which is used to compute the AAI, is significantly increased in 95% of the shadow pixels. So, cloud shadows are bluer than surrounding non-shadow pixels. Our simulations explain that the traditional AAI formula intrinsically already corrects for this cloud shadow effect, via the lower retrieved scene albedo. This cancellation of cloud shadow signatures is not always perfect, sometimes yielding second order low and high biases in the AAI which we also successfully reproduce with our simulations. We show that the magnitude of those second order cloud shadow effects depends on various cloud parameters which are difficult to determine for the shadows measured with TROPOMI. We conclude that a potential cloud shadow correction strategy for the TROPOMI AAI would therefore be complicated if not unnecessary.

SAMENVATTING

Aardobservatiesatellieten die de luchtkwaliteit en wolken monitoren, halen hun informatie over de atmosfeer uit het gereflecteerde zonlicht door de aarde. Schattingen van bijvoorbeeld de hoeveelheid aerosolen, de concentratie spoorgassen of de optische dikte van wolken zijn gebaseerd op metingen van het gereflecteerde zonlicht, vergeleken met modelberekeningen van dit gereflecteerde zonlicht. De modelatmosfeer en -oppervlakken in deze 'stralingstransportmodellen' zijn gebaseerd op aannames, en elke afwijking van de werkelijkheid kan leiden tot verstoringen van de metingen van het atmosferische bestanddeel dat van belang is. Een van de verschijnselen die nog niet is opgenomen in de stralingstransportmodellen van de satellietalgoritmen zijn schaduwen. In dit proefschrift worden de schaduwen van wolken en de schaduw van de maan behandeld, de laatste ook vaak een zonsverduistering genoemd. Naast de meetverstoringen die ze zouden kunnen introduceren, bieden ze ook de mogelijkheid om de werkelijke gevoeligheid van de aardatmosfeer voor andere variaties in zonlicht dan de dagcyclus te bestuderen, maar alleen als er betrouwbare metingen beschikbaar zijn.

Tijdens een zonsverduistering wordt de zonne-instraling die de top van de atmosfeer (TOA) bereikt, gereduceerd in de schaduw van de Maan. De zonne-instraling wordt gewoonlijk gemeten door aardobservatiesatellieten voor het begin van de zonsverduistering en wordt niet gecorrigeerd voor deze vermindering, wat resulteert in een afname van de berekende TOA-reflectanties. Bijgevolg worden luchtkwaliteit- en wolkenproducten die afgeleid zijn van TOA-reflectiespectra, zoals de ultraviolette (UV) Absorbing Aerosol Index (AAI), de optische dikte van de wolken (COT) en de wolkenfractie, vervormd of ongedefinieerd in de schaduw van de Maan. De beschikbaarheid van satellietgegevens over luchtkwaliteit en wolken in de schaduw tijdens zonsverduisteringen is echter van bijzonder belang voor gebruikers die de atmosferische respons op zonsverduisteringen bestuderen. Gegeven de tijd en locatie van een punt op het aardoppervlak, leggen we in dit proefschrift uit hoe de verduistering tijdens een zonsverduistering berekend kan worden, rekening houdend met golflengte-afhankelijke verduistering van de zonnelimb. Met de berekende verduisteringsfracties herstellen we de TOA-reflecties en vervolgens de metingen van luchtkwaliteit en wolken.

De eerste toepassing van onze eclipscorrectiemethode is op de AAI. We bestuderen de penumbra (d.w.z. het gedeeltelijke eclipsgebied) tijdens de ringvormige zonsverduisteringen op 26 december 2019 en 21 juni 2020, gemeten door het TROPOMI/S5P-instrument. We vergelijken de berekende verduistering met de geschatte verduistering met behulp van een satellietbaan zonder verduistering. In de gecorrigeerde producten is de signatuur van de maanschaduw verdwenen, maar alleen als rekening wordt gehouden met golflengte-afhankelijke verduistering van de zonnelimb. We vinden dat de maanschaduwafwijking in de ongecorrigeerde AAI wordt veroorzaakt door een vermindering van de gemeten reflectie bij 380 nm, in plaats van een kleurverandering van het gemeten licht. We herstellen veelvoorkomende AAI-kenmerken zoals woestijnstof en de

glint in de oceaan, en we bevestigen de herstelde AAI-afdruk op 21 juni 2020 in de Taklamakan woestijn door metingen van het GOME-2C satellietinstrument op dezelfde dag maar buiten de maanschaduw. Er zijn geen aanwijzingen gevonden voor lokale absorberende aerosolveranderingen veroorzaakt door de verduisteringen.

De tweede toepassing van onze eclipscorrectiemethode is op de metingen van wolkenfractie en COT. Wolken die worden beïnvloed door zonsverduisteringen kunnen de weerkaatsing van zonlicht in de ruimte beïnvloeden en lokale neerslagpatronen veranderen. Satellietmetingen van wolken hebben tot nu toe geen rekening gehouden met de maanschaduw, wat een betrouwbare beoordeling vanuit de ruimte van de wolkenevolutie door eclipsen belemmert. In dit proefschrift gebruiken we satellietwolkenmetingen tijdens drie zonsverduisteringen tussen 2005 en 2016 die zijn gecorrigeerd voor de gedeeltelijke maanschaduw, samen met large-eddy simulaties om de wolkenevolutie door eclipsen te analyseren. Onze gecorrigeerde gegevens laten zien dat, boven afkoelende landoppervlakken, ondiepe cumuluswolken beginnen te verdwijnen bij zeer kleine verduisteringen (15%). Onze simulaties verklaren dat de wolkenreactie vertraagd was en begon bij nog kleinere verduisteringen. We tonen aan dat het verwaarlozen van het verdwijnen van wolken tijdens een zonsverduistering kan leiden tot een aanzienlijke overschatting van de eclipsgerelateerde vermindering van de netto inkomende zonnestraling. Deze bevindingen zouden een impuls moeten geven aan simulaties van wolkenmodellen voor de directe gevolgen van voorstellen voor geoengineering-concepten die het zonlicht tegenhouden, waarvoor onze resultaten een unieke benchmark vormen.

Het andere type schaduwen in dit proefschrift zijn de schaduwen van wolken. Wolkenschaduwen kunnen worden gedetecteerd in de stralingsmetingen van het TROPOMI-instrument aan boord van de Sentinel-5P satelliet vanwege de hoge ruimtelijke resolutie, en kunnen mogelijk de luchtkwaliteitsproducten beïnvloeden. De door de wolkenschaduw veroorzaakte signaturen zijn echter niet altijd duidelijk en kunnen afhankelijk zijn van verschillende wolken- en omgevingsparameters. Daarom vereist de kwantificering van de invloed van wolkschaduwen de analyse van grote datasets. Als de schaduwen uit de gegevens moeten worden verwijderd of als schaduwen moeten worden bestudeerd, is een automatische detectie van de schaduwpixels nodig.

In dit proefschrift presenteren we het Detection AlgoRithm for CLOud Shadows (DARCLOS) voor TROPOMI, het eerste algoritme voor detectie van wolkschaduwen voor een spectrometer in de ruimte. DARCLOS maakt potentiële wolkschaduwvlaggen (PCSF's), werkelijke wolkschaduwvlaggen (ACSF's) en spectrale wolkschaduwvlaggen (SCSF's) aan. De PCSF's geven de TROPOMI-grondpixels aan die mogelijk worden beïnvloed door wolkschaduwen op basis van een geometrische overweging met veiligheidsmarges. De ACSF's zijn een verfijning van de PCSF's met behulp van spectrale reflectantie-informatie van de PCSF-pixels en identificeren de TROPOMI-grondpixels die met zekerheid worden beïnvloed door wolkenschaduw. Omdat we aanwijzingen vinden voor de golflengteafhankelijkheid van de lengte van wolkenschaduwen in het UV, is de SCSF een golflengteafhankelijk alternatief voor de ACSF op de golflengten van de TROPOMI-producten. We valideren de PCSF en ACSF met true color beelden gemaakt door het VIIRS-instrument aan boord van Suomi NPP dat in een baan dicht bij TROPOMI aan boord van Sentinel-5P draait. We stellen vast dat de wolkenevolutie tijdens het tijdsverschil tussen TROPOMI en VIIRS deze validatiestrategie bemoeilijkt, wat impliceert dat een alternatieve

aanpak voor de detectie van wolkenschaduwen met behulp van VIIRS-waarnemingen op dezelfde locatie problematisch kan zijn. We concluderen dat de PCSF kan worden gebruikt om wolkenschaduwvervuiling uit TROPOMI-data te verwijderen, terwijl de ACSF en SCSF kunnen worden gebruikt om pixels te selecteren voor de wetenschappelijke analyse van wolkschaduweffecten.

We hebben DARCLOS toegepast om wolkschaduwpixels te detecteren in het TROPOMI absorbing aerosol index (AAI) product boven Europa gedurende 8 maanden. Voor elke schaduwpixel selecteren we automatisch wolken- en schaduwvrije naastliggende pixels om de door wolkenschaduw veroorzaakte signatuur te schatten. Daarnaast simuleren we de gemeten wolkschaduwimpact op de AAI met ons nieuw ontwikkelde 3D stralingstransportalgoritme MONKI. Zowel de metingen als de simulaties laten zien dat het gemiddelde effect van wolkenschaduw op de AAI dicht bij nul ligt (respectievelijk 0.06 en 0.16). De reflectantieverhouding tussen 340 en 380 nm aan de top van de atmosfeer, die wordt gebruikt om de AAI te berekenen, wordt echter aanzienlijk verhoogd in 95% van de schaduwpixels. Wolkenschaduwen zijn dus blauwer dan omringende pixels die niet in de schaduw liggen. Onze simulaties leggen uit dat de traditionele AAI-formule intrinsiek al corrigeert voor dit wolkenschaduweffect, via het lagere albedo van de scène. Deze annulering van wolkenschaduw signaturen is niet altijd perfect, wat soms resulteert in tweede orde lage en hoge biases in de AAI die we ook met succes reproduceren met onze simulaties. We laten zien dat de grootte van deze tweede orde wolkschaduweffecten afhangt van verschillende wolkenparameters die moeilijk te bepalen zijn voor de schaduwen gemeten met TROPOMI. We concluderen dat een mogelijke wolkschaduwcorrectiestrategie voor de TROPOMI AAI daarom gecompliceerd, zo niet onnodig, zou zijn.

1

INTRODUCTION

Earth observation satellite spectrometer instruments are designed to measure the optical properties of particles and the concentration of trace gases in the Earth's atmosphere. They retrieve this information from the spectrum (i.e. the light at various wavelengths) of the top-of-atmosphere (TOA) reflectance, at wavelengths in the ultraviolet (UV), visible (VIS), near-infrared (NIR) and short-wave infrared (SWIR) spectral domains. The TOA reflectance is obtained by dividing the radiance reflected by the Earth, by the sunlight (or solar irradiance) incident on the Earth, both at the top of the atmosphere. The Earth radiance is commonly measured continuously, while the solar irradiance is calculated or measured only once a day.

Spaceborne monitoring of the atmosphere using spectrometers started in 1978 with the launch of the first Total Ozone Mapping Spectrometer (TOMS) instrument on board the Nimbus-7 satellite. TOMS measured aerosol properties and concentrations of ozone (O_3) and sulfur dioxide (SO_2) in the Earth's atmosphere globally on a daily basis, retrieved from the Earth's TOA reflectance using six UV wavelength bands [57]. The Global Ozone Monitoring Experiment (GOME) [19] launched in 1995 was the first high-spectral resolution spectrometer, followed by the SCanning Imaging Absorption spectroMeter for Atmospheric ChartograpHY (SCIAMACHY) [17], the Ozone Monitoring Instrument (OMI) [89], the GOME-2 A/B/C instruments [106] and, launched in October 2017, the TROPOspheric Monitoring Instrument (TROPOMI) [177] on board of the ESA Sentinel-5P satellite.

TROPOMI is the spaceborne spectrometer with the highest spatial resolution to date: the ground pixels have dimensions of 7.2 × 3.6 km^2 in the nadir viewing direction, and decreased to 5.6 × 3.6 km^2 on 6 August 2019 [93]. TROPOMI operates in a near-polar, Sun-synchronous orbit at an average altitude of 824 km above the Earth's surface, and completes an orbit approximately every 101 minutes. TROPOMI is a nadir-looking instrument with a local equator crossing time of 13:30 LT. During its ascending node, it collects measurements every 1.08 seconds in a 2600 km swath width. TROPOMI provides daily global maps of aerosol properties and concentrations of O_3, NO_2, SO_2 and HCHO from ultraviolet-visible (UV–VIS, 267–499 nm) wavelengths, of cloud properties

from near-infrared (NIR, 661–786 nm) wavelengths and concentrations of CO and CH_4 from shortwave infrared (SWIR, 2300–2389 nm) wavelengths. Because of its high spatial resolution and data quality, TROPOMI has, for example, shown to be able to observe local NO_2 emission sources such as power plants [10], gas compressor stations [174] and cities [92], detailed volcanic SO_2 plumes [157], and CH_4 leakage from oil/gas fields [110, 176, 137], volcanic SO_2 plumes [157] and NO_2 trails along ship tracks [46].

Satellite instruments in geostationary orbit can continuously scan one side of the entire Earth, as they orbit the Earth with the angular speed and direction of the Earth's rotation. That is, unlike the satellite instrument mentioned in the previous two paragraphs, geostationary satellite instruments provide a temporal resolution of the measurements in certain regions throughout the day. An example is the Spinning Enhanced Visible and InfraRed Imager (SEVIRI) instrument on board the Meteosat Second Generation (MSG) series of geostationary satellites, operated by EUMETSAT. It should be noted that SEVIRI is not a spectrometer but an imager: SEVIRI measures TOA radiances over the full Earth disk centered at 0° latitude and 0° longitude every 15 minutes in twelve channels across the visible and near-infrared part of the spectrum [135]. Eleven channels have a narrow bandwidth at low spatial resolution (3 x 3 km^2 at sub-satellite point) and one channel has a broad bandwidth (0.6 - 0.9 μm) at high spatial resolution (1 x 1 km^2). The EUMETSAT Nowcasting and Very Short Range Forecasting Satellite Application Facility (NWC SAF) [76] processes the signals of those SEVIRI channels into cloud properties, such as cloud masks, cloud optical thickness (COT) and cloud top height, allowing for the continuous space-based monitoring of clouds throughout the diurnal cycle.

The gas abundances, aerosol and cloud properties mentioned above are retrieved by the comparison of spaceborne measurements of the reflected sunlight by the local Earth's atmosphere-surface system with model simulations of this reflected sunlight. If physical phenomena occur in the Earth's atmosphere-surface system that are not included in the model atmosphere of the simulations, the retrieval may be biased. Examples of such phenomena are cloud shadows and the shadow of the Moon during solar eclipses, which are usually not taken into account in atmospheric retrieval algorithms of satellite spectrometers. However, if the shadows would accurately be captured by the model, actual measurements of the potential physical impact of shadows on the atmosphere could be derived. This thesis focuses on determining the impact of cloud shadows on aerosol and cloud retrievals, in particular of TROPOMI and SEVIRI. In the rest of this section, an introduction is given to the topic 'shadows in satellite remote sensing of aerosols and clouds' (Sects. 1.1 to 1.1.3). Then, the research questions are stated (Sect. 1.2) and the thesis structure is provided (Sect. 1.3).

1.1. SHADOWS IN SATELLITE MEASUREMENTS

1.1.1. SHADOW TYPES

Shadows can be found in volumes or on surface areas where direct light from a light source, such as the sun, is (partly) blocked by a(n) (partly) opaque object, such as a cloud, mountain, or the Moon during a solar eclipse. Shadows are not the volumes or surface areas themselves, but refer to absence, or decrease, of their direct illumination. Those volumes or surface areas appear darker than their illuminated surroundings, causing

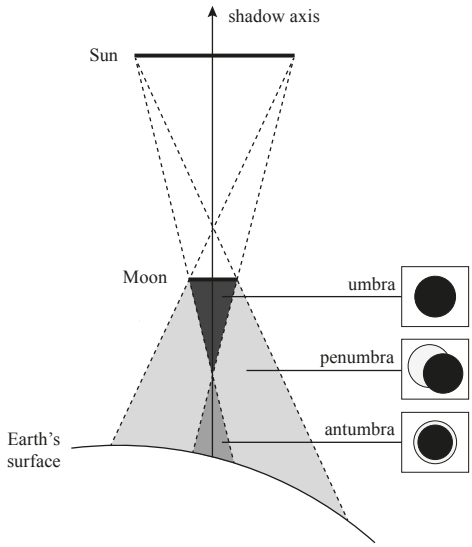

Figure 1.1: Sketch of the Moon shadow types that may occur during a solar eclipse (not to scale). In this example, an annular solar eclipse is experienced at the Earth's surface.

shadows to be able to be perceived. Those shadows are said to be 'cast' on the volumes or surface areas. For example, a cloud can cast a shadow on another cloud, a volume of the atmosphere, or the surface below the cloud. Another type of shadow is the self-shadow, referring to the part of the light-blocking object which is not illuminated by direct light.

The cast shadow can consist of either one of the following two types of shadows: the umbra (or total shadow) or the penumbra (or half-shadow). For an observer in the umbra of an opaque object, the light source cannot directly be perceived. All light that reaches the observer has been reflected by objects or scattered at least once inside the atmosphere. Examples are the umbra during a total solar eclipse, or a the umbra of a large and thick cloud. In the penumbra during a partial solar eclipse, or in the penumbra along the cloud edge, the observer still sees part of the unattenuated solar disk, as illustrated in Fig. 1.1. The size, shape and relative darkness of a shadow depend on the size, shape and brightness of the light source, on the size, shape and opacity of the light-blocking object, on the composition of the medium through which the light (and shadows) travel(s), and on the locations of the light source, the light-blocking object, and the volume or surface area that is cast by the shadow.

1.1.2. SOLAR ECLIPSES IN SATELLITE MEASUREMENTS

During a solar eclipse, the solar irradiance reaching TOA is reduced as the Moon blocks (part of) the sunlight, consequently reducing the radiance reflected by the Earth. Because the solar irradiance is commonly calculated or measured only once a day as already mentioned above, it does not include the eclipse effect, and the computed TOA reflectance is biased. Consequently, the atmosphere measurements retrieved from the TOA reflectance are distorted in the shadow of the Moon or, after raising an eclipse flag,

undefined. It should be noted that, also in the case of a total solar eclipse, the vast majority (> 99%) of the Moon shadow on the Earth's surface is penumbra, in which solar obscuration percentages between 0 and almost 100% are encountered. In those regions, there is still direct sunlight illuminating the scene and satellites still receive the reflected sunlight, albeit in a reduced amount.

An example of an air quality product of TROPOMI that is clearly affected by solar eclipses is the ultraviolet (UV) Absorbing Aerosol Index (AAI). The AAI is a qualitative measure of absorbing aerosols in the atmosphere such as desert dust, volcanic ash and anthropologically produced soot, and can be used to daily and globally track the aerosol plumes from dust storms, forest fires, volcanic eruptions and biomass burning [80, 30, 165, 150]. The AAI is retrieved from TOA reflectance measurements at two wavelengths in the UV-range, 340 nm and 380 nm, hence the AAI is directly affected by the obscuration during a solar eclipse. Since the start of the nominal operational mode of the TROPOMI spectrometer instrument on board the S5P satellite in May 2018, 14 solar eclipses occurred, and the solar eclipses left strong positive signatures in the AAI maps. TROPOMI data contains an eclipse flag indicating the eclipse occurrence at a ground pixel. For satellite instruments that do not contain an eclipse flag, such as the GOME-2 instrument, these eclipse anomalies propagate into anomalies in temporal average maps, potentially resulting in false conclusions about the mean aerosol effect in that time period. Another example of affected satellite data during solar eclipses are satellite images of the SEVIRI instrument. They show spatio-temporally varying darkening [47, 113] and satellite retrievals of cloud cover and cloud optical thickness (COT) show significantly decreased values. This thesis deals with the question to what extent the AAI increases and the cloud abundance decreases during a solar eclipse are physical, and to what extent the retrieval algorithms are biased due to the solar eclipse.

In general, the unavailability of satellite data during solar eclipses is unfortunate, because solar eclipses provide the opportunity to study the impact of variations of sunlight on the Earth's atmosphere. This knowledge is becoming increasingly relevant nowadays as artificially reducing the net incoming solar radiation, or solar geoengineering, by placing solar reflectors in space [36, 6, 43, 99, 112, 130] or injecting reflecting aerosols into the stratosphere [29, 126], is considered as a possibly strategy to counteract the current and future global temperature rise [74, 88, 140, 81]. However, solar eclipses show that the reduction of the solar irradiance might influence the photochemical activity in the atmosphere [48, 2, 59, 187], or may affect the clouds [54, 5]. Because the geometry of the Moon shadow on the Earth's surface is an astronomical well-understood problem [39, 101], solar eclipses are ideal to compare with, and possibly improve, atmospheric chemistry and cloud models. Until this thesis, measurements of trace gases and clouds during solar eclipses only have been taken from the ground [48, 2, 59, 187, 54]. Measuring the atmospheric responses from the ground only provides information a single location. The precise locations of the eclipse-induced physical phenomena can be hard to predict and are sometimes inaccessible for ground-based observers. In particular for studying the eclipse-induced evolution of cumulus clouds (which naturally change size and shape constantly), space-based measurements of large areas are desired.

1.1.3. CLOUD SHADOWS IN SATELLITE MEASUREMENTS

The spatial resolutions of TOMS, GOME, SCIAMACHY, OMI and GOME-2 have been 50 × 50 km^2, 320 × 40 km^2, 60 × 30 km^2, 24 × 13 km^2 and 80 × 40 km^2, respectively. Those resolutions are too coarse to discern kilometer-scale clouds or cloud shadows. The pixels of those spectrometers often have been partly cloudy, such that the effects of clouds, cloud shadows and cloud-free regions are blended. Because of the inability to distinguish between those effects and the complexity of three-dimensional (3-D) radiative transfer, state-of-art algorithms for satellite spectrometers employ one-dimensional (1-D) radiative transfer models, which neglect 3-D cloud effects on cloud-free regions inside the partly cloudy pixels or on adjacent cloud-free pixels. For example, the FRESCO (Fast REtrieval Scheme for Clouds from the Oxygen A band) cloud retrieval algorithm uses the independent pixel approximation, and does not take into account cloud shadows [78, 183]. However, although cloud shadows are hardly visible on the coarse resolution measurement grids of those spectrometers, they do in principle contaminate the total radiances of the large pixels.

The small pixel size of 5.6 × 3.6 km^2 of TROPOMI causes cloud shadows to be detectable. Cloud shadow signatures can be found along cloud edges, manifested as pixels with smaller radiances than measured in their cloud-free neighborhood. Contrary to the large pixel sizes of its predecessors, the small pixel size of TROPOMI sometimes causes one or several pixels to be fully covered by a single cloud shadow, particularly for high clouds at large viewing and/or solar zenith angles. Smaller measured radiances result in lower derived TOA reflectances, potentially affecting TROPOMI's air quality products. For example, cloud shadows are not yet taken into account in the current AAI retrieval, and their influence on the AAI has not yet been investigated. The AAI is an important input for the retrieval algorithms of other TROPOMI products. For example, the pixel selection for the aerosol layer height (ALH) [131, 108] and aerosol optical thickness (AOT) [31] retrievals of TROPOMI is based on the AAI. Hence, AAI features that are not related to absorbing aerosols, for example caused by the ocean glint, clouds at specific scattering geometries [80], and cloud shadows, may be undesired for those retrievals.

The natural horizontal variation of the AAI complicates the quantification of the cloud shadow induced AAI signatures. Individual cloud shadow pixels may be identified manually in maps of TROPOMI data through visual inspection. For the automatic removal or correction of shadow contaminated TROPOMI data, and for the statistical analysis of shadow effects on large TROPOMI data sets, a cloud shadow detection algorithm is needed. In addition, in order to understand the cloud shadow impact on air quality products such as the AAI, a 3D radiative transfer code is needed that can simulate the effect of 3D cloud structures.

1.2. RESEARCH QUESTIONS

The research questions of this thesis are:

1. What is the impact of **solar eclipses** on the **AAI** as measured by TROPOMI?
2. What is the impact of **solar eclipses** on **clouds** as measured by SEVIRI?
3. What is the impact of **cloud shadows** on the **AAI** as measured by TROPOMI?

All research questions stated above consist of two subquestions:

A What is the shadow-induced bias in the respective satellite retrieval algorithm?

B What is the physical impact of the shadow on the atmospheric constituent?

1.3. THESIS STRUCTURE

This thesis is structured as follows. Chapter 2 explains how to restore the top-of-atmosphere (TOA) reflectance, measured by Earth observation satellites, during solar eclipses. As a proof of concept, we show the restored UV Absorbing Aerosol Index (AAI) measurements by TROPOMI, which is retrieved from the TOA reflectance, in the shadow of the Moon. In Chapter 3, we apply the similar data recovery method, but now to the cloud retrieval algorithm of the SEVIRI instrument on board of the geostationary satellite Meteosat, and we demonstrate the impact of solar eclipses on clouds.

In Chapters 4 to 5, other shadow types in satellite measurements are discussed: the shadows of clouds. Chapter 4 demonstrates DARCLOS, our cloud shadow detection algorithm for TROPOMI. In Chapter 5, we apply DARCLOS to TROPOMI data to analyze the cloud shadow impact on the TROPOMI AAI. Here, we also show simulations of the cloud shadow effect on the AAI using our newly developed 3D polarized radiative transfer code MONKI. Finally, in Chapter 6 we state the most important conclusions of this thesis.

Chapters 2, 3, 4, and 5 have been published as scientific articles in the scientific journals Atmospheric Chemistry and Physics (ACP), Nature Communications Earth and Environment (Nat. Commun. Earth Environ.), and Atmospheric Measurement Techniques (AMT). The links to the papers are provided in those chapters.

2

RESTORING THE TOP-OF-ATMOSPHERE REFLECTANCE DURING SOLAR ECLIPSES

A proof of concept with the UV Absorbing Aerosol Index measured by TROPOMI

During a solar eclipse the solar irradiance reaching the top-of-atmosphere (TOA) is reduced in the Moon shadow. The solar irradiance is commonly measured by Earth observation satellites before the start of the solar eclipse and is not corrected for this reduction, which results in a decrease of the computed TOA reflectances. Consequently, air quality products that are derived from TOA reflectance spectra, such as the ultraviolet (UV) Absorbing Aerosol Index (AAI), are distorted or undefined in the shadow of the Moon. The availability of air quality satellite data in the penumbral and antumbral shadow during solar eclipses, however, is of particular interest to users studying the atmospheric response to solar eclipses. Given the time and location of a point on the Earth's surface, we explain how to compute the obscuration during a solar eclipse taking into account wavelength-dependent solar limb darkening. With the calculated obscuration fractions, we restore the TOA reflectances and the AAI in the penumbral shadow during the annular solar eclipses on 26 December 2019 and 21 June 2020 measured by the TROPOMI/S5P instrument. We compare the calculated obscuration to the estimated obscuration using an uneclipsed orbit. In the corrected products, the signature of the Moon shadow disappeared, but only if wavelength-dependent solar limb darkening is taken into account. We find that the Moon shadow anomaly in the uncorrected AAI is caused by a reduction of the measured reflectance at 380 nm, rather than a color change of the measured light. We restore common

This chapter has been published in Atmospheric Chemistry and Physics **21**, 8593–8614 (2021) [168].

AAI features such as the sunglint and desert dust, and we confirm the restored AAI feature on 21 June 2020 at the Taklamakan desert by measurements of the GOME-2C satellite instrument on the same day but outside the Moon shadow. No indication of local absorbing aerosol changes caused by the eclipses was found. We conclude that the correction method of this paper can be used to detect real AAI rising phenomena during a solar eclipse and has the potential to restore any other product that is derived from TOA reflectance spectra. This would resolve the solar eclipse anomalies in satellite air quality measurements in the penumbra and antumbra, and would allow for studying the effect of the eclipse obscuration on the composition of the Earth's atmosphere from space.

2.1. INTRODUCTION

Earth observation satellite spectrometer instruments are designed to measure the particles and gases in the Earth's atmosphere. They rely upon the reflectance of the incident sunlight on the top-of-atmosphere (TOA) at various wavelengths in the UV, visible, near-infrared and shortwave-infrared spectral domains. These TOA reflectances are calculated through the division of the measured Earth radiance by the measured solar irradiance. During a solar eclipse, the solar irradiance reaching TOA is reduced as the Moon blocks (part of) the sunlight, reducing the Earth radiance. Because the solar irradiance is commonly measured before the start of the eclipse, the atmosphere measurements are distorted in the shadow of the Moon or, after raising an eclipse flag, undefined.

Since the start of the nominal operational mode of the TROPOMI spectrometer instrument on board the S5P satellite in May 2018, 7 solar eclipses occurred, 6 of which have been measured by TROPOMI. An example of an air quality product of TROPOMI that suffers from the Moon shadow is the ultraviolet (UV) Absorbing Aerosol Index (AAI). The AAI is a qualitative measure of absorbing aerosols in the atmosphere such as desert dust, volcanic ash and anthropologically produced soot, and can be used to daily and globally track the aerosol plumes from dust storms, forest fires, volcanic eruptions and biomass burning. The AAI is retrieved from TOA reflectance measurements at two wavelengths in the UV-range, hence the AAI may directly be affected by the obscuration during a solar eclipse. Figure 2.1 is a near-global AAI map on 21 June 2020, using TOA reflectance measurements at 340 nm and 380 nm by TROPOMI. Dust aerosol plumes over the Atlantic Ocean originating from the Sahara can be identified through the AAI increase of ~ 2 to ~ 4 points relative to their surrounding regions. In Western China an AAI larger than 5 is measured, which is caused by the shadow of the Moon. TROPOMI data contains an eclipse flag indicating the eclipse occurrence at a ground pixel. For satellite instruments that do not contain an eclipse flag, such as the GOME-2 instrument, these eclipse anomalies propagate into anomalies in temporal average maps, potentially resulting in false conclusions about the mean aerosol effect in that time period.[1]

The reduction of the solar irradiance during an eclipse might influence the photochemical activity, and therefore the composition, of the Earth's atmosphere. Measurements of the speed and significance of this atmospheric response could contribute to the understanding of the sensitivity of planetary atmospheres to (variations in) their solar or stellar illumination and could possibly be used to verify atmospheric chemistry models. Ground-based measurements during solar eclipses of local ozone column fluctuations have been taken using Dobson and Brewer spectrophotometers, but the reported results are contradictory [16, 103, 23, 22]. Zerefos et al. [189] pointed out the importance of solar limb darkening and the direct to diffuse irradiance on the ozone column retrieval, but also the change in effective temperature in the ozone layer or other atmospheric conditions (different cloudiness, solar zenith angle and turbidity) may have influenced the measurements [186]. Unambiguous increases in local NO_2 concentration have been measured from the ground during solar eclipses resulting from the reduced photodissociation of NO_2 in the stratosphere [48, 2]. Unlike ozone, NO_2 reacts on a timescale of

[1] An example of a *monthly average* AAI map of the GOME-2 satellite instrument that is distorted by a solar eclipse can be found on https://d1qb6yzwaaq4he.cloudfront.net/airpollution/absaai/GOME2B/monthly/images/2019/GOME-2B_AAI_map_201912.png, visited on 22 February 2021.

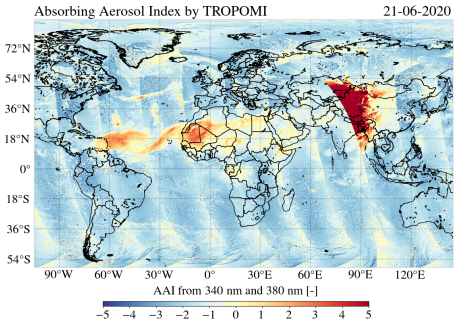

Figure 2.1: The Absorbing Aerosol Index from the 340/380 nm wavelength pair by TROPOMI on 21 June 2020. The anomaly centered at Western China is caused by the shadow of the Moon.

several minutes directly responding to the eclipse obscuration [59, 187]. Although similar information could be obtained during sunrise and sunset, Wuebbles and Chang [187] pointed out that the relatively short time durations of solar eclipses allow for a more clear identification of the major photochemical cycles in the stratosphere, due to the smaller bias from atmospheric transport, mixing and interfering chemical reactions throughout the diurnal cycle. Ground-based measurements, however, are taken at a single location. Being able to restore satellite data in the Moon shadow would allow for studying the effect of solar eclipses on the Earth's atmosphere from space at various locations with the same instrument.

The geometry of the Moon shadow on the Earth's surface is an astronomical well-understood problem and predictions of the eclipse time, location and local eclipse circumstances can be done with high accuracy [39, 101]. The eclipse obscuration at a point in the shadow can be approximated by the fraction of the area of the apparent solar disk occulted by the Moon [138]. Montornès et al. [104] approximated the eclipse obscuration by the fraction of the solar disk *diameter* occulted by the Moon in order to correct the TOA solar irradiance in the Advanced Research Weather and Forecasting (WRF-ARW) model and modeled a local surface temperature response of ~ -1 K to ~ -3 K, with a time lag between ~ 5 and ~ 15 minutes after the instant of maximum obscuration. Such wavelength-independent approximations of the eclipse obscuration fraction based on the the overlapping disks indeed could work well to estimate the shortwave fluxes, depending on the desired accuracy. If the spectral variation of the measured light is to be studied, however, the wavelength dependence of the eclipse obscuration fraction, caused by solar limb darkening, cannot be neglected. Koepke, Reuder, and Schween [79] provided the formulae to compute the eclipse obscuration fraction for total eclipses taking into account solar limb darkening if the relative position and apparent dimensions of the lunar and solar disks are known. They showed that the error in the solar irradiance close to total obscuration may become 30% at 1500 nm and 60% at 310 nm if solar limb darkening is not taken into account.

Emde and Mayer [38], Kazantzidis et al. [73] and Ockenfuß et al. [109] performed extensive 3-D radiative transfer modelling of total solar eclipses, taking into account solar limb darkening. Their work gives insight into the spectral behaviour of sunlight reach-

ing a ground sensor located in or close to the total Moon shadow and the importance of the various 3-D radiative transfer components. Emde and Mayer [38] pointed out that solar eclipses provide excellent opportunities to test 3-D radiative transfer codes against measurements because, unlike broken cloud fields, the Moon shadow's geometry is well-defined.

In this paper, we present a method to restore the TOA reflectance as measured by Earth observation satellites in the penumbra and antumbra of solar eclipses, by combining accurate eclipse predictions with the computation of the eclipse obscuration fraction taking into account wavelength-dependent solar limb darkening. We apply this method to the TOA reflectances measured by the TROPOMI/S5P satellite instrument in the penumbra during the annular solar eclipses on 26 December 2019 and 21 June 2020, and we show how the calculated obscuration fraction can be compared to the estimated obscuration fraction from measurements in an uneclipsed orbit. With the restored TOA reflectances, we compute a corrected version of the AAI and analyze the features that were otherwise hidden in the shadow of the Moon.

This paper is structured as follows. In Sect. 2.2, we explain the method to restore the measured TOA reflectance during a solar eclipse. In Sect. 2.3, we show the results of applying this method to the eclipsed TROPOMI orbits during the annular solar eclipses on 26 December 2019 and 21 June 2020. In Sect. 2.4, we discuss the limits of the method and the points of attention for future applications. In Sect. 2.5, we summarize the results and state the most important conclusions of this paper.

2.2. METHOD

Here, we explain the method to restore the measured TOA reflectance during a solar eclipse. We start with explaining the situation of measuring the TOA reflectance during a solar eclipse and how these measurements can be restored with the eclipse obscuration fraction (Sect. 2.2.1). Then, we explain the Moon shadow types (Sect. 2.2.2) and how we compute the eclipse obscuration fraction taking into account solar limb darkening, knowing the local eclipse circumstances (Sect. 2.2.3). In Sect. 2.2.4 and Appendix A.1 we explain how we compute the local eclipse circumstances from the measurement time and location of a point on the Earth's surface.

2.2.1. SOLAR IRRADIANCE CORRECTION

The spectral TOA reflectance of an atmosphere-surface system as measured by a satellite is defined as

$$R^{\text{meas}}(\lambda) = \frac{\pi I(\lambda)}{\mu_0 E_0(\lambda)}, \tag{2.1}$$

where I is the radiance reflected by the atmosphere-surface system in W m^{-2}sr^{-1}nm^{-1} and E_0 is the extraterrestrial solar irradiance perpendicular to the beam in W m^{-2}nm^{-1}. The units nm^{-1} indicate that both I and E_0 depend on wavelength λ. Also, I depends on the viewing zenith angle θ, the solar zenith angle θ_0, the viewing azimuth angle φ and the solar azimuth angle φ_0. Furthermore, we use the definitions $\mu = \cos\theta$ and $\mu_0 = \cos\theta_0$. I is measured by TROPOMI continuously at the dayside of the Earth. E_0 is measured by

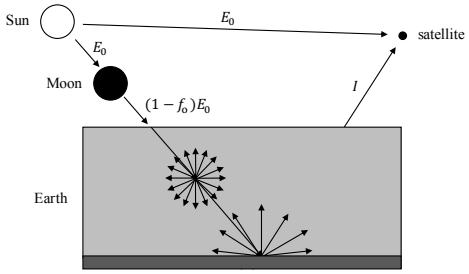

Figure 2.2: Schematic sketch of a satellite retrieving the top-of-atmosphere reflectance during a solar eclipse. I is the measured radiance reflected by the atmosphere-surface system, f_o is the eclipse obscuration fraction and E_0 is the uneclipsed solar irradiance.

TROPOMI near the North Pole once every 15 orbits, which is approximately once every calendar day.

During a solar eclipse, the solar irradiance reaching TOA is reduced, as illustrated in Fig. 2.2. The fraction of the spectral irradiance $E_0(\lambda)$ that is blocked by the Moon is the wavelength-dependent eclipse obscuration fraction, $f_o(\lambda)$. The remaining spectral irradiance at TOA is $[1\text{-}f_o(\lambda)]E_0(\lambda)$. We neglect the contribution of the Sun's corona[2]. The intrinsic spectral reflectance of the atmosphere-surface system (i.e. the fraction of the emerging radiance to the incident irradiance), is then obtained by correcting the solar irradiance:

$$R^{\text{int}}(\lambda) = \frac{\pi I(\lambda)}{\mu_0[1-f_o(\lambda)]E_0(\lambda)}. \tag{2.2}$$

If the optical properties of the atmosphere-surface system are constant just before and during the eclipse, then R^{int} is expected to be constant regardless of the eclipse conditions. We compute R^{int} from R^{meas} by combining Eq. 2.1 and 2.2:

$$R^{\text{int}}(\lambda) = \frac{R^{\text{meas}}(\lambda)}{1-f_o(\lambda)}. \tag{2.3}$$

Properties of the atmosphere-surface system can be derived during a solar eclipse from the spectrum of R^{int}. Note that potential changes of the atmosphere-surface system that are caused by the eclipse obscuration may affect R^{int}, depending on the significance and nature of these changes.

We assume that the solar irradiance is randomly polarized. Also, we neglect light travelling horizontally in the atmosphere from one ground pixel to the other. The importance of horizontal light travelling between adjacent pixels is expected to increase with increasing f_o, but will only become significant close to totality [38]. In Sect. 2.4, we reflect back on these assumptions.

[2] Emde and Mayer [38] estimated that the radiance of the corona is approximately $5.9 \cdot 10^6$ times smaller than the radiance originating from the center of solar disk.

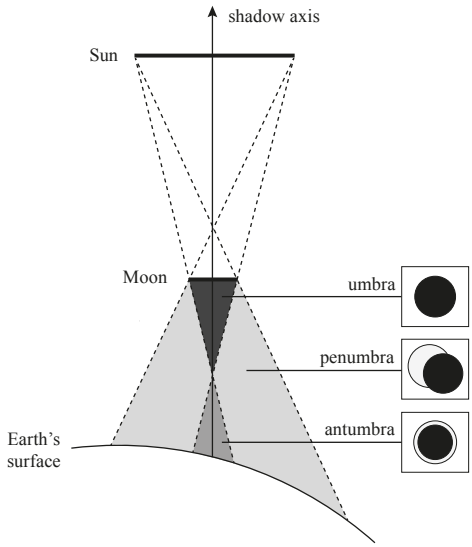

Figure 2.3: Sketch of the Moon shadow types that may occur during a solar eclipse (not to scale). In this example, an annular solar eclipse is experienced at the Earth's surface.

2.2.2. MOON SHADOW TYPES

The experienced obscuration fraction $f_o(\lambda)$ depends on the location with respect to the position of the Sun and the Moon. Figure 2.3 illustrates the shadow types that may be experienced during a solar eclipse: (1) the umbra, where the lunar disk fully occults the solar disk ($f_o(\lambda) = 1$) during a total eclipse, (2) the antumbra, where every part of the lunar disk occults the solar disk but full obscuration is not reached ($0 < f_o(\lambda) < 1$) during an annular eclipse, and (3) the penumbra, where only a part of the lunar disk occults the solar disk ($0 < f_o(\lambda) < 1$) during a partial, total or annular eclipse. The Moon-Sun axis is often referred to as the 'shadow axis' as indicated in Fig. 2.3. The penumbra is always present during an eclipse. Whether an umbra or an antumbra is present on the Earth's surface depends on the distances to the Moon and the Sun, which vary in time as the Moon orbits the Earth and the Earth orbits the Sun, both in elliptical orbits.

In this paper, we do not study the umbra because Eq. 2.3 breaks down when $f_o(\lambda) = 1$. The solar irradiance correction only applies to pixels located in the penumbra or antumbra, and for which the signal-to-noise is sufficient (we set the constraint $R^{\text{meas}} > 50\sigma$ where σ is the 1 standard deviation of R^{meas}). It is important to note that the area in the penumbra on the Earth's surface is always much larger than the area in the (ant)umbra on the Earth's surface, as will be shown in Sect. 2.3.

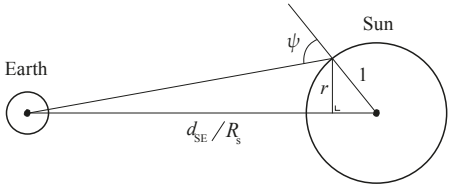

Figure 2.4: Definition of the heliocentric angle ψ used in Eq. 2.5 (not to scale). Distance d_{SE} is the geocentric Earth-Sun distance and r is the apparent distance on the solar disk from the solar disk center. All dimensions are per solar radius R_S. We neglect the effect of the sphericity of the Sun on the apparent solar disk radius, such that $r = 1$ for $\psi = 90°$.

2.2.3. OBSCURATION FRACTION

In geometrical solar eclipse predictions, the eclipse obscuration f_o is commonly computed as the fraction of the solar disk occulted by the lunar disk [138].[3] Indeed, during an eclipse, the phase angle of the Moon approaches 180 degrees and, due to its solid composition, its near-spherical shape and its optically insignificant exosphere, the apparent eclipsing Moon can be approximated by an opaque circular disk. Not every part of the solar disk, however, contributes equally to the total solar flux, as a result of darkening of the apparent solar disk toward the solar limb, which is caused by the temperature decrease with height in the Sun's photosphere [26]. As the Moon covers different parts of the solar disk during an eclipse, the relative contributions of the solar limb and the solar disk center to the total brightness varies. Furthermore, because the emitted radiance from the hot center peaks at shorter wavelengths than the emitted radiance from the cooler limb, the reduction of the solar irradiance during an eclipse is wavelength-dependent [79, 12].

We use the definition of the solar limb darkening function of Koepke, Reuder, and Schween [79]:

$$\Gamma(\lambda, r) = \frac{I_0(\lambda, r)}{I_0(\lambda, r = 0)}, \tag{2.4}$$

where $I_0(\lambda, r = 0)$ is the radiance originating from the solar disk center and $I_0(\lambda, r)$ is the radiance originating from the circle with radius r from the solar disk center, with r ranging from 0 (center) to 1 (limb). Koepke, Reuder, and Schween [79] parameterized the function Γ by using the simple wavelength-dependent formula of Waldmeier [181] based on the temperature of the Sun's surface. We, instead, follow Ockenfuß et al. [109] employing the parametrization of Pierce and Slaughter [118] based on observations by the McMath-Pierce Solar Telescope, for which the limb darkening predictions showed a better agreement with measurements of the solar spectral irradiance during the total solar eclipse on 21 August 2017 [12]. Function Γ is computed using the 5^{th} order polynomial

$$\Gamma(\lambda, r) = \sum_{k=0}^{5} a_k(\lambda) \cos^k(\psi(r)), \tag{2.5}$$

[3] The eclipse obscuration fraction should not be confused with the eclipse magnitude, which is the fraction of the diameter of the solar disk occulted by the Moon.

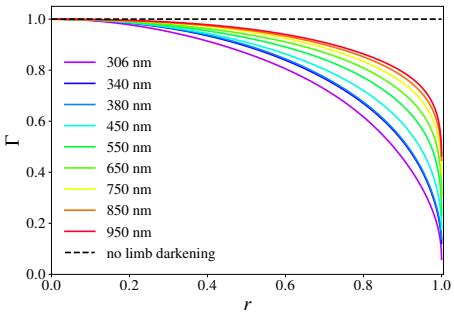

Figure 2.5: Limb darkening function Γ for wavelengths ranging from 306 nm to 950 nm, using the limb darkening coefficients of Pierce and Slaughter [118] and Pierce, Slaughter, and Weinberger [120], as a function of distance r from the solar disk center (where $r = 0$), with $r = 1$ the solar limb. The dashed line is the result without solar limb darkening taken into account ($\Gamma = 1$).

where a_k are the limb darkening coefficients tabulated by Pierce and Slaughter [118] for wavelengths between 303.3 nm and 729.7 nm, and by Pierce, Slaughter, and Weinberger [120] for wavelengths between 740.4 and 2401.8 nm. Angle ψ is the heliocentric angle as illustrated in Fig. 2.4 and can be computed, for any r with $0 < r < 1$, from the radius of the Sun, $R_s = 695700$ km, and from the Earth-Sun distance, d_{SE}, which we retrieve from a geocentric ephemeris of the Sun[4]. We linearly interpolate Γ between the tabulated wavelengths in order to compute Γ at the wavelengths of interest. In Fig. 2.5, Γ is plotted against r. Solar limb darkening is most significant at the shortest wavelengths, for which the difference between the hot center and relatively cooler limb is most pronounced [109].

Figure 2.6 is a sketch of the lunar disk occulting the solar disk during an annular solar eclipse. The dimensions of the disks are normalized by the solar disk radius, such that the solar disk radius equals 1. The lunar disk radius is denoted by r_m. The solar disk and lunar disk centers are denoted by C_s and C_m, respectively. Area $r\,d\alpha'\,dr$ is a differential area element of a circular ring with radius r centered at C_s. If no eclipse occurs, the expression for the irradiance from the solar disk, E_0, follows from the integration of I_0 (Eq. 2.4) over the solar disk area [79]:

$$\begin{aligned} E_0(\lambda) &= \int_0^1 \int_0^{2\pi} I_0(\lambda, r=0) \cdot \Gamma(\lambda, r) \cdot r\,d\alpha'\,dr \\ &= 2\pi \cdot I_0(\lambda, r=0) \cdot \int_0^1 \Gamma(\lambda, r) \cdot r\,dr. \end{aligned} \tag{2.6}$$

During an eclipse, the irradiance from the solar disk is reduced by f_o, resulting from the lunar disk overlapping the solar disk. At distance r from C_s, the angle of the sector of the solar disk that is occulted by the lunar disk is 2α (see Fig. 2.6). The solar irradiance that is blocked by the Moon is

[4]Geocentric Ephemeris for the Sun, Moon and Planets Courtesy of Fred Espenak, http://www.astropixels.com/ephemeris/sun/sun2019.html, visited on 3 September 2020.

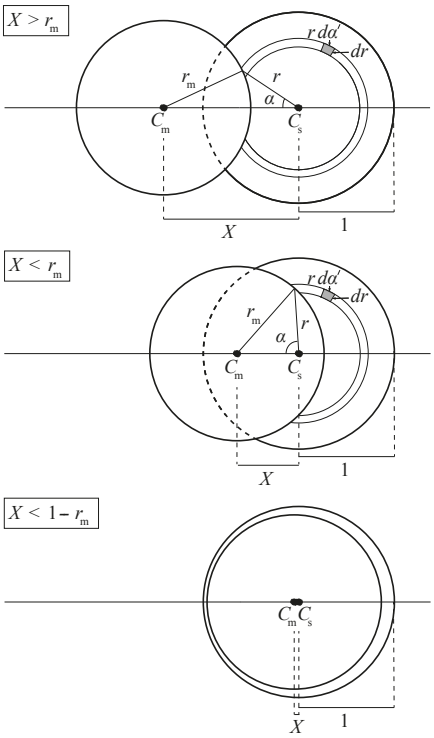

Figure 2.6: Sketches of the lunar disk (centered at C_m) occulting the solar disk (centered at C_s) during an annular solar eclipse. Here, $r_m < 1$ where r_m is the radius of the lunar disk and the solar disk radius equals 1. X is the distance between C_m and C_s. For $X < r_m + 1$, the lunar disk occults the solar disk. The eclipse obscuration fraction f_o increases with decreasing X. The annular phase occurs when $X < 1 - r_m$ (bottom sketch). Angle α is half the sector angle of the solar disk occulted at distance r by the lunar disk.

$$
\begin{aligned}
f_o(\lambda)E_0(\lambda) &= 2\int_0^1 \int_0^\alpha I_0(\lambda, r=0)\cdot\Gamma(\lambda,r)\cdot r\,d\alpha'\,dr \\
&= 2\pi\cdot I_0(\lambda, r=0)\cdot\int_0^1 \frac{\alpha(r,X,r_m)}{\pi}\Gamma(\lambda,r)\cdot r\,dr. \qquad (2.7)
\end{aligned}
$$

The expression for α follows from the geometrical consideration of the solar and lunar disks, based on X, r and r_m:

$$
\alpha(r,X,r_m) = \qquad (2.8)
$$

$$
\begin{cases}
0 & \text{if} \quad r \le |X - r_m| \ \text{ and } \ X > r_m, \\
\pi & \text{if} \quad r \le |X - r_m| \ \text{ and } \ X \le r_m, \\
\cos^{-1}\left[\frac{r^2+X^2-r_m^2}{2\cdot r\cdot X}\right] & \text{if} \quad r > |X - r_m| \ \text{ and } \ r \le X + r_m, \\
0 & \text{if} \quad r > |X - r_m| \ \text{ and } \ r > X + r_m.
\end{cases}
$$

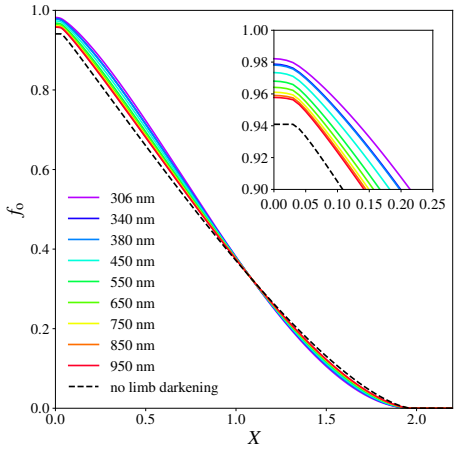

Figure 2.7: The obscuration fraction f_o as a function of Moon-Sun disk center distance normalized to the solar disk radius, X, for wavelengths ranging from 306 nm to 950 nm, using the limb darkening coefficients of Pierce and Slaughter [118] and Pierce, Slaughter, and Weinberger [120]. The dashed line is the result without solar limb darkening taken into account ($\Gamma = 1$). The assumed value for r_m is 0.97, corresponding to the instant of greatest eclipse during the annular solar eclipse on 26 December 2019.

Our expression for α slightly differs from the one of Koepke, Reuder, and Schween [79], who studied a total solar eclipse ($r_m \geq 1$). Their expression is not valid during the annular phase ($X < 1 - r_m$) of an annular eclipse, where r can be larger than $X + r_m$ while $r > |X - r_m|$ (cf. bottom sketch in Fig. 2.6), and therefore cannot be used to compute obscuration variations in the antumbra. Obscuration variations in the antumbra are most significant for annular eclipses with a relatively small r_m, for which the duration of the annular phase is relatively long. Equation 2.8 is valid in the umbra, penumbra and in the antumbra, and thus can be used during all phases of any solar eclipse type.

The eclipse obscuration fraction is computed by combining Eq. 2.6 and 2.7:

$$f_o(X, r_m, \lambda) = \frac{\int_0^1 \frac{\alpha(r,X,r_m)}{\pi} \Gamma(\lambda, r) \cdot r\, dr}{\int_0^1 \Gamma(\lambda, r) \cdot r\, dr}. \tag{2.9}$$

Figure 2.7 shows f_o as a function of X, for wavelengths ranging from 306 nm to 950 nm, compared to the computations without limb darkening taken into account ($\Gamma = 1$), for an assumed r_m of 0.97 corresponding to the instant of greatest eclipse[5] during the annular solar eclipse on 26 December 2019. The first point of contact occurs at $X = 1 + r_m = 1.97$. As the disk centers move closer to each other, X decreases and f_o increases. The differences with the results for $\Gamma = 1$ are again most pronounced at the shortest wavelengths (cf. Fig. 2.5). During the starting phase of the eclipse, the Moon occults the limb of the Sun, and not taking into account solar limb darkening results in a maximum overestimation of f_o of 0.025 at 306 nm and $X = 1.52$. When the eclipse approaches the annular phase, the Moon occults the center of the Sun, and not taking into account solar limb darkening results in a maximum underestimation of f_o of 0.069 at 306 nm and $X = 0.33$.

[5] The instant of greatest eclipse is the point in time when the shadow axis passes closest to Earth's center.

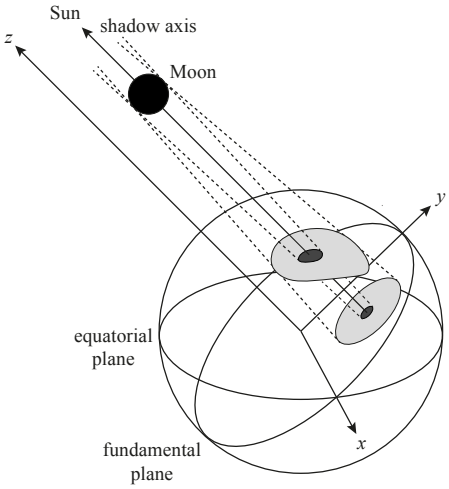

Figure 2.8: Sketch of the fundamental reference frame (not to scale). The Moon shadow that is cast on the Earth's surface has a complicated shape, but the shadow on any plane parallel to the fundamental plane ($z = 0$) has a circular shape, and the local eclipse circumstances solely depend on the distance to the shadow axis.

The annular phase occurs when $X < 1 - r_m = 1 - 0.97 = 0.03$. Note that, for total eclipses, totality would occur when $X < r_m - 1$. The maximum obscuration for the ground-based observer, for a certain value of r_m, is reached when the centers of the lunar disk and the solar disk coincide ($X = 0$). From Eq. 2.8, we derive that if $X = 0$, $\alpha = \pi$ for $0 < r \leq r_m$ and $\alpha = 0$ for $r > r_m$. Given r_m, the maximum obscuration during an annular ($r_m < 1$) or a total ($r_m \geq 1$) eclipse is expressed by

$$f_o(X = 0, r_m, \lambda) = \begin{cases} \frac{\int_0^{r_m} \Gamma(\lambda,r)\cdot r dr}{\int_0^1 \Gamma(\lambda,r)\cdot r dr} & \text{if} \quad r_m < 1, \\ 1 & \text{if} \quad r_m \geq 1. \end{cases} \tag{2.10}$$

If $\Gamma = 1$, the maximum obscuration equals the area of the lunar disk divided by the area of the solar disk: $f_o(X = 0) = \pi r_m^2/\pi = 0.941$ at the instant of greatest eclipse on 26 December 2019. At 306 nm, f_o at $X = 0$ equals 0.982. Note that f_o for $\Gamma = 1$ is constant within the annular phase, while the limb darkened curves (colored lines in Fig. 2.7) show variations of f_o within the annular phase.

2.2.4. ECLIPSE GEOMETRY

The lunar disk radius, r_m, and the separation between the lunar and solar disk, X, depend on the location on Earth with respect to the position of the Moon and the Sun. X and r_m can be defined for each combination of location and measurement time of a ground pixel at the Earth's surface, i.e.

$$X = X(\delta, \vartheta, h, t_1), \tag{2.11}$$

$$r_m = r_m(\delta, \vartheta, h, t_1), \tag{2.12}$$

where δ and ϑ are the ground pixel's geodetic latitude and longitude, respectively, h is the height with respect to the Earth reference ellipsoid and t_1 is the measurement time belonging to the ground pixel. We transform δ, ϑ and h to geocentric coordinates in the so-called fundamental reference frame. The z-axis of the fundamental reference frame is parallel to the shadow axis, as illustrated in Fig. 2.8, which simplifies geometrical eclipse computations significantly. This idea was developed by Friedrich Wilhelm Bessel in the 19$^{\text{th}}$ century and has widely been employed to predict local circumstances of solar eclipses [25, 101, 138]. Even in this era of digital computers it is the most powerful eclipse prediction technique[6]. The elements that define the orientation of the fundamental reference frame and the dimensions of the shadow are the so-called Besselian elements which are precomputed for every eclipse separately and published by NASA [39]. For a certain value of z in the fundamental reference frame, the local eclipse circumstances solely depend on the ground pixel's distance to the shadow-axis. In Appendix A.1, we provide the recipe for the computation of X and r_{m} from δ, ϑ, h and t_1. We verified r_{m} and the ground track of the shadow axis ($X = 0$) on 26 December 2019 with the eclipse predictions by Fred Espenak, NASA/Goddard Space Flight Center[7]. The mean absolute differences between our results and the NASA results for r_{m}, δ and ϑ were 0.002, 0.015° and 0.089°, respectively.[8]

2.3. RESULTS

Here, we present the results of our computations of the eclipse obscuration fractions (Eq. 2.9) in the TROPOMI orbits and the corresponding restored TOA reflectance spectra (Eq. 2.3) during the annular solar eclipses on 26 December 2019 (Sect. 2.3.1) and 21 June 2020 (Sect. 2.3.2). With the restored TOA reflectance spectra, we correct the UV Absorbing Aerosol Index (AAI) and analyze the results. We use the example of 26 December 2019 to compare the calculated obscuration fractions to the estimated obscuration fractions from observations in an uneclipsed orbit, and to explain the AAI correction in detail. The example of 21 June 2020 is discussed more qualitatively, in which we focus on the AAI feature that we restore.

2.3.1. ANNULAR SOLAR ECLIPSE ON 26 DECEMBER 2019

On the 26$^{\text{th}}$ of December, 2019, the Moon shadow during the annular solar eclipse followed a path along parts of Northeast Africa, Asia, and Northwest Australia. Figure 2.9 shows the area on the Earth's surface that was located in the penumbra (in blue) and in the antumbra (in yellow) at the instant of greatest eclipse, computed on a latitude-longitude grid with a step size of 0.05°. At the instant of greatest eclipse, the duration of the annular phase for a local observer at 1.0°N latitude and 102.2°E longitude was 3 minutes and 40 seconds, while the complete eclipse duration was 3 hours, 51 minutes

[6] For more details, see https://eclipse.gsfc.nasa.gov/SEcat5/beselm.html, visited on 13 August 2020.

[7] See https://eclipse.gsfc.nasa.gov/SEpath/SEpath2001/SE2019Dec26Apath.html, visited on 9 October 2020.

[8] Fred Espenak rounded r_{m} to 3 decimal digits while our results were double precision numbers. The differences in δ and ϑ were of the order of magnitude 0.01°, which was the step size of the latitude-longitude grid that we used for this verification.

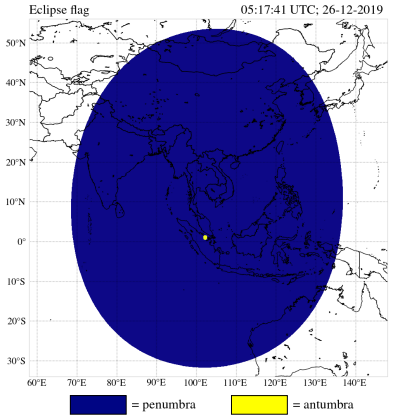

Figure 2.9: Moon shadow types at the instant of greatest eclipse during the annular solar eclipse on 26 December 2019.

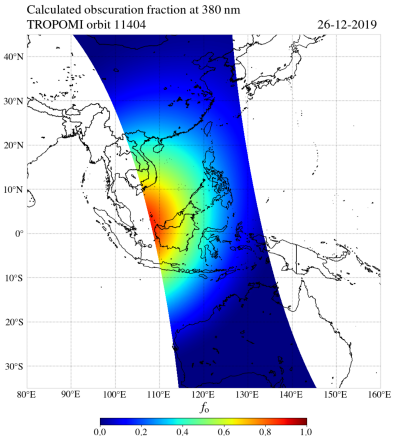

Figure 2.10: The calculated eclipse obscuration fraction at 380 nm for the ground pixels in TROPOMI orbit 11404.

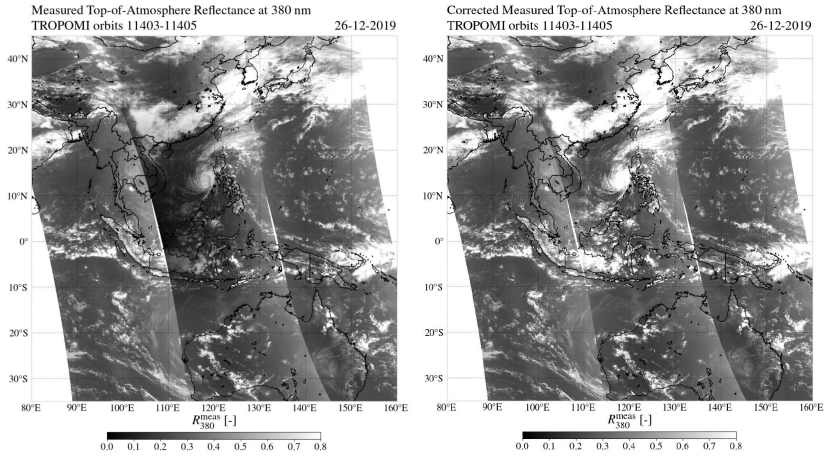

Figure 2.11: The measured top-of-atmosphere reflectance at 380 nm by TROPOMI on 26 December 2019 at Southeast Asia in orbits 11403-11405, uncorrected (left) and after the solar irradiance correction (right).

and 13 seconds.[9] We compute that the penumbral shadow radius, perpendicular to the shadow axis at the Earth's surface, was 3537.3 km, while the antumbral shadow radius, perpendicular to the shadow axis at the Earth's surface, was 53.7 km. The area in the antumbra on the Earth's surface was 0.02% of the total area in the shadow of the Moon (antumbra + penumbra) on the Earth's surface.

RESTORED TOA REFLECTANCE

During the annular solar eclipse on 26 December 2019, TROPOMI measured the penumbra in orbit 11404 between 04:49:46 UTC and 05:48:19 UTC. The left image in Fig. 2.11 shows the measured TOA reflectance (without solar irradiance correction) at 380 nm on 26 December 2019, R_{380}^{meas}, in three adjacent orbits over Southeast Asia. An apparent decrease of R_{380}^{meas} may be observed between 5°S and 25°N latitude, as shown by the dark shade in orbit 11404. Note that the brightening of the sky at larger viewing zenith angles, due to the increase of multiple Rayleigh scattering, is also observed in each orbit, manifesting itself in a subtle increase of R_{380}^{meas} toward the east and west edges of the swaths.

Figure 2.10 shows f_o at 380 nm that we calculated for the ground pixels of the TROPOMI UVIS detector in orbit 11404. The antumbra, in which f_o at 380 nm peaks at 0.976 (see Fig. 2.7), was not captured because the antumbra was located slightly out of sight in the West. The maximum calculated f_o for this orbit is 0.89 at 2.27°N latitude and 108.12°E longitude. Figure 2.10 shows that the eclipse obscuration in orbit 11404 was not limited to the Gulf of Thailand and the South China Sea: small obscuration fractions ($0 < f_o < 0.4$) could be experienced in Eastern China and the Northwest coast of Australia.

The right image in Fig. 2.11 shows the restored TOA reflectance at 380 nm, that is, after the correction for the eclipse obscuration (Eq. 2.3) in orbit 11404. The dark shade that could be observed in the left image in Fig. 2.11, resulting from the decreased R_{380}^{meas} in the Moon shadow, has disappeared. The appearance of the corrected R_{380}^{meas} in orbit 11404 is comparable to the appearance of R_{380}^{meas} in orbits 11403 and 11405.

To analyze the reflectance correction more quantitatively, Fig. 2.12 shows the average R_{380}^{meas} per scanline[10] in orbit 11404 against the mean latitude in the scanline (i.e., the average of all pixel rows), and the corresponding average calculated f_o at 380 nm. The dotted line represents R_{380}^{meas} before the solar irradiance correction, and the solid line represents R_{380}^{meas} after the solar irradiance correction. The peak in both curves at 14°N is caused by the spiral cloud deck between Vietnam and the Philippines, and the peak at 25°N latitude is caused by the cloud deck above Southeast China (cf. Fig. 2.11). Before the solar irradiance correction, the lowest values are measured where f_o is highest, between 3°S and 10°N latitude. After the solar irradiance correction, the R_{380}^{meas} curve is increased, but only at the latitudes where the Moon shadow resided.

COMPARISON TO THE OBSERVED OBSCURATION FRACTION

The restored TOA reflectance during an eclipse that we showed in Sect. 2.3.1 can be considered the intrinsic reflectance R^{int} of the atmosphere-surface system, as explained in Sect. 2.2.1. If the optical properties of the atmosphere-surface system are not affected

[9] See https://eclipse.gsfc.nasa.gov/SEgoogle/SEgoogle2001/SE2019Dec26Agoogle.html, visited on 9 September 2020.

[10] The line at the Earth's surface perpendicular to the flight direction defined by the satellite swath which is roughly oriented West-East.

by the eclipse, R_{int} approximates the TOA reflectance as if there were no eclipse. Consequently, the eclipse obscuration f_o at 380 nm can be estimated from the comparison of observations of R_{380}^{meas} inside and outside the Moon shadow, and can be used to verify the calculated f_o at 380 nm from theory.

Orbit 11403 (east of orbit 11404) was not eclipsed and preceded the eclipsed orbit 11404. We compare each ground pixel of orbit 11404 to its equivalent in orbit 11403, i.e., for the same scanline and pixel row, such that differences in illumination and viewing

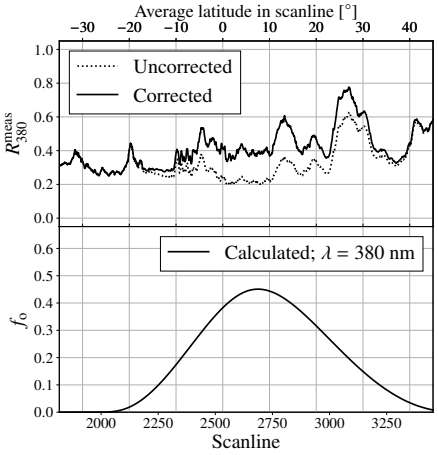

Figure 2.12: The average solar irradiance corrected (solid line) and uncorrected (dotted line) measured top-of-atmosphere reflectance at 380 nm by TROPOMI at 26 December 2019 in orbit 11404 per scanline (top image), and the corresponding average calculated obscuration fraction f_o at 380 nm (bottom image).

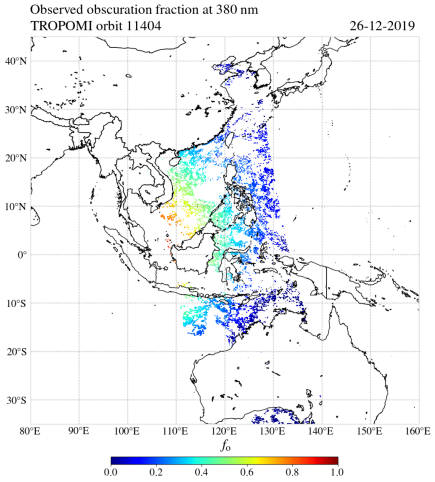

Figure 2.13: The observed eclipse obscuration fraction at 380 nm for the ground pixels in TROPOMI orbit 11404 that passed the filters described in Sect. 2.3.1.

geometry are negligible. That is, we compute the observed f_o at 380 nm as (cf. Eq. 2.3)

$$f_o(\lambda = 380 \text{ nm}) \approx 1 - \frac{\left[R_{380}^{\text{meas}}\right]_{\text{eclipse}}}{\left[R_{380}^{\text{meas}}\right]_{\text{no eclipse}}}, \tag{2.13}$$

where the label 'eclipse' indicates orbit 11404 and the label 'no eclipse' indicates orbit 11403. We can compute Eq. 2.13 for pixels that have a comparable atmosphere-surface system. Therefore, we only compare ocean pixels, because, at the latitudes where the eclipse was measured in orbit 11404, orbit 11403 was mainly above the Pacific Ocean. Also, we only consider cloud-free pixels as the cloud types and cloud fractions in the two pixels will hardly be identical. In Fig. 2.7 we showed that the difference of f_o between 340 nm and 380 nm is insignificant (the f_o curves for 340 nm and 380 are virtually indistinguishable), so the ratio $R_{340}^{\text{meas}}/R_{380}^{\text{meas}}$ should not be affected by the eclipse for a constant atmosphere-surface system. That is, if the atmosphere-surface system of the pixel in orbit 11404 is approximately identical to the atmosphere-surface system of its equivalent pixel in orbit 11403, the ratio $R_{340}^{\text{meas}}/R_{380}^{\text{meas}}$ is expected to be approximately identical regardless of the eclipse conditions. Before estimating f_o from observations, we therefore apply the filter

$$\left| \left[\frac{R_{340}^{\text{meas}}}{R_{380}^{\text{meas}}}\right]_{\text{eclipse}} - \left[\frac{R_{340}^{\text{meas}}}{R_{380}^{\text{meas}}}\right]_{\text{no eclipse}} \right| < 0.01. \tag{2.14}$$

Some cloudy pixels may pass the filter of Eq. 2.14, because clouds can alter the TOA reflectance spectra at both 340 nm and 380 nm. The cloud fraction product FRESCO [78, 183] is available on the TROPOMI UVIS grid, but suffers from the eclipse. For this comparison, we apply the simple cloud filter

$$R_{340}^{\text{meas}} \cdot 0.95 > R_{380}^{\text{meas}} \tag{2.15}$$

to both orbits, which deletes the majority of the pixels with thick bright clouds. This filter is based on the fact that the TOA reflectance over the cloud-free ocean generally decreases with increasing wavelength from 340 nm to 380 nm [162], while the presence of clouds may increase the TOA reflectance spectrum toward 380 nm.

Figure 2.13 shows the observed f_o at 380 nm, computed with Eq. 2.13, that passed the filters described in this section. Note the good agreement with the calculated f_o at 380 nm in Fig. 2.10. The missing values result mostly from land or cloudy pixels in orbit 11403 or 11404. Between 0°N and 10°N latitude, at the very west side of the swath in orbit 11404, many pixels did not pass the filter of Eq. 2.14, which can be explained by the thin clouds that were present (see Fig. 2.11), but also possibly by a difference in aerosol type and concentration or ocean color with respect to the pixels in orbit 11403.

Figure 2.14 shows the calculated f_o at 380 nm (solid line) and the observed f_o at 380 nm (diamond dots) for pixel row 6 (out of 450, i.e., at the west side of the swath) and scanline 2000 to 3500. The dashed line is the calculated f_o when solar limb darkening is not taken into account ($\Gamma = 1$). Taking into account limb darkening in the calculation of f_o results in a much better agreement with the observed f_o at 380 nm. This can also be concluded from Fig. 2.15, where we show the calculated and observed f_o at 380 nm for all pixels in Fig. 2.13 plotted against the Moon-Sun disk center distance normalized to

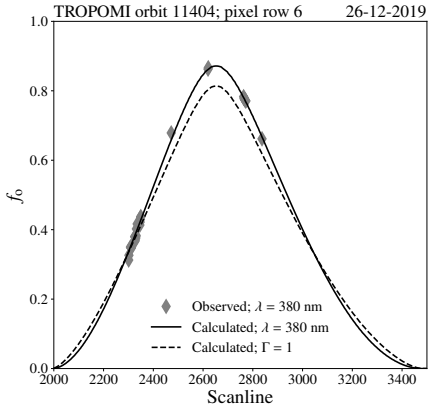

Figure 2.14: The observed eclipse obscuration fraction by TROPOMI in orbit 11404 on 26 December 2019 (grey diamond dots), compared to the calculated eclipse obscuration fraction at 380 nm including solar limb darkening (black solid line) and for $\Gamma = 1$ which excludes solar limb darkening (black dashed line), per scanline in pixel row 6.

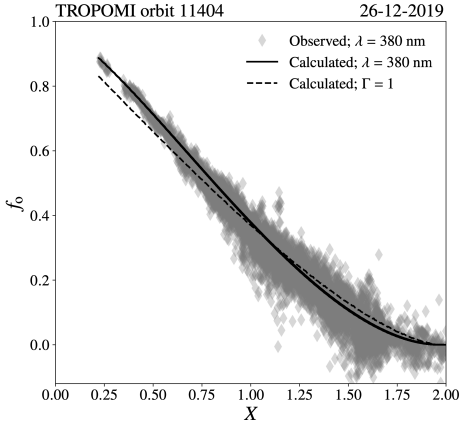

Figure 2.15: Similar to Fig. 2.14, but plotted against the disk center separation X.

the solar disk radius, X, computed for each of those pixels.[11] On the domain $X < 0.5$, the total mean absolute difference between the observed and calculated f_o at 380 nm was 0.008, while the total mean absolute difference between the observed and the calculated f_o for $\Gamma = 1$ was 0.053. The maximum underestimation of f_o at 380 nm when using $\Gamma = 1$,

[11] The density of points increases with increasing X because the Earth's surface area for which a certain value of X applies increases with increasing X. Making the filter of Eq. 15 more strict (e.g. $R_{340}^{\text{meas}} \cdot 0.75 > R_{380}^{\text{meas}}$), decreases the scatter but also decreases the number of points. Another reason for the increasing scatter with increasing X is that for low f_o the compared pixels may have more differences, resulting from natural variations, than caused by the obscuration ($\left[R_{380}^{\text{meas}}\right]_{\text{eclipse}} / \left[R_{380}^{\text{meas}}\right]_{\text{no eclipse}}$ in Eq. 2.13 and the impact of its variations on f_o are relatively large).

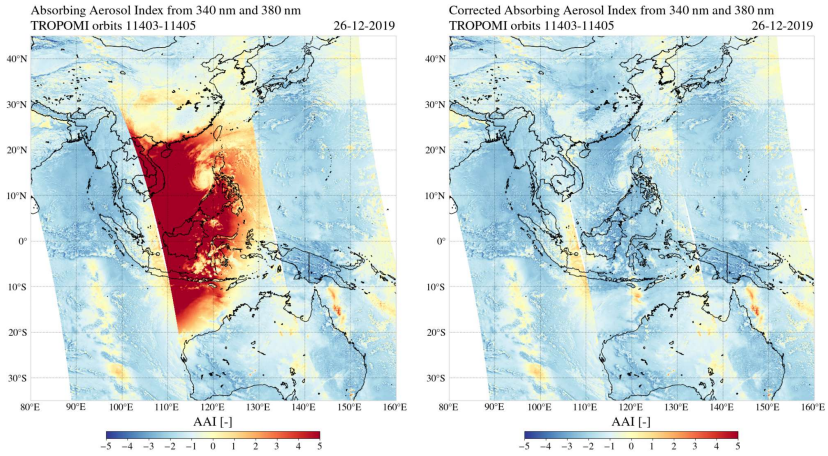

Figure 2.16: The Absorbing Aerosol Index from the 340/380 nm wavelength pair by TROPOMI on 26 December 2019 at Southeast Asia in orbits 11403-11405, uncorrected (left) and after the solar irradiance correction (right).

with respect to f_o at 380 nm when solar limb darkening is taken into account, was 0.06 at 6.04°N latitude and 107.19°E longitude.

RESTORED UV ABSORBING AEROSOL INDEX

The AAI as derived by TROPOMI is computed from the ratio of the measured reflectances at 340 and 380 nm and the ratio of the modeled reflectances at those wavelengths, according to Herman et al. [60] and Torres et al. [165]

$$\mathrm{AAI} = -100 \cdot \left[\log_{10}\left(\frac{R_{340}}{R_{380}}\right)^{\mathrm{meas}} - \log_{10}\left(\frac{R_{340}}{R_{380}}\right)^{\mathrm{model}} \right], \tag{2.16}$$

where 'meas' indicates the measured TOA reflectances and 'model' indicates the modeled TOA reflectances. The modeled TOA reflectances are computed for a cloud-free and aerosol-free atmosphere-surface model with the 'Doubling-Adding KNMI' (DAK) radiative transfer code [53, 149], version 3.1.1, taking into account single and multiple Rayleigh scattering and absorption of sunlight by molecules in a pseudo-spherical atmosphere, including polarization. The Lambertian surface albedo A_s in the model is assumed independent of wavelength λ and is adjusted such that the model reflectance equals the measured reflectance at 380 nm:

$$R_{380}^{\mathrm{model}}(A_s) = R_{380}^{\mathrm{meas}}. \tag{2.17}$$

The value of A_s that satisfies Eq. 2.17 is often referred to as the 'scene albedo' or the 'Lambertian equivalent reflectance (LER)'. Because A_s is assumed wavelength independent, it is also used to compute R_{340}^{model}. More details about the TROPOMI AAI algorithm can be found in Stein Zweers, Apituley, and Veefkind [150]. For our solar eclipse application, it should be noted that a lower R_{380}^{meas} results in a smaller (spectrally flat) surface contribution in the model, which increases $R_{340}^{\mathrm{model}} / R_{380}^{\mathrm{model}}$ and increases the AAI.

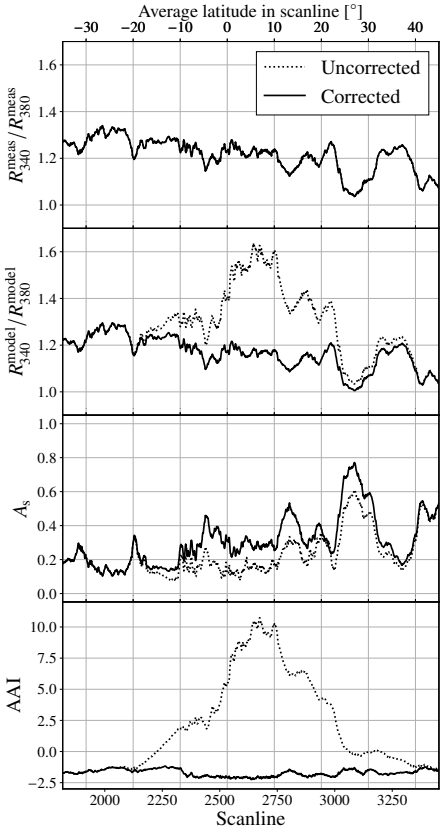

Figure 2.17: The scanline averages of (from top to bottom) $R_{340}^{meas}/R_{380}^{meas}$, $R_{340}^{model}/R_{380}^{model}$, A_s and AAI in orbit 11404, 26 December 2019. The average latitudes in the scanlines are indicated at the top. The dotted lines are the results before the solar irradiance correction and the solid lines are the results after the solar irradiance correction. The lines for the uncorrected and corrected $R_{340}^{meas}/R_{380}^{meas}$ overlap.

The UV Absorbing Aerosol Index (AAI) can be interpreted as a comparison of the measured TOA reflectance UV color to the TOA reflectance UV color of a cloud-free and aerosol-free atmosphere-surface model. The AAI generally increases in the presence of absorbing aerosols and can, unlike the aerosol optical depth, also be computed when the aerosol layer is above clouds. For more details about the sensitivity of the AAI to atmosphere and surface parameters, we refer to Herman et al. [60], Torres et al. [165], de Graaf et al. [30], Penning de Vries, Beirle, and Wagner [115] and Kooreman et al. [80]. In Appendix A.2 we provide an analysis of the precision of the AAI during the solar eclipses studied in this paper.

The left image in Fig. 2.16 shows the AAI measured by TROPOMI during the annular solar eclipse on 26 December 2019, in the three adjacent orbits over Southeast Asia considered in Sect. 2.3.1. We use a color scale ranging from AAI = −5 to AAI = 5. This range usually covers most aerosol events. Significantly elevated AAI values are measured at the

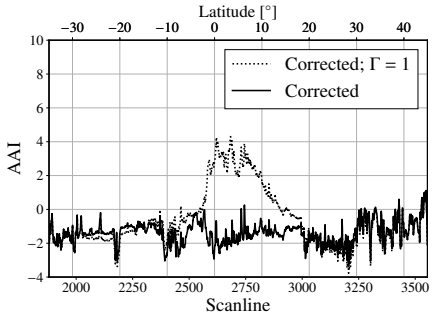

Figure 2.18: The AAI in pixel row 6 in orbit 11404, 26 December 2019. The latitudes in the scanlines are indicated at the top. The solid line is the result after the solar irradiance correction, the dotted line is the result after the solar irradiance correction when solid limb darkening is not taken into account ($\Gamma = 1$).

location of the penumbra: in orbit 11404, most apparent between 20°S and 30°N latitude (cf. f_o in Fig. 2.10). The maximum AAI was 53.9 at 2.17°N latitude and 108.14°E longitude. The mean AAI in orbit 11404 was 0.15. At the spiral cloud deck centered at 15°N latitude and 118°E longitude, the AAI increase is less significant. Similarly, the clouds observed in Fig. 2.11 between 10°S and 0°N latitude, and between 22°N and 32°N, are located in the penumbra but show a less significant AAI increase.

Outside the Moon shadow, in orbits 11403 and 11405, the mean AAI is −1.52 and −1.48, respectively. At the locations in orbit 11404 where $f_o < 0.2$, the mean AAI is also negative (~ -1.5). The negative mean AAI are partly caused by the scattering of light by cloud droplets, but also due to a radiometric calibration offset and degradation in the TROPOMI irradiance data [162, 93]. The degradation in the irradiance leads to an increase of the derived reflectance, decreasing the AAI values over time. The total AAI bias of ~ -1.5 will be solved with the release of the version 2.0.0 TROPOMI level 1b processor, foreseen for the first half of 2021. The bias is expected to be independent of viewing geometry, hence, it will not affect the relative AAI values nor the conclusions of this paper.

The right image in Fig. 2.16 is similar to the left image in Fig. 2.16, but then for the corrected AAI product. That is, in Eq. 2.16 and 2.17, we replaced the measured TOA reflectances, R_{340}^{meas} and R_{380}^{meas}, by the restored TOA reflectances, R_{340}^{int} and R_{380}^{int}, which we computed with Eq. 2.3. The red spot between 20°S and 30°N in orbit 11404 that was observed in the uncorrected AAI product has disappeared. The mean of the corrected AAI in orbit 11404 is −1.58. At the location of the thick spiral cloud deck the AAI is closer to zero. We note that no significant absorbing aerosol events can be identified in Figure 2.16. At 12°S latitude and 122°E longitude, an AAI increase is measured in the corrected product, which could not be observed in the uncorrected image. This feature is caused by the specular reflection off the sea surface, often called the sunglint (see also Fig. 2.11). The sunglint can also be observed in the middle of the swath of orbits 11403 and 11405, between 20°S and 10°S latitude and 34°S and 5°S latitude, respectively. Kooreman et al. [80] explain that, when a strongly anisotropic reflector such as the sea surface is viewed from its reflective side, the AAI may increase: the model assumes a Lambertian (isotropic reflecting) surface, which increases the relative importance of the

Rayleigh scattered light in the model and therefore computes a higher R_{340}/R_{380} than is measured. From Eq. 2.16, it follows that a deficit in the measured R_{340}/R_{380} results in an increased AAI. Note that the shape and size of the apparent sunglint may vary per orbit, as they depend on the roughness of the sea surface (i.e. the wind speed), the presence of clouds and aerosols, and the illumination and viewing geometries.

In Fig. 2.17, we show the average $R_{340}^{\text{meas}}/R_{380}^{\text{meas}}$, $R_{340}^{\text{model}}/R_{380}^{\text{model}}$, A_{s} and AAI of the pixels in the scanlines of orbit 11404, before the solar irradiance correction (dotted line) and after the solar irradiance correction (solid line). The average latitudes in the scanlines are also shown. The fraction $R_{340}^{\text{meas}}/R_{380}^{\text{meas}}$ is not affected by the solar irradiance correction, which is expected from the wavelength independence of f_{o} between 340 and 380 nm (see Fig. 2.7). Here, we did not detect signatures of sky color changes in the measured UV reflectance due to secondary effects such as horizontally travelled light (see Sect. 2.4, for a detailed discussion). Before the solar irradiance correction, $R_{340}^{\text{model}}/R_{380}^{\text{model}}$ is significantly higher than $R_{340}^{\text{meas}}/R_{380}^{\text{meas}}$ between 20°S and 30°N where the Moon shadow resided, which increases the AAI. The high $R_{340}^{\text{model}}/R_{380}^{\text{model}}$ is caused by the relatively low A_s in the Moon shadow (Fig. 2.17), which is caused by the decrease of R_{380}^{meas} by f_{o} (Fig. 2.12). The maximum scanline average AAI is 10.7 in scanline 2672 (see bottom graph in Fig. 2.17). After the solar irradiance correction, the AAI increase in the Moon shadow disappeared because $R_{340}^{\text{model}}/R_{380}^{\text{model}}$ follows an approximately similar pattern as $R_{340}^{\text{meas}}/R_{380}^{\text{meas}}$, albeit with an offset ranging from −0.03 to −0.06, which was also observed outside the Moon shadow. We conclude that the increased AAI between 20°S and 30°N latitude in orbit 11404 before the solar irradiance correction was caused by the relatively low A_{s} used in the model due to the reduction of the measured reflectance at 380 nm, rather than a UV color change of the measured TOA reflectance in the Moon shadow.

Figure 2.18 shows the AAI in the scanlines of orbit 11404, but only for pixel row 6 (cf. Fig. 2.14). The solid line is the eclipse corrected AAI and the dotted line is the eclipse corrected AAI but without taken into account limb darkening ($\Gamma = 1$). If solar limb darkening is not taken into account, the corrected AAI still shows an apparent increase between 14.9°S and 21.6°N latitude, with a maximum of AAI = 4.3 at 3.37°N latitude. Note that these are the latitudes at which the f_{o} was underestimated if $\Gamma = 1$ as we showed in Fig. 2.14, caused by the Moon occulting different parts of the solar disk during the eclipse (see Sect. 2.2.3). In line with the discussion of the previous paragraph, an underestimation of f_{o} at 380 nm results, after the solar irradiance correction, in too low R_{380}^{meas} and A_{s}, in too high $R_{340}^{\text{model}}/R_{380}^{\text{model}}$ and, therefore, in too high AAI. We find a maximum overestimation of the AAI of 6.7 points in scanline 2671 and pixel row 4 when using $\Gamma = 1$. It can be concluded that not taking into account solar limb darkening would still result in a 'red spot' anomaly in the AAI map. The opposite effect occurs at the latitudes where f_{o} was overestimated if $\Gamma = 1$ in Fig. 2.14: south from 14.9°S and north from 21.6°N latitude, the AAI after the correction without limb darkening is slightly lower than the AAI after the correction where limb darkening was taken into account. We conclude that, if the artificial Moon shadow signatures are to be removed in the corrected AAI product, solar limb darkening cannot be neglected.

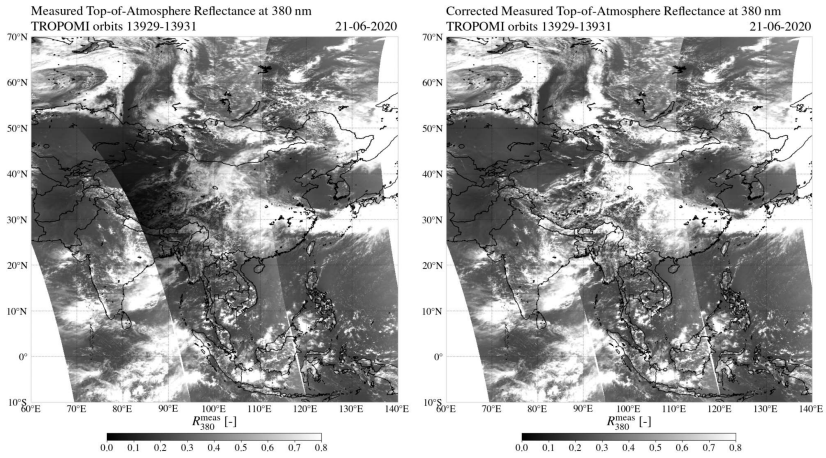

Figure 2.19: The measured top-of-atmosphere reflectance at 380 nm by TROPOMI on 21 June 2020 over Asia in orbits 11403-11405, uncorrected (left) and after the solar irradiance correction (right).

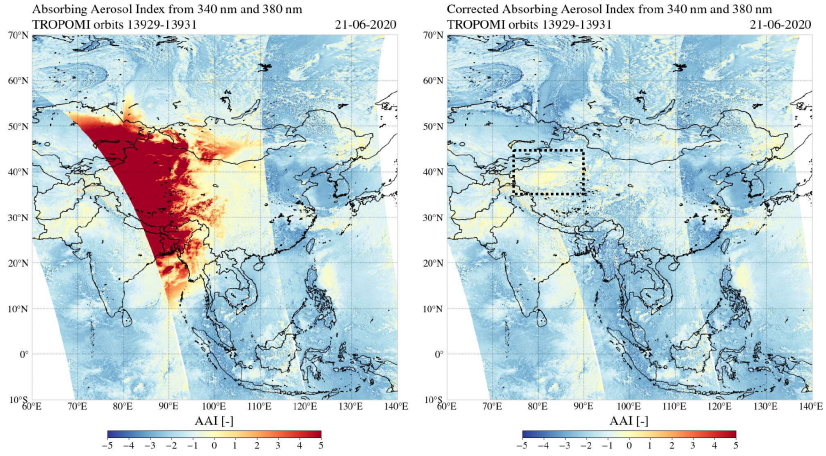

Figure 2.20: The Absorbing Aerosol Index from the 340/380 nm wavelength pair by TROPOMI on 21 June 2020 over Asia in orbits 13929-13931, uncorrected (left) and after the solar irradiance correction (right). In the corrected image, the Taklamakan desert is located in the rectangular dotted box.

2.3.2. ANNULAR SOLAR ECLIPSE ON 21 JUNE 2020

On the 21st of June, 2020, the Moon shadow during an annular solar eclipse could be experienced in the majority of Africa (from South Africa to Libya) and almost all parts of Asia. At the instant of greatest eclipse, r_m was 0.994 and the duration of the annular phase for a local observer at 30.5°N latitude and 80.0°E longitude was 38 seconds, while the complete eclipse duration was 3 hours, 26 minutes and 53 seconds.[12] We compute that the penumbral shadow radius, perpendicular to the shadow axis at the Earth's surface, was 3493.9 km, while the antumbral shadow radius, perpendicular to the shadow axis at the Earth's surface, was 10.5 km. The area in the antumbra on the Earth's surface was 0.0008% of the total area in the shadow of the Moon (antumbra + penumbra) on the Earth's surface.

Figure 2.19 shows R_{380}^{meas} by TROPOMI on 21 June 2020 over Asia, before the solar irradiance correction (left image) and after the solar irradiance correction (right image). The shadow of the Moon was captured in orbit 13930, as shown by the apparent decrease of R_{380}^{meas} between 10°N and 55°N latitude. Only the penumbra was captured. The antumbra was located out of sight in the west of orbit 13930. The maximum calculated f_o at 380 nm was 0.92 at 31.94°N latitude and 82.51°E longitude.

The left image in Fig. 2.20 shows the TROPOMI AAI in orbits 13929 to 13931 over Asia, before the solar irradiance correction. Before the solar irradiance correction, the AAI is significantly increased in the shadow of the Moon. The edge of the red spot in the uncorrected AAI in orbit 13930 is shaped by the local cloudiness. For example, the AAI > 2 signature in West Mongolia (40-50°N latitude and 90-110°E longitude), is spatially correlated with low cloud fraction area. Note that this suppression of the eclipse anomaly by clouds in the AAI product was also observed at the cloudy areas in the shadow of the Moon on 21 December 2019 (left image of Fig. 2.16).

The right image in Fig. 2.20 is similar to the left image in Fig. 2.20, but after the solar irradiance correction. The red spot between 10°N and 55°N latitude in orbit 13930 that was observed in the uncorrected AAI product has disappeared. In Northwest China, a region of relatively high AAI values appears in the corrected product: at 36°-42°N latitude and 78°-86°E longitude, the AAI is increased by ~ 1.5 points. Note that this AAI change is larger than the maximum standard AAI error in orbit 13930 of 0.40 (see Appendix A.2). We verify this AAI feature using AAI measurements of the Global Ozone Monitoring Experiment–2 (GOME-2) instrument on board the Metop-C satellite (referred to as 'GOME-2C' in what follows). Figure 2.21 shows the AAI measured by GOME-2C on 21 June 2020 in orbits 8411 to 8415 in the Middle-East and Western Asia, from the Polarization Measurement Detectors (PMDs) using λ = 338 nm and λ = 381 nm for the AAI retrieval [173]. In order to show the eclipse location during the GOME-2C measurements, we did not apply the solar irradiance correction to the GOME-2C data. Figure 2.21 shows that two GOME-2C orbits were affected by the eclipse: significantly elevated AAI were measured in the shadow of the Moon in orbit 8413 and 8414. The location 36°-42°N latitude and 78°-86°E longitude was not eclipsed during the measurements of GOME-2C. Indeed, GOME-2C also measured an AAI increase of ~ 1.5 points in this same area in Northwest China. At this location, the Taklamakan Desert is located. The Taklamakan desert is

[12] See https://eclipse.gsfc.nasa.gov/SEgoogle/SEgoogle2001/SE2020Jun21Agoogle.html, visited on 28 September 2020.

the largest desert in China, about 960 km long and 420 km wide, and consists mostly of shifting sand dunes that reach elevations of 800 m to 1500 m above sea level [117]. It is an important source for the global atmospheric dust budget and for dust storms in Eastern Asia [64]. Hence, we attribute this ~ 1.5 points increase to the desert surface and, possibly, desert dust aerosol.

2.4. DISCUSSION

The eclipse obscuration theory provided in Sect. 2.2.3 applies to any phase of any solar eclipse type. The TROPOMI orbits during the annular solar eclipses analyzed in this paper did not capture the antumbra. The maximum f_o at 380 nm calculated in the TROPOMI orbits were 0.89 and 0.92 on 26 December 2019 and 21 June 2020, respectively, while the annular phase for these eclipses at 380 nm occurred for $f_o > 0.976$ and $f_o > 0.997$, respectively. In this section, we reflect back on the assumptions we made and we discuss some points of attention for potential future applications of the solar irradiance correction to measurements closer to the (ant)umbra, and/or in the antumbra.

In this paper, we assumed that the solar irradiance is randomly polarized. Sunlight scattered in the Sun's atmosphere may become polarized. This linearly polarized spectrum is also known as the 'Second Solar Spectrum' and its significance increases towards the solar limb [152]. If there is no eclipse, this polarization cancels out due to the symmetry and only very small linear degrees of polarization of the disk-integrated sunlight can be measured (on the order of 10^{-6}, see Kemp et al. [75], who attributed this polarization in their ground-based observations to multiple scattering in the Earth's atmosphere). During an eclipse, the symmetry is broken, however, measurements show that a few arcseconds inside the solar limb the degree of polarization is lower than 0.01 and in most

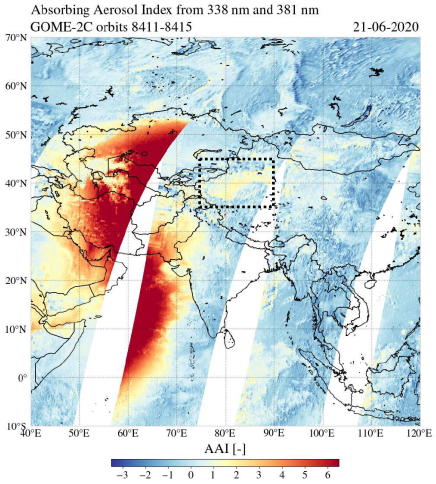

Figure 2.21: The Absorbing Aerosol Index from the 338/381 nm wavelength pair by GOME-2C on 21 June 2020 over Asia in orbits 8411-8415. The Taklamakan desert is located in the rectangular dotted box.

cases less than 0.001 [151][13]. Only at $0.99 < r < 1$, the degree of polarization can be larger than 0.01, but never will grow bigger than the theoretical limit of 0.117 [151]. Note that, during the annular solar eclipse of 26 December 2019, $r_m = 0.97$ and the minimum disk center separation X in the TROPOMI pixels was 0.22, meaning that, at the straight line through the solar disk and lunar disk centers, the most narrow visible solar limb (when the opposite solar limb was occulted) was $0.75 < r < 1$. For 21 June 2020, $r_m = 0.994$ and the minimum encountered X was 0.20, giving $0.79 < r < 1$. Hence, it may be expected that, integrated over the visible solar disk, the polarization of the sunlight was negligible.

For this paper we did not take into account light travelling horizontally in the atmosphere from one ground pixel to the other. A well-known phenomenon during total solar eclipses, for a local observer in the umbra, is the reddening of the sky near the horizon, i.e., of light scattered from outside the umbra [139]. The path lengths of scattered beams reaching a ground sensor in the umbra are relatively long, i.e., Rayleigh scattering may cause the reddening near the horizon, while overhead the sky may appear more blue [44]. 3-D radiative transfer code simulations by Emde and Mayer [38] suggest that scattered horizontal visible irradiance reaching a ground sensor in the umbra is about 20000 times smaller at 330 nm and about 23000 smaller at 500 nm than the total (direct + diffuse) irradiance received in uneclipsed conditions. Outside the umbra where, for example, $f_o < 0.99$, already > 1% of the uneclipsed solar irradiance is received at TOA which is expected to dominate the horizontally travelled light. Emde and Mayer [38] compared their 3-D simulations to a 1-D approach and computed that longer than 10 minutes before or after totality the uncertainty of a 1-D method is lower than 1%. An analysis of this 1-D bias for the TOA reflectance versus f_o could give a definite limit in terms of f_o. In the TROPOMI orbits studied in this paper, the maximum calculated f_o at 380 nm were 0.89 and 0.92, which explains why we did not detect anomalies in the restored TOA reflectances, nor in the corrected AAI, that could be attributed to 3-D effects or a reddening of the measured UV spectrum.

A second reason for the potential reddening of the sky during a solar eclipse has a fundamentally different origin. Yellow and orange cloud tops have been observed, for example, in true color MODIS satellite images in the penumbra during the total eclipse of 2 July 2019 and during the annular solar eclipse on 26 December 2019 [45]. During the total solar eclipse of 20 March 2015, reddened Arctic Ocean sea ice and clouds have been observed, 13 minutes after totality. Gedzelman [45] use a simple radiative transfer model to suggest that these yellow and orange colors observed from space are mainly caused by solar limb darkening. Figure 2.7 indeed shows that on 26 December 2019, the spectra in uncorrected satellite measurements could redden for $f_o > 0.33$. Because this reddening is described by the wavelength dependence of f_o, the reddening is automatically solved for with the solar irradiance correction of this paper and can therefore not be detected in a corrected product. Hence, the solar irradiance correction of this paper could be used to potentially prove that the yellow and orange colors in satellite images are indeed caused by solar limb darkening.

The solar irradiance correction is, besides the assumptions about the unpolarized state of E_o and ignorance of 3-D effects, limited by the performance of the measure-

[13] See also https://ethz.ch/content/dam/ethz/special-interest/phys/particle-physics/cosmologygroup-dam/People/StenfloPDFs/stenflo_spse06.pdf, visited on 8 October 2020.

ment instrument. For this paper, all TROPOMI TOA reflectance measurements had a SNR larger than 50. Measurement errors, 3-D effects and polarization of sunlight are expected to only play a role closer to the (ant)umbra and/or in the antumbra, and therefore did not leave signatures in the results of this paper. For potential applications of the solar irradiance correction to these regions in the future, it is advised to compare the calculated f_o to the observed f_o as in Sect. 2.3.1, which can help distinguishing between those artefacts and real air quality measurements.

The solar irradiance correction presented in this paper is a correction of the TOA reflectance spectrum. We have shown that the AAI successfully can be restored with the corrected TOA reflectances. Theoretically, any other product that is derived from TOA reflectance spectrum can be restored. The AAI is based on a ratio of absolute TOA reflectances in the UV which are directly affected by the eclipse obscuration. Differential spectral features are not expected to be directly affected by the eclipse obscuration. Therefore, we speculate that the solar irradiance correction could certainly also work for products that are based on differential spectral features, such as ozone, nitrogen dioxide and sulfur dioxide. However, high spectral resolution solar spectrum features that are not captured by the solar limb darkening measurements may have to be taken into account in the retrieval. As the photochemical activity in the Earth's atmosphere is driven by the TOA irradiation, solar eclipse related changes in the concentration of these gases could potentially be studied from space.

2.5. SUMMARY AND CONCLUSIONS

In this paper, we presented a method to restore the TOA reflectance spectra in the penumbra and antumbra during solar eclipses, by computing the eclipse obscuration fraction as a function of location and time, fully taking into account wavelength-dependent solar limb darkening. We applied the correction to UV TOA reflectances measured by TROPOMI in the penumbra during the annular solar eclipses on 26 December 2019 and 21 June 2020. We showed that the dark shade in the TOA reflectance maps for 380 nm, at the location of the Moon shadow, disappeared after the correction. For the eclipse on 26 December, we compared the calculated obscuration fractions to the estimated obscuration fractions at the ground pixels using measurements of the previous orbit and found a close agreement. Not taking into account solar limb darkening, however, resulted on 26 December 2019 in a mean underestimation of the obscuration fraction f_o at 380 nm of 0.053 at disk center separations $X < 0.5$, and a maximum underestimation of 0.06.

The UV Absorbing Aerosol Index (AAI) is an air quality product derived from the TOA reflectance spectra. If no correction is applied, a significant increase of the TROPOMI AAI is measured in the shadow of the Moon. We explain this anomaly by the decreased measured TOA reflectance at 380 nm, which is used to define the Lambertian surface albedo in the model reflectance computations and propagates in the AAI formulae into a more 'blue' model UV spectrum, resulting in an increased AAI. That is, the AAI increase in the Moon shadow is not caused by a 'redder' measured UV spectrum.

With the restored TOA reflectance spectra, we computed a corrected version of the TROPOMI AAI on 26 December 2019 and 21 June 2020. For both eclipses, the AAI anomaly in the shadow of the Moon disappeared after the correction. For the eclipse on 26 December 2019, we showed that not taking into account solar limb darkening, however,

could still result in an AAI overestimation of 6.7 points. We conclude that solar limb darkening cannot be neglected if the artificial Moon shadow signatures are to be removed.

For the eclipse on 21 June 2020, we found an AAI increase of ~1.5, as compared to its surrounding regions, in the restored TROPOMI product in Northwest China. We verified this AAI increase with AAI measurements by the GOME-2C satellite instrument on the same day but outside the Moon shadow. We attribute this restored AAI feature to the surface of the Taklamakan Desert and, possibly, desert dust aerosol. In this paper, we did not find an indication of absorbing aerosol changes in the Moon shadow (e.g. which are spatially correlated with the recent eclipse ground track). We conclude that the restored AAI product successfully can be used to detect real AAI rising phenomena.

The antumbra was not captured by the TROPOMI orbits during the annular solar eclipses studied in this paper, and the maximum f_o was 0.92. Therefore, measurement errors, light travelling horizontally through the atmosphere between adjacent ground pixels and polarization of sunlight did not leave signatures in the corrected products, but their effect should carefully be reconsidered when restoring measurements in areas where $f_o > 0.92$ in the future.

We have demonstrated that the restored TOA reflectances during solar eclipses can be applied successfully to derive the AAI product. Since the method we developed has taken into account the wavelength dependence of the solar limb darkening, the method is applicable to the measured reflectances or radiances at all TROPOMI wavelengths. A solar eclipse flag is already included in the TROPOMI level 1B product. With the addition of the obscuration fraction in the level 1B product, all TROPOMI level 2 products will benefit from the restored TOA reflectances or radiances. In principle, the method can also be applied to GOME-2, Sentinel-4/5 and other satellite instruments which measure the back-scattered and reflected solar radiation.

3

CLOUDS DISSIPATE QUICKLY DURING SOLAR ECLIPSES AS THE LAND SURFACE COOLS

Clouds affected by solar eclipses could influence the reflection of sunlight back into space and might change local precipitation patterns. Satellite cloud retrievals have so far not taken into account the lunar shadow, hindering a reliable spaceborne assessment of the eclipse-induced cloud evolution. Here we use satellite cloud measurements during three solar eclipses between 2005 and 2016 that have been corrected for the partial lunar shadow together with large-eddy simulations to analyze the eclipse-induced cloud evolution. Our corrected data reveal that, over cooling land surfaces, shallow cumulus clouds start to disappear at very small solar obscurations (~15%). Our simulations explain that the cloud response was delayed and was initiated at even smaller solar obscurations. We demonstrate that neglecting the disappearance of clouds during a solar eclipse could lead to a considerable overestimation of the eclipse-related reduction of net incoming solar radiation. These findings should spur cloud model simulations of the direct consequences of sunlight-intercepting geoengineering proposals, for which our results serve as a unique benchmark.

This chapter has been published in Nature Communications Earth & Environment **5**, 71 (2024) [171].

3.1. INTRODUCTION

Blocking part of the solar radiation incident on the Earth's (lower) atmosphere and surface is one of the proposed strategies to counteract the current and future global temperature rise, which may be inevitable if climate change mitigation efforts prove to be insufficient [74, 88, 140, 81]. This type of (solar) geoengineering is based on placing sun shields or reflecting particles in space between the Earth and the Sun [36, 6, 43, 99, 112, 130], or on the injection of aerosols into the stratosphere [29, 126]. General circulation models (GCMs) suggest that an insolation reduction of 3.5-5.0% can largely undo the global temperature rise and intensified hydrological cycle associated with a quadrupled pre-industrial CO_2 concentration [94, 82, 8, 70]. However, those GCMs also predict latitudinal variations in temperature response, and an extra reduction of precipitation in the tropics. Moreover, although clouds play a vital role in the Earth's radiation balance [125], the impact of solar dimming on clouds is still poorly understood [136, 129, 83, 179]. GCMs modeling the response to (extraterrestrial) dimming of sunlight are based on idealized scenarios [84]. They inherently suffer from uncertainties [71], mainly focus on the long-term impact, and highly parameterize short-term and small-scale processes such as cloud formation [71, 83]. Twice a year on average, for a few hours the opportunity arises to take measurements of the Earth experiencing gradual insolation reductions from 0 to nearly 100%, during the partial phase of a solar eclipse. Although the time scales involved with solar geoengineering will most likely not be equivalent to those of solar eclipses, these measurements can help to better understand (and test models that predict) the immediate cloud response to the deployment of sunlight intercepting material.

Ground-based meteorological observations during solar eclipses have primarily focused on fast drops in air temperature, winds and turbulence, and on changing (photo)-chemistry [7, 56]. Weather publications contain anecdotal descriptions of dissipating low-level cumulus clouds right before totality, while mid- and high-level clouds survived [5, 54]. The timing of the eclipse-induced effect on cumulus clouds is difficult to quantify with ground-based measurements due to the chaotic nature of cumulus cloud evolution and the missing observation of the non-eclipse state, and atmospheric model studies of eclipses did not yet analyze the cumulus cloud sensitivity [41, 104, 27, 18]. Additionally, the precise locations of the affected clouds can be hard to predict and are sometimes inaccessible for ground-based observers. Earth observation satellites in geostationary orbit can continuously monitor clouds in large geographical areas [128, 153, 11] and hints of dissipating cumulus clouds have been observed by comparing satellite images before and after a total solar eclipse, without estimating the non-eclipse state [5, 47]. However, during solar eclipses, satellite images show spatio-temporally varying darkening [47, 113] and satellite retrievals of cloud cover and cloud optical thickness (COT) are biased. This bias is caused by not taking into account the insolation reduction in the calculation of the top-of-atmosphere (TOA) reflectance from which cloud properties are derived. Hence, it has remained unknown how fast clouds are modified by various solar obscuration fractions.

Here, we present geostationary satellite measurements of clouds during three solar eclipses between 2005 and 2016 that have been corrected for the insolation reduction. Our corrected measurements reveal that shallow cumulus clouds start to dissipate at a

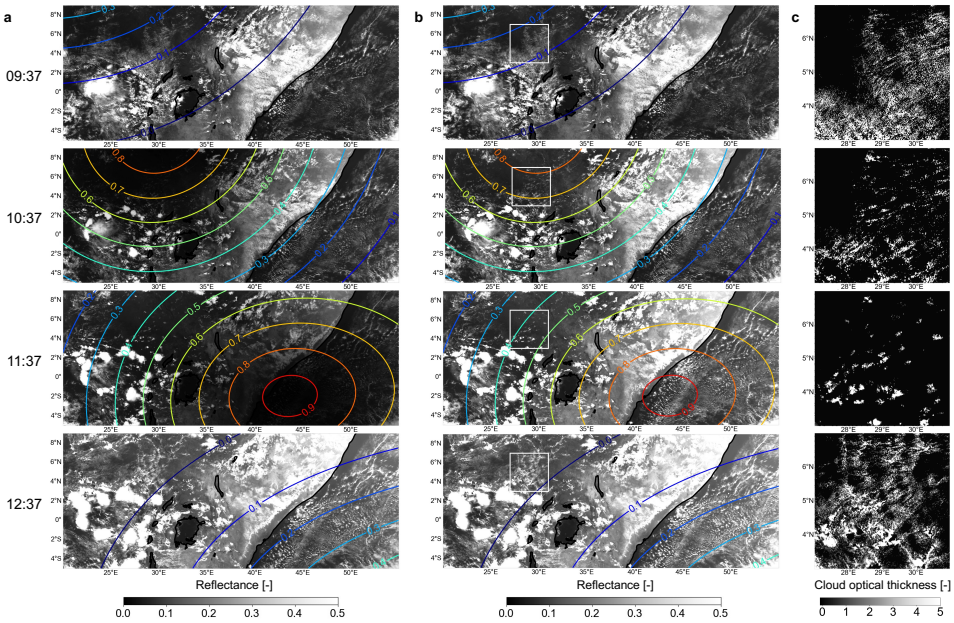

Figure 3.1: SEVIRI images of the annular solar eclipse on 3 October 2005. (a) The original and (b) the eclipse corrected TOA VIS reflectance over East Africa (in the West) and Indian Ocean (in the East), at 09:37, 10:37, 11:37 and 12:37 UTC (from top to bottom). The colored contour lines indicate the solar obscuration fraction and the white squares over land mark the study area. (c) The corresponding eclipse corrected cloud optical thickness zoomed-in on the study area.

solar obscuration of ~15% over cooling land surfaces, which would have been hidden in the partial lunar shadow without insolation reduction correction. Using large-eddy simulations we explain the timing of the cloud dissipation and demonstrate that the rising air parcels in the atmospheric boundary layer are already affected by the solar eclipse at even smaller obscurations. We calculate that neglecting the dissipating cloud behaviour in the simulations would result in an overestimation of 20 W m^{-2} of the eclipse-related reduction of net incoming shortwave radiation at the top-of-atmosphere. Finally, we discuss that the high cloud sensitivity to rather small insolation reductions should spur cloud model simulations of the short-term impact of sunlight-intercepting geoengineering concepts.

3.2. RESULTS

SATELLITE OBSERVATIONS

Figure 3.1 shows the uncorrected and corrected TOA visible (VIS) reflectance over East Africa and part of the Indian Ocean, at four subsequent hours during the annular solar eclipse on 3 October 2005, obtained by the Spinning Enhanced Visible and InfraRed Imager (SEVIRI) instrument (see Methods). In the first hour, cumulus clouds were present over land. They are better visible in the corrected high resolution images of the COT zoomed in on the specific area over land at 3°-7° latitude and 27°-31° longitude (Fig.

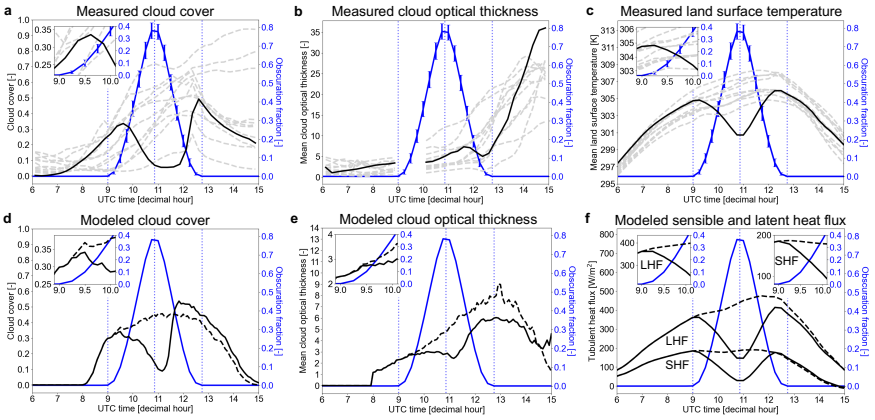

Figure 3.2: Time series of cloud and land surface parameters in the study area (i.e., the white square in Fig. 3.1). (a) The retrieved cloud cover by SEVIRI. (b) The cloud optical thickness (COT) retrieved by SEVIRI. (c) The spatial mean land surface temperature (LST) retrieved by SEVIRI. (d) The modeled cloud cover with DALES. (e) The COT simulated with DALES. (f) The sensible and latent heat fluxes modeled with DALES. The black solid lines are for the day of the solar eclipse (3 October 2005). The grey dashed lines in (a), (b) and (c) are for the comparable days but without solar eclipse. The black dashed lines in (d), (e) and (f) are the results of the modeled reference case. The blue solid lines illustrate the spatial average obscuration fraction, with error bars in (a), (b) and (c) representing the standard deviation of the spatial variation. The blue vertical dotted lines indicate the start, maximum, and end of the eclipse (from left to right). The missing observations between 9 and 10 UTC in (b) are caused by COT retrieval errors at that scattering geometry due to the cloud bow. The insets show the time series zoomed in on 09:00 to 10:00 UTC. Local noon occurred at 10:04 UTC.

3.1c), which we call the study area. The derived COT in the cloudy pixels was $\lesssim 5$ and SEVIRI estimated a cloud top altitude of ~2 km (see Supplementary Figure 3.6), indicating that they were shallow and located in the planetary boundary layer. Similar large-scale daytime shallow cumulus cloud fields over land can be found in central Africa and the Amazonian rainforest throughout the year, and in northeast America and Siberia during the boreal summer [124, 58]. When the obscuration increased in the second hour, the cloud cover in the study area diminished, although remnants of the cloud pattern of the previous hour are still recognizable. In the third hour, the insolation increased again, but the shallow cumulus clouds stayed away while the clouds that survived had grown in size and COT. It was only during the final stage of the eclipse that shallow cumulus clouds returned throughout the study area. Over ocean, the cumulus clouds did not disappear. In Supplementary Figures 3.7 and 3.8, we provide two more examples of vanishing shallow cumulus clouds over land during solar eclipses.

The disappearance of shallow cumulus clouds only occurred on the day of the solar eclipse. Figure 3.2a shows the time series of the cloud cover in the study area, compared to that during 11 comparable days which we selected based on a similar type of cloud pattern before the eclipse started (see Methods). Also depicted in Fig. 3.2 is the obscuration fraction on the eclipse day. The time series shows that the increasing cloud cover in the morning already halted at low obscuration fractions (~0.15), happening at around 09:30 UTC which was 30 minutes after the start of the eclipse. Secondly, there was a ~50 minutes time lag with respect to the instant of maximum obscuration at 10:52 UTC be-

fore the clouds started to return. During the increase in cloud cover between 12:00 and 12:30 UTC, the mean COT in the cloudy pixels decreased (see Fig. 3.2b), which can be attributed to the contribution of the newly formed shallow clouds. This decrease is absent in the time series of the comparable days.

Because shallow cumulus clouds in the boundary layer are generated by rising thermals originating from air close to the surface [142], we collected land surface temperature (LST) measurements from space by SEVIRI, derived from infrared radiation emitted by the shallow land surface layer (see Methods). Figure 3.2c shows the spatially averaged LST in the study area on the eclipse day and the comparable days. The maximum LST on the comparable days was two hours delayed with respect to local noon at 10:04 UTC, which could possibly be explained by the smaller heat flux into the ground due to the warmed subsurface layer in the afternoon [155]. On the eclipse day, the LST drops instantly with the obscuration fraction, due to the direct response of the shallow land surface layer temperature to net radiation forcing [155]. We estimate a maximum LST drop of 5.8 K induced by the eclipse at 11.00 UTC (see Methods). Comparable fast drops in satellite LST measurements have been found in a study over Europe during the total solar eclipse of 20 March 2015 by Good [49] who showed dependencies of the drop magnitude on the eclipse duration and time of the day (earlier eclipses gave larger drops), vegetation, surface height and distance to the coast. We did not detect a time lag in the LST minimum with respect to maximum solar obscuration: a time lag of ~1.5 minutes as reported in literature [49] is not resolved in our LST data at 15 minutes intervals. Hence, the measured time lag of ~50 minutes before clouds return in Fig. 3.2a cannot be explained by a time lag in the LST. Over ocean, we found no sea surface temperature drop when the eclipse passed (see Supplementary Figure 3.9), due to the large heat capacity of water and the efficient heat transport from the sea surface to deeper water layers through turbulent mixing [155].

LARGE-EDDY SIMULATIONS

In order to explain the land-cloud interaction in the study area, we simulated the evolution of shallow cumulus clouds during a solar eclipse with the Dutch Atmospheric Large-Eddy Simulation (DALES) model [63]. Figures 3.2d and 3.2e show the time series of the simulated cloud cover and mean COT, respectively, as would be measured from space (see Methods), and Supplementary Figure 3.10 contains snapshots of the spatially resolved cloud fields. We present the results for the solar eclipse case, using the measured LST as input, and a reference case without eclipse-induced LST drop (see Methods). Indeed, in the solar eclipse case, our simulations show a substantial decrease in cloud cover with respect to the reference case. The cloud cover already differed ~15 to ~20 minutes after the start of the eclipse when the obscuration was still smaller than 10%. As in the observations (Fig. 3.2a), there is a time lag in the instant of minimum cloud cover with respect to mid-eclipse, after which the cloud cover rapidly increases. We note that the simulated cloud cover right after the eclipse is even larger than in the reference case, while the simulated COT is lower. A larger cloud cover after the eclipse compared to the hypothetical non-eclipse scenario is difficult to prove with our observations, due to the large variability of the cloud cover on the comparable days in the afternoon (cf. Fig. 3.2a). During the rapid increase in cloud cover, the simulated COT also increases,

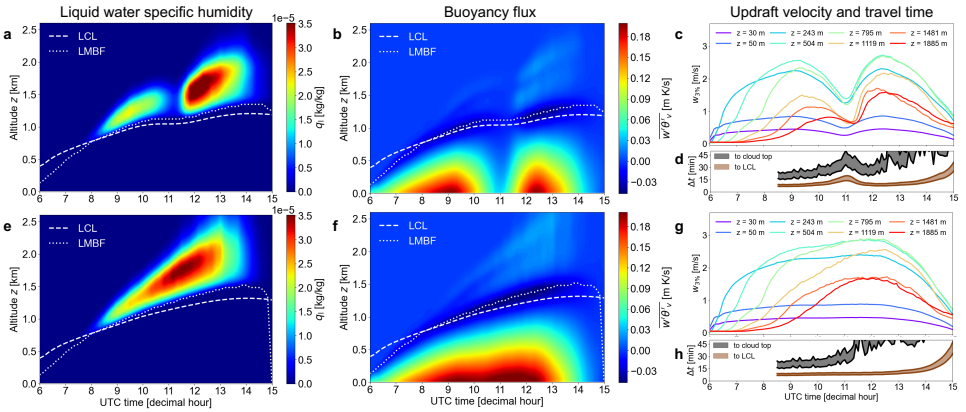

Figure 3.3: Large-eddy simulation results from DALES for the solar eclipse and reference case. (a) Time-varying vertical profiles of the horizontal mean liquid water specific humidity q_l and (b) the buoyancy flux $\overline{w'\theta'_v}$ for the solar eclipse case. (c) The vertical updraft velocity $w_{3\%}$ of the 3-percentile fastest rising parcels at various altitudes and (d) the travel time Δt of the 1- to 5-percentile fastest rising parcels from the surface to lifting condensation level (LCL) and to the cloud top (indicated with brown and grey color shades, respectively), for the solar eclipse case. Similar for Figs. (e), (f), (g) and (h), but then for the reference case. In Figs. (a), (b), (e) and (f), the LCL and level of minimum buoyancy flux (LMBF) are indicated with a dashed and dotted line, respectively.

which is not in agreement with the observations, but can be attributed to the absence of the deeper convective clouds in the south part of the study area due to the horizontally averaged input settings in our simulations (see Methods).

The disappearing clouds during a solar eclipse can be explained by the drop in sensible (thermal) and latent (moisture) heat fluxes from the surface to the lowest atmosphere layer (Fig. 3.2f), as a result of the dropping LST (see Eqs. 3.1 and 3.2). Those heat fluxes drive the buoyancy flux (Figs. 3.3b and f) of relatively warm and moist air parcels from the surface, through the well-mixed boundary layer, up to the level of minimum buoyancy flux (LMBF) where the parcels are capped by a temperature inversion (see Supplementary Figure 3.11). The rising parcels are cooled through adiabatic expansion which increases the parcel relatively humidity (RH) up to 100% at the lifting condensation level (LCL) where shallow cumulus clouds are formed that can extend to higher altitudes (Figs. 3.3a and e). During a solar eclipse, this process is suppressed, which is clear from the overall drop in buoyancy flux. The drop in surface and buoyancy fluxes is consistent with the diminished boundary layer turbulence during solar eclipses found in other studies [37, 98, 18]. It should be noted that the LMBF is still higher in our model than the LCL, but with smaller upward parcel velocities (Fig. 3.3c) which are controlled by the surface buoyancy flux, fewer parcels reach the LCL.

The ~15 to ~20 minutes delay of the simulated vanishing cloud cover with respect to the dropping LST can be related to the ~16 to ~24 minutes travel time around 09:00 UTC of the fastest rising parcels from the lowest atmospheric layer to the cloud top as shown in Fig. 3.3d, after which the first individual clouds could fully disappear. We note that the vertical updraft velocity of the lowest layer responded within 5 minutes to dif-

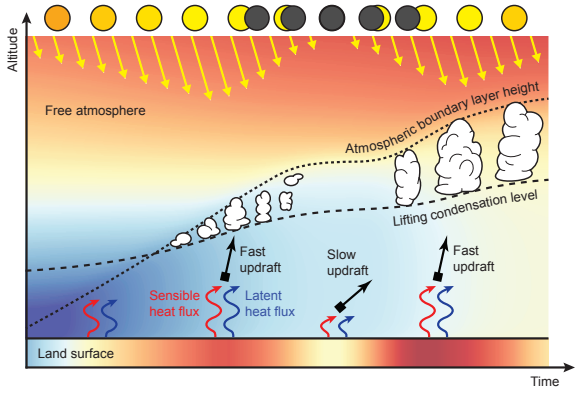

Figure 3.4: Conceptual model of shallow cumulus cloud evolution during a solar eclipse. The time progresses in the horizontal direction to the right. Background color shading indicates the virtual potential temperature of the atmosphere and land surface in our simulation. The red and blue arrows are the sensible and latent heat fluxes, respectively, which depend strongly on the temperature difference between the surface and the atmosphere just above the surface. The yellow arrows represent the amount of incoming solar radiation, which is largest around noon but is reduced during a solar eclipse as illustrated by the lunar disk covering the solar disk. When the growing atmospheric boundary layer height (dotted line) intersects with the lifting condensation level (dashed line), clouds are formed, but they are diminished when the updrafts are slowed down during a solar eclipse, as indicated by the smaller inclination of the black arrow.

ferences in surface fluxes. The travel time depends on the cloud top height and vertical updraft velocities (see Figs. 3.3c and g and Methods). Thus, the cloud response was initiated when the parcels affected by the eclipse started rising, at even smaller obscuration fractions than at which this response could be observed. The ~18 minutes time lag of the simulated cloud cover minimum with respect to mid-eclipse can be related to the relatively long travel time around 11:10 UTC of ~13 to ~19 minutes to LCL at which the newly formed clouds started influencing the cloud cover. Furthermore, we note that the LCL and cloud base remained slightly lower after the eclipse compared to the reference case, due to the continued colder air near the surface (see Supplementary Figure 3.12 and Eq. 3.4). In Fig. 3.4 we provide a conceptual model in which we summarize the most important processes responsible for the shallow cumulus cloud behavior during a solar eclipse.

The disappearance of the shallow cumuli during the solar eclipse has a notable feedback on the solar radiative fluxes. This can be understood from Fig. 3.5, which shows the simulated reflected and net incoming shortwave (SW) radiative flux at TOA, for both the reference and solar eclipse cases. As a result of the solar eclipse the net incoming SW flux started to decrease at 09:00 UTC. However, this change, which has solar dimming as its main cause, is also affected by the decrease of SW radiation reflected back into space due to the clearance of the sky. Indeed, the latter indirect effect causes an opposing increase in the net incoming SW flux at TOA. Neglecting the solar eclipse-induced cloud disappearance in our simulations (as illustrated by dotted line in Fig. 3.5), resulted in an overestimation of 20 W m^{-2} of the eclipse-related reduction of net incoming SW flux at TOA at 11:22 UTC. We note that this error would further increase with longer time lags of

the cloud return with respect to mid-eclipse, such as found in the satellite observations (Fig 3.2a), because then more sunlight illuminates the cloud-free scenes.

3.3. DISCUSSION

The observed response of shallow cumulus clouds to a solar eclipse at already ~15% obscuration, initiated at even smaller obscurations due to the parcel travel time, reveals the potential direct consequence of deploying sunlight intercepting material in the stratosphere or in space. We note that the duration of the cloud response is expected to depend on the speed and magnitude of the local obscuration variations, as the altered difference between the near-surface air and surface temperature, which causes the response, may possibly restore after a certain period. Diminished shallow cumulus clouds would partly oppose the objective of solar geoengineering which is to decrease the amount of net incoming solar radiation, and could prevent the growth into deeper convective and possibly precipitating clouds [51]. While solar geoengineering proposals aim to reduce the solar radiation reaching the (lower) atmosphere and surface globally by only a few percent (depending on the required compensation), the use of non-uniform reductions to achieve this goal could increase the locally experienced variations in obscuration [130]. Space-based examples are the deployment of solar reflectors in Earth orbit [99, 112] or in orbit around the 1st Lagrange point [130], offering daily and seasonally varying shading, respectively. Injected stratospheric aerosols can also exhibit spatio-temporally varying patterns due to seasonally changing global stratospheric circulation, depending on the injection location [158] and strategy employed (whether constant or step-wise) [180, 87]. Consequently, aerosol optical depths of 0.4-0.6 could be attained locally [180, 158, 87], causing up to ~45% of the local direct sunlight to be scattered or absorbed by the aerosols before it reaches the lower atmosphere. Our results should spur model simulations investigating the response of shallow cumulus clouds to those geoengineering concepts, particularly for scenes over land where the surface temperature can adjust quickly. Additionally, our measurements provide an opportunity to validate these models, enhancing their reliability in predicting cloud behavior under natural conditions and in a world influenced by solar geoengineering.

3.4. METHODS

3.4.1. CLOUD MEASUREMENTS

The primary data set used in this research consists of measurements from the Spinning Enhanced Visible and InfraRed Imager (SEVIRI) on board the Meteosat Second Generation (MSG) series of geostationary satellites operated by EUMETSAT. We used data from Meteosat-8 and Meteosat-10, for the 2005-2006 and 2016 cases, respectively. SEVIRI measures TOA radiances over the full Earth disk centered at 0° latitude and 0° longitude every 15 minutes in twelve channels across the visible and near-infrared part of the spectrum [135]. Eleven channels have a narrow bandwidth at low spatial resolution (3 x 3 km^2 at sub-satellite point) and one channel has a broad bandwidth (0.6 - 0.9 μm) at high spatial resolution (1 x 1 km^2), the latter being referred to as the HRV channel. Shortwave channel reflectances were obtained from the observed radiances and the calculated solar irradiance, and were calibrated with MODIS following Meirink, Roebeling,

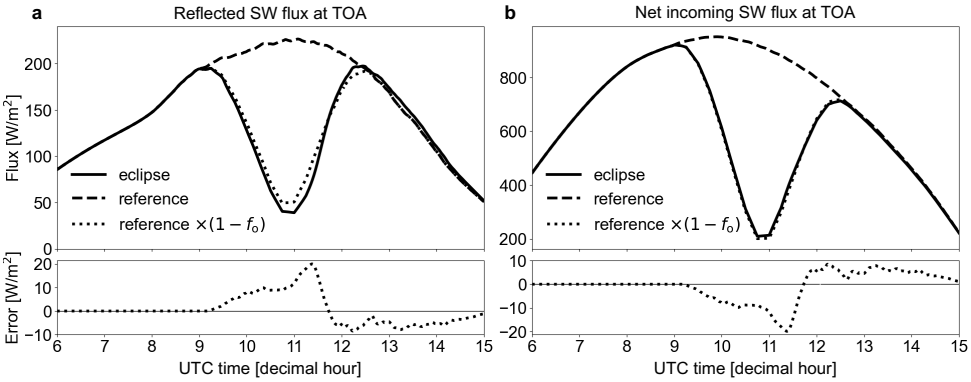

Figure 3.5: Simulated radiative fluxes at the top-of-atmosphere (TOA). (a) The reflected and (b) the net incoming shortwave (SW) radiation (note the different scales of the vertical axes). The solid line is for the solar eclipse case, the dashed line is for the reference case, and the dotted line is for reference case multiplied by (1 - f_o), with f_o the solar obscuration fraction. The bottom panels show the deviation of the latter from the solar eclipse case.

and Stammes [102]. For the longwave channels, the operational calibration from EUMETSAT was used.

For the surface temperature analyses at low spatial resolution (see Surface temperature measurements), cloud masks were calculated using the EUMETSAT Nowcasting and Very Short Range Forecasting Satellite Application Facility (NWC SAF) v2021 cloud algorithm [76]. The NWC SAF software also provided the cloud top height at low spatial resolution. For the cloud analyses at high spatial resolution, we used the low-resolution NWC SAF cloud mask as a basis and improved the spatial resolution of the cloud mask using the HRV TOA reflectances by comparing with a HRV TOA reflectance climatology, which was generated for each pixel with HRV TOA reflectance measurements in a 16-day period centered at the day of the eclipse, following the method of Bley and Deneke [13]. The TOA reflectances of the 0.6 and 1.6 μm channels were paired to simultaneously retrieve the COT and effective droplet radius [107, 11], which were downscaled to high spatial resolution using the HRV channel as described in more detail in [34, 33]. The COT of the pixels that were not masked as cloudy was set equal to zero. For the study area (3-7° N latitude, 27-31° E longitude on 3 October 2005) and between 06:00 and 09:00 UTC, pixels with a TOA reflectance value larger than 1.0, originating from the sunglint in the rivers, were removed from the cloud product.

3.4.2. SOLAR ECLIPSE CORRECTION

We corrected the TOA reflectance for its reduction during a solar eclipse, that was due to the ignorance of the reduced solar irradiance in its calculation, through a division by 1 - f_o, with f_o the solar obscuration fraction. In previous work [168], we validated this approach with the TROPOMI satellite instrument, which allowed for accurate monitoring of aerosols in the partial lunar shadow up to f_o = 0.92. Recently, Wen et al. [185] applied a similar type of correction to images of the Earth Polychromatic Imaging Camera (EPIC) instrument on the Deep Space Climate Observatory (DSCOVR), to quantify

the measured TOA reflectance error without eclipse correction of the sunlit side of the Earth during the annular solar eclipse on 21 June 2020. The value of f_o is different for every pixel as it depends on measurement time, surface height, latitude and longitude, which are provided with the SEVIRI data. The so-called Besselian elements describing the temporal variation of the Moon shadow's geometry were taken from Espenak and Meeus [39]. The value of f_o also depends on wavelength through the wavelength dependent limb darkening of the solar disk [79]. For the corrections of the TOA reflectances in the HRV channel and 0.6 μm, 0.8 μm and 1.6 μm channels, we used the limb darkening coefficients of Pierce and Slaughter [119] and Pierce, Slaughter, and Weinberger [121] at 0.7 μm and the central wavelengths 0.635 μm, 0.81 μm and 1.64 μm, respectively. We refer to Trees et al. [168] for more details about the solar eclipse correction of the TOA reflectance. Applying the cloud algorithms to the corrected TOA reflectance yielded the corrected cloud mask and COT.

3.4.3. SURFACE TEMPERATURE MEASUREMENTS

For the measurements of land surface temperature (LST), we used the LST product of the Land Surface Analysis Satellite Application Facility (LSA SAF) [172] derived from the 10.8 μm and 12 μm SEVIRI channels [182] with an uncertainty of 1 to 2 K [42] which is expected to be stable within the time scales of solar eclipses [49]. We computed the horizontal average LST in the study area in every 15 minutes time step, after replacing the cloudy pixels by interpolated nearest neighbour values using the corrected SEVIRI NWC SAF cloud mask (see Cloud algorithm and Solar eclipse correction). The maximum LST drop due to the eclipse was estimated with respect to the average LST of comparable days (see Selection of comparable days). For the measurements of the sea surface temperature (SST), we used the hourly SST product of the Ocean and Sea Ice Satellite Application Facility (OSI SAF) [133] derived from the 10.8 μm and 12 μm SEVIRI channels with an uncertainty well below 1 K [132].

3.4.4. SELECTION OF COMPARABLE DAYS

The selection of days without solar eclipse that are comparable to our study case on 3 October 2005 in East Africa was done by first selecting 100 days from September and October in 2004, 2005 and 2006 with the smallest differences with respect to our study case in the sums of the predicted sensible and latent heat fluxes by ERA5 [62] (which does not take into account the solar eclipse effect) in the complete diurnal cycle. Subsequently, we refined the selection by removing the days for which the mean of the absolute differences in high spatial resolution cloud cover with respect to our study case between 06:00 and 09:00 UTC was larger than the threshold of 0.1. In this way, we obtained 11 days for which we find the cloud cover comparable in the morning before the lunar shadow reached the study area: 2004-09-10, 2004-10-24, 2005-09-03, 2005-09-19, 2005-09-25, 2005-09-29, 2005-10-04, 2006-09-01, 2006-09-04, 2006-09-08, 2006-10-06. We visually inspected the HRV TOA reflectance and COT for those comparable days and indeed found between 06:00 and 09:00 UTC similar types of shallow cumulus clouds throughout the scene, with low COTs ($\lesssim 5$) as shown in Fig. 3.2b.

3.4.5. CLOUD SIMULATIONS

The cloud simulations were performed with the Dutch Atmospheric Large-Eddy Simulation (DALES) model [63]. The setup was a horizontally cyclic domain of 50 by 50 km^2 with horizontal cell sizes of 100 by 100 m^2 and 209 vertical layers between 0 and 14 km altitude. The vertical extent of each layer was stretched by a factor 1.01 with respect to the layer just below, and it was 20 m in the lowest layer. The ground surface was assumed flat. The atmosphere variables in the domain were initialized with horizontally homogeneous vertical profiles of the liquid potential temperature, total water specific humidity, and horizontal wind speed and direction. Those profiles were the horizontal mean profiles at 02:00 UTC in the study area (3°-7°N latitude, 27°-31°E longitude on 3 October 2005), taken from ERA5 [62]. The pressure profile was determined with the use of the thermodynamic profiles, the gas law and mean hydrostatic balance. After 02:00 UTC, the simulation freely propagated those variables, until 15:00 UTC when the simulations ended. The time and altitude dependent mean horizontal advective tendencies of heat and moisture, in addition to the geostrophic winds, were all diagnosed from ERA5 and prescribed in the DALES runs. That is, we neglect the horizontal in- and outflow of eclipse-induced atmospheric changes at the boundaries of the domain, e.g. due to short-term disturbances in the horizontal pressure gradient [52]. At the top boundary during the simulation, we imposed large-scale subsidence, also taken from ERA5.

The surface fluxes of heat and moisture were computed according to the vertical difference of potential temperature θ and the water vapor specific humidity q_v between the ground surface and the lowest atmospheric model layer (indicated by the subscript 'bot'), respectively. With the appropriate conversion of potential temperature to temperature the sensible and latent fluxes can be expressed as

$$F_{SH} = \frac{\rho c_p}{r_{a,T}}(T_{sfc} - T_{bot} - \frac{g z_{bot}}{c_p}) \tag{3.1}$$

$$F_{LH} = \frac{\rho L_v}{r_{a,q}}(q_{sat}(T_{sfc}) - q_{v,bot}) \tag{3.2}$$

where ρ is the air density in kg m^{-3}, c_p = 1004 J kg^{-1} K^{-1} the heat capacity of dry air, g = 9.81 m s^{-2} the gravitational acceleration, $L_v = 2.5{\cdot}10^6$ J kg^{-1} the latent heat for vaporization of water, and q_{sat} the temperature dependent saturation specific humidity. The aerodynamic resistance coefficients for heat and moisture, $r_{a,T}$ and $r_{a,q}$, respectively, depend on the atmospheric stability near the surface following Monin-Obukhov similarity theory [63]. The dependencies of the r_a values on the surface roughness length and the actual soil water content, which for land conditions will typically be much lower than the saturated value q_{sat}, were taken into account by multiplying them with constant correction factors. This calibration step was made to obtain sensible and heat fluxes that were consistent with the ECMWF model for the reference case. As a consequence, the surface heat fluxes were not parameterized as functions of net incoming radiation, to avoid unnecessary complexity and uncertainties. Instead, the surface temperature T_{sfc} was prescribed using the SEVIRI LST measurements in the study area (see Satellite measurements), and shifted to the ERA5 skin temperature at 02:00 UTC through a positive offset of 2.0274 K applied to the complete LST time series, for consistency with the initial atmospheric profiles. In the simulation without eclipse and until 09:00 UTC, T_{sfc} was

identical to that in the simulation with eclipse, but after 09:00 UTC it was the average of the LST time series of the comparable days shifted to the ERA5 skin temperature at 02:00 UTC.

The simulated cloud cover in the study area was computed as follows. First, we re-gridded the DALES output liquid water specific humidity q_l in kg kg^{-1} to a grid with cell sizes of 1 x 1 km^2, for a fair comparison with the SEVIRI observations. Secondly, we computed the COT by evaluating the following integral from the surface (0) to TOA (z_{TOA}) [154]:

$$\mathrm{COT}(x,y) = \int_0^{z_{\mathrm{TOA}}} \frac{\frac{3}{2}\rho_{\mathrm{air}}(z)\, q_l(x,y,z)}{\rho_{\mathrm{liq}}\, r_{\mathrm{eff}}}\, dz \tag{3.3}$$

where ρ_{air} is the air density in kg m^{-3}, $\rho_{\mathrm{liq}} = 1000$ kg m^{-3} is the density of liquid water, and r_{eff} is the droplet effective radius which we assumed to be constant and equal to 10^{-5} m. Thirdly, the columns (x, y) with a COT larger than 1 were flagged as a cloudy column. The cloud cover was computed as the number of cloudy columns divided by the total number of columns in the domain. For the mean COT time series, we computed the horizontal average COT considering the cloudy columns only.

The lifting condensation level (LCL) in m was computed from the DALES output of air temperature T_{bot} in K and relative humidity $\mathrm{RH}_{\mathrm{bot}}$ in % of the bottom atmospheric layer (at 10 meter altitude), using the suggested formula by Lawrence [86]:

$$z_{\mathrm{LCL}} = \left(20 + \frac{T_{\mathrm{bot}} - 273.15}{5}\right) \cdot (100 - \mathrm{RH}_{\mathrm{bot}}) \tag{3.4}$$

The level of minimum buoyancy flux (LMBF) was computed as the altitude at which the buoyancy flux $\overline{w'\theta'_v}$ was minimum, where θ_{v} is the virtual potential temperature which depends on specific humidity q_{v} in kg kg^{-1}, temperature T in K, pressure p in Pa, reference pressure $p_0 = 10^5$ Pa, c_{p}, the gas constant for dry air $R_{\mathrm{d}} = 287.0$ J kg^{-1} K^{-1}, and the gas constant for water vapor $R_{\mathrm{v}} = 461.5$ J kg^{-1} K^{-1} [28]:

$$\theta_{\mathrm{v}} = T\left(\frac{p_0}{p}\right)^{\frac{R_{\mathrm{d}}}{c_{\mathrm{p}}}} \left(1 + \left(\frac{R_v}{R_d} - 1\right) \cdot q_{\mathrm{v}}\right) \tag{3.5}$$

and $\overline{w'\theta'_{\mathrm{v}}}$ was defined as:

$$\overline{w'\theta'_{\mathrm{v}}} = \frac{\sum_{i=1}^{N_x}\sum_{j=1}^{N_y} w_{ij}(\theta_{\mathrm{v},ij} - \overline{\theta}_{\mathrm{v}})}{N_x N_y} \tag{3.6}$$

in which N_x and N_y are the number of grid cells in the horizontal x- and y directions, and the overbar indicates a horizontal mean value. The mean updraft virtual potential temperature, $\overline{\theta}_{\mathrm{v,up}}(z)$, was computed as the mean of $\theta_{\mathrm{v}}(z)$ of the updrafts only (i.e., the grid points at a certain altitude z for which $w_{ij} > 0$). The velocities of the fast rising parcels were defined by the p-percentile velocities $w_{\mathrm{p\%}}$ (with $p = 1$, 3 and 5), which were the vertical velocities at a certain altitude z for which a percentage p of the w-distribution contained grid points with $w_{ij} > w_{\mathrm{p\%}}$ (see [143]). The travel time Δt of the fast rising

parcels from the surface to a certain altitude z_*, using vertical velocity $w_{p\%}$, was computed by numerically evaluating

$$\Delta t = \int_0^{z_*} \frac{dz}{w_{p\%}(z)} \tag{3.7}$$

with $z_* = z_{LCL}$ for the travel time to LCL and $z_* = z_{CT}$ for the travel time to the cloud top. The cloud top was defined as the highest altitude for which $q_l > 0$.

DALES uses the Rapid Radiative Transfer Model for Global climate model applications (RRTMG) radiation scheme [68, 14] to compute the shortwave (SW) and longwave (LW) radiative fluxes through the atmosphere, emitted and reflected by the surface, and emerging from TOA during the simulation. In the solar eclipse case, the SW radiation incident at TOA was multiplied by $(1 - f_o)$, where f_o was the horizontal mean obscuration fraction in the study area taken at 0.635 μm (see Solar eclipse correction). We used vertical profiles of the ozone mass mixing ratios in the study area from ERA5 [62]. The surface albedo was the horizontal mean white-sky albedo in the study area measured by MODIS [134].

SUPPLEMENTARY INFORMATION

This article has accompanying supplementary videos of the corrected SEVIRI TOA VIS reflectance and cloud optical thickness during the solar eclipses of 3 October 2005, 29 March 2006, and 1 September 2016 (corresponding to Fig. 3.1 and Supplementary Figures 3.7 and 3.8, respectively) at 15 minutes temporal resolution.

ACKNOWLEDGMENTS

The authors thank Richard Bintanja (KNMI) for the discussions during manuscript preparation and David Donovan (KNMI) for reading the manuscript before submission. VT acknowledges funding by the User Support Programme Space Research (GO), project number ALWGO.2018.016, of the Dutch Research Council (NWO). SdR acknowledges funding by the Refreeze the Arctic Foundation for research on geoengineering techniques at TU Delft.

COMPETING INTERESTS

The authors declare no competing interests.

AUTHOR CONTRIBUTIONS

VT wrote the manuscript with contributions from SdR, JW and JFM. VT computed the solar obscuration fractions. SdR did the DALES computations. JW and JFM prepared the SEVIRI observations and JW converted the observations to high spatial resolution. VT, SdR, JW, JFM, PW, PS and APS reviewed the manuscript and were involved in the analysis and selection of the presented results.

DATA AVAILABILITY

The data required to replicate the timeseries presented in this article, as well as the input and boundary conditions for our model simulations, are available in the public repository Zenodo (https://doi.org/10.5281/zenodo.10371414).

CODE AVAILABILITY

The Dutch Atmospheric Large-Eddy Simulation (DALES) software used for this research is publicly available under the terms of the GNU GPL version 3 on https://github.com/dalesteam/dales.

3.5. SUPPLEMENTARY MATERIAL

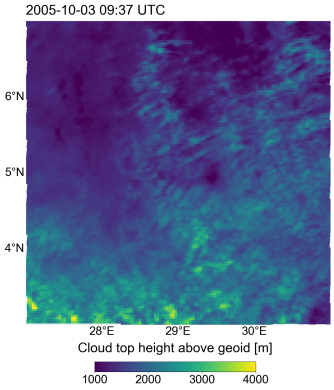

Figure 3.6: Cloud top height above geoid in the study area on 3 October 2005 measured by SEVIRI. The surface height above geoid in this area varies between 300 and 1700 m.

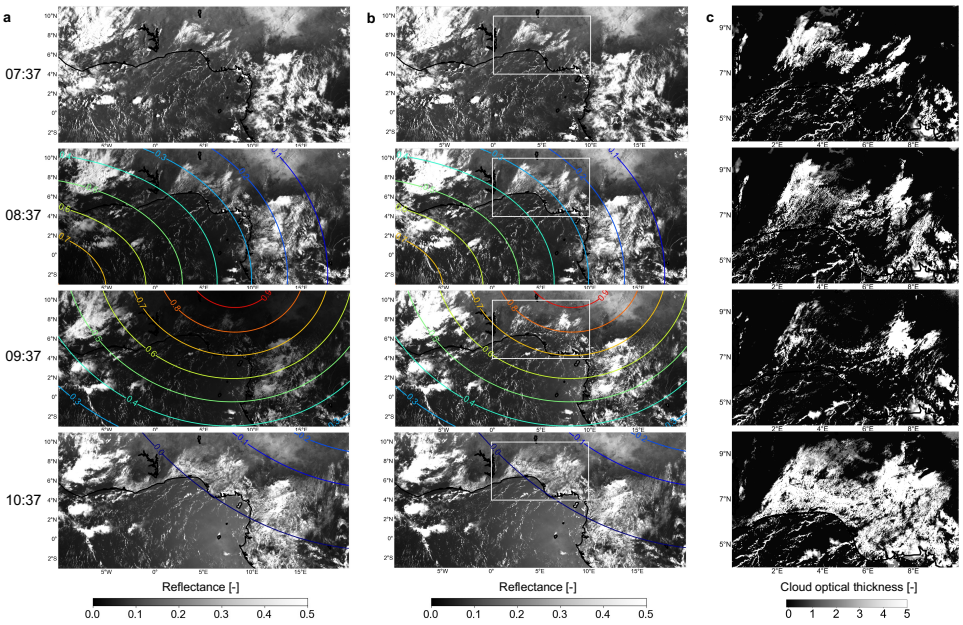

Figure 3.7: Similar to Fig. 3.1, but for the total solar eclipse of 29 March 2006 passing over West Africa (in the North-East) and the Atlantic ocean (in the South-West) at 07:37, 08:37, 09:37 and 10:37 UTC (from top to bottom). The white squares in (b) indicate the zoom area for the cloud optical thickness in (c).

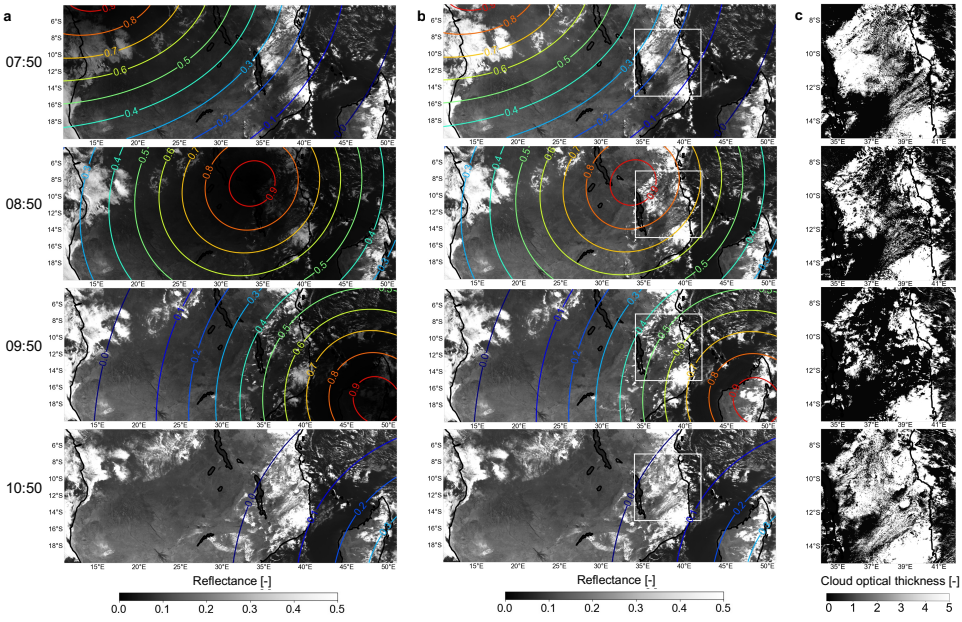

Figure 3.8: Similar to Fig. 3.1, but for the annular solar eclipse of 1 September 2016 passing over Middle Africa and the Indian Ocean (in the East) at 07:50, 08:50, 09:50 and 10:50 UTC (from top to bottom). The white squares in (b) indicate the zoom area for the cloud optical thickness in (c).

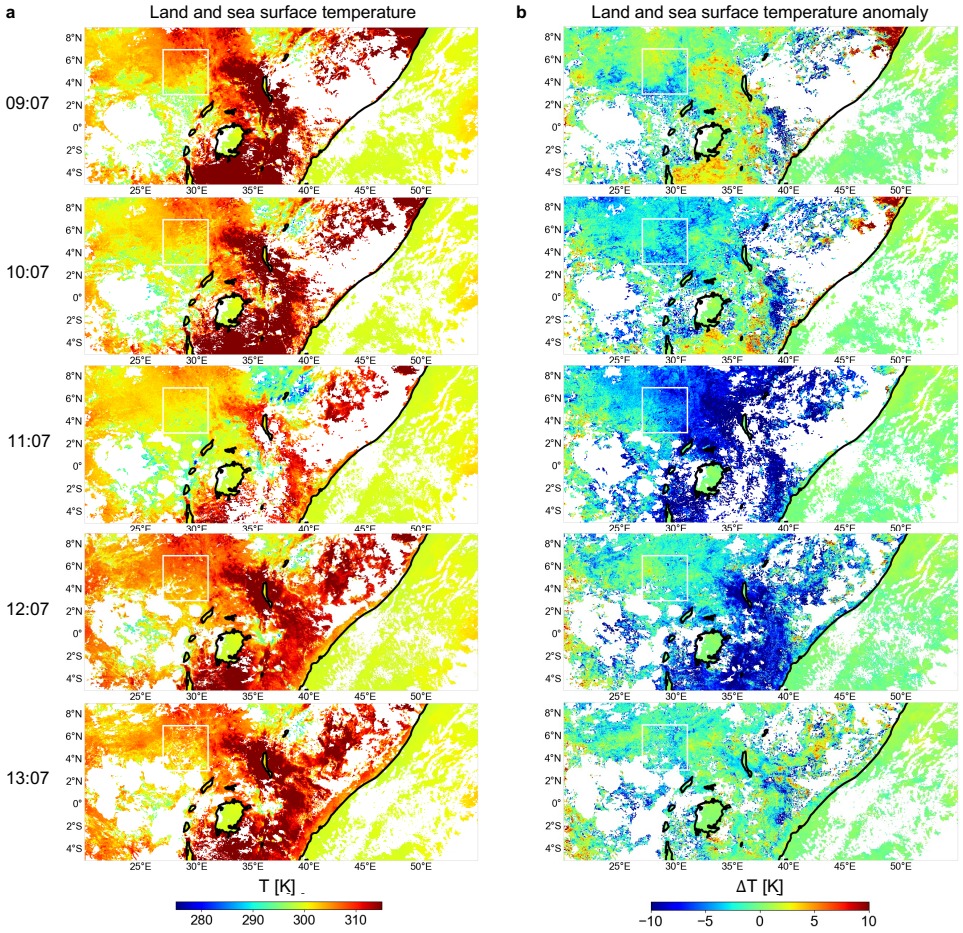

Figure 3.9: SEVIRI images of the land and sea surface temperature and their anomaly over East Africa and part of the Indian Ocean during the annular solar eclipse on 3 October 2015. (a) The land surface temperature measurements at five subsequent hours (from top to bottom) and (b) the deviation from the mean of the comparable days. The white square indicates the study area. The negative deviation over land at 10:07, 11:07 and 12:07 UTC was caused by the solar eclipse.

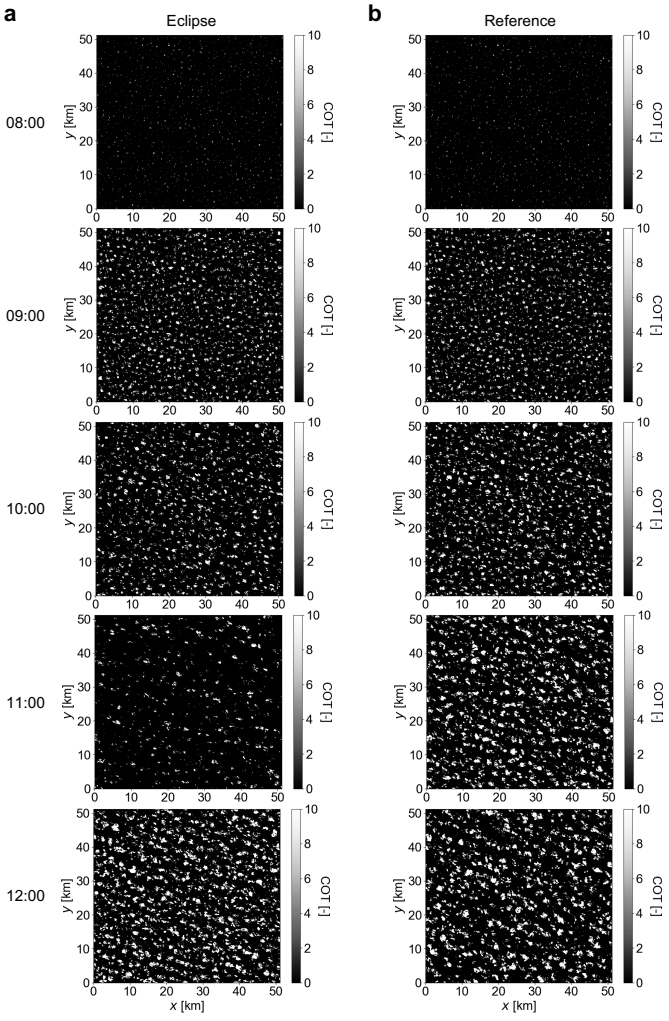

Figure 3.10: Simulated cloud optical thickness (top view) with DALES for (a) the solar eclipse case and (b) the reference case, at 08:00, 09:00, 10:00, 11:00 and 12:00 UTC (from top to bottom).

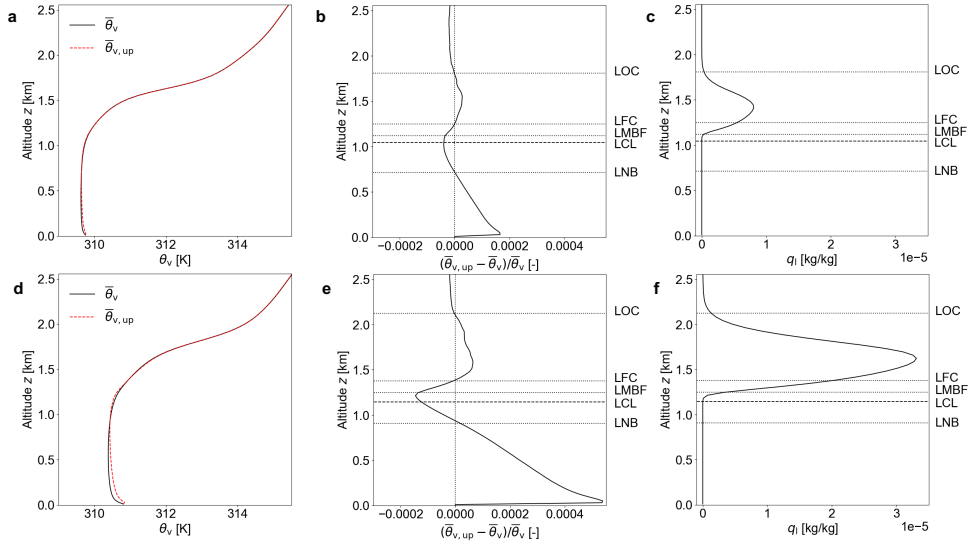

Figure 3.11: Vertical profiles of atmospheric horizontal mean quantities simulated by DALES at 11.00 UTC. (a) The virtual potential temperature taking all columns (black solid line) and columns with updrafts only (red solid line), and (b) their normalized difference, for the solar eclipse case. (c) The liquid water specific humidity for the solar eclipse case. Similar for (d), (e) and (f) but then for the reference case. Positive values in (b) and (e) indicate positive buoyancy. In (b), (c), (e) and (f), the level of neutral buancy (LNB), lifting condensation level (LCL), level of minimum buoyancy flux (LMBF), level of free convection (LFC) and limit of convection (LOC) are indicated.

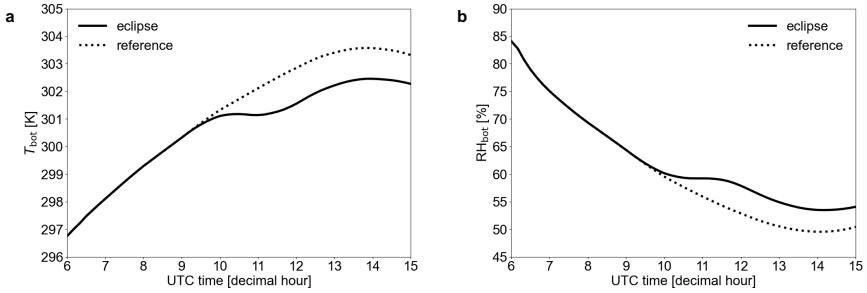

Figure 3.12: (a) Simulated horizontal mean air temperature and (b) relative humidity by DALES of the bottom atmospheric layer (at 10 meter altitude) for the study area in the solar eclipse case (solid line) and reference case (dotted line).

4

DARCLOS: A CLOUD SHADOW DETECTION ALGORITHM FOR TROPOMI

Cloud shadows are observed by the TROPOMI satellite instrument as a result of its high spatial resolution as compared to its predecessor instruments. These shadows contaminate TROPOMI's air quality measurements, because shadows are generally not taken into account in the models that are used for aerosol and trace gas retrievals. If the shadows are to be removed from the data, or if shadows are to be studied, an automatic detection of the shadow pixels is needed. We present the Detection AlgoRithm for CLOud Shadows (DARCLOS) for TROPOMI, which is the first cloud shadow detection algorithm for a spaceborne spectrometer. DARCLOS raises potential cloud shadow flags (PCSFs), actual cloud shadow flags (ACSFs) and spectral cloud shadow flags (SCSFs). The PCSFs indicate the TROPOMI ground pixels that are potentially affected by cloud shadows based on a geometric consideration with safety margins. The ACSFs are a refinement of the PCSFs using spectral reflectance information of the PCSF pixels, and identify the TROPOMI ground pixels that are confidently affected by cloud shadows. Because we find indications of the wavelength dependence of cloud shadow extents in the UV, the SCSF is a wavelength dependent alternative for the ACSF at the wavelengths of TROPOMI's air quality retrievals. We validate the PCSF and ACSF with true color images made by the VIIRS instrument on board of Suomi NPP orbiting in close proximity to TROPOMI on board of Sentinel-5P. We find that the cloud evolution during the overpass time difference between TROPOMI and VIIRS complicates this validation strategy, implicating that an alternative cloud shadow detection approach using co-located VIIRS observations could be problematic. We conclude that the PCSF can be used to exclude cloud shadow contamination from TROPOMI data, while the ACSF and SCSF can be used to select pixels for the scientific analysis of cloud shadow effects.

This chapter has been published in Atmospheric Measurement Techniques **15**, 3121–3140 (2022) [169].

4.1. INTRODUCTION

Air quality monitoring from space using satellite spectrometers started in 1978 with the launch of the first Total Ozone Mapping Spectrometer (TOMS) instrument on board the Nimbus-7 satellite. TOMS globally measured aerosol properties and concentrations of O_3 and SO_2 in the Earth's atmosphere on a daily basis, retrieved from the Earth's reflectance of sunlight using six ultraviolet (UV) wavelength bands [57]. The first high-spectral resolution spectrometer was the Global Ozone Monitoring Experiment (GOME) [19] launched in 1995, followed by the SCanning Imaging Absorption spectroMeter for Atmospheric ChartograpHY (SCIAMACHY) [17], the Ozone Monitoring Instrument (OMI) [89], the GOME-2 A/B/C instruments [106] and, most recently, the TROPOspheric Monitoring Instrument (TROPOMI) [177], allowing for trace gas retrieval using differential absorption features in the spectra of the Earth's reflectance [122].

The spatial resolutions of TOMS, GOME, SCIAMACHY, OMI and GOME-2 have been 50 × 50 km^2, 320 × 40 km^2, 60 × 30 km^2, 24 × 13 km^2 and 80 × 40 km^2, respectively. Those resolutions are too coarse to discern kilometer-scale clouds or cloud shadows. The pixels of those spectrometers often have been partly cloudy, such that the effects of clouds, cloud shadows and cloud-free regions are blended. Because of the inability to distinguish between those effects and the complexity of three-dimensional (3-D) radiative transfer, state-of-art algorithms for satellite spectrometers employ one-dimensional (1-D) radiative transfer models, which neglect 3-D cloud effects on cloud-free regions inside the partly cloudy pixels or on adjacent cloud-free pixels. For example, the FRESCO (Fast REtrieval Scheme for Clouds from the Oxygen A band) cloud retrieval algorithm uses the independent pixel approximation, and does not take into account cloud shadows [78, 183]. However, although cloud shadows are hardly visible on the coarse resolution measurement grids of those spectrometers, they do in principle contaminate the total radiances of the large pixels.

TROPOMI on board of the ESA Sentinel-5P satellite was launched in October 2017 and is the spaceborne spectrometer with the highest spatial resolution to date: the ground pixels have dimensions of 7.2 × 3.6 km^2 in the nadir viewing direction, and decreased to 5.6 × 3.6 km^2 on 6 August 2019.[1] TROPOMI provides daily global maps of aerosol properties and concentrations of O_3, NO_2, SO_2 and HCHO from ultraviolet-visible (UV–VIS, 267–499 nm) wavelengths, of cloud properties from near-infrared (NIR, 661–786 nm) wavelengths and concentrations of CO and CH_4 from shortwave infrared (SWIR, 2300–2389 nm) wavelengths. Because of its high spatial resolution and data quality, TROPOMI has, for example, shown to be able to observe local NO_2 emission sources such as power plants [10], gas compressor stations [174] and cities [92], detailed volcanic SO_2 plumes [157], and CH_4 leakage from oil/gas fields [110, 176, 137]. Recently, NO_2 plumes from individual ships have been identified with TROPOMI in areas where the ocean sunglint enhances the signal-to-noise [46].

The small pixel size of TROPOMI also causes cloud shadows to be detectable. Cloud shadow signatures can be found along cloud edges, manifested as pixels with smaller radiances than measured in their cloud-free neighborhood. Smaller measured radiances result in lower derived reflectance values, potentially affecting TROPOMI's air quality

[1] The radiance co-addition time reduced from 1080 to 840 ms starting in orbit 9388. This resulted in a decrease of the minimal along-track sampling distance from 7 km at nadir to 5.5 km at nadir [93].

products. Cloud shadow effects on air quality data sets can only be studied, discarded and/or corrected if the cloud shadow contaminated pixels are identified. Individual shadow pixels may be identified manually in maps of TROPOMI data through visual inspection. However, for the automatic removal or correction of shadow contaminated data, and for the statistical analysis of shadow effects on large data sets, an automatic shadow detection is needed.

For satellite spectrometer measurements, cloud shadow detection is a new topic and will become more important with the increasing spatial resolution in future satellite spectrometer missions, such as Sentinel-5 (7.5×7.3 km^2) [116], CO2M ($< 2 \times 2$ km^2) [144] and TANGO (300×300 m^2) [85]. For high spatial resolution aerial and satellite imagers, shadow detection is not new. Shadows of buildings affect the applications of aerial images, such as urban change detection and traffic monitoring [3]. The screening of clouds and their shadows is an important step in the preprocessing of satellite imager data of for example Landsat and MODIS [193, 184]. Shadows degrade the quality of the images lowering the accuracy of their applications such as land cover classification and change detection [188]. If cloud shadows are not screened correctly, they may be confused with dark surface features such as, for example, water bodies affecting the remote sensing performance of flood detection [90].

Several approaches have been followed by aerial and spaceborne imagers to detect cloud shadows. The main approaches can be categorized into geometry-based methods [145, 146, 67] where the shadow location is computed with known or assumed parameters of the cloud shadow geometry, and spectral-based methods [1] where the shadow is determined with spectral tests applied to the measured radiance. Often, a combination of those approaches is being used, first determining the potential cloud shadow locations with one of the two approaches and subsequently refining the shadows with the other approach [65, 192, 156]. The spectral tests may consist of simple darkness thresholds, however dark surface features can easily incorrectly be interpreted as shadows. Luo, Trishchenko, and Khlopenkov [95] therefore presented a method to detect cloud shadows in MODIS images exploiting the ratio between the blue and NIR (or SWIR) spectral bands, arguing that shadows may appear more blue due to the lack of direct solar illumination. [95] concluded that their method is problematic over water regions and wetlands, because the relatively dark spectra of water and shadows are difficult to distinguish. Additionally, the blueness of shadows may depend on the shadow geometry and cloud parameters such as thickness and height.

Unsupervised machine learning (clustering) techniques have been proposed for urban shadow detection in aerial images, but the spectral variability of the shadowed materials can complicate the choice of the number of classes [3]. Because various cloud and land surface types may be mixed within individual pixels of satellite imagery, [15] proposed a fuzzy clustering algorithm for cloud and cloud shadow detection in Landsat images, in which pixels can belong to multiple classes with associated weighting factors. Supervised machine learning techniques (neural networks and support vector machines) have been proposed for cloud shadow detection in satellite images also [66, 69], but are generally computationally expensive, require large training data sets with classified shadows (which itself is the problem to be solved), and trained classifiers may not work for new scenes with different shadow patterns [3, 193].

The most suitable approach for shadow detection for a satellite imager depends on the characteristics of the instrument and its host satellite. For example, the cloud and cloud shadow detection algorithm Fmask for Landsat 4-7, introduced by Zhu and Woodcock [192], uses for its geometry-based part the thermal band (10.4 to 12.5 μm) measuring the cloud's brightness temperature. Assuming a constant lapse rate, Fmask computes the cloud top height and projection of the cloud shadow onto the surface. For imagers that do not have a thermal band, a range of potential cloud heights can be assumed [190] or the approach can be limited to spectral tests only. Parmes et al. [111] proposed a cloud and cloud shadow detection method for Suomi NPP VIIRS only based on spectral tests avoiding the usage of a thermal band, and suggested that the method could therefore also work for Sentinel-2 which does not have a thermal band. However, the accuracy of their shadow detection was low (36.1%), with a false alarm rate of 82.7%. Goodwin et al. [50], Zhu and Woodcock [191], Candra, Phinn, and Scarth [20] and Candra, Phinn, and Scarth [21] chose to perform spectral tests based on the reflectance differences with cloud-free historical reference images, for Landsat cloud shadow detection. Such multi-temporal shadow detection approaches generally enhance the shadow detection performance [193], but require the availability of cloud-free seasonally dependent reference images which may be challenging for satellites with long revisit periods.

In this paper we present the Detection AlgoRithm for CLOud Shadows (DARCLOS), a fast cloud shadow detection algorithm for TROPOMI and the first cloud shadow detection algorithm for a spaceborne spectrometer. DARCLOS starts with a geometry-based computation of potential shadow locations, using the cloud fraction, cloud height, viewing and illumination geometries, and surface height stored in the already available TROPOMI NO_2 product and cloud product FRESCO. Climatological cloud-free surface albedo reference data is available for TROPOMI and is used to perform spectral tests refining the shadows. The spectral tests are only based on the darkness of shadows relative to the reference data. This means that no assumptions are made about the color of cloud shadows. As TROPOMI is a spectrometer, DARCLOS exploits the spectra of TROPOMI by using the wavelength for shadow detection where the surface reflectance is strongest, independent of surface classification. We validate the PCSF and ACSF with true color images of Suomi NPP VIIRS which orbits in close proximity to TROPOMI. Because geometrical shadow extents may be wavelength dependent, DARCLOS also outputs a wavelength dependent cloud shadow flag for the wavelengths at which TROPOMI's air quality products are retrieved. Such a cloud shadow detection at the precise wavelengths of TROPOMI's air quality products is unique for DARCLOS and cannot be done with data from an imager.

This paper is structured as follows. In Sect. 4.2, we explain the method to detect cloud shadows in TROPOMI data. In Sect. 4.3, we show the results of the cloud shadow detection algorithm with three case studies. In Sect. 4.4, the validation results are presented. In Sect. 4.5, we discuss the limits of the algorithm and raise several points of attention for future applications. In Sect. 4.6, we summarize the results and state the most important conclusions of this paper.

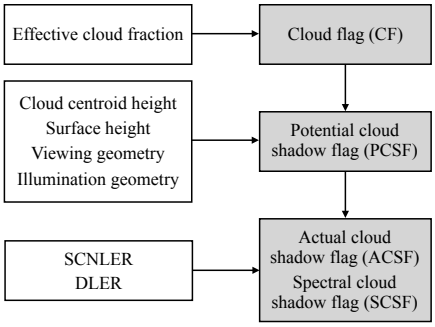

Figure 4.1: Summary of the inputs and outputs of DARCLOS. The white boxes describe the main input data and the grey boxes describe the calculated output products. SCNLER refers to the reflectivity of the scene (Sect. 4.2.2) and DLER refers to the climatological directionally dependent surface reflectivity (Sect. 4.2.2). More details are provided in the main text.

4.2. METHOD

Here, we explain the method to detect cloud shadows in TROPOMI data. We first compute the potential cloud shadow flag (PCSF), explained in Sect. 4.2.1, and then compute the actual cloud shadow flag (ACSF), explained in Sect. 4.2.2. Figure 4.1 summarizes the inputs and outputs of DARCLOS. The PCSFs indicate the TROPOMI ground pixels that are potentially affected by cloud shadows based on a geometric consideration with safety margins. The ACSFs are a refinement of the PCSFs using spectral reflectance information of the PCSF pixels, and indicate the TROPOMI ground pixels that are confidently affected by cloud shadows. The PCSF can be used to exclude cloud shadow contamination from the TROPOMI Level 2 data, while the ACSF can be used to select pixels for the scientific analysis of cloud shadow effects. The spectral cloud shadow flag (SCSF) is a wavelength dependent alternative for the ACSF and will be explained in Sect. 4.5.

4.2.1. POTENTIAL CLOUD SHADOW FLAG (PCSF)

The PCSFs indicate the pixels that are potentially affected by cloud shadows. The PCSF is intended to be useful for filtering any cloud shadow contaminated TROPOMI data. Therefore, the number of false negative shadow detections in the PCSF should be minimized (see Sect. 4.4). Hence, the PCSF shadow is an overestimation of the true shadowed area.

The PCSF is computed in two steps. First, we compute the maximum potential geometric shadow extent from the cloud, with additional safety margins. Then, we flag the area between the cloud and the maximum potential shadow extent. Both steps are explained in more detail below.

THE MAXIMUM POTENTIAL SHADOW EXTENT

Figure 4.2 illustrates the cloud shadow geometry in the local reference frame at the Earth's surface. The reference frame is equivalent to the topocentric reference frame of TROPOMI [91], except for the xy-plane which is now lifted in the zenith direction with the surface

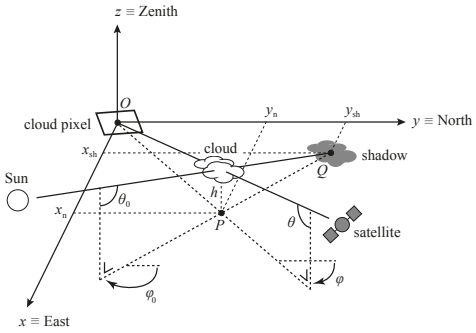

Figure 4.2: Sketch of the cloud shadow geometry in the local reference frame at the Earth's surface. The cloud as observed by the satellite is located at point O, resulting in a TROPOMI cloud pixel at O (indicated by the white quadrilateral), while the actual cloud is located at height h above point P. The shadow is located at point Q.

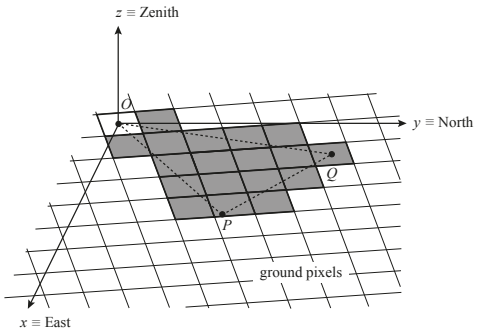

Figure 4.3: Sketch of the PCSF flagging of the TROPOMI ground pixels in the local reference frame at the Earth's surface. The PCSF pixels are indicated in grey and the cloud pixel is indicated by the white quadrilateral. Points O, P. and Q correspond to points O, P and Q in Fig. 4.2.

height h_{sfc} w.r.t. the WGS84 Earth reference ellipsoid. Here, the origin (point O) of the reference frame is set at the center of a cloud pixel, which represents the projection of the cloud's centroid in the viewing direction onto the Earth's surface at geodetic latitude δ_{c} and longitude ϑ_{c}. The cloud pixels are the TROPOMI ground pixels with a raised cloud flag (CF) and are determined by an effective cloud fraction (the cloud fraction assuming a cloud albedo of 0.8) larger than 0.05. The effective cloud fraction was determined in the NO_2 spectral window and taken from the TROPOMI NO_2 data product [175]. Angles θ_0 and θ are the solar and viewing zenith angles, respectively. Angles φ_0 and φ are the solar and viewing azimuth angles, respectively, measured positively clockwise from the North when looking in the nadir direction. The values for θ_0, θ, φ_0 and φ are provided in the TROPOMI data for the origin of the *unlifted* topocentric reference frame, i.e., when $h_{\mathrm{sfc}} = 0$. In the problem of finding the cloud shadow belonging to the cloud pixel at the origin, we neglect variations of θ_0, θ, φ_0 and φ in the horizontal (x and y) and vertical (z) direction, and we assume that h_{sfc} is constant.

The location, dimensions and darkness of a cloud shadow cast on the Earth's surface and/or atmosphere below the cloud, as observed from space, may depend on (1) the cloud's location in 3-dimensional space, (2) the location of the underlying surface and/or atmosphere on which the shadow is cast in 3-dimensional space, (3) the horizontal and vertical extents of the cloud, (4) the optical thickness of the cloud, (5) the optical thickness of the atmospheric layers, (6) the illumination geometry (θ_0 and φ_0), and (7) the viewing geometry (θ and φ). Because in the first step of the PCSF determination we search for the maximum potential shadow extent, we assume an opaque cloud and neglect the optical thickness of the atmospheric layers, such that the computed shadows are cast on the Earth's surface where the shadow separation from the cloud is largest.

In Fig. 4.2, the cloud is located at $(x_{\mathrm{n}}, y_{\mathrm{n}}, h)$. Point P at $(x_{\mathrm{n}}, y_{\mathrm{n}}, 0)$ is the nadir projection of the cloud's centroid onto the surface and h is the cloud height w.r.t. the surface,

which can be computed as

$$h = (1 + C)\,(h_c - h_{sfc})\,. \tag{4.1}$$

In Eq. (4.1), h_c is the FRESCO cloud height [78, 183], which is an approximation of the true height of the cloud's centroid w.r.t. the WGS84 Earth reference ellipsoid. Because, for the PCSF, we search for the maximum potential shadow extent, we have introduced the safety margin C which increases the cloud height proportional to $h_c - h_{sfc}$. We set $C = 0.5$, for which the number of false negative shadow detections (i.e. the omission error of the PCSF, see Sect. 4) resulting from underestimated maximum potential shadow extents converged to a minimum.

If we assume that the center of the cloud pixel is the projection of the cloud's centroid in the viewing direction onto the Earth's surface, x_n and y_n can be computed as [95]:

$$x_n = h \cdot \tan\theta \sin\varphi, \tag{4.2}$$
$$y_n = h \cdot \tan\theta \cos\varphi. \tag{4.3}$$

The location of point Q in the cloud shadow on the Earth's surface, (x_{sh}, y_{sh}), then follows from:

$$x_{sh} = x_n - h \cdot \tan\theta_0 \sin\varphi_0, \tag{4.4}$$
$$y_{sh} = y_n - h \cdot \tan\theta_0 \cos\varphi_0. \tag{4.5}$$

Finding the geodetic latitude, δ_{sh}, and longitude, ϑ_{sh}, of Q is an example of the direct geodetic problem for which the solution involves an iterative procedure [178]. However, because of the small distances in the cloud shadow geometry relative to the Earth's radii of curvature, δ_{sh} and ϑ_{sh} can accurately be approximated by differential northing and easting formulae:

$$\delta_{sh} \approx \delta_c + \frac{y_{sh}}{M + h_{sfc}}, \tag{4.6}$$
$$\vartheta_{sh} \approx \vartheta_c + \frac{x_{sh}}{(N + h_{sfc})\cos\delta_c}, \tag{4.7}$$

where M and N are the Earth's ellipsoidal meridian radius of curvature and radius of curvature in the prime vertical, respectively, which both vary with latitude δ_c [164].

The center of the cloud pixel may not coincide with the projection of the cloud's centroid in the viewing direction onto the Earth's surface, as was assumed in Eqs. (4.2) and (4.3). This is particularly true, for example, when small clouds in the pixel are located near the pixel edges or corners, or when the edge of a large cloud deck traverses the pixel. Moreover, the actual projections of the unknown true horizontal and vertical cloud extents are located inside but near the edges of the cloud pixel.[2] Therefore, we repeat the computation of point Q four times, now placing the *corners* of the cloud pixel in the origin of the reference frame (not shown in Fig. 4.2).

[2] An even larger horizontal or vertical cloud extent would be part of an adjacent cloud pixel.

RAISING THE PCSF

In the second step of the PCSF determination, we select the area in which PCSFs are to be raised, based on the calculated points P and Q. As illustrated in Fig. 4.3, we flag all the cloud-free ground pixels (i.e. for which no CF is raised) within or intersected by the triangle OPQ.

All cloud-free ground pixels intersected by line segment OQ are flagged for two reasons. First, OQ is the projection in the viewing direction onto the Earth's surface of a line segment, between the cloud's centroid and point Q, where the shadowed atmosphere is located (e.g., an optically thick atmosphere may lead to short shadows, cast on the atmospheric layers, projected onto the surface close to point O). Secondly, a possible overestimation of h implies an actual cloud's nadir projection closer to O (along line OP) which, with an unchanged illumination geometry, results in a shadow location between O and Q on line segment OQ.

All cloud-free ground pixels intersected by line segment PQ are flagged because the vertical cloud extent below the cloud's centroid is unknown. Although the vertical cloud extent of an isolated cloud may result in an adjacent cloud pixel, the vertical extent *below* the cloud's centroid may be invisible from space if neighboring clouds cover the volume below the cloud's centroid. For that reason, line segment PQ represents the potential shadow locations of a hypothetical cloud extending from the cloud's centroid to the surface.

All cloud-free ground pixels within or intersected by triangle OPQ are flagged, because combinations of the aforementioned situations may occur. For similar reasons as mentioned in Sect. 4.2.1, we repeat the flagging four times for the triangles OPQ where O is placed in the corners of the cloud pixel (not shown in Fig. 4.3).

4.2.2. ACTUAL CLOUD SHADOW FLAG (ACSF)

In this section, the computation of the ACSF is explained. The ACSFs indicate the pixels that are confidently affected by cloud shadows. They are a subset of the PCSFs, and are intended to be useful for selecting pixels for the scientific analysis of cloud shadows. The number of false positive shadow detections in the ACSF should therefore be minimized (see Sect. 4.4).

The ACSF is determined in two steps. First, we apply a Rayleigh scattering correction to the measured reflectance at the top of the atmosphere for the PCSF pixels. Then, we compare the corrected reflectance to the expected surface reflectance from climatological observations by TROPOMI, revealing the actual shadowed pixels. This comparison is done at the wavelength where the surface reflectance is strongest. Both steps are explained in more detail below.

LAMBERTIAN-EQUIVALENT REFLECTIVITY OF THE SCENE (SCNLER)

The spectral Earth's reflectance at the top of the atmosphere (TOA) as measured by a satellite is defined as

$$R^{\text{meas}}(\mu,\mu_0,\varphi,\varphi_0,\lambda) = \frac{\pi I(\mu,\mu_0,\varphi,\varphi_0,\lambda)}{\mu_0 E_0(\lambda)}, \tag{4.8}$$

where I is the radiance reflected by the atmosphere-surface system in W m^{-2}sr^{-1}nm^{-1}, E_0 is the extraterrestrial solar irradiance perpendicular to the beam in W m^{-2}nm^{-1} and

$\mu_0 = \cos\theta_0$. I and E_0 depend on wavelength λ in nm, and I additionally depends on $\mu = \cos\theta$, μ_0, φ and φ_0.

First, we calculate the albedo of the surface, A_s, needed to match a modeled TOA reflectance, R^{model}, to the measured TOA reflectance, R^{meas}. The model assumes a Lambertian (i.e., depolarizing and isotropic reflecting) surface below a cloud-free and aerosol-free atmosphere, such that the modeled TOA reflectance can be expressed as [24]:

$$R^{\text{model}}(\mu,\mu_0,\varphi-\varphi_0,\lambda) = R^0(\mu,\mu_0,\varphi-\varphi_0,\lambda) + \frac{A_s(\lambda)\,T(\mu,\mu_0,\lambda)}{1-A_s(\lambda)\,s^*(\lambda)}. \tag{4.9}$$

The first term at the right-hand side of Eq. (4.9), R^0, is the so-called path reflectance, which is the modeled TOA reflectance of the atmosphere bounded below by a black surface. The second term is the modeled surface contribution to the TOA reflectance, where A_s is the albedo of the Lambertian surface, T is the total transmittance of the atmosphere for illumination from above and below, and s^* is the spherical albedo of the atmosphere for illumination from below. Quantities R^0, T and s^* of the cloud-free and aerosol-free atmosphere-surface model were prepared with the 'Doubling-Adding KNMI' (DAK) radiative transfer code [53, 149], version 3.2.0, taking into account single and multiple Rayleigh scattering of sunlight by molecules in a pseudo-spherical atmosphere, including polarization. Absorption by O_3, NO_2, O_2, H_2O and the O_2-O_2 collision complex was taken into account. For more details about the computation of the quantities in Eq. (4.9), we refer to Tilstra [159].

The albedo A_s for which $R^{\text{model}}(\lambda) = R^{\text{meas}}(\lambda)$ holds is in this paper indicated by A_{scene}. The expression for A_{scene} follows from Eq. (4.9) [163]:

$$A_{\text{scene}}(\lambda) = \frac{R^{\text{meas}}(\lambda) - R^0(\lambda)}{T(\lambda) + s^*(\lambda)\left(R^{\text{meas}}(\lambda) - R^0(\lambda)\right)}, \tag{4.10}$$

where the notation for the dependency on μ, μ_0, φ and φ_0 is omitted. We compute A_{scene} for λ = 402, 416, 425, 440, 463, 494, 670, 685, 696.97, 712.7, 747, 758 and 772 nm, and co-register the results at NIR wavelengths to the Level 2 UVIS ground pixel grid. The values of A_{scene} can be interpreted as the TOA reflectances of the scene corrected for molecular Rayleigh scattering. They are in fact scene albedos, because they include non-Lambertian surface, aerosol, cloud and shadow effects. Therefore, in what follows, we refer to A_{scene} as the Lambertian-equivalent reflectivity of the scene (SCNLER). Only in the absence of non-Lambertian effects, A_{scene} is independent of μ, μ_0, φ and φ_0 and approximates the true surface albedo.

DIRECTIONALLY DEPENDENT LAMBERTIAN-EQUIVALENT REFLECTIVITY (DLER) CLIMATOLOGY

In the second step of the ACSF determination, the SCNLER of the PCSF pixels is compared to climatological observations at the same coordinates and time of the year. For the climatological observations, we use the directionally dependent Lambertian-equivalent reflectivity (DLER) data[3] version 0.6 generated with TROPOMI observations of the SCNLER since the start of TROPOMI's operational phase in May 2018. The DLER is available

[3] See https://www.temis.nl/surface/albedo/tropomi_ler.php, visited on 23 October 2021.

on a global 0.125° by 0.125° resolution latitude-longitude grid for each calendar month at 21 one-nm wide wavelength bins between 328 and 2314 nm [159]. We linearly interpolate the DLER data to the TROPOMI Level 2 UVIS ground pixel grid and measurement times. Unless stated otherwise, the wavelength bins we use are centered at 402, 416, 425, 440, 463, 494, 670, 685, 696.97, 712.7, 747, 758 and 772 nm.

In the DLER algorithm, an initial cloud screening was performed on the basis of NPP-VIIRS cloud information. After that, the 10% lowest SCNLER measurements in the seasonal grid cell were used which serves as a second-stage cloud filter, and measurements containing aerosols were excluded [159]. The DLER can generally be considered shadow-free. The DLER takes into account the viewing zenith angle dependence of the SCNLER caused by non-Lambertian surface reflectance. The DLER is a more accurate estimate of the expected aerosol-, cloud- and shadow-free SCNLER than the traditionally used LER (without viewing zenith angle dependence). The viewing zenith angle dependence of the DLER is only taken into account over land surfaces. Over water surfaces, DLER = LER. For more details about the DLER theory, we refer to [161].

RAISING THE ACSF

In order to select the pixels for which an ACSF is to be raised, we define the SCNLER-DLER contrast parameter Γ:

$$\Gamma(\lambda) = \frac{A_{\text{scene}}(\lambda) - A_{\text{DLER}}(\lambda)}{A_{\text{DLER}}(\lambda)} \times 100\%. \tag{4.11}$$

The division by A_{DLER} (the value of the DLER) in Eq. (4.11) allows us to search for a A_{DLER}-independent ACSF threshold for Γ, that is, a single threshold that can be used for both dark and bright surface types. Because of the division by the DLER, Γ is more stable (i.e., less susceptible to potential offset errors in the DLER) when the DLER is high. For each PCSF pixel, we compute the wavelength for shadow detection, λ_{max}, at which the pixel's DLER is maximum:

$$\lambda_{\text{max}} = \underset{\lambda}{\text{argmax}}\ A_{\text{DLER}}(\lambda). \tag{4.12}$$

We raise an ACSF at PCSF pixels for which

$$\Gamma(\lambda_{\text{max}}) < q, \tag{4.13}$$

where q is the contrast threshold. We set $q = -15\%$, yielding the highest actual shadow detection score in the validation (see Sect. 4.4).

RATIONALE BEHIND THE SCNLER-DLER CONTRAST PARAMETER

Here, we demonstrate the behavior of the variables in Eqs. (4.11) to (4.13) which determine the SCNLER-DLER contrast parameter Γ with an example measurement. Figure 4.4 is a true color image made by the Visible Infrared Imager Radiometer Suite (VIIRS) instrument on board the Suomi National Polar-orbiting Partnership (NPP) satellite, on 3 August 2019 above Southern Chile and Argentina. Suomi NPP orbits in close proximity to Sentinel-5P: the measurement time intervals of TROPOMI and VIIRS were 19:00-19:01 UTC and 18:57-18:58 UTC, respectively. A specific land region (52.5°-50.5°S latitude and 71.5°-70°W longitude) and water region (53°-51.5°S latitude and 67.5°-66°W

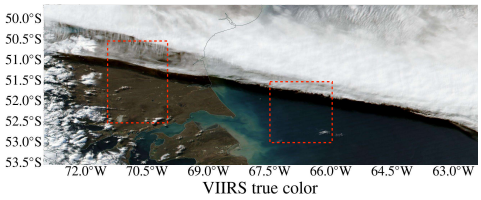

Figure 4.4: VIIRS-NPP true color image of Southern Chile and Argentina on 3 August 2019. The land and water regions belonging to the spectra of Fig. 4.5 are indicated by red dashed boxes.

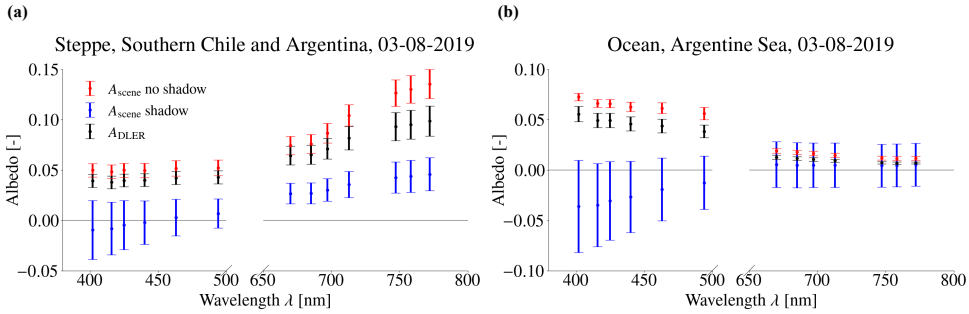

Figure 4.5: Spectra of the mean and 1-σ of the Lambertian-equivalent scene reflectivity (SCNLER) measured by TROPOMI at Southern Chile and Argentina on 3 August 2019, for the steppe region within 52.5°-50.5°S latitude and 71.5°-70°W longitude (Fig. 4.5a) and for the ocean region within 53°-51.5°S latitude and 67.5°-66°W longitude (Fig. 4.5b). Here, all measurements are cloud-free (i.e., without CF). The measurements affected by shadow (i.e., with ACSF) are presented in blue, and the shadow-free measurements (i.e., without PCSF) are presented in red. The additional black spectra are of the mean and 1-σ of the directionally dependent climatological Lambertian-equivalent reflectivity (DLER) at the TROPOMI ground pixels in the particular regions.

longitude) are indicated by red dashed boxes. The main surface types in those regions are steppe and ocean, respectively. Figures 4.5a and 4.5b show the spectral behavior of the mean and 1-σ of SCNLER measurements affected by shadow (A_{scene} shadow) and not affected by shadows (A_{scene} no shadow) of cloud-free TROPOMI pixels in the land and water region, respectively. We used the PCSF to remove shadow pixels and the ACSF to select shadow pixels. Also shown are the mean and 1-σ of the DLER interpolated on the TROPOMI Level 2 UVIS grid.

Figure 4.5a shows that over land (steppe), the DLER and the cloud- and shadow-free SCNLER follow a typical surface reflectivity spectrum for grasslands [163]: they increase with increasing wavelength, and include a subtle signature of the so-called 'red edge' (i.e., the sudden surface albedo increase at $\lambda \sim 700$ nm caused by vegetation). Over ocean, the DLER and cloud- and shadow-free SCNLER follow a typical surface reflectivity spectrum for ocean water: they increase with decreasing wavelength, and peak at $\lambda \sim$ 400 nm where the peak significance depends on the water constituents [105]. The mean value of A_{scene} affected by shadow is smaller than the DLER and cloud- and shadow-free A_{scene} at all wavelengths, for both the land and water region. The shadow signature in the difference $A_{\text{scene}} - A_{\text{DLER}}$ is most evident at the wavelength where the DLER is highest. The Rayleigh scattering correction results in negative A_{scene} for part of the shadowed

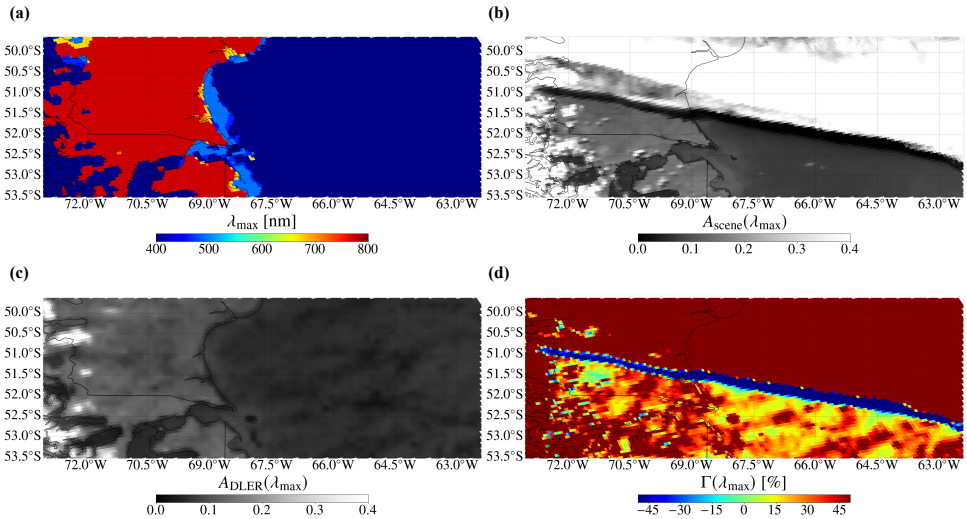

Figure 4.6: The wavelength at which DLER is maximum λ_{max} (Fig. 4.6a), the SCNLER at λ_{max} (Fig. 4.6b), the DLER at λ_{max} (Fig. 4.6c), and contrast parameter Γ at λ_{max} (Fig. 4.6d), for Southern Chile and Argentina on 3 August 2019.

pixels. Above land, a slight increase of the shadowed A_{scene} can still be observed with increasing wavelength, but above ocean, the water albedo increase in the UV cannot be observed anymore. Note that the mean DLER is consistently smaller than the mean cloud- and shadow-free SCNLER measured at all wavelengths, which is expected since the DLER at a certain location was generated with the 10% lowest SCNLER values at that location.

Figure 4.6a shows λ_{max} on the TROPOMI Level 2 UVIS ground pixel grid for this measurement example. As expected from Fig. 4.5, λ_{max} = 772 nm for the majority of the land covered pixels and λ_{max} = 402 nm for the majority of the water covered pixels. In shallow water regions near the coast line, however, λ_{max} = 494 nm, while in some land coast regions we find λ_{max} = 670 nm. Indeed, employing λ_{max}, the usage of surface type classification flags is avoided [127]. That is, λ_{max} does not rely upon assumptions made in a surface type classification product, and will also give the most suitable wavelength for shadow detection when mixed and/or rare surface types are present within the pixel.

Figures 4.6b, 4.6c and 4.6d show A_{scene}, A_{DLER} and Γ, respectively, at λ_{max}. Cloud- and shadow-free pixels yield $\Gamma(\lambda_{max}) \sim 0\%$ or slightly positive (up to $\sim 50\%$), because the DLER is generated with the 10% lowest SCNLER values in the particular calendar month that passed an aerosol- and cloud screening. The clouds at latitudes larger than 52.5° increase A_{scene} significantly relative to A_{DLER} , which results in $\Gamma(\lambda_{max}) > 50\%$. Pixels affected by true shadows show a significantly decreased A_{scene} relative to A_{DLER}, which is most apparent for the elongated cloud shadow along the edge of the cloud deck.

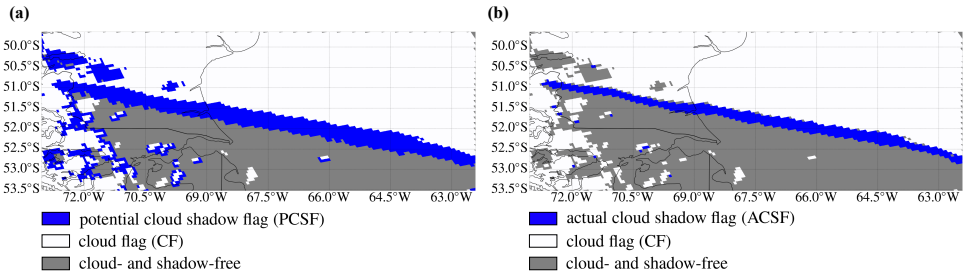

Figure 4.7: The TROPOMI Level 2 UVIS ground pixels for Southern Chile and Argentina on 3 August 2019 with raised PCSFs (Fig. 4.7a) and with raised ACSFs (Fig. 4.7b), indicated in blue. The white pixels are cloud pixels and grey pixels do not contain a raised cloud or shadow flag.

4

4.3. RESULTS

Here, we discuss the potential and actual cloud shadow flag results for three case studies with different cloud and surface types: the cloud deck example above steppe and ocean surfaces introduced in Sect. 4.2.2 (Sect. 4.3.1), an example with patchy clouds above grass and forest surfaces (Sect. 4.3.2) and an example of a relatively large area above the Sahara desert containing thin cirrus clouds (Sect. 4.3.3).

4.3.1. SOUTHERN CHILE AND ARGENTINA, 3 AUGUST 2019

Figures 4.7a and 4.7b show (in blue) the TROPOMI Level 2 UVIS ground pixels with raised PCSFs and ACSFs, respectively, for the cloud shadow example on 3 August 2019 at Southern Chile and Argentina.

Figure 4.7a shows that the PCSFs indicate the presence of an elongated cloud shadow southward of the edge of the cloud deck longitudinally traversing the scene from ~ 51°S to ~ 52.5°S latitude. The southward shadow is expected because in this example the Sun is located in the Northwest (φ_0 ranges from -29.3° in the West to -41.7° in the East). The Sun is located relatively low in the sky because of the local winter season (θ_0 ranges from 72.2° in the Northwest to 79.7° in the Southeast), which is geometrically beneficial for the existence of long shadows (see Eq. (4.5)). The latitudinal extent of the elongated shadow is relatively large compared to the shadows of the isolated small clouds found at latitudes southward of 51.5°S. This variation of shadow extent can be explained by the difference in cloud height: $h \sim 15$ km for the cloud deck, while $h \sim 1$ km for the isolated small clouds. The cloud deck shadow extent is larger than expected from visual inspection of the true color image (Fig. 4.4), which is caused by the cloud height safety margin C that we included in Eq. (4.1).

Figure 4.7b shows that the latitudinal extent of the cloud deck shadow detected with the ACSF is a more realistic approximation of the latitudinal cloud deck shadow extent observed in the true color image of Fig. 4.4. Only a few shadows of small isolated clouds are detected by the ACSF. Note that part of the small isolated clouds are in fact false positive cloud detections in the cloud product caused by bright surfaces. This can readily be concluded by comparing Fig. 4.7b to Fig. 4.4. For example, the water constituents along the coast between 53°S and 53.5°S latitude, but also the snowy mountains westward of

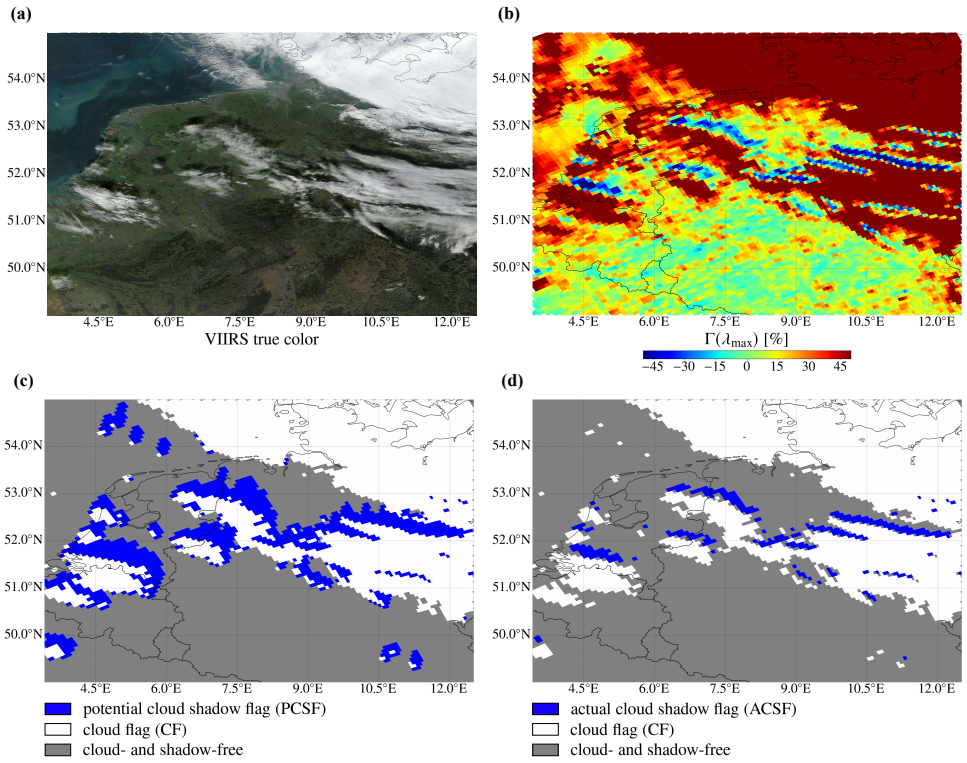

Figure 4.8: VIIRS-NPP true color image (Fig. 4.8a), SCNLER-DLER contrast parameter Γ at λ_{max} measured by TROPOMI (Fig. 4.8b), TROPOMI Level 2 UVIS ground pixels with raised PCSFs (Fig. 4.8c), and with raised ACSFs (Fig. 4.8d), for the Netherlands and Germany on 18 November 2018. In Figs. 4.8c and 4.8d, white pixels are cloud pixels and grey pixels do not contain a raised cloud or shadow flag.

71°W, are falsely interpreted as clouds. These false cloud shadow detections in the PCSF are correctly filtered out by the threshold for $\Gamma(\lambda_{max})$ (Eq. (4.13)), and are therefore not part of the ACSF. Indeed, the performance of the shadow detection algorithm depends on the quality of the input cloud and DLER products. The gaps in the cloud deck between 51°S and 50°S are caused by undefined cloud fractions in the cloud product, but again, the false PCSF shadow detections within those gaps are (except for 2 pixels) correctly removed from the ACSF.

4.3.2. THE NETHERLANDS AND GERMANY, 18 NOVEMBER 2018

Figures 4.8a and 4.8c show the true color image and the TROPOMI Level 2 UVIS ground pixels with raised PCSFs, respectively, for an example on 18 November 2018 above the Netherlands and Germany. TROPOMI orbits northwestward, and the viewing geometry is southwestward: θ ranges from 8.8° in the Northeast to 54.3° in the Southwest. The Sun is located in the South (φ_0 ranges from -180.0° in the West to -165.7° in the East) and the solar zenith angle θ_0 ranges from 65.8° in the South to 76.8° in the North.

With the PCSF, long potential cloud shadows are found extending towards the North-

east. Here, all clouds that produce shadows are relatively high ($h \sim 10$ km or higher). Note that at the location of the small isolated clouds above the sea at ~ 54°N latitude and 4.5-6°E longitude, the Sun is almost directly located in the South. The eastward component of the potential shadow at these longitudes is caused by the parallax effect (cf. Fig. 4.2): the southwestward looking instrument projects the cloud as a cloud pixel onto the surface southwestward from the cloud's actual nadir location. Although the path from the cloud's nadir location to the actual shadow is strictly northward, the path from the cloud *pixel* to the actual shadow is northeastward.

The majority of the cloud shadows in this example are found above land surface. The main land surface types in this part of Europe are grassland and forest, with in general a higher vegetation density than for the steppe land in the example shown in Sect. 4.3.1. Consequently, the red edge is more pronounced in this example resulting in a stronger surface reflectance in the near-infrared. Hence, we find that λ_{max} = 772 nm for all pixels over land. The relatively high surface reflectance in the near-infrared results in a clear shadow signature in $\Gamma(\lambda_{max})$ (see Fig. 4.8b): in the cloud- and shadow-free regions $\Gamma(\lambda_{max})$ equals 0 or is slightly positive, while strong negative $\Gamma(\lambda_{max})$ values are confined to cloud shadows (cf. Fig. 4.8a).

Figure 4.8d shows the TROPOMI Level 2 UVIS ground pixels with raised PCSFs for this example. Comparing the shadows detected with the ACSF to the true color image of Fig. 4.8a shows that ACSF shadows are detected where they can be expected. The small high isolated clouds above the sea do not produce dark enough shadows for an ACSF to be raised, similar to the small high isolated clouds above land at ~49.5°N latitude and ~10.5°-11°E longitude.

4.3.3. SAHARA DESERT, 18 JANUARY 2021

Figure 4.9 is equivalent to Fig. 4.8, but then for an example above the Sahara desert on 18 January 2021. The area of this example covers most of the orbit swath of TROPOMI traveling north-northwestward: θ ranges from 66.5° in the West-southwest to -58.1° in the East-northeast. Although the latitudes in this example are relatively small, the local winter season causes the Sun not to be located directly overhead (θ_0 ranges from 28.4° in the South to 59.3° in the North, and φ_0 ranges from -178.7° in the West to -140.3° in the East).

With the PCSF, northward shadows of longitudinally elongated cirrostratus clouds between 25°N and 28°N latitude, and of cirrocumulus clouds between 13°N and 22.5°N latitude, are detected. For both cloud types, $h > 10$ km. The vertical location of the detected foggy patch at 15°-17.5°N latitude and 14°-19°E longitude is just above the surface, hence the absence of the potential shadow (see Fig. 4.9c). This example is a clear demonstration of the parallax effect: on the west side of the area, TROPOMI looks westward projecting the clouds as cloud pixels onto the surface 'too far' westward, resulting in an *eastward* component of the potential shadow locations w.r.t. the cloud pixels. Similarly, on the east side of the area, TROPOMI looks eastward and potential shadows tend to be located *westward* of the cloud pixels.

With the ACSF, the detected shadows are a more accurate approximation of the shadows observed in the true color image (cf. Figs. 4.9d and 4.9a). The most distinctive shadow signature in the true color image, which is the northward shadow of the longi-

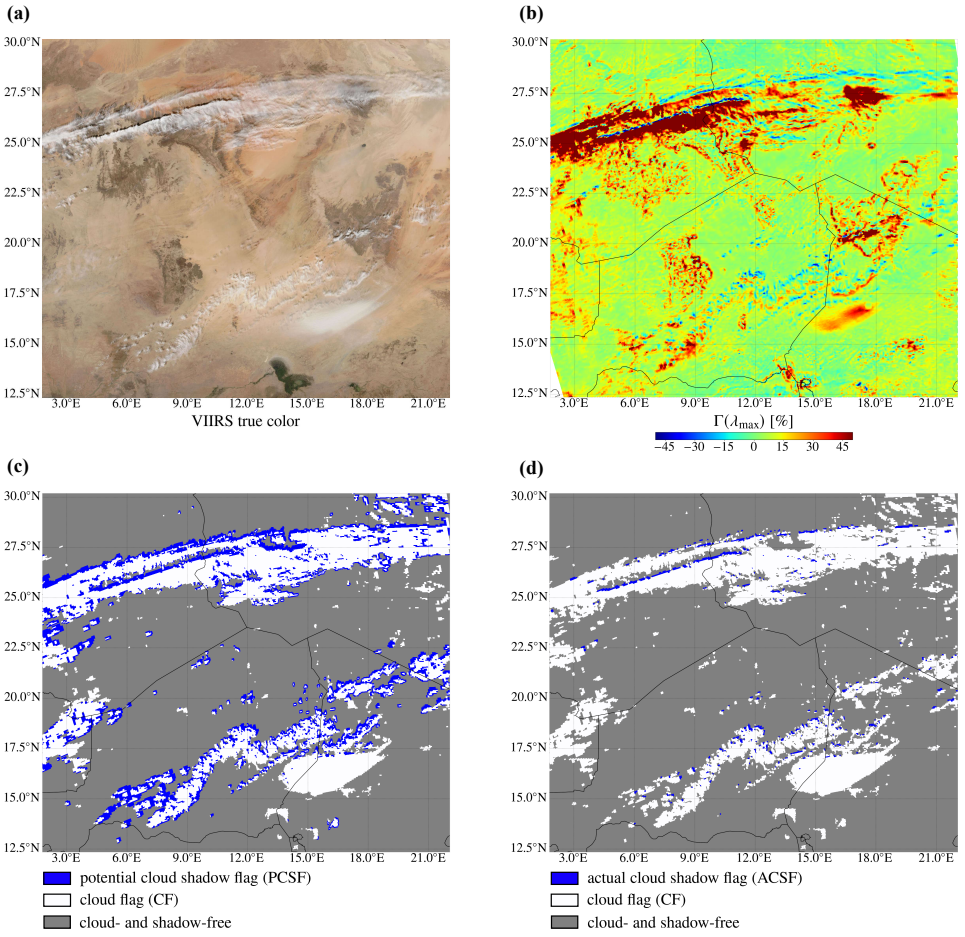

Figure 4.9: Similar to Fig. 4.8, but for the Sahara desert on 18 January 2021.

tudinally elongated cirrostratus cloud between 25°N and 27°N latitude, is indeed also detected by the ACSF. Although, geometrically, many other clouds in this example are high enough to produce potential cloud shadows, some of those clouds are too small and/or too thin to produce actual cloud shadows. This can be seen in Fig. 4.9b: for example, the cirrocumulus clouds near 13.5°N latitude and 4.5°E longitude are not able to decrease $\Gamma(\lambda_{\max})$ significantly enough for an ACSF to be raised.

The spectral reflectance of desert surface does not contain a red edge, but is relatively strong already at $\lambda < 700$ nm and further increases with increasing wavelength [163]. We find that for almost all pixels in this example, $\lambda_{\max} = 772$ nm. Comparing Fig. 4.9b with the false color image of Fig. 4.9a shows that strong negative $\Gamma(\lambda_{\max})$ are strictly confined to cloud shadows (except for a few pixels near 12.7°N latitude and 17.8°E longitude). The cloud- and shadow-free area yield $\Gamma(\lambda_{\max}) \sim 0$ or slightly positive. That is, dark surface features in the Sahara desert are not falsely detected as cloud shadows.

4.4. VALIDATION

In this section, we validate DARCLOS by comparing the computed PCSFs and ACSFs to the shadows visually found at similar locations and time in VIIRS-NPP true color images. For the visual inspection of the true color images, we have developed an interactive Python tool which plots the TROPOMI Level 2 UVIS grid on top of the true color image. The software allows for the manual selection and de-selection of TROPOMI pixels containing VIIRS shadows by clicking on the image, after which the row and scanline numbers of the selected TROPOMI pixels are saved.

Figure 4.11a shows a VIIRS-NPP true color image of cloud shadows found at the Taklamakan desert at Xinjiang, China, on 22 December 2019. The red lines represent the TROPOMI Level 2 UVIS grid, and the blue crosses indicate the TROPOMI pixels with a raised ACSF. If, also, a VIIRS shadow is visually found at the TROPOMI pixel with a raised shadow flag, we speak of a true positive (TP) shadow detection. Similarly, we register the false positive (FP), false negative (FN), and true negative (TN) shadow detections (see Fig. 4.10).

The overestimation of the VIIRS shadow by DARCLOS can be expressed by the commission error, ϵ_C [20]:

$$\epsilon_C = \frac{N_{FP}}{N_{TP} + N_{FP}}, \tag{4.14}$$

where N_{FP} and N_{FN} are the number of false positive detections and the number of false negative detections, respectively. The underestimation of the VIIRS shadow by DARCLOS can be expressed by the omission error, ϵ_O:

$$\epsilon_O = \frac{N_{FN}}{N_{TP} + N_{FN}}, \tag{4.15}$$

where N_{FN} are the number of false negative detections. For the definition of the VIIRS shadows, we distinguish between TROPOMI pixels that are totally shadowed (with geometrical shadow fractions $\gtrsim 0.75$), and partly shadowed (with geometrical shadow fractions $\gtrsim 0$ and $\lesssim 0.75$). For the computation of ϵ_O, we use only the totally shadowed pixels, while for the computation of ϵ_C, we use both the totally and partly shadowed pixels. That is, we consider the underestimation of the totally shadowed pixels, and the overestimation of the totally and partly shadowed pixels, to be erroneous. The overall performance of the algorithm can be assessed with the F_1 score which combines ϵ_C and ϵ_O as follows [40]:

	VIIRS shadow	VIIRS no shadow
TROPOMI shadow	True positive (TP)	False positive (FP)
TROPOMI no shadow	False negative (FN)	True negative (TN)

Figure 4.10: Confusion matrix of the shadow detection on the TROPOMI Level 2 UVIS grid. TROPOMI shadows are detected with the PCSF or ACSF of DARCLOS. VIIRS shadows are manually determined by visual inspection of VIIRS true color images.

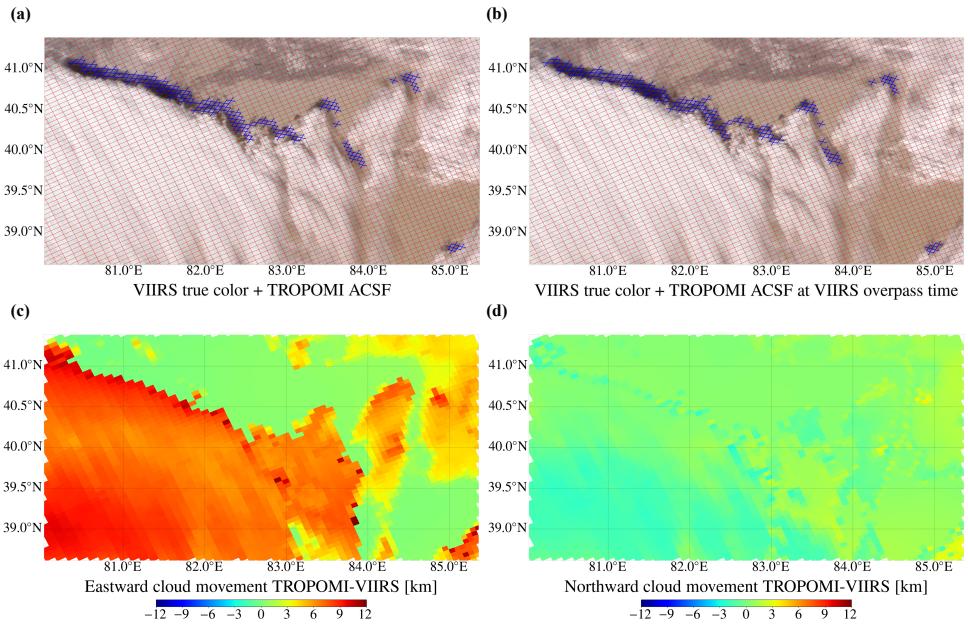

Figure 4.11: VIIRS-NPP true color image of the Taklamakan desert at Xinjiang, China, 22 December 2019, with the TROPOMI Level 2 UVIS grid plotted on top (in red) and the detected ACSF by DARCLOS (blue crosses), uncorrected (Fig. 4.11a) and at the VIIRS measurement times (Fig. 4.11b). Figures 4.11c and 4.11d show, respectively, the eastward and northward atmospheric movement at the cloud height during the TROPOMI-VIIRS measurement time difference, computed using ERA5 reanalysis wind data.

$$F_1 = \frac{2(1-\epsilon_C)(1-\epsilon_O)}{(2-\epsilon_C-\epsilon_O)}. \tag{4.16}$$

In the hypothetical case of a perfect shadow detection, we would obtain $\epsilon_O = 0$, $\epsilon_C = 0$ and F_1 score = 1. For the ACSF in a slightly larger area than shown in Fig. 4.11a (36.5 - 43.0 °N, 76.0 - 88.0 °E), the results are $\epsilon_O = 0.27$, $\epsilon_C = 0.21$ and F_1 score = 0.76.

It can be observed that the TROPOMI pixels with a raised ACSF in Fig. 4.11a are consistently located slightly eastwards of the shadows found in the VIIRS true color image. The eastward shift can be explained by the motion of the clouds during the measurement time difference of TROPOMI and VIIRS. In the example of Fig. 4.11, the VIIRS measurements were on average taken 4.33 minutes ahead of the TROPOMI measurements, with a 1-σ of 0.07 minutes[4]. We interpolate ERA5 data [61] of hourly eastward and northward wind speed components, provided at 37 vertical pressure levels on a 0.25° by 0.25° latitude-longitude grid, onto the FRESCO cloud pressure on the TROPOMI Level 2 UVIS grid (i.e., *without* manually raising the cloud height such as in Eq. (4.1)). The cloud deck in the South-west in Fig. 4.11 is relatively high (the cloud pressure is ~ 400 hPa), where eastward wind speeds between 20 and 40 m/s are found. The eastward and northward

[4]TROPOMI-VIIRS measurement times differences were taken from the S5P-NPP cloud product, which is the cloud product of VIIRS regridded to the TROPOMI Level 2 grid [141].

Example	Coordinates	Date	Orbit	Omission error PCSF	Commission error PCSF	Omission error ACSF	Commission error ACSF	F_1 score ACSF
Southern Chile and Argentina	53.528 - 49.626 °S 73.047 - 62.418 °W	03-08-2019	9355	**0.05**	0.48	0.10	0.01	**0.94**
The Netherlands and Germany	49.004 - 54.991 °N 3.4119 - 12.5062 °E	18-11-2018	5690	**0.06**	0.52	0.16	0.04	**0.90**
Sahara desert, North Africa	24.802 - 27.400 °N 3.506 - 12.011 °E	18-01-2021	16927	**0.14**	0.70	0.18	0.13	**0.84**
Taklamakan desert, China	36.500 - 43.000 °N 76.000 - 88.000 °E	22-12-2019	11348	**0.02**	0.77	0.08	0.02	**0.95**
The Netherlands, Belgium and Luxembourg	48.995 - 55.004 °N 2.000 - 8.000 °E	09-10-2018	5123	**0.05**	0.61	0.20	0.07	**0.86**
Taklamakan desert, China	37.006 - 42.005 °N 80.005 - 88.007 °E	21-12-2020	16527	**0.10**	0.51	0.13	0.11	**0.88**

Table 4.1: Results of the validation of the PCSF and ACSF by inspection of VIIRS-NPP true color images. The final results are shown in bold.

cloud displacements are shown in Fig. 4.11c and 4.11d, respectively. The cloud displacements from ~ 6 to ~ 9 km are significant enough to shift some clouds, and hence some cloud shadows, at least one TROPOMI ground pixel in the eastward direction.[5]

In Fig. 4.11b we have corrected the locations of the TROPOMI cloud and cloud shadow pixels for the eastward and northward movement of the clouds during the TROPOMI-VIIRS measurement time difference. Note the much better agreement between the ACSF and the VIIRS shadows compared to Fig. 4.11a. Indeed, using the corrected ACSF, the errors decreased and the F_1 score increased: ϵ_O = 0.08, ϵ_C = 0.02 and F_1 score = 0.95. It should be noted that the validation may suffer from an imperfect correction of the cloud movement during the TROPOMI-VIIRS measurement time difference, because the cloud evolution is ignored and because of the relatively coarse resolution of the wind product. Therefore, we expect the true shadow detection performance at the TROPOMI measurement time to be even better than the performance presented with this validation.

The last 3 columns of Table 4.1 show the results for ϵ_O, ϵ_C and the F_1 score of the ACSF for the three examples discussed in this paper, and three additional examples (on the 22nd of December 2019, on the 9th of October 2018, and on the 21st of December 2020) not shown in this paper. The F_1 score is 0.84 or higher for all examples. The F_1 score is highest (0.94 and 0.95 respectively) for Southern Chile and Argentina, 3 August 2019, and for the Taklamakan desert, 22 December 2019. The shadows in those examples are caused by relatively large and thick cloud decks, and are therefore relatively distinctive. The examples with the lowest F_1 scores (0.84 and 0.86 respectively) are the Sahara desert, 18 January 2021, and The Netherlands, Belgium and Luxembourg, 9 October 2018. The shadows in those examples are caused by relatively thin and small clouds, and are therefore relatively subtle. Subtle shadows lead to less distinctive shadow signatures in Γ,

[5] It should be noted that the cloud movement during the TROPOMI-VIIRS measurement time difference implies that the cloud flags (retrieved at the TROPOMI measurement time) cannot be replaced in DARCLOS by cloud flags from the S5P-NPP cloud product (retrieved at the VIIRS measurement time). Moreover, Fig. 4.11 is a general warning for all applications of the S5P-NPP cloud product which require a spatial cloud precision of about the size of a TROPOMI ground pixel.

leading to more false negative shadow detections and a higher ϵ_O of the ACSF. Also, thin and/or small clouds are sometimes not detected by the cloud product because the cloud fraction is too low to raise a CF, resulting in false negative PCSFs and ACSFs. Moreover, we speculate that thinner and/or smaller clouds are more likely to appear and disappear during the TROPOMI-VIIRS measurement time difference, complicating the cloud movement correction and validation of these examples.

The fourth and fifth column of Table 4.1 show ϵ_O and ϵ_C, respectively, of the PCSF. The value of ϵ_C of the PCSF is higher than 0.48 and higher than that of the ACSF, since the shadow in the PCSF is, by definition, an overestimation of the actual shadow. Because the PCSF is intended to be useful for excluding any cloud shadow contamination from TROPOMI Level 2 data, ϵ_O of the PCSF should be minimized. The value of ϵ_O for all examples is 0.14 or lower. Also here, we attribute the nonzero ϵ_O to the imperfect correction of the cloud movement during the TROPOMI-VIIRS measurement time difference, and to thin and/or small clouds resulting in false negative CF. Again, the best performances are found for Southern Chile and Argentina, 3 August 2019, and for the Taklamakan desert, 22 December 2019, with an ϵ_O of 0.05 and 0.02, respectively.

In order to put the validation results in perspective, we note that the state-of-the art imager cloud and cloud shadow detection code Fmask version 4.0 [123] reports shadow detection commission errors of 0.49 for Landsat 4-7 and 0.38 for Landsat 8, and omission errors of 0.27 for Landsat 4-7 and 0.31 for Landsat 8. Using multi-temporal reference images of specific regions, Candra, Phinn, and Scarth [21] achieved omission and commission errors ranging from 0.001 to 0.084 and 0 to 0.058, respectively, depending on the region. The PCSF omission errors and ACSF commission errors in Table 4.1 are lower than those of Fmask 4.0, and are of the same order of magnitude as those achieved by Candra, Phinn, and Scarth [21]. Of course, because of the much higher spatial resolution of Landsat than that of TROPOMI, the error values for Landsat actually refer to a much larger number of pixels.

4.5. DISCUSSION

Here, we discuss some limitations and points of attention for the usage of the DARCLOS cloud shadow flags. Also, we point out the possible spectral dependence of cloud shadow extents, and present the (unvalidated) spectral cloud shadow flag as an auxiliary product of DARCLOS.

4.5.1. LIMITATIONS OF THE ACSF AND PCSF

The PCSF depends on the CF which is determined by the effective cloud fraction. As discussed in Section 4.3.1, false negative cloud detections in the CF can result in falsely detected gaps in cloud decks, resulting in false positive PCSFs inside the gaps (Fig. 4.7a). Note that false negative cloud detections in the CF can also result in false *negative* shadow detections in the PCSF and ACSF, since there is no shadow to be detected in the absence of a cloud detection. The surface albedo input for the effective cloud fraction calculation in the NO_2 product is the LER climatology made by the Ozone Monitoring Instrument (OMI) at 440 nm available at a 0.5° × 0.5° latitude-longitude grid [77]. With a future implementation of the TROPOMI DLER climatology, which uses a 0.125° × 0.125°

latitude-longitude grid instead (see Sect. 4.2.2), in the effective cloud fraction algorithm, the accuracy of the CF, PCSF and ACSF is expected to further increase.

DARCLOS has not been tested at regions covered by ice and/or snow, nor at sunglint geometries over ocean. In these circumstances, the performance of the current effective cloud fraction is limited, often resulting in false positive CFs. For the ACSF, we have discarded the cloud pixels (and corresponding shadows) that contain a raised sunglint flag and/or snow/ice flag. For the PCSF, these pixels are not discarded, such that they are removed from the data when the PCSF and CF are used together to both remove cloud and cloud shadow contaminations. With future potential improvements of FRESCO above glint and snow/ice regions, DARCLOS could be tested above glint and snow/ice regions. Then, the DLER for snow/ice conditions [159] should be employed in DARCLOS, and possibly an ocean surface reflectance calculation can help distinguishing between clouds and then glint.

The performance of the ACSF depends on the quality of the DLER climatology. Although the DLER takes into account monthly surface reflectivity changes throughout the year, temporary deviations from this climatology (e.g., agricultural land usage changes, forest fires, precipitation, flooding and snow cover) are measured by the SCNLER, and may affect Γ and possibly the ACSF. In addition, the spatial resolution of the DLER of $0.125^\circ \times 0.125^\circ$ is somewhat coarser than the spatial resolution of the TROPOMI Level 2 UVIS grid at which the SCNLER is measured. Dark small-scale surface features not captured by the DLER may, theoretically, give too low Γ and may result in false positive ACSF. In the examples treated in this paper, however, dark small-scale forest (Sect. 4.3.2) and desert (Sect. 4.3.3) features did not convincingly deteriorate the ACSF performance.

Both the irradiance and radiance measurements by TROPOMI have degraded during its operational lifetime. The irradiance measurements are known to degrade faster than the radiance measurements (and most significantly at the shortest wavelengths), leading to an increasing derived reflectance over time [162, 93]. Since the release of the version 2.0.0 TROPOMI level 1b processor on 5 July 2021, the irradiance degradation is being corrected. The thresholds used in this paper for clouds and cloud shadows, which were set at an effective cloud fraction of 0.05 and $\Gamma = -15\%$ respectively, may have to be adjusted for the corrected data.

4.5.2. SPECTRAL CLOUD SHADOW FLAG (SCSF)

In Sect. 4.4, the ACSF has been validated by visual inspection of true color images of the VIIRS instrument. Hence, the shadows found with the ACSF can be interpreted as the shadows that could be observed from space by the human eye. We find, however, a significant wavelength dependency of the contrast parameter Γ in the UV part of the spectrum. For example, Fig. 4.12a shows Γ at 340 nm for the example above the Netherlands and Germany on 18 November 2018. Comparing to Γ at λ_{max} (Fig. 4.8b), where $\lambda_{max} = 772$ nm over land, the negative Γ related to cloud shadows between 52°-53°N latitude and 9°-12°E longitude have disappeared. Also, the locations of some pixels with significant negative Γ have changed. Although these shadows have not been validated (they could possibly not be observed by the human eye) or could be a result of noisy Γ in dark scenes (cf. Eq. (4.11)), they may be relevant for studying shadow effects on TROPOMI air quality products retrieved at particular UV wavelengths, such as the Ab-

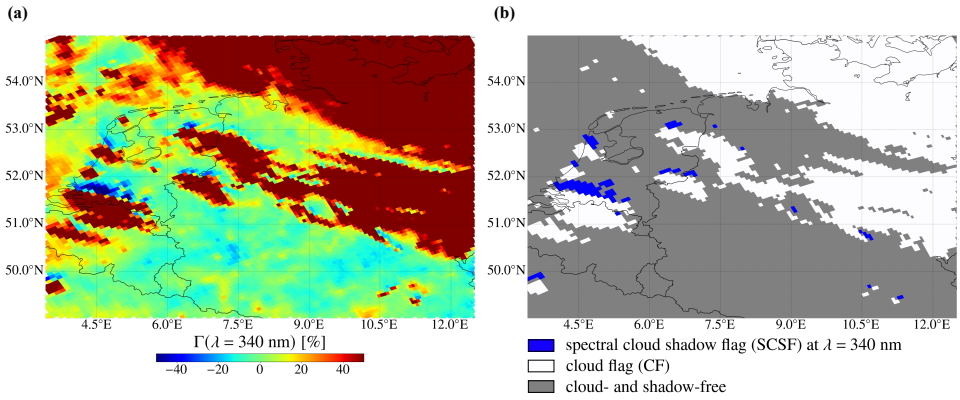

Figure 4.12: SCNLER-DLER contrast parameter Γ at λ = 340 nm measured by TROPOMI (Fig. 4.12a) and TROPOMI Level 2 UVIS ground pixels with raised SCSFs at λ = 340 nm (Fig. 4.12b), for the Netherlands and Germany on 18 November 2018. In Fig. 4.12b, white pixels are cloud pixels and grey pixels do not contain a raised cloud or shadow flag.

sorbing Aerosol Index (AAI) at λ = 340 nm and λ = 380 nm [30, 150, 80] or the NO_2 column at λ = 440 nm [175]. Therefore, DARCLOS also outputs the spectral cloud shadow flag (SCSF), which is raised at PCSF pixels for which:

$$\Gamma(\lambda) < q, \tag{4.17}$$

where q is again set at −15%. Contrary to the ACSF (Eq. 4.13), the SCSF is by definition wavelength dependent. The SCSF is computed at 328, 335, 340, 354, 367, 380, 388, 402, 416, 425, 440, 463, 494 nm.

Figure 4.12b shows the SCSF at λ = 340 nm for the example above the Netherlands and Germany on 18 November 2018. Comparing to Fig. 4.8d shows that part of the shadow flags has disappeared or has changed location. For example, the cloud shadow detected with the SCSF at ~ 49.5°N latitude and ~ 11.3°E longitude has shifted closer to the cloud as compared to the corresponding ACSF shadow. We speculate that the wavelength dependence of shadow locations in the UV can be explained by the wavelength dependence of the molecular scattering optical thickness of the atmosphere: at shorter wavelengths, the molecular scattering optical thickness is higher such that higher atmospheric layers are probed from space, decreasing the observed shadow extents with TROPOMI. The explanation and validation of the wavelength dependence of observed cloud shadow extents in the UV is subject to future research.

4.6. SUMMARY AND CONCLUSIONS

In this paper, we have demonstrated DARCLOS, a cloud shadow detection algorithm for TROPOMI. DARCLOS provides a potential cloud shadow flag (PCSF) based on geometric variables stored in TROPOMI Level 2 data, and an actual cloud shadow flag (ACSF) based on the contrast of the measured scene reflectivity with the climatological surface reflectivity. For each TROPOMI pixel, this contrast is computed at the wavelength where the DLER is largest. The ACSFs are a subset of the PCSFs.

Three case studies with different spectral surface albedo and cloud types have been discussed in detail. We have shown that the PCSF vastly overestimates the shadows observed in true color images of the VIIRS-NPP instrument, as expected. The shadows detected with the ACSF are better approximations of these true shadows, but may miss some shadows that are produced by thin and/or small clouds. We showed that the shadow signatures in the contrast between the scene reflectivity and the climatological surface reflectivity can, for almost all pixels, only be attributed to cloud shadows. That is, dark surface features are not falsely detected as cloud shadows in the ACSF.

The PCSF and ACSF are validated by visual inspection of true color images made by the VIIRS-NPP instrument, for in total six cases. We found that the cloud motion during the measurement time difference between TROPOMI and VIIRS complicates this validation strategy. We showed that a cloud movement correction using the wind speed vectors at the cloud height significantly improves the validation results. The best detection scores were achieved for the cases with relatively thick and horizontally large cloud decks (ACSF F_1 score ≥ 0.94 and PCSF omission error ≤ 0.05). After the cloud movement correction, the validation may still suffer from cloud evolution and the relatively coarse resolution of the wind product. Hence, the true shadow detection performance at the TROPOMI measurement times may be expected to be even better than presented with the validation in this paper.

At UV wavelengths, we have found cloud shadow signatures at different locations than determined with the ACSF, potentially indicating a wavelength dependence of cloud shadow extents. Because TROPOMI's air quality products are retrieved at specific wavelengths or wavelength ranges, DARCLOS also outputs the spectral cloud shadow flag (SCSF), which is a wavelength dependent alternative for the ACSF. Such a cloud shadow detection at the precise wavelengths of TROPOMI's air quality products is unique for DARCLOS and cannot be done with data from an imager.

The shadow flags of DARCLOS are planned for implementation in the TROPOMI L2 SCNLER product. DARCLOS is, to the best of our knowledge, the first cloud shadow detection algorithm for a spaceborne spectrometer instrument. In principle, DARCLOS can also be used for other spectrometer instruments than TROPOMI which have a spatial resolution high enough to observe cloud shadows. An effective cloud fraction and climatological surface albedo are prerequisites for DARCLOS, and should therefore be available at the ground pixel grid of the instrument. It should be noted that, when computing the ACSF using UVIS and NIR wavelengths from different detectors, a co-registration of the SCNLER measurements from one detector ground pixel grid to the other has to be performed. Ideally, true color images are available of the scenes with approximately the same measurement times, in order to validate the PCSF and ACSF by visual inspection and to optimize the cloud and cloud shadow thresholds.

We conclude that the PCSF can be used to remove cloud shadow contaminated pixels from TROPOMI Level 2 UVIS data, and that the ACSF can be used to select pixels for further analysis of cloud shadow effects. If both cloud and cloud shadow effects are to be removed, the PCSF and CF can be used together. Also, the ACSF can be used to demonstrate and/or count the true shadows that would be observed from space by the human eye. However, at UV wavelengths, we have found indications of the wavelength dependence of cloud shadow signatures, and a spectrally dependent cloud shadow flag such

as the SCSF could possibly be more suitable when selecting shadow pixels in air quality products retrieved at UV wavelengths. Further research is needed to explain and validate the spectral dependence of these cloud shadow signatures. The detection of shadows with the ACSF and SCSF allows users to perform this analysis, and is a first step towards the understanding and correction of cloud shadow effects on satellite spectrometer air quality measurements.

AUTHOR CONTRIBUTIONS

V.T. did all computations and wrote the manuscript. P.W. weekly commented on the intermediate results and guided V.T. to focus on the most relevant aspects. L.G.T. provided the SCNLER algorithm and commented on intermediate results. All authors read the manuscript, provided feedback that led to improvements and were involved in the selection of the results presented in this paper.

COMPETING INTERESTS

The authors declare that they have no conflict of interest.

ACKNOWLEDGEMENTS

This work is part of the research programme User Support Programme Space Research (GO) with project number ALWGO.2018.016, which is (partly) financed by the Dutch Research Council (NWO).

5

CANCELLATION OF CLOUD SHADOW EFFECTS IN THE ABSORBING AEROSOL INDEX RETRIEVAL ALGORITHM OF TROPOMI

Cloud shadows can be detected in the radiance measurements of the TROPOMI instrument on board the Sentinel-5P satellite due to its high spatial resolution, and could possibly affect its air quality products. The cloud shadow induced signatures are, however, not always apparent and may depend on various cloud and scene parameters. Hence, the quantification of the cloud shadow impact requires the analysis of large data sets. Here we use the cloud shadow detection algorithm DARCLOS to detect cloud shadow pixels in the TROPOMI absorbing aerosol index (AAI) product over Europe during 8 months. For every shadow pixel, we automatically select cloud- and shadow-free neighbour pixels, in order to estimate the cloud shadow induced signature. In addition, we simulate the measured cloud shadow impact on the AAI with our newly developed 3D radiative transfer algorithm MONKI. Both the measurements and simulations show that the average cloud shadow impact on the AAI is close to zero (0.06 and 0.16, respectively). However, the top-of-atmosphere reflectance ratio between 340 and 380 nm, which is used to compute the AAI, is significantly increased in 95% of the shadow pixels. So, cloud shadows are bluer than surrounding non-shadow pixels. Our simulations explain that the traditional AAI formula intrinsically already corrects for this cloud shadow effect, via the lower retrieved scene albedo. This cancellation of cloud shadow signatures is not always perfect, sometimes yielding second order low and high biases in the AAI which we also successfully reproduce with our simulations. We show that the magnitude of those second order cloud shadow effects depends on various cloud parameters which are difficult to determine for

This chapter has published in Atmospheric Measurement Techniques **18**, 73–91 [170].

the shadows measured with TROPOMI. We conclude that a potential cloud shadow correction strategy for the TROPOMI AAI would therefore be complicated if not unnecessary.

5.1. INTRODUCTION

The TROPOspheric Monitoring Instrument (TROPOMI) is a spectrometer onboard the Sentinel-5 Precursor (S5P) satellite in low Earth orbit, launched on October 13, 2017 [177]. TROPOMI provides daily global maps of trace gases, aerosols and clouds, derived from the spectrum of sunlight reflected by the Earth. The spatial resolution TROPOMI of 5.6×3.6 km^2 in the nadir-viewing direction is very high compared to its predecessors, such as OMI with 24×13 km^2 [89], GOME-2 with 80×40 km^2 [106] and SCIAMACHY with 60×30 km^2 [17]. Because of this unprecedented spatial resolution and its high data quality, TROPOMI is able to observe local NO_2 emission sources such as power plants [10], gas compressor stations [174], and cities [92], CH_4 leakage from oil/gas fields [110, 176, 137], volcanic SO_2 plumes [157] and NO_2 trails along ship tracks [46].

TROPOMI also effectively tracks aerosols that absorb light in the UV part of the spectrum, such as desert dust, volcanic ash, and smoke from biomass burning, by providing the Absorbing Aerosol Index (AAI) in every pixel of each orbit [150, 30]. Unlike most other aerosol retrieval products, the AAI can also successfully be derived above clouds and bright surfaces. In addition, the AAI is an important input for the retrieval algorithms of other TROPOMI products. For example, the pixel selection for the aerosol layer height (ALH) [131, 108] and aerosol optical thickness (AOT) [31] retrievals of TROPOMI is based on the AAI. Hence, AAI features that are not related to absorbing aerosols, for example caused by the ocean glint, absorbing constituents in the ocean water, and clouds at specific scattering geometries [80], may be undesired for those retrievals.

The effect of clouds on the AAI in cloudy pixels has been studied before using data of SCIAMACHY [115, 114], OMI [167, 72] and TROPOMI [80]. Besides cloud signatures in cloudy pixels, clouds can also leave signatures in cloud-free adjacent pixels, for example in the form of cloud shadows. Contrary to the large pixel sizes of its predecessors, the small pixel size of TROPOMI sometimes causes one or several pixels to be fully covered by a single cloud shadow, particularly for high clouds at large viewing and/or solar zenith angles [169]. Those three-dimensional radiative transfer effects are not yet taken into account in the current AAI retrieval algorithm, and their influence on the AAI has not yet been investigated. The natural horizontal variation of the AAI complicates the quantification of the cloud shadow induced AAI signatures. Recently, we developed an accurate and fast cloud shadow detection algorithm for TROPOMI, called DARCLOS [169], which allows for a statistical analysis of the cloud shadow effect on the AAI in large data sets.

In this paper, we present a statistical analysis of the cloud shadow effect on the measured TROPOMI AAI for all pixels above Europe during 8 months. We use the cloud shadow detection algorithm DARCLOS to detect the cloud shadow pixels, and we select cloud- and shadow-free neighbour pixels for comparison to the non-shadow state. In addition, we simulate the measured cloud shadow effect on the AAI for various scenes using our 3D radiative transfer code MONKI, recently developed by us at KNMI. Using our simulations, we explain the measured cloud shadow effects on the AAI. Finally, we discuss the implications of our findings for the TROPOMI AAI product.

This paper is structured as follows. In Sect. 5.2, we describe the methods we used to measure and to simulate cloud shadow effects on the Absorbing Aerosol Index product of TROPOMI. In Sect. 5.3., we show the results of those measured and simulated cloud shadow effects. In Sect. 5.5, we discuss the implications of our results and state the most

important conclusions of this paper.

5.2. METHOD

In this section, we first give a brief description of TROPOMI (Sect. 5.2.1), the Absorbing Aerosol Index product (Sect. 5.2.2) and the data set we selected (Sect. 5.2.3). Then, we explain the employed methods to detect cloud shadow pixels (Sect. 5.2.4) and their shadow-free neighbour pixels (Sect. 5.2.5). Finally, we describe our model to simulate cloud shadow effects (Sect. 5.2.6).

5.2.1. DESCRIPTION OF TROPOMI

The TROPOspheric Monitoring Instrument (TROPOMI) was launched on October 13, 2017, as the only instrument onboard the Sentinel-5 Precursor (S5P) satellite [177]. Operating in a near-polar, Sun-synchronous orbit at an average altitude of 824 km above the Earth's surface, TROPOMI completes an orbit approximately every 101 minutes. TROPOMI is a nadir-looking instrument. During its ascending node, it collects measurements every 1.08 seconds in a 2600 km swath width, providing a daily global coverage. The local equator crossing time of TROPOMI is 13:30 LT. TROPOMI initially featured a footprint size of 7.2 × 3.6 km^2 in the nadir viewing direction, which was later adjusted to 5.6 × 3.6 km^2 on August 6, 2018 [93].

TROPOMI is a spectrometer continuously measuring the Earth radiance, I_λ, at wavelengths λ and in units of W m^{-2} nm^{-1} sr^{-1}, and the solar irradiance, $E_{0\lambda}$, in units of W m^{-2} nm^{-1} daily, to derive the measured local top-of-atmosphere (TOA) reflectance R_λ^{meas}:

$$R_\lambda^{\text{meas}}(\mu,\mu_0,\phi,\phi_0) = \frac{\pi I_\lambda(\mu,\mu_0,\phi,\phi_0)}{\mu_0 E_{0\lambda}}, \tag{5.1}$$

where $\mu = \cos\theta$ and $\mu_0 = \cos\theta_0$, and with θ, θ_0, φ and φ_0 the viewing zenith, solar zenith, viewing azimuth and solar azimuth angles, respectively. From R_λ^{meas}, properties of the local Earth's atmosphere and surface can be retrieved. Covering wavelengths in the ultraviolet-visible (UV-VIS, 267–499 nm), near-infrared (NIR, 661–786 nm), and shortwave infrared (SWIR, 2300–2389 nm) with high spectral resolution, TROPOMI globally and daily retrieves the concentrations of trace gases (NO_2, O_3, CH_4, CO, and SO_2) and properties of aerosols and clouds with unprecedented accuracy.

5.2.2. ABSORBING AEROSOL INDEX (AAI)

The air quality product that we analyze is the TROPOMI level 2 Absorbing Aerosol Index (AAI). The AAI is retrieved from the measured and calculated TOA reflectances at 340 and 380 nm as follows [see 165, 30, 150]:

$$\text{AAI} = -100 \cdot \left[\log_{10}\left(\frac{R_{340}}{R_{380}}\right)^{\text{meas}} - \log_{10}\left(\frac{R_{340}}{R_{380}}\right)^{\text{calc}} \right], \tag{5.2}$$

where 'meas' and 'calc' indicate the measured (Eq. (5.1)) and calculated TOA reflectances, respectively. The calculated TOA reflectances are for a clear-sky atmosphere above a

Lambertian (i.e., isotropically reflecting and fully depolarizing) surface, and were obtained using the formula of Chandrasekhar [24]:

$$R_\lambda^{\text{calc}}(\mu,\mu_0,\phi-\phi_0) = R_\lambda^0(\mu,\mu_0,\phi-\phi_0) + \frac{A_s T_\lambda(\mu,\mu_0)}{1-A_s s_\lambda^\star}. \tag{5.3}$$

In Eq. (5.3), R^0 is the path reflectance, which represents the contribution to the TOA reflectance of the clear-sky atmosphere bounded below by a black surface. The second term in Eq. (5.3) represents the effect of the surface on the TOA reflectance. It contains the Lambertian surface albedo A_s, the total two-way transmittance of the atmosphere T, and the spherical albedo $s^\star$ of the atmosphere for illumination from below. Quantities R^0, T, and $s^\star$ are computed with the 'Doubling-Adding KNMI' (DAK) radiative transfer code [53, 149]. This computation accounts for the effects of single and multiple Rayleigh scattering and the absorption of sunlight by molecules within a pseudo-spherical atmosphere, fully taking into account the polarization of light.

The Lambertian surface albedo, A_s, in Eq. (5.3) is retrieved at $\lambda = 380$ nm assuming that $R_{380}^{\text{calc}}(A_s) = R_{380}^{\text{meas}}$. The value of A_s which satisfies this assumption is known as the 'scene albedo' or the 'scene Lambertian equivalent reflectance (scene LER)', and denoted in this paper as A_{scene}. From Eq. (5.3) it then follows that

$$A_{\text{scene}} = \frac{R_{380}^{\text{meas}} - R_{380}^0}{T_{380}(\mu,\mu_0) + s_{380}^\star (R_{380}^{\text{meas}} - R_{380}^0)}. \tag{5.4}$$

A_{scene} is assumed wavelength independent, allowing for the computation of R_{340}^{calc} using Eq. (5.3) but with $\lambda = 340$ nm. Finally, the AAI is computed using Eq. (5.2).

In a scene without aerosols and clouds, above a spectrally neutral Lambertian surface, the AAI is, in theory, equal to zero. The AAI of TROPOMI has an offset of ~ -2. The offset in the collection 1 AAI data used for this paper is due to radiometric calibration offsets and degradation in the TROPOMI radiance and irradiance data [162, 93]. The degradation in the radiance and irradiance results in an increase in the derived reflectances at 340 and 380 nm, decreasing the average AAI values over time. The AAI tends to increase in the presence of absorbing aerosols and can also identify aerosols that are located above clouds [see, e.g., 166]. We refer to [60], [165], [30], [115] and [80] for more details about the sensitivity of the AAI to aerosols, surfaces and clouds. For this research about cloud shadow effects, it should be noted that dark pixels (low R_{380}^{meas}) give low A_{scene} (Eq. (5.4)) resulting in relatively small contributions of the surface to R_{340}^{calc} and R_{380}^{calc} (Eq. (5.3)).

5.2.3. SELECTED DATA SET

We analyzed 8 months of TROPOMI AAI collection 1 data (processor version 1.3.0), from 1 November 2020 to 30 June 2021. For each day in the data set, we use all pixels that fall in the selected area, on average resulting in 511616 pixels per day available for our analysis. The selected area ranges from 34 °S to 61 °N latitude, and from 11 °W to 40 °E longitude, as shown in the left figure of Fig. 5.1. This area covers all capitals of Europe (except for Reykjavik), Ankara, Moscow, and some northern African cities such as Tanger, Algiers and Tunis. The area of interest in Europe was covered by TROPOMI during three

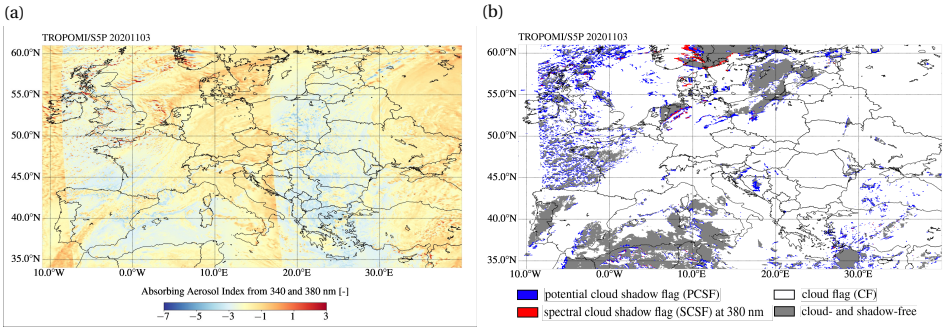

Figure 5.1: Example of the AAI (left) and cloud shadow flags (right) in three partly overlapping TROPOMI orbit swaths covering the selected area for this research, here on 3 November 2020. In the right figure, the blue pixels contain a potential cloud shadow flag (PCSF), the red pixels contain (in addition) a spectral cloud shadow flag (SCSF), the white pixels contain a cloud flag (CF) and the grey pixels are cloud- and shadow-free.

5

successive, partially overlapping overpasses on November 11, 2020, as shown in Fig. 5.1. Days with missing data (2021-05-23, 2021-05-20 and 2021-06-29), inconsistent ground pixel grids of the AAI and NO_2 products (2021-06-24) and solar eclipse (2021-06-10) were removed from the data set.

5.2.4. CLOUD SHADOW DETECTION

The flagging of pixels affected by cloud shadows was performed with the cloud shadow detection algorithm DARCLOS, recently developed for TROPOMI at KNMI [see 169].

In DARCLOS, first, cloud pixels are identified using a threshold on the already available effective cloud fraction in the TROPOMI NO_2 product [175], after which cloud flags (CFs) are raised. Then, potential cloud shadow flags (PCSFs) are raised, indicating TROPOMI ground pixels that are potentially affected by cloud shadows. The PCSFs are determined using a geometrical calculation of the shadow location based on the cloud height from the TROPOMI cloud product FRESCO [78, 183] and illumination and viewing geometries. The PCSFs generally overestimate the true visible cloud shadow area but minimize the omission of pixels affected by cloud shadows.

After the PCSFs are raised, DARCLOS raises spectral cloud shadow flags (SCSFs). The SCSFs are a subset of the PCSFs, based on a threshold on the contrast Γ between the retrieved scene albedo, A_{scene} (see Eq. 5.4), and the expected surface albedo from a climatology, A_{DLER}. An SCSF is raised for a pixel if [see Eqs. 11 and 17 of 169]

$$\Gamma(\lambda) < -15\%, \tag{5.5}$$

where

$$\Gamma(\lambda) = \frac{A_{\text{scene}}(\lambda) - A_{\text{DLER}}(\lambda)}{A_{\text{DLER}}(\lambda)} \times 100\%. \tag{5.6}$$

The variable A_{DLER} is also known as the directionally dependent Lambertian-equivalent reflectivity or DLER [see 160]. For this research about cloud shadow effects on the AAI retrieved at 340 and 380 nm, we employ λ = 380 nm. The SCSFs are a better estimate of

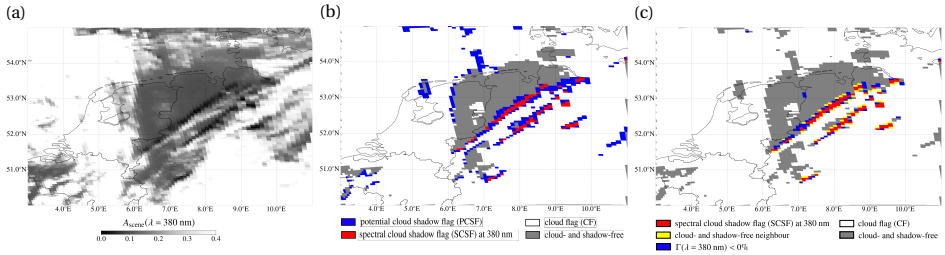

Figure 5.2: The scene albedo at 380 nm, $A_{\text{scene}}(\lambda = 380\text{ nm})$, derived by TROPOMI on 3 November 2020 above the Netherlands, Belgium and north-west Germany (Fig. 5.2a), the potential cloud shadow flags (PCSFs) in blue, spectral cloud shadow flags (SCSFs) in red, cloud flags (CFs) in white (Fig. 5.2b), and the first cloud- and shadow-free neighbour pixels in yellow and possibly shadow affected pixels according to Eq. (5.7) in blue (Fig. 5.2c).

the cloud shadows than the PCSFs. As an example, Fig. 5.1b shows the SCSFs indicated in red, the PCSFs indicated in blue and the CFs indicated in white, in three TROPOMI orbits covering the area of our case study, at 3 November 2020 which is one of the days in our data set. Figure 5.2b shows the SCSFs and PCSFs zoomed in on north-west Germany. From visual comparison of Fig. 5.2b to the map of the scene albedo A_{scene} (Fig. 5.2a), it may be observed that the SCSFs are indeed located at pixels where A_{scene} is lower than at surrounding pixels along cloud edges, which may be interpreted as cloud shadows. For more details about the cloud shadow flagging with DARCLOS, we refer to Trees et al. [169].

5.2.5. SELECTING CLOUD- AND SHADOW-FREE NEIGHBOURS

In order to be able to quantify the cloud shadow effect on the AAI in a shadow pixel (i.e., for which a SCSF was raised), we identify cloud- and shadow-free reference pixels in the proximity of the shadow pixel and assume that they represent the hypothetical non-shadow state of the shadow pixel, that is, as if the shadow pixel would not be affected by cloud shadow. In what follows, we call those reference pixels the neighbour pixels. We distinguish between first and second neighbour pixels, for the closest and second-closest neighbour pixels respectively. The second neighbour pixels are used for comparison to the first neighbour pixels as a control case, since both the first and second neighbour pixels should not be affected by cloud shadow.

First, for each shadow pixel, we define a search area with potential neighbour pixels within a two-pixel radius around the shadow pixel. That is, a neighbour pixel cannot be located more than two scanlines, or more than two pixel rows, away from the shadow pixel. The cloud pixels and shadow pixels are removed from the search area. Some pixels that are darker than expected are possibly (partly) affected by cloud shadows but not severely enough to raise a SCSF by DARCLOS (see Eqs. 5.5 and 5.6). Because we do not trust them as shadow-free pixels, they are removed from the search area when

$$\Gamma(\lambda = 380\text{ nm}) < 0\%. \tag{5.7}$$

For each left-over potential neighbour pixel in the search area, we compute the distance

in latitude-longitude space from the center of the potential neighbour to the center of the shadow pixel. The left-over potential neighbour pixel with the closest distance to the shadow pixel is selected as the first neighbour pixel for this shadow pixel. Similarly, we define the second neighbour pixel as the left-over potential neighbour pixel with the second-closest distance to the shadow pixel. Only if both a first and second neighbour pixel can be determined, the shadow pixel is considered in our analysis.

Figure 5.2c shows an example of the SCSFs at $\lambda = 380$ nm indicated in red and the first neighbour pixels indicated in yellow, for 3 November 2020 above north-west Germany. In this scene, cloud shadows are found northward of the clouds between 6.0° and 10°E longitude. The pixels that could not be selected as a neighbour because $\Gamma < 0\%$ (see Eq. (5.7)) are indicated in blue. Note that there are less neighbour pixels than raised SCSFs, because (1) some shadow pixels do not have at least two cloud- and shadow-free pixels with $\Gamma \geq 0\%$ in their search area and (2) neighbours can be recycled for multiple shadow pixels. In Fig. 5.2, the first neighbour pixels are indeed not located where there are clouds (i.e., pixels for which $A_{\text{scene}} \gtrsim 0.3$ in Fig. 5.2a) or where possibly cloud shadow darkening occurs.

5

5.2.6. SIMULATING THE CLOUD SHADOW EFFECT

Three-dimensional radiative transfer simulations are required for the explanation of cloud shadow effects on the AAI as found in the observations. In this research, we use the three-dimensional radiative transfer code MONKI (Monte Carlo KNMI), that we recently developed at KNMI. MONKI computes the TOA reflectance of an atmosphere-surface system defined in a 3D Cartesian grid in a horizontally cyclic domain, using a forward Monte Carlo technique [see, e.g., 97], and fully takes into account linear and circular polarization of light for all orders of scattering. The simulated photon packets travelling through the grid cells of the atmosphere-surface system are scattered by the atmospheric gas through (anisotropic) Rayleigh scattering [55], and by cloud droplets through Mie scattering [32] if the grid cell is cloudy. Absorption of the light by the gas and by cloud droplets is taken into account. The surface reflects Lambertian (i.e., isotropic and fully depolarizing), with a specified surface albedo. Instead of collecting the reflected photon packets at TOA in the very small solid angle subtended by the satellite, MONKI uses the more efficient 'local estimation method' [96, 97], commonly used in Monte Carlo radiative transfer algorithms [see e.g. 147, 100, 35], in which at each scattering event the contribution to the reflectance is computed as the probability that the photon is being scattered towards the satellite. The TOA reflectance of MONKI has been compared to the DAK (Doubling Adding KNMI) polarized radiative transfer code [53, 149], for plane-parallel and horizontally homogeneous cloudy and cloud-free scenes, and shows an excellent agreement.

For this research, we use 50 by 50 grid cells in the horizontal directions of the 200 by 200 km^2 cyclic domain and 33 grid cells in the vertical direction ranging from 0 km to 100 km. Ozone is the only absorbing gas in our model, with absorption cross-sections taken from [9]. The pressure, temperature and ozone volume mixing ratios solely depend on altitude according to the standard Mid-Latitude Summer profile [4]. We assume that the pressure-temperature ratio decreases exponentially with height within each grid cell [see 148, for the calculation of the gaseous absorption and scattering optical thicknesses].

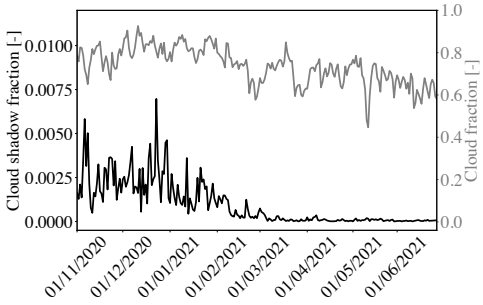

Figure 5.3: Daily cloud fraction (grey curve) and cloud shadow fraction (black curve) in the selected area over Europa from 1 November 2020 until 30 June 2021.

For our analysis, we vary the cloud optical thickness, cloud height, cloud horizontal dimensions, solar and viewing zenith and azimuth angles, and surface albedo, resulting in various sizes and shades of cloud shadows in the atmosphere and cast on the surface.

5.3. RESULTS

In this section, we present the results of the determined cloud shadow fraction in our selected data set (Sect. 5.3.1), and of the measured (Sect. 5.3.2) and simulated (Sect. 5.3.3) cloud shadow effect on the TROPOMI AAI.

5.3.1. CLOUD SHADOW FRACTION

Figure 5.3 shows the cloud fraction and cloud shadow fraction in the selected area over Europe, from 1 November 2020 to 30 June 2021. The cloud fraction and cloud shadow fraction were defined as the fraction of pixels with a raised CF and SCSF, respectively. The cloud shadow fraction was relatively large from 1 November to 31 January with an average daily mean value of 0.002, which corresponds to 1124 cloud shadow pixels on average per day. After January, the cloud shadow fraction decreases. From 1 March to 30 June, the average daily mean cloud shadow fraction was $7.4 \cdot 10^{-5}$, corresponding to 38 cloud shadow pixels on average per day. We note that changes in the trend of the daily mean cloud fraction are much less apparent. The higher cloud shadow fraction in the winter months than in the spring and summer months can be explained by the larger solar zenith angles resulting in longer shadow extents.

5.3.2. MEASURED CLOUD SHADOW EFFECTS ON THE AAI

Here we present the results of the measured cloud shadow effect on the TROPOMI AAI. That is, we compare the AAI in the shadow pixels of our data set with the AAI in their first cloud- and shadow-free neighbour pixels. To show the natural variation irrespective of cloud shadows, we also compare the AAI in the first and second neighbour pixels. In addition, we analyze the results for the measured TOA reflectance ratio $(R_{340}/R_{380})^{\text{meas}}$ and calculated TOA reflectance ratio $(R_{340}/R_{380})^{\text{calc}}$ which determine the AAI (Eq. (5.2)), and the retrieved scene albedo A_{scene} which determines $(R_{340}/R_{380})^{\text{calc}}$ via R_{340}^{calc} (Eq. (5.3)).

FIRST ORDER CLOUD SHADOW EFFECT

Figure 5.4 shows the AAI (top row) in the first neighbour pixels compared in a scatter plot to the second neighbour pixels (first column), and to the shadow pixels (second column). In both cases, the scatter plots show a high positive correlation (r = 0.82 and 0.81, respectively). The AAI in the shadow pixels is not consistently larger or smaller than the AAI in the first neighbour pixels: 55% of the shadow pixels show a larger AAI compared to their first neighbour pixels. This inconsistency is observed throughout the complete time span the data set, which is clear from the daily mean AAI time series in the third column of Fig. 5.4: the daily mean AAI in the shadow pixels is higher on some days and lower on other days compared to their first neighbour pixels. Note that the number of shadow pixels is significantly smaller in the spring months in the second half of the data set, as seen in Fig. 5.3, which increases the uncertainty of the daily mean AAI. The fourth column of Fig. 5.4 shows that the histograms of the AAI difference between the shadow pixels and first neighbour pixels is approximately centered around 0 (the mean AAI difference is 0.055 ± 0.002), and is about an order of magnitude smaller than the standard deviation of the data set (σ = 0.316).

The second row of Fig. 5.4 shows the measured TOA reflectance ratio $(R_{340}/R_{380})^{\text{meas}}$. Interestingly, although in the previous paragraph we reported no consistent cloud shadow effect on the AAI, the value of $(R_{340}/R_{380})^{\text{meas}}$ in the AAI formula (Eq. (5.2)) is consistently higher in the shadow pixels than in their first neighbour pixels: 95% of the shadow pixels show a larger $(R_{340}/R_{380})^{\text{meas}}$ compared to their first neighbour pixels. This higher reflectance ratio in the shadow pixels is observed on all days (figure in the third column and second row of Fig. 5.4) and clearly alters its distribution (figure in the fourth column and second row of Fig. 5.4). The difference of the mean $(R_{340}/R_{380})^{\text{meas}}$ in the shadow pixels with respect to their neighbours is 0.036, which is larger than the standard deviation σ = 0.026. Those results imply that the measured TROPOMI UV TOA reflectances were consistently 'more blue' in the shadow pixels than in the neighbour pixels.

The missing cloud shadow effect on the AAI, while TROPOMI consistently measured higher values for $(R_{340}/R_{380})^{\text{meas}}$ in the cloud shadows, can be explained by the behaviour of the calculated reflectance ratio $(R_{340}/R_{380})^{\text{calc}}$. Indeed, as shown in the third row of Fig. 5.4, $(R_{340}/R_{380})^{\text{calc}}$ is also elevated in the shadow pixels, which happens to be similar to the increase of $(R_{340}/R_{380})^{\text{meas}}$. This increase of $(R_{340}/R_{380})^{\text{calc}}$ is caused by the lower retrieved scene albedo A_{scene} in the shadow pixels, as a result of the lower measured reflectance R_{380}^{meas} in the cloud shadows (see Eq. (5.4)). With lower A_{scene}, the contribution of the (spectrally flat) Lambertian surface in the DAK model decreases, which increases the 'blueness' of the calculated TOA reflectances (Eq. (5.3)) and thus increases $(R_{340}/R_{380})^{\text{calc}}$. A similar effect on $(R_{340}/R_{380})^{\text{calc}}$ can be found during solar eclipses [168]. However, in contrast to cloud shadows, the lunar shadow is imposed from outside the Earth system, such that the light paths in principle do not change and $(R_{340}/R_{380})^{\text{meas}}$ is not altered, resulting in a strong increase of the AAI during solar eclipses. In cloud shadows, simultaneous increases of $(R_{340}/R_{380})^{\text{meas}}$ and $(R_{340}/R_{380})^{\text{calc}}$ lead, to the first order, to cancellations of cloud shadow effects in the AAI through Eq. (5.2). The explanation of the missing first order cloud shadow effect is explained in more detail using our simulation results in Section 5.3.3.

The cancellation of the cloud shadow effect on the AAI is also apparent in the AAI

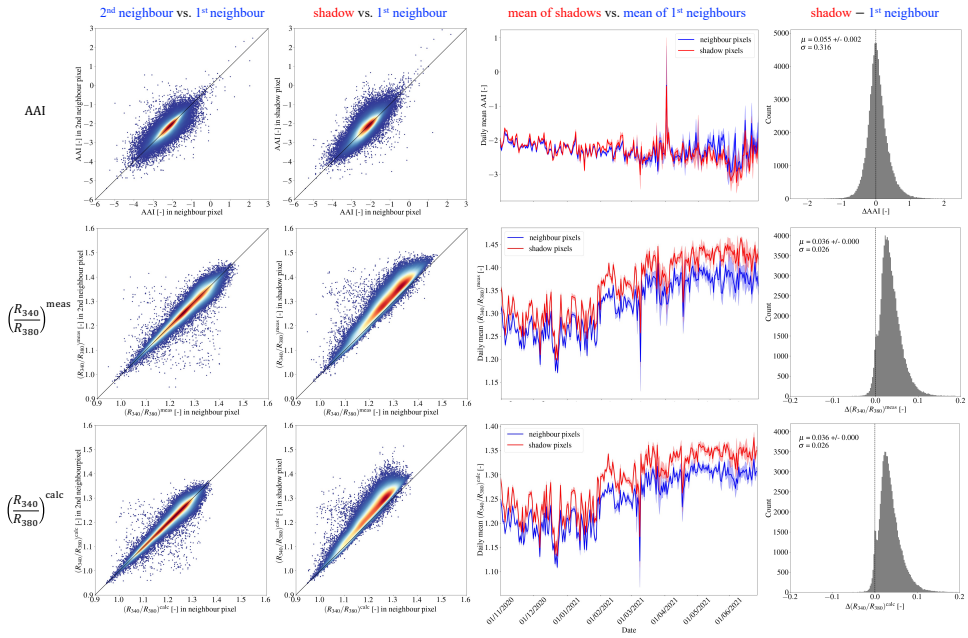

Figure 5.4: Comparison of the values in the second and first neighbour pixels (first column), the cloud shadow pixels and the first neighbour pixels (second column), the daily mean values of the cloud shadow pixels and the first neighbour pixels (third column), and the histograms of their differences (shadow - first neighbour, fourth column), for the TROPOMI AAI (first row), the measured TOA reflectance ratio between 340 and 380 nm (second row), and the calculated TOA reflectance ratio between 340 and 380 nm in the AAI retrieval algorithm (third row).

map of a single cloud shadow case. Fig. 5.5 shows maps of the AAI (first column), $(R_{340}/R_{380})^{\text{meas}}$ (second column) and $(R_{340}/R_{380})^{\text{calc}}$ (third column) over the Netherlands, Belgium and north-west Germany on 3 November 2020. From Fig. 5.2, it was known that cloud shadows were present in this scene northward of the clouds between 6.0° and 10°E longitude. Indeed, those cloud shadows appear to have increased $(R_{340}/R_{380})^{\text{meas}}$ and $(R_{340}/R_{380})^{\text{calc}}$, which is clear from the darker blue shade compared to their cloud- and shadow-free surroundings. In the AAI map, the cloud shadows can hardly be distinguished from their surroundings.

SECOND ORDER CLOUD SHADOW EFFECTS

Although $(R_{340}/R_{380})^{\text{meas}}$ and $(R_{340}/R_{380})^{\text{calc}}$ are more blue in the shadow than their surroundings in almost all cases, we found that the cancellation of cloud shadow effects in the measured AAI as discussed in the previous Section is not always perfect. We investigated the dependency of the second order cloud shadow effect on the AAI to physical parameters, and found a slight dependency on the illumination and viewing geometries, and the surface albedo. We call those the second-order cloud shadow effects.

Figure 5.6 shows the AAI difference between the shadow and first neighbour pixels (bottom row) versus the solar zenith angle θ_0 (first column), viewing zenith angle θ (sec-

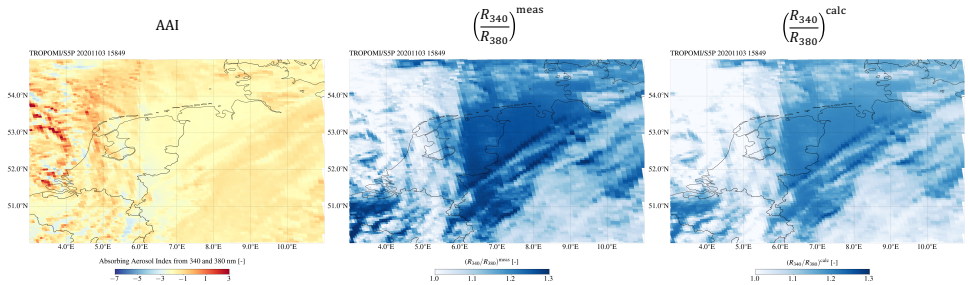

Figure 5.5: Examples of the TROPOMI AAI (first column), the measured TOA reflectance ratio between 340 and 380 nm (second column) and the calculated TOA reflectance ratio between 340 and 380 nm in the TROPOMI AAI retrieval (third column), for 3 November 2020 over the Netherlands and Germany.

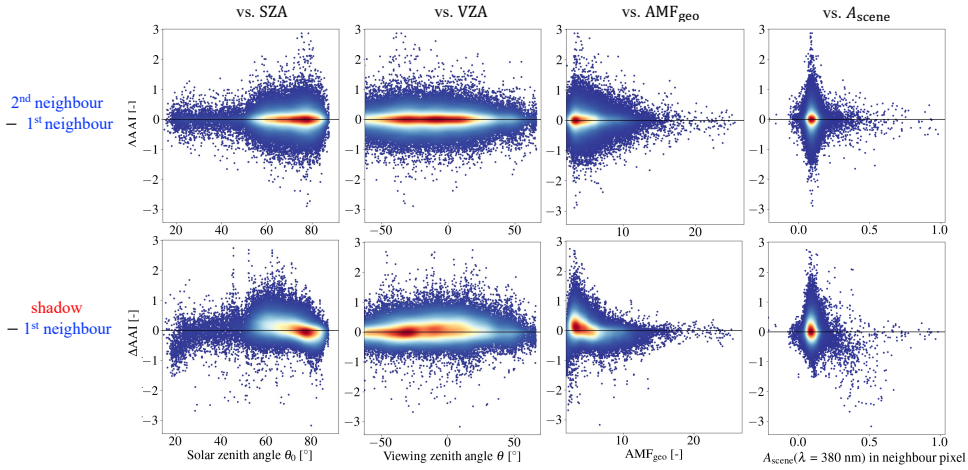

Figure 5.6: Similar AAI data as in Fig. 5.4, but now plotted as the differences between the second and first neighbour pixels (first row) and between the cloud shadow pixels and first neighbour pixels (second row), as functions of solar zenith angle (first column), viewing zenith angle (second column), geometric air mass factor (third column) and retrieved scene albedo at 380 nm in the first neighbour pixel (fourth column).

ond column), geometric air mass factor $AMF_{geo} = 1/\mu + 1/\mu_0$ (third column), and scene albedo A_{scene} of the first neighbour pixel (fourth column). Also, we present the differences between the second and first neighbour pixels (top row), which represent the natural AAI variation irrespective of cloud shadows. From the results in the bottom row, it can be concluded that cloud shadows tend to increase the AAI slightly for decreasing θ_0 from 80° to ~50° (the mean ΔAAI is 0.18 in the shadow case between $\theta_0 = 50°$ and 70°), and for small θ (the mean ΔAAI is 0.09 in the shadow case for $|\theta| < 30°$). This dependency, however, seems to be more apparent when combining θ and θ_0 in the geometric air mass factor: smaller AMF_{geo} give slightly increased AAI (the mean ΔAAI is 0.14 in the shadow case for $AMF_{geo} < 5$). We count an increase of 377 pixels for which ΔAAI > 1, when cloud shadow pixels instead of second neighbour pixels are compared with first neighbour pixels, provided that $AMF_{geo} < 5$. This number corresponds to 0.47% of the

total number of shadow pixels. Another dependency can be measured in A_{scene}: bright surfaces ($A_{\text{scene}} \gtrsim 0.2$) tend to decrease the AAI. However, for most pixels in our data set A_{scene} equals approximately 0.1, for which this dependency does not seem apparent. We count an increase of 70 pixels for which $\Delta\text{AAI} < -1$, when cloud shadow pixels instead of second neighbour pixels are compared with first neighbour pixels, provided that $A_{\text{scene}} > 0.2$. This number corresponds to 0.09% of the total number of shadow pixels.

5.3.3. SIMULATED CLOUD SHADOW EFFECTS ON THE AAI

Here we present the results of the simulated cloud shadow effect on the TROPOMI AAI using our 3D radiative transfer code MONKI. We considered a box-shaped cloud with dimensions of 10 x 10 x 1 km^3 consisting of spherical droplets with effective radius r_{eff} of 2.0 μm, and placed it at three altitudes: at 2, 5 and 10 km cloud base height h_{c}. Furthermore, we varied the cloud optical thickness ($\tau_{\text{c}} = 1$, 5, or 10), the surface albedo ($A_{\text{s}} = 0$, 0.1, or 0.2), the viewing zenith angle ($\theta = 0°$, 30°, 45°, 60°, or 75°), the solar zenith angle ($\theta_0 = 0°$, 30°, 45°, 60°, or 75°), and the azimuth difference ($\phi - \phi_0 = 0°$ or 180°), resulting in 1350 simulated scenes.

5

FIRST ORDER CLOUD SHADOW EFFECT

The first row of Fig. 5.7 shows an example of the simulated TOA reflectances that would be measured with TROPOMI at 340 and 380 nm, R_{340}^{meas} and R_{380}^{meas} respectively, together with their ratio $R_{340}^{\text{meas}}/R_{380}^{\text{meas}}$, for a scene with $h_{\text{c}} = 5$ km, $\tau_{\text{c}} = 10$, $\theta_0 = 75°$, $\theta = 0°$ and $\phi - \phi_0 = 0°$ (i.e., the instrument is nadir-viewing and the Sun is located on the left side of the scene). Here, we assume a black surface ($A_{\text{s}} = 0.0$). The cloud, located at $x = 48$ – 68 km and $y = 28$ – 48 km gives the strongest signal in both R_{340}^{meas} and R_{380}^{meas}, due to light multiply scattered by the rather thick cloud towards the satellite instrument, which is approximately wavelength-independent resulting in a white appearance of the cloud ($R_{340}^{\text{meas}}/R_{380}^{\text{meas}} \approx 1$). Outside the cloudy region, the signal is more 'blue' ($R_{340}^{\text{meas}}/R_{380}^{\text{meas}} > 1$), due to the λ^{-4} dependence of the Rayleigh scattering optical thickness of the gas. In the cloud shadow, located along the right edge of the cloud, the signal of R_{340}^{meas} and R_{380}^{meas} is smallest. Indeed, the 'blueness' of the cloud shadow is even larger than that of the cloud- and shadow-free region ($R_{340}^{\text{meas}}/R_{380}^{\text{meas}} \gg 1$), which was also found in the observations by TROPOMI (see Sect. 5.3.2).

In order to explain the 'blue' appearance of cloud shadows as seen from space, we analyze the vertical profiles of the contributions to R_{340}^{meas}, R_{380}^{meas} and $R_{340}^{\text{meas}}/R_{380}^{\text{meas}}$, in the second row of Figure 5.7. In the cloud- and shadow-free region, most signal originates from below ~ 15 km where the gaseous atmosphere is most dense. This signal of the background gas is larger at 340 nm than at 380 nm due to the λ^{-4} dependence of the Rayleigh scattering optical thickness of the gas. We note that the 'color' of the background contribution changes from 'blue' ($R_{340}^{\text{meas}}/R_{380}^{\text{meas}} > 1$), through 'white' ($R_{340}^{\text{meas}}/R_{380}^{\text{meas}} = 1$), to 'red' ($R_{340}^{\text{meas}}/R_{380}^{\text{meas}} < 1$), with decreasing altitude, as the blue light has been scattered out of the direct beam that is incident on the lowest atmospheric layers. The contribution from the surface is equal to 0, because all the light reaching the surface is absorbed as $A_{\text{s}} = 0.0$ in this example.

Directly below the cloud, from 5 km to the surface, the contribution to both R_{340}^{meas}

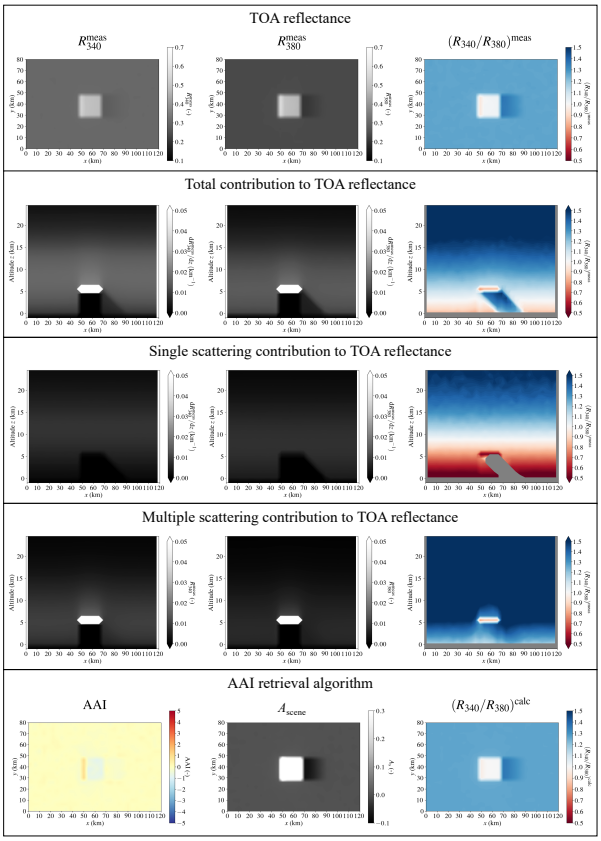

Figure 5.7: Simulations by MONKI of the measured TOA reflectance (top row) and the vertical profiles (in km^{-1}) of the contribution to the TOA reflectance for all photons (second row), for single scattering only (third row) and for multiple scattering only (fourth row), at 340 nm (first column), at 380 nm (second column) and for their ratio (third column). The bottom row shows the corresponding AAI (first column), the scene albedo at 380 nm (second column) and the calculated TOA reflectance ratio between 340 and 380 nm using the TROPOMI AAI retrieval algorithm (third column). The vertical profiles were made using the mean values from $y = 30$ to $y = 46$ km. The data point below 0 km altitude represents the contribution of the surface.

and R_{380}^{meas} is approximately 0, as the nadir-looking instrument cannot look through the rather thick cloud. Inside the cloud shadow volume, located on the lower right side of the cloud, the contributions are indeed smaller than in the cloud- and shadow-free region but still larger than 0 (see second row of Fig. 5.7). Contrary to the cloud- and shadow-free contribution at those altitudes, the color of the cloud shadow contribution is blue ($R_{340}^{\text{meas}}/R_{380}^{\text{meas}} > 1$). Comparing the vertical profiles in the cloud- and shadow-free region (e.g., at $x = 26$ km) and through the cloud shadow (e.g., at $x = 74$ km), it can readily be concluded that a vertical integration of the contribution indeed leads to a relatively blue cloud shadow signal at TOA, thus a higher $R_{340}^{\text{meas}}/R_{380}^{\text{meas}}$ in the cloud shadow than in the cloud- and shadow-free surroundings (see upper right figure in Fig. 5.7).

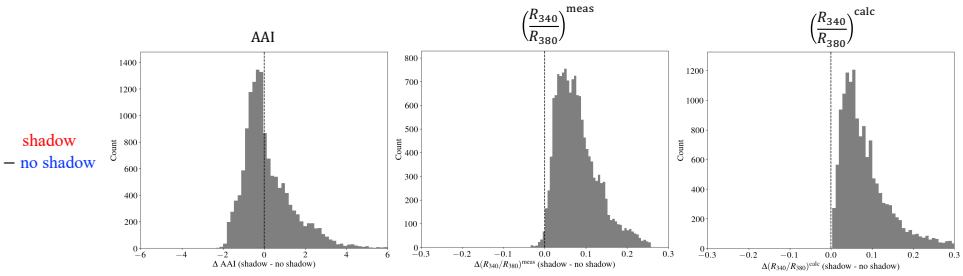

Figure 5.8: Histograms of the differences in the simulated values by MONKI between cloud shadow pixels and cloud- and shadow-free pixels, for the AAI (first column), the measured TOA reflectance ratio between 340 and 380 nm (second column) and the calculated TOA reflectance ratio between 340 and 380 nm using the TROPOMI AAI retrieval algorithm (third column), for all 1350 simulated scenes. The total count is higher than the number of scenes, because a scene can have multiple cloud shadow pixels.

We investigated the cause of the nonzero and blue contribution of the cloud shadow volume by separating the vertical profiles of the contributions from single scattering only (third row of Fig. 5.7) and of multiple scattering only (fourth row of Fig. 5.7). Note that the sum of those contributions is again the total contribution as shown in the second row of Fig. 5.7. In the cloud shadow, there is no contribution from single scattering in our simulation, as shown by the black shades in the contributions to R_{340}^{meas} and R_{380}^{meas}, and the undefined values in the contribution to $R_{340}^{\text{meas}}/R_{380}^{\text{meas}}$. Apparently, all photons were scattered away from the direct beam passing through the cloud before reaching the cloud base. In multiply scattered light, however, photons can reach the cloud shadow volume after being scattered by the gas in the cloud- and shadow-free region, as illustrated by the nonzero values in the cloud shadow in the fourth row of Fig. 5.7. Also, it should be noted that, regardless of cloud shadows, the signal from multiple scattering is more blue than that of single scattering (cf. third and fourth rows of Fig. 5.7). Thus, because in cloud shadows the singly scattered light is intercepted and the multiply scattered light is left, and because the multiply scattered light is more blue than singly scattered light, the appearance of cloud shadows is relatively blue (second row).

Finally, we computed the AAI that would be retrieved from our simulated TOA reflectances. That is, we used the simulated R_{340}^{meas} and R_{380}^{meas} as input for the TROPOMI AAI retrieval algorithm (see Sect. Sect. 5.2.2). The last row of Fig. 5.7 shows the retrieved AAI, $A_{\text{scene}}(380\text{ nm})$, and $R_{340}^{\text{calc}}/R_{380}^{\text{calc}}$. In the cloud- and shadow-free region the simulated AAI equals 0, since R_{380}^{meas} and R_{380}^{calc} are virtually identical due to the excellent agreement between MONKI and DAK for clear-sky scenes. In the cloud shadow, the AAI is also approximately 0 but $A_{\text{scene}}(380\text{ nm})$ appears dark as a direct result of the lower R_{380}^{meas} (see Eq. (5.4)). Note that for this scene with a black surface, the retrieved $A_{\text{scene}}(380\text{ nm})$ is even negative in the cloud shadow (it should be noted that a negative albedo is nonphysical and a result of the AAI algorithm as explained in Sect. 5.2.2). Consequently, the calculated (spectrally flat) surface contribution to R_{340}^{calc} is relatively small in the cloud shadow and is negative, resulting in a relatively large and blue contribution of the path reflectance R^0 (see Eq. (5.3)). Indeed, $R_{340}^{\text{calc}}/R_{380}^{\text{calc}}$ is enhanced in the cloud shadow, as shown in the last row of Fig. 5.7. Because cloud shadows are more blue in both R^{calc} and

R^{meas} (note that the figures of $R^{calc}_{340}/R^{calc}_{380}$ and $R^{meas}_{340}/R^{meas}_{380}$ look approximately identical in Fig. 5.7), there is no visible cloud shadow signature in the AAI (lower left figure in Fig. 5.7). In conclusion, the AAI retrieval already automatically corrects for cloud shadows via the lower retrieved scene albedo, which is in agreement with the first order cloud shadow effect that we found in the TROPOMI observations (Sect. 5.3.2).

We note that at the opposite side of the cloud, the AAI is slightly increased in our simulations (AAI ~1). This increase is found on the cloud itself at x = 50 km, where the cloud is directly illuminated by the sun from the side. We speculate that this result demonstrates the positive TROPOMI AAI signatures at the bright side of vertical cloud structures at high latitudes, that were found by [80] (see their Figs. 1 and 2). Numerical experiments indeed showed that an increase of the cloud vertical extent from 1 km to 5 km further increased this positive AAI signature. Because the scope of our article is the analysis of shadows, we leave the analysis of the bright side of clouds for future research.

In the previous paragraphs of this Section, we discussed the results of one simulated scene. As mentioned in the beginning of this Section, we did those simulations for 1350 scenes. Figure 5.8 shows the difference between the AAI in the simulated shadow pixels and the AAI in the cloud- and shadow-free regions of all simulated scenes. In addition, we show those differences for $R^{meas}_{340}/R^{meas}_{380}$ and $R^{calc}_{340}/R^{calc}_{380}$. For almost all cases (99% and 100% for the measured and calculated values respectively), indeed the cloud shadow pixels are more blue than their cloud- and shadow-free surroundings, and $\Delta R^{meas}_{340}/R^{meas}_{380}$ = 0.079 and $\Delta R^{calc}_{340}/R^{calc}_{380}$ = 0.086. The consistent enhanced blueness in both R^{calc} and R^{meas} resulted in a mean AAI difference close to zero (ΔAAI = 0.16 while σ = 1.2), showing that, on average, cloud shadow effects are approximately cancelled out in our simulated data set. In Fig. 5.9 we summarize the cancellation of cloud shadow effects in the AAI with a conceptual model.

5

SECOND ORDER CLOUD SHADOW EFFECTS

Although the simulated average AAI difference between pixels inside and outside the cloud shadow is close to 0, in some cases the cloud shadows leave signatures in the simulated AAI. This can be concluded from the negative and positive tails of the ΔAAI-histogram in Figure 5.8, indicating that the cancellation was not always perfect and could have values of several AAI points. Those imperfect cancellations, while both R^{calc} and R^{meas} are both more blue in the cloud shadow, were also found in the observations (Sect. 5.3.2). They are the second order cloud shadow effects.

In the TROPOMI observations (Sect. 5.3.2) we found a slight dependency of the second order cloud shadow effects on geometric air mass factor and surface albedo (through the scene albedo of the first cloud- and shadow-free neighbour). We did not analyze the dependency on cloud parameters in the observations, because our cloud shadow detection algorithm DARCLOS does not allow for a precise determination of the clouds responsible for certain cloud shadows. Figure 5.10 shows $R^{meas}_{340}/R^{meas}_{380}$ and $R^{calc}_{340}/R^{calc}_{380}$ for all shadow pixels in our simulated scenes, grouped per cloud height (upper left), cloud optical thickness (upper right), geometric air mass factor (lower left) and surface albedo (lower right). Data points on the symmetry line $R^{meas}_{340}/R^{meas}_{380} = R^{calc}_{340}/R^{calc}_{380}$ are related to an AAI of 0 (see Eq. (5.2)) just as in the cloud- and shadow-free region in our simulations, and to a perfect cancellation of cloud shadow effects. Data points in

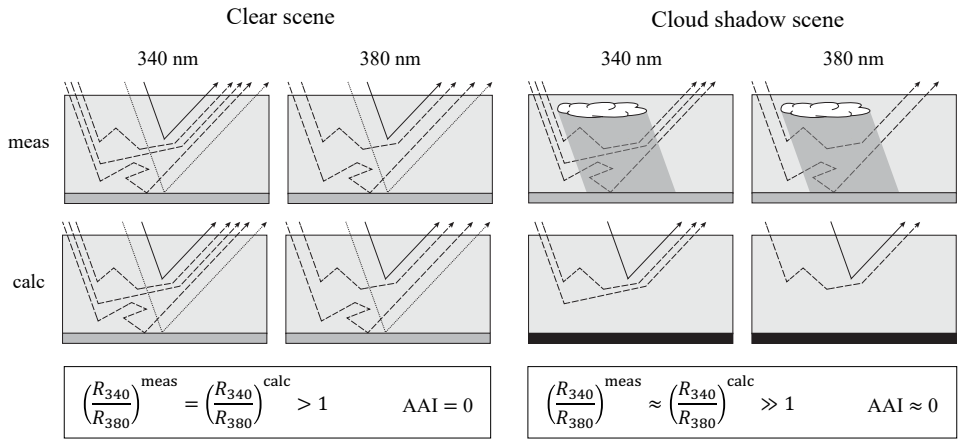

Figure 5.9: Sketches explaining the first order cloud shadow effect on the Absorbing Aerosol Index (AAI). The top and bottom sketches are for the measured (meas) and the calculated (calc) top-of-atmosphere (TOA) reflectances, respectively. The left four sketches are for the clear case (i.e., without clouds and shadows), and the right four sketches are for the cloud shadow case, where the first row is for 340 nm and the second row for 380 nm. Solid arrows indicate singly scattered light, dashed arrows indicate multiply scattered light, and dotted arrows indicate light reflected once by the surface. The number of arrows leaving TOA illustrate the magnitude of the respective TOA reflectance. The AAI retrieval algorithm automatically assumes a dark surface when the measured reflectance is low due to the shadow (Eq. 5.4), as illustrated by the black shaded surface area. Because cloud shadows increase the ratio of the TOA reflectance at 340 nm with respect to 380 nm in both the measurements and the retrieval algorithm calculations by approximately the same amount, the AAI is more or less unaffected (Eq. 5.2).

the regions for which $R_{340}^{\text{meas}}/R_{380}^{\text{meas}} > R_{340}^{\text{calc}}/R_{380}^{\text{calc}}$ and $R_{340}^{\text{meas}}/R_{380}^{\text{meas}} < R_{340}^{\text{calc}}/R_{380}^{\text{calc}}$ result in cloud shadow signatures with negative and positive AAI, respectively. Regardless of the grouping of the data points, Fig. 5.10 demonstrates that the strongest positive AAI cloud shadow signatures are caused by the bluest shadows: when $R_{340}/R_{380} \gtrsim 1.4$ the data points deviate towards the right from the symmetry line. The negative AAI signatures seem to be caused by cloud shadows with $R_{340}/R_{380} \lesssim 1.4$.

Figure 5.10 (upper left) shows that the strong positive AAI cloud shadow signatures are primarily caused by high clouds (h_c = 10 km). Note that the low clouds (h_c = 1 km) group only contain few data points, because for too small viewing- and or illumination geometries the size of the cloud shadow is too small to be visible from space. Figure 5.10 (upper right) shows that the thick clouds (τ_c = 10) give stronger (negative and positive) AAI cloud shadow signatures than thin clouds (τ_c = 1). Figure 5.10 (lower left) shows that the AAI cloud shadow signatures tend to become more positive with decreasing geometric air mass factor, which was also found in the TROPOMI observations (see Fig. 5.6). Figure 5.10 (lower right) shows that the AAI cloud shadow signatures tend to become more negative with increasing surface albedo, which is also consistent with the TROPOMI observations.

The explanation of the positive second order cloud shadow AAI signature can be found by analyzing the differences in the shadow simulation results between a low and high cloud. Figure 5.11 shows a top view of the AAI (first row), vertical profiles of the

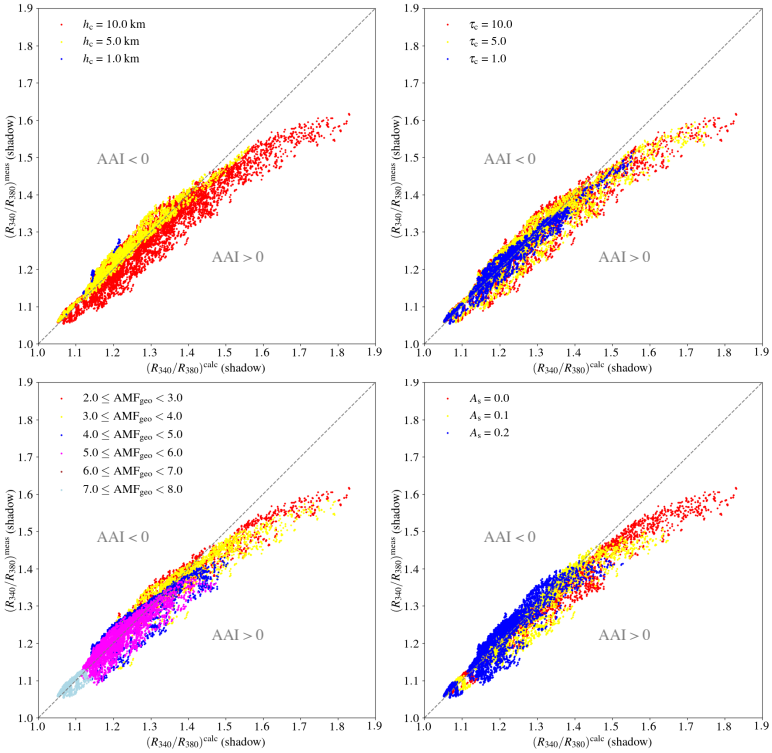

Figure 5.10: Analysis of the simulated measured and calculated TOA reflectance ratios between 340 and 380 nm for the 1350 simulated scenes with MONKI. The results are grouped per cloud height (upper left), cloud optical thickness (upper right), geometric air mass factor (lower left), and surface albedo (lower right).

simulated altitude dependent $R_{340}^{meas}/R_{380}^{meas}$ contribution (second row), cross-sections of $R_{340}^{meas}/R_{380}^{meas}$ and $R_{340}^{calc}/R_{380}^{calc}$ at TOA (third row), and the vertical profiles of the contributions of R_{340}^{meas} and R_{380}^{meas} at several locations for x (fourth row). The left column shows the results again for a cloud at 5 km altitude (similar as in Fig. 5.7), while in the middle column the cloud is raised to an altitude of 10 km. For this higher cloud, the AAI is increased up to ~3 points in the shadow, but only close to the cloud (x = 74 km) where the shadow is located in the atmosphere above ~3 km altitude. Here, more light is being intercepted than at lower altitudes, since the contribution to the TOA signal in the shadow-free background (x = 26 km) at these higher altitudes is larger than close to the surface (see orange lines in the bottom figures in Fig. 5.11). Hence, A_{scene} is much darker than for the low cloud at x = 74 km, which strongly increases $R_{340}^{calc}/R_{380}^{calc}$ (see Sect. 5.2.2). Also, $R_{340}^{meas}/R_{380}^{meas}$ is larger for this shadow at higher altitudes, as multiple scattering contributions at those higher altitudes are more blue (see fourth row in Fig. 5.7) and the shadow only contains multiply scattered light (see Sect. 5.3.3). However, the latter effect on the vertically integrated signal is relatively weak, because the single scattering background contribution that is being intercepted is also more blue at higher altitudes than at lower altitudes (cf. third row in Fig. 5.7), which suppresses the increase in measured blueness

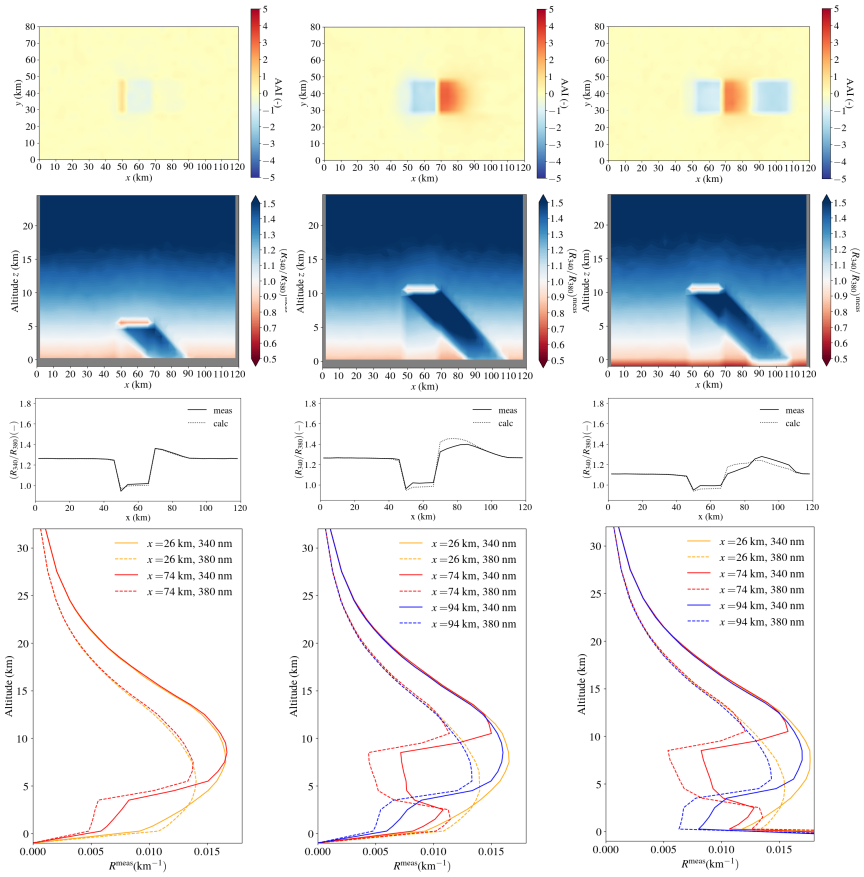

Figure 5.11: Simulations by MONKI of the AAI (first row), vertical profiles of the simulated altitude dependent $R_{340}^{\text{meas}}/R_{380}^{\text{meas}}$ TOA contribution (second row), cross-sections of $R_{340}^{\text{meas}}/R_{380}^{\text{meas}}$ and $R_{340}^{\text{calc}}/R_{380}^{\text{calc}}$ at TOA (third row), and the vertical profiles of the TOA contributions of R_{340}^{meas} and R_{380}^{meas} (fourth row) at $x = 26$ km (unshadowed region), $x = 74$ km (atmosphere shadow), and $x = 94$ km (surface shadow). The scene parameters in the first column are similar as in Fig. 5.7: $h = 5$ km, $\tau_c = 10$, $r_{\text{eff}} = 2.0$ μm, $A_s = 0.0$, $\theta_0 = 75°$, $\theta = 0°$, $\varphi - \varphi_0 = 0°$. In the second row, h was modified into 10 km. In the third row, in addition A_s was modified into 0.2. The vertical profiles were made using the mean values from $y = 30$ to $y = 46$ km. The data point below 0 km altitude represents the contribution of the surface.

of the high shadow as seen from space. The suppression of the increase in measured shadow blueness is most effective at small geometric AMF, for which the vertical profiles of the single scattering background contribution are more blue due to the relatively short path lengths (not shown), and because the contribution peaks at lower altitudes (i.e., the lower atmosphere, where the shadows usually occur, are better visible from space). Consequently, the positive second order cloud shadow signature increases with decreasing geometric AMF. In summary, both $R_{340}^{\text{meas}}/R_{380}^{\text{meas}}$ and $R_{340}^{\text{calc}}/R_{380}^{\text{calc}}$ at TOA are larger for shadows located higher in the atmosphere, but $R_{340}^{\text{calc}}/R_{380}^{\text{calc}}$ increases stronger with altitude than $R_{340}^{\text{meas}}/R_{380}^{\text{meas}}$, causing the AAI to become positive according to Eq. 5.2.

The explanation of the negative second order cloud shadow AAI signature can be found by increasing the surface albedo A_s from 0 to 0.2 (see third column in Fig. 5.11, and Fig. 5.12 for more detailed simulation results). Without shadows, wavelength independent Lambertian surface reflection makes the signal at TOA stronger but more 'white', resulting in both smaller $R^{meas}_{340}/R^{meas}_{380}$ and $R^{calc}_{340}/R^{calc}_{380}$ (see upper and lower right figures, respectively, in Fig. 5.12), and a neutral effect on the AAI [see 30] (see lower right figure in Fig. 5.12). In our simulations, at a relatively large distance from the cloud where the shadow is cast on the surface (at $x = 94$ km), the AAI is decreased by ~1.5 points. Here, incident light on the surface is being reflected, resulting in a larger TOA reflectance compared to that in the black surface case. Consequently, A_{scene} in the AAI retrieval is higher (see bottom middle figure in Fig. 5.12), such that the Lambertian surface in the DAK model reflects more direct and scattered scattered light, which relatively decreases $R^{calc}_{340}/R^{calc}_{380}$. However, in reality in the cloud shadow on the surface at $x = 94$ km, the surface only reflects light that has been scattered before at least once (see third row in Fig. 5.12). Because the multiply scattered light contribution is more blue (see fourth row in Fig. 5.12) than that of singly reflected light by the surface in the background, the measured surface shadow is relatively blue, which increases $R^{meas}_{340}/R^{meas}_{380}$. In summary, the Lambertian surface reflection decreases both $R^{meas}_{340}/R^{meas}_{380}$ and $R^{calc}_{340}/R^{calc}_{380}$ in the cloud shadow cast on the surface, but because the decrease of $R^{calc}_{340}/R^{calc}_{380}$ is stronger the AAI becomes negative.

5.4. MONKI SIMULATIONS OF A SHADOW CAST ON A REFLECTING SURFACE PRODUCED BY A HIGH CLOUD

Figure 5.12 shows the MONKI output results as in Fig. 5.7, but then for a high cloud ($h = 10$ km) above a reflecting Lambertian surface ($A_s = 0.2$). Although cloud shadows in the atmosphere and on the surface are more blue than their shadow-free surroundings in both $R^{meas}_{340}/R^{meas}_{380}$ and $R^{calc}_{340}/R^{calc}_{380}$ (first order effect), the blueness is not increased equally resulting in a positive AAI signature of ~ 2.5 in the atmosphere close to the cloud, at $x = 74$ km, and a negative AAI signature of ~ −1.5 in the shadow cast on the surface, at $x = 94$ km (second order effects).

5.5. DISCUSSION AND CONCLUSION

The cancellation of cloud shadow effects on both the measured and simulated TROPOMI AAI (Sect. 5.3.2 and 5.3.3, respectively) shows that the traditional AAI retrieval by itself already (partly) corrects for cloud shadows via the retrieved scene albedo. Simultaneously, we measure and simulate that cloud shadows are almost always more blue than cloud- and shadow-free regions. If the traditional AAI retrieval would not correct for this enhanced blueness, strong cloud shadow signatures could have been expected in the AAI. But, due to the automatic cancellation, the average AAI difference between shadow and non-shadow cases is close to zero. We note that other TROPOMI products that depend on the pixel blueness, such as the aerosol optical thickness (AOT) [31], may be affected by cloud shadows, but that was not studied in this paper.

We have shown that, for individual cases in the measurements and in the simula-

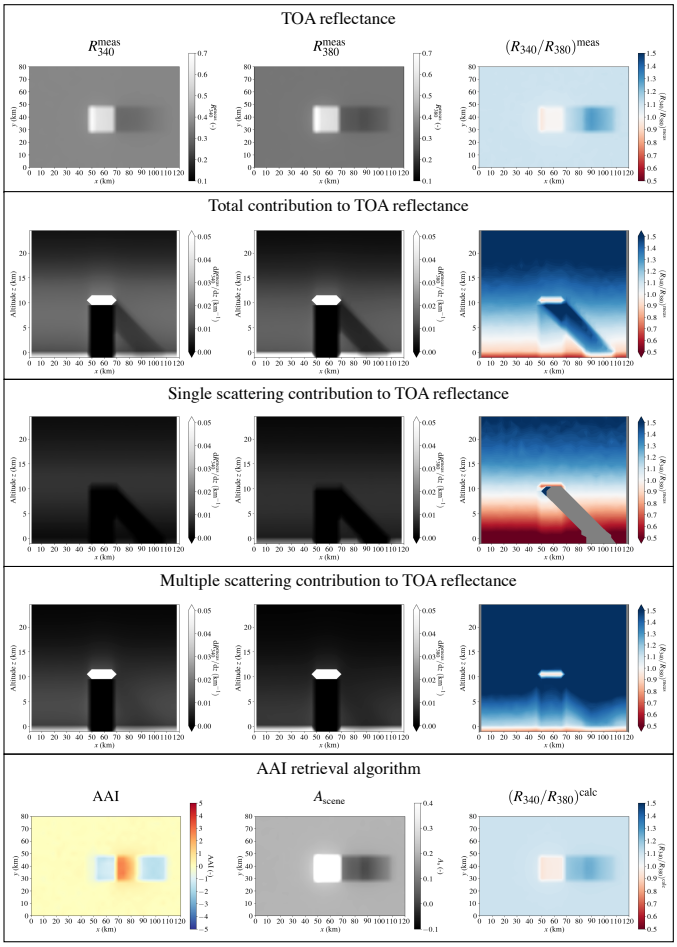

$h = 10$ km, $\tau_c = 10$, $r_{eff} = 2.0$ μm, $A_s = 0.2$, $\theta_0 = 75°$, $\theta = 0°$, $\phi - \phi_0 = 0°$

Figure 5.12: Similar as Fig. 5.7, but for $h = 10$ km and $A_s = 0.2$.

tions, the blueness of the clouds shadows is not always perfectly compensated for by the lower scene albedo in the AAI retrieval. This results in second-order cloud shadow effects which sometimes yield lower, and sometimes higher, AAI than in the cloud- and shadow-free regions. In the observations, we found weak positive and negative relations of those second order cloud shadow effects to the geometric air mass factor and surface albedo, respectively. Our simulations indeed demonstrated that positive AAI cloud shadow signatures can mostly be related to high thick clouds with small geometric air mass factor above dark surfaces, while negative AAI cloud shadow signatures should be most prominent near thick clouds above bright surfaces. In the observations, 0.47% and 0.09% of the shadow pixels show an absolute AAI difference larger than 1, with respect to their cloud- and shadow-free neighbours, that can be attributed to the cloud shadow, when selecting data with $AMF_{geo} < 5$ and $A_{scene} > 0.2$, respectively. We did not specifi-

cally select scenes that also include absorbing aerosol for this paper. We note that only 0.01% of the shadow pixels also may contain absorbing aerosols [based on a AAI > 0.8 threshold for the cloud- and shadow-free neighbour pixels, see 31].

Our simulations thus suggest that a potential correction of the second order cloud shadow effects on the AAI should depend on cloud height, optical thickness, surface albedo and geometric air mass factor. However, the height and thickness of the clouds responsible for the measured cloud shadows are uncertain. That is because, although the cloud height is a TROPOMI product [e.g. FRESCO, see 78, 183], the cloud height product has a limited accuracy (the cloud height obtained with FRESCO is in fact the cloud centroid height) and the optical thickness and vertical extent of the clouds are not retrieved. Moreover, the clouds responsible for certain cloud shadows are difficult to determine in the observations. The responsible clouds are not an output of DARCLOS, as DARCLOS uses spectral tests to determine the cloud shadow flags in the final step of its algorithm. Additionally, the accuracy of a 'reverse calculation' of the responsible cloud (height) would never be better than the ~4 km spatial resolution of TROPOMI in the nadir viewing direction, and again the cloud optical thickness and vertical extent would be unknown. Hence, we conclude that a reliable correction method for the second order cloud shadow effects on the TROPOMI AAI would be complicated. Moreover, because of the automatic cancellation of the cloud shadow effects to the first order, such a correction method may not be needed.

For this study, we have developed the 3D radiative transfer code MONKI which successfully simulated the effect of cloud shadows on the TROPOMI AAI. MONKI fully takes into account the polarization of light for all orders of scattering, and can store the vertical profiles of the altitude dependent reflected light contribution at TOA, for the total, singly, and multiply scattered light. In future research, MONKI can be used to find explanations of more cloud effects on sensitive retrieval algorithms, such as the AAI algorithm, in which polarization and geometry play on important role. For example, the positive AAI increases at the bright side of clouds that are found in both our simulations and previous observations, can be further analyzed using the MONKI model.

AUTHOR CONTRIBUTIONS

V.T. did all computations and wrote the manuscript. P.W. weekly commented on the intermediate results. All authors read the manuscript, provided feedback that led to improvements and were involved in the selection of the results presented in this paper.

COMPETING INTERESTS

The authors declare that they have no conflict of interest.

ACKNOWLEDGEMENTS

This work is part of the research programme User Support Programme Space Research (GO) with project number ALWGO.2018.016, which is (partly) financed by the Dutch Research Council (NWO).

6

CONCLUSION AND OUTLOOK

In this Chapter, we answer the research questions that were stated in the Introduction (Sect. 1.2), and provide outlooks for the different topics.

6.1. CONCLUSION

THE IMPACT OF **SOLAR ECLIPSES** ON THE **AAI** AS MEASURED BY TROPOMI

The UV Absorbing Aerosol Index (AAI) is an air quality product derived from the TOA reflectance spectra. If no correction is applied, a significant increase of the TROPOMI AAI is measured in the shadow of the Moon. The magnitude of the AAI enhancement increases with solar obscuration fraction, but can exceed 10 AAI points in the darkest parts of the partial lunar shadow. We explain this anomaly by the decreased measured TOA reflectance at 380 nm, which is used to define the Lambertian surface albedo in the model reflectance computations and propagates in the AAI formulae into a more 'blue' model UV spectrum, resulting in an increased AAI. That is, the AAI increase in the Moon shadow is caused by the way the AAI algorithm responds to unexpected decreases in solar irradiance, and not by a potentially 'redder' measured signal, nor by a physical eclipse-induced effect on aerosols.

In this thesis, we presented a method to restore the TOA reflectance spectra in the penumbra and antumbra during solar eclipses, by computing the eclipse obscuration fraction as a function of location and time, fully taking into account wavelength-dependent solar limb darkening. We applied the correction to UV TOA reflectances measured by TROPOMI in the penumbra during the annular solar eclipses on 26 December 2019 and 21 June 2020. We showed that the dark shade in the TOA reflectance maps for 380 nm, at the location of the Moon shadow, disappeared after the correction. For the eclipse on 26 December, we compared the calculated obscuration fractions to the estimated obscuration fractions at the ground pixels using measurements of the previous orbit and found a close agreement. Not taking into account solar limb darkening, however, resulted on 26 December 2019 in a mean underestimation of the obscuration fraction f_o at 380 nm of 0.053 at disk center separations $X < 0.5$, and a maximum underestimation of 0.06.

With the restored TOA reflectance spectra, we computed a corrected version of the TROPOMI AAI on 26 December 2019 and 21 June 2020. For both eclipses, the AAI anomaly in the shadow of the Moon disappeared after the correction. For the eclipse on 26 December 2019, we showed that not taking into account solar limb darkening, however, could still result in an AAI overestimation of 6.7 points. We conclude that solar limb darkening cannot be neglected if the artificial Moon shadow signatures are to be removed.

For the eclipse on 21 June 2020, we found an AAI increase of ~1.5, as compared to its surrounding regions, in the restored TROPOMI product in Northwest China. We verified this AAI increase with AAI measurements by the GOME-2C satellite instrument on the same day but outside the Moon shadow. We attribute this restored AAI feature to the surface of the Taklamakan Desert and, possibly, desert dust aerosol. We did not find an indication of absorbing aerosol changes in the Moon shadow (e.g. which are spatially correlated with the recent eclipse ground track). We conclude that the restored AAI product successfully can be used to detect real AAI rising phenomena.

THE IMPACT OF **SOLAR ECLIPSES** ON **CLOUDS** AS MEASURED BY SEVIRI

In this thesis, we have used satellite cloud measurements by SEVIRI during three solar eclipses over Africa between 2005 and 2016 that have been corrected for the partial lunar shadow together with large-eddy simulations to analyze the eclipse-induced cloud evolution. Our corrected data revealed that, over cooling land surfaces, shallow cumulus clouds start to disappear at very small solar obscurations (~15%). Our simulations explain that the cloud response was delayed and was initiated at even smaller solar obscurations. Over ocean, we did not find a change in shallow cumulus cloud cover, as the ocean surface does not cool down so rapidly during a solar eclipse. We have demonstrated that neglecting the disappearance of clouds over land during a solar eclipse could lead to a considerable overestimation of the eclipse-related reduction of net incoming solar radiation.

THE DETECTION OF **CLOUD SHADOWS** IN TROPOMI DATA

Before the impact of cloud shadows on air quality can be quantified, a cloud shadow detection algorithm had to be developed in order to analyze large data sets. In this thesis, we have demonstrated DARCLOS, a cloud shadow detection algorithm for TROPOMI. DARCLOS provides a potential cloud shadow flag (PCSF) based on geometric variables stored in TROPOMI Level 2 data, and an actual cloud shadow flag (ACSF) based on the contrast of the measured scene reflectivity with the climatological surface reflectivity. The PCSF and ACSF are validated by visual inspection of true color images made by the VIIRS-NPP instrument, for in total six cases. We found that the cloud motion during the measurement time difference between TROPOMI and VIIRS complicates this validation strategy. We showed that a cloud movement correction using the wind speed vectors at the cloud height significantly improves the validation results.

At UV wavelengths, we have found cloud shadow signatures at different locations than determined with the ACSF, potentially indicating a wavelength dependence of cloud shadow extents. Because TROPOMI's air quality products are retrieved at specific wavelengths or wavelength ranges, DARCLOS also outputs the spectral cloud shadow flag (SCSF), which is a wavelength dependent alternative for the ACSF. Such a cloud shadow

detection at the precise wavelengths of TROPOMI's air quality products is unique for DARCLOS and cannot be done with data from an imager.

We conclude that the PCSF can be used to remove cloud shadow contaminated pixels from TROPOMI Level 2 UVIS data, and that the ACSF can be used to select pixels for further analysis of cloud shadow effects. If both cloud and cloud shadow effects are to be removed, the PCSF and CF can be used together. Also, the ACSF can be used to demonstrate and/or count the true shadows that would be observed from space by the human eye.

THE IMPACT OF **CLOUD SHADOWS** ON THE **AAI** AS MEASURED BY TROPOMI

In this thesis, we have used DARCLOS to quantify the cloud shadow effect on the TROPOMI AAI. We selected shadow pixels and shadow-free neighbour pixels over Europe during 8 months. In addition, we simulated the measured cloud shadow impact ton the AAI with our newly developed 3D radiative transfer algorithm MONKI. We measure and simulate that cloud shadows are in principle always more blue than cloud- and shadow-free regions. The shadow pixels are also darker than the non-shadow pixels, and consequently, the traditional AAI retrieval by itself already (partly) corrects for cloud shadows via the retrieved scene albedo. If the traditional AAI retrieval would not correct for this enhanced blueness, strong cloud shadow signatures could have been expected in the AAI.

We have shown that, for individual cases in the measurements and in the simulations, the blueness of the clouds shadows is not always perfectly compensated for by the lower scene albedo in the AAI retrieval. This results in second-order cloud shadow effects which sometimes yield lower, and sometimes higher, AAI than in the cloud- and shadow-free regions. In the observations, we found weak positive and negative relations of those second order cloud shadow effects to the geometric air mass factor and surface albedo, respectively. Our simulations indeed demonstrated that positive AAI cloud shadow signatures can mostly be related to high thick clouds with small geometric air mass factor above dark surfaces, while negative AAI cloud shadow signatures should be most prominent near thick clouds above bright surfaces.

6.2. OUTLOOK

THE IMPACT OF **SOLAR ECLIPSES** ON THE **AAI** AS MEASURED BY TROPOMI

We have demonstrated that the restored TOA reflectances during solar eclipses can be applied successfully to derive the AAI product. Since the method we developed has taken into account the wavelength dependence of the solar limb darkening, the method is applicable to the measured reflectances or radiances at all TROPOMI wavelengths. A solar eclipse flag is already included in the TROPOMI level 1B product. With the addition of the obscuration fraction in the level 1B product, all TROPOMI level 2 products will benefit from the restored TOA reflectances or radiances. In principle, the method can also be applied to GOME-2, Sentinel-4/5 and other satellite instruments which measure the back-scattered and reflected solar radiation.

THE IMPACT OF **SOLAR ECLIPSES** ON **CLOUDS** AS MEASURED BY SEVIRI

The observed response of shallow cumulus clouds to a solar eclipse at already ~15% obscuration, initiated at even smaller obscurations due to the parcel travel time, reveals the

potential direct consequence of deploying sunlight intercepting material in the stratosphere or in space. We note that the duration of the cloud response is expected to depend on the speed and magnitude of the local obscuration variations, as the altered difference between the near-surface air and surface temperature, which causes the response, may possibly restore after a certain period. Diminished shallow cumulus clouds would partly oppose the objective of solar geoengineering which is to decrease the amount of net incoming solar radiation, and could prevent the growth into deeper convective and possibly precipitating clouds. Our findings of the high cloud sensitivity to solar radiation variations should spur cloud model simulations of the direct consequences of sunlight-intercepting geoengineering proposals, for which our results serve as a unique benchmark.

THE DETECTION OF **CLOUD SHADOWS** IN TROPOMI DATA

At UV wavelengths, we have found indications of the wavelength dependence of cloud shadow signatures, and a spectrally dependent cloud shadow flag such as the SCSF could possibly be more suitable when selecting shadow pixels in air quality products retrieved at UV wavelengths. Further research is needed to explain and validate the spectral dependence of these cloud shadow signatures. The detection of shadows with the ACSF and SCSF allows a user to perform this analysis.

THE IMPACT OF **CLOUD SHADOWS** ON THE **AAI** AS MEASURED BY TROPOMI

Our simulations thus suggest that a potential correction of the second order cloud shadow effects on the AAI should depend on cloud height, optical thickness, surface albedo and geometric air mass factor. However, the height and thickness of the clouds responsible for the measured cloud shadows are uncertain. That is because, although the cloud height is a TROPOMI product, the cloud height product has a limited accuracy[1] and the optical thickness and vertical extent of the clouds are not retrieved. Moreover, the clouds responsible for certain cloud shadows are difficult to determine in the observations. The responsible clouds are not an output of DARCLOS, as DARCLOS uses spectral tests to determine the cloud shadow flags in the final step of its algorithm. Additionally, the accuracy of a 'reverse calculation' of the responsible cloud (height) would never be better than the ~4 km spatial resolution of TROPOMI in the nadir viewing direction, and again the cloud optical thickness and vertical extent would be unknown. Hence, we conclude that a reliable correction method for the second order cloud shadow effects on the TROPOMI AAI would be complicated. Moreover, because of the automatic cancellation of the cloud shadow effects to the first order, such a correction method may not be needed.

For this study, we have developed the 3D radiative transfer code MONKI which successfully simulated the effect of cloud shadows on the TROPOMI AAI. MONKI fully takes into account the polarization of light for all orders of scattering, and can store the vertical profiles of the altitude dependent reflected light contribution at TOA, for the total, singly, and multiply scattered light. In future research, MONKI can be used to find explanations of more cloud effects on sensitive retrieval algorithms, such as the AAI algorithm, in which polarization and geometry play on important role. For example, the

[1] The cloud height obtained with FRESCO is in fact the cloud centroid height.

positive AAI increases at the bright side of clouds that are found in both our simulations and previous observations, can be further analyzed using the MONKI model. MONKI can in principle also be used to simulate the TOA reflectances of other planets, such as Mars, Venus, and exoplanets, if the input model atmosphers and surfaces are provided.

ACKNOWLEDGEMENTS

First and foremost, I would like to express my deepest gratitude to my daily supervisor, Dr. Ping Wang from the R&D Satellite Observations department at KNMI. For four years, we had weekly progress meetings where I could freely discuss my ideas in a safe and constructive environment. Ping was always generous with her time, an attentive listener, and asked exactly the right questions. She consistently looked out for my workload and helped me make strategic decisions throughout my PhD journey. I am immensely thankful for her guidance, for sharing her knowledge and wisdom, and for her patience and trust, especially in allowing me to pursue ideas that were not part of the original plan. These opportunities ultimately led to the discoveries that form the core of this thesis. I hope we will continue to collaborate for many years to come.

I would also like to thank my promotor, Prof. dr. Pier Siebesma, for his supervision of the PhD process and the administrative support that made this work possible. I greatly appreciated his enthusiasm for the subject, as well as his critical perspective when I presented him with yet another one of my unconventional ideas.

My sincere thanks go to my co-promotor, Dr. Stephan de Roode, for the enjoyable and productive collaboration on our project concerning the impact of solar eclipses on clouds. Our insightful discussions, often late in the day, sometimes stretching into the evening, were always inspiring. I am especially grateful for the countless DALES simulations he ran. Stephan was always willing to launch a new simulation whenever we had a new idea, enabling us to perform robust research and publish a solid paper.

I would also like to thank Dr. Jan-Fokke Meirink and Job Wiltink for their support with the satellite observations of clouds during solar eclipses. Their hard work, responsiveness and flexibility made for a very smooth and enjoyable collaboration leading to robust results.

Special thanks to Dr. Piet Stammes for sharing his brilliant ideas. It was Piet who initially proposed studying solar eclipses as a way to understand cloud shadows. It was a privilege to exchange thoughts with a radiative transfer expert like Piet. I also greatly appreciated his keen eye for detail, both in providing precise feedback on manuscripts and in spotting language errors.

I am grateful to Dr. Dave Donovan for sharing his insights into Monte Carlo radiative transfer modeling using the EarthCARE Simulator (ECSIM), and to Dr. Gijsbert Tilstra for our stimulating discussions and valuable feedback on my work. Collaborating with Gijs on integrating the cloud shadow flag into the TROPOMI DLER algorithm was a rewarding experience.

I also wish to thank the members of my PhD defense committee: Dr. Daphne Stam, Dr. Folkert Boersma, Dr. ir. Chiel van Heerwaarden, Prof. dr. ir. Herman Russchenberg, Dr. Stephan de Roode, Dr. Ping Wang, and Prof. ir. Pier Siebesma, for reviewing my thesis and being part of the defense committee.

Last but certainly not least, I want to thank my parents for their immense support throughout this PhD journey. A PhD comes with its share of highs and lows, and they were always there to listen, encourage, and offer their patience, wisdom, and understanding, especially during the more stressful times. I truly would not be where I am today without them.

A

APPENDIX OF CHAPTER 2

A.1. ECLIPSE GEOMETRY AT THE GROUND PIXEL

In this appendix, we provide the method to compute the apparent lunar disk radius r_m and separation between the lunar and solar disk X as experienced at the location of a ground pixel, from the geodetic coordinates (δ, ϑ, h) and measurement time t_1 of that ground pixel.

The latitude δ is defined w.r.t. the Earth's equatorial plane and the longitude ϑ is defined w.r.t. the Greenwich meridian. Height h is defined w.r.t. the Earth reference ellipsoid. The transformation of the ground pixel's geodetic coordinates (δ, ϑ, h) to Cartesian coordinates in the geocentric Earth-fixed reference plane (x_c, y_c, z_c) is given by

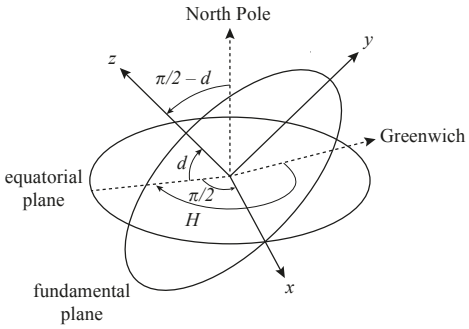

Figure A.1: Transformation of the Earth-fixed coordinates to coordinates in the fundamental reference frame. Take the Earth-fixed x-axis pointed at Greenwich and rotate it around the z-axis (toward the North Pole) to $-(H-\pi/2)$. Then, rotate around the new x-axis by $\pi/2-d$ to make the new z-axis parallel to the shadow axis (cf. Fig. 2.8).

A

$$x_c = (N_\delta + h)\cos\delta\cos\vartheta, \tag{A.1}$$
$$y_c = (N_\delta + h)\cos\delta\sin\vartheta, \tag{A.2}$$
$$z_c = ((1-e^2)N_\delta + h)\sin\delta, \tag{A.3}$$

with

$$e = \sqrt{2f - f^2}, \tag{A.4}$$
$$N_\delta = \frac{a}{\sqrt{1 - e^2\sin^2\delta}}, \tag{A.5}$$

where $a = 6378137$ m is the equatorial radius of the Earth and $f = 1/298.257223563$ is the flattening parameter of the Earth reference ellipsoid.

The fundamental reference frame is a geocentric Cartesian coordinate system defined w.r.t. the shadow axis, which is the axis through the centers of the Moon and the Sun, as illustrated in Fig. 2.8. The z-axis of the fundamental reference frame originates in the Earth's center of mass and is parallel to the shadow axis. The x-axis is located in the equatorial plane and is positive toward the East. The y-axis completes the positive right-handed Coordinate system and is positive toward the North. The xy-plane of the fundamental reference frame ($z = 0$) is called the fundamental plane.

The orientation of the fundamental reference frame with respect to the Earth-fixed reference frame is defined by the shadow axis declination angle d and the shadow axis Greenwich hour angle H (see Fig. A.1). The transformation of the Cartesian coordinates in the Earth-fixed reference plane to the Cartesian coordinates in the fundamental reference frame is computed as [138]:

$$x_f = \frac{1}{a}\left(x_c\sin H + y_c\cos H\right), \tag{A.6}$$
$$y_f = \frac{1}{a}\left(-x_c\sin d\cos H + y_c\sin d\sin H + z_c\cos d\right), \tag{A.7}$$
$$z_f = \frac{1}{a}\left(x_c\cos d\cos H - y_c\cos d\sin H + z_c\sin d\right). \tag{A.8}$$

The declination d is one of the Besselian elements, published by NASA[1] [39]. A Besselian element is published as coefficients of a 3$^{\text{rd}}$ order polynomial B of time:

$$B = \sum_{N=0}^{3} c_n t^n, \tag{A.9}$$

where time t in Terrestrial Dynamical Time (TDT) is the measurement time t_1 in decimal hours with respect to a reference time t_0 commonly chosen close to the instant of greatest eclipse. Because t_1 by TROPOMI is stored as UTC, t is computed as

[1] The Besselian elements data can be retrieved from https://eclipse.gsfc.nasa.gov/SEcat5/SE2001-2100.html, by clicking on the gamma value.

$$t = t_1 + \frac{\Delta T}{3600} - t_0, \tag{A.10}$$

where ΔT = TDT − UTC is in seconds. The values of ΔT and t_0 are published together with the Besselian elements for each eclipse. Another Besselian elements is the ephemeride hour angle M. Angle H is computed as [101]

$$H = M - \frac{360}{23 \times 3600 + 56 \times 60 + 4.098904} \Delta T, \tag{A.11}$$

where H and M are in degrees. Note that all angular Besselian elements are published in degrees, and all dimensional Besselian elements are published per Earth's equatorial radius, a.

The Besselian elements l_1 and l_2 are the radii of the penumbral and (ant)umbral shadow circle on the fundamental plane, respectively, as illustrated in Fig. A.2. The vertex angles f_1 and f_2 of the penumbral and (ant)umbral shadow, respectively, are also published as Besellian elements. Note that l_2 is positive for annular eclipses and negative for total eclipses, while l_1 is always positive.

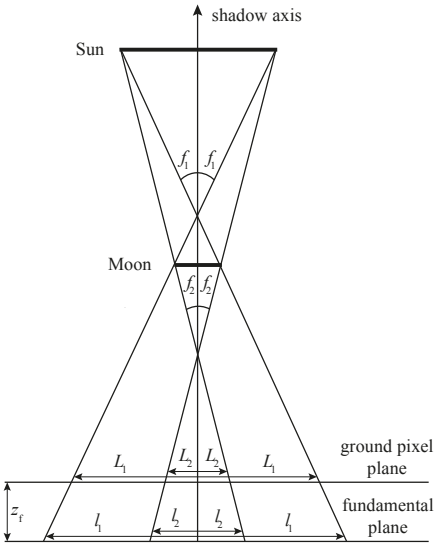

Figure A.2: Definition of l_1, l_2, L_1, L_2, f_1 and f_2.

The coordinates of the shadow axis in the fundamental reference frame, x_{sdw}, y_{sdw} and z_{sdw} are also published as Besselian elements. The distance m from the ground pixel to the shadow axis, parallel to the fundamental plane, is then

$$m = \sqrt{(x_{\mathrm{f}} - x_{\mathrm{sdw}})^2 + (y_{\mathrm{f}} - y_{\mathrm{sdw}})^2}. \tag{A.12}$$

A

The plane parallel to the fundamental plane through the ground pixel is the so-called ground pixel plane. The radii of the penumbra and the (ant)umbra on the ground pixel plane, L_1 and L_2 respectively, can readily be computed by

$$L_1 = l_1 - z_f \tan(f_1), \tag{A.13}$$

$$L_2 = l_2 - z_f \tan(f_2). \tag{A.14}$$

If $z_f > 0$, a ground pixel can be eclipsed. One can compute whether a ground pixel is eclipsed and what shadow type is experienced by comparing m to L_1 and L_2. Quantities r_m and X can be expressed in terms of L_1, L_2 and m, as

$$r_m = \frac{L_1 - L_2}{L_1 + L_2}, \tag{A.15}$$

$$X = \frac{2m}{L_1 + L_2}. \tag{A.16}$$

For the derivations of Eq. A.15 and A.16, we refer to Sect. 8.3623 of Seidelmann [138].

A.2. ERROR PROPAGATION

In this appendix, we show the effect of the solar irradiance correction on the precision of the AAI. It should be recalled from Eq. 2.3 that the corrected measured TOA reflectance, $R^{\text{int}}(\lambda)$, is computed from the measured TOA reflectance by TROPOMI, $R^{\text{meas}}(\lambda)$, and the calculated obscuration fraction, $f_o(\lambda)$. We assume that the noise of $R^{\text{meas}}(\lambda)$ and the noise of $f_o(\lambda)$ are normally distributed with standard deviations $\sigma_{R^{\text{meas}}(\lambda)}$ and $\sigma_{f_o(\lambda)}$, respectively. Also, we assume that the noise of $R^{\text{meas}}(\lambda)$ is not correlated with the noise of $f_o(\lambda)$. Then, we may compute the precision of $R^{\text{int}}(\lambda)$ as follows:

$$\sigma_{R^{\text{int}}} = R^{\text{int}} \cdot \sqrt{\left(\frac{\sigma_{R^{\text{meas}}}}{R^{\text{meas}}}\right)^2 + \left(\frac{\sigma_{f_o}}{1 - f_o}\right)^2}. \tag{A.17}$$

$\sigma_{R^{\text{meas}}(\lambda)}$ is provided in the current operational TROPOMI L2 AAI product for $\lambda = 340$ nm and $\lambda = 380$ nm. $\sigma_{f_o(\lambda)}$ depends on the precision of the geometrical eclipse prediction, i.e. α in Eq. 2.9, and the precision of the solar limb darkening function, Γ. The geometrical eclipse prediction was verified with the predictions by NASA (see Sect. 2.2.4). The largest source of uncertainty for α in the present era (1800 CE to present) is the Moon's surface topography, which causes the lunar disk circumference to deviate from a perfect circle.[2] Our and NASA's eclipse predictions do not include these effects of mountains and valleys along the edge of the Moon, which may shift the limits of the eclipse path north or south by ~ 1 to 3 kilometers, and may change the eclipse duration by ~ 1 to 3 seconds.[3] For the solar eclipse of 21 June 2020, we added a time increment of 3 seconds to estimate the effect of a local eclipse timing error due to the Moon's topography on f_o and the AAI. At the ground pixels for which $f_o > 0$, the average absolute changes in f_o and

[2] See https://eclipse.gsfc.nasa.gov/SEhelp/limb.html, visited on 27 March 2021.

[3] See https://eclipse.gsfc.nasa.gov/SEpath/SEpath2001/SE2020Jun21Apath.html, visited on 27 March 2021.

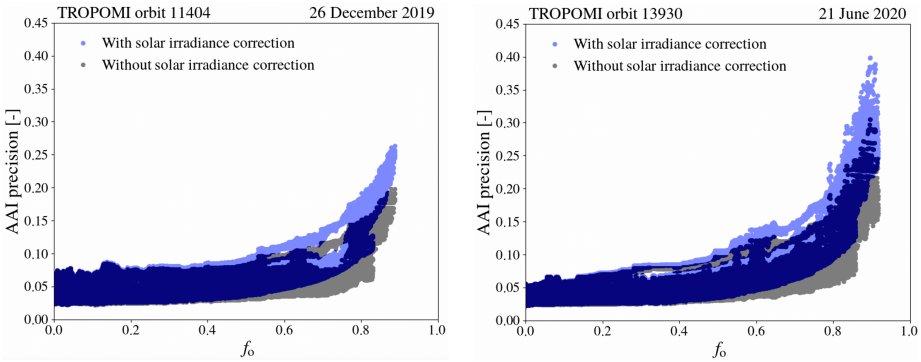

Figure A.3: Precision of the AAI in the eclipsed TROPOMI orbits on 26 December 2019 (left) and 21 June 2020 (right) as a function of obscuration fraction f_o at 380 nm, with solar irradiance correction such that both $\sigma_{R^{\text{meas}}}$ and σ_Γ are propagated (semi-transparent blue dots) and without solar irradiance correction such that only $\sigma_{R^{\text{meas}}}$ is propagated (semi-transparent black dots).

the AAI were 0.00049 and 0.00588, respectively. Hence, in what follows in this appendix, we assume that there is no error in α.

Pierce and Slaughter [118] provide the probable error, Pe, of the estimated solar limb darkening function $\Gamma(\lambda, r)$ for the tabulated set of λ's, which is independent of r. We assume that the measurement noise of Γ was normally distributed with standard deviation $\sigma_\Gamma(\lambda) = Pe(\lambda)/0.6745$. We also assume that the noise of Γ was uncorrelated in r-space. We performed a Monte Carlo error propagation simulation to estimate the error of the obscuration fraction, $\sigma_{f_o}(\lambda)$. That is, to each $\Gamma(\lambda, r)$ at $\lambda = 340$ nm and 380 nm, we added 100 times a randomly generated normally distributed error $\sigma_\Gamma(\lambda)$, repeated the computation of f_o (Eq. 2.9) for each sample, and computed σ_{f_o} as the standard deviation of f_o. The precision of the AAI can be computed as follows:

$$\sigma_{\text{AAI}} = 100\sqrt{\left(\frac{\sigma_{R_{340}^{\text{model}}}}{\ln(10)R_{340}^{\text{model}}}\right)^2 + \left(\frac{\sigma_{R_{340}^{\text{int}}}}{\ln(10)R_{340}^{\text{int}}}\right)^2}. \tag{A.18}$$

The expression for the precision of the modeled reflectance at 340 nm, $\sigma_{R_{340}^{\text{model}}}$, as a function of $\sigma_{R_{380}^{\text{int}}}$, can readily be derived by analytically solving $\sigma_{R_{340}^{\text{model}}} = \sigma_{A_s}|\partial R_{340}^{\text{model}}/\partial A_s|$ and $\sigma_{A_s} = \sigma_{R_{380}^{\text{int}}}|\partial A_s/\partial R_{380}^{\text{int}}|$. Possible calibration (offset) errors of TROPOMI and model uncertainties of DAK are excluded from this analysis.

Figure A.3 shows σ_{AAI} at the ground pixels of the eclipsed TROPOMI orbits during the solar eclipses that were discussed in this paper. The results are presented as a function of obscuration fraction f_o at 380 nm, with solar irradiance correction applied (semi-transparent blue dots) and without solar irradiance correction applied (semi-transparent black dots). In the absence of a solar eclipse ($f_o = 0$), σ_{AAI} for with and without solar irradiance correction is identical, since $R^{\text{int}} = R^{\text{meas}}$ and $\sigma_{R^{\text{int}}} = \sigma_{R^{\text{meas}}}$ (see Eq. A.17). In the presence of a solar eclipse, σ_{AAI} increases with increasing f_o. When no solar irradiance correction is applied, again $R^{\text{int}} = R^{\text{meas}}$, but R^{int} is decreased at both 340 and 380

nm in the Moon shadow, which increases σ_{AAI} through the division by R_{340}^{int} and through the increased $\sigma_{A_{\mathrm{s}}}$ and $\sigma_{R_{340}^{\mathrm{model}}}$ (Eq. A.18). When a solar irradiance correction is applied, $R^{\mathrm{int}} > R^{\mathrm{meas}}$ and is not decreased anymore by the eclipse. However, the additional solar limb darkening noise term in Eq. A.17 increases σ_{AAI}, which is most significant at relatively large f_{o} resulting from the division by $1 - f_{\mathrm{o}}$. The maximum AAI precisions, after a solar irradiance correction in the TROPOMI orbits on 26 December 2019 and 21 June 2016, are 0.26 and 0.40 respectively. The precisions in the uncorrected case are respectively ~ 0.05 and ~ 0.10 better, but the uncorrected AAI value itself is off by many points as shown in for example Fig. 2.17.

BIBLIOGRAPHY

[1] Steven A. Ackerman et al. “Discriminating clear sky from clouds with MODIS”. In: *Journal of Geophysical Research* 103.D24 (Dec. 1998), pp. 32, 141–32, 157. DOI: 10.1029/1998JD200032.

[2] Cristen Adams et al. “Ozone and NO2 variations measured during the 1 August 2008 solar eclipse above Eureka, Canada with a UV-visible spectrometer”. In: *Journal of Geophysical Research: Atmospheres* 115.D19 (2010). DOI: https://doi.org/10.1029/2010JD014424. eprint: https://agupubs.onlinelibrary.wiley.com/doi/pdf/10.1029/2010JD014424. URL: https://agupubs.onlinelibrary.wiley.com/doi/abs/10.1029/2010JD014424.

[3] K. R. M. Adeline et al. “Shadow detection in very high spatial resolution aerial images: A comparative study”. In: *ISPRS Journal of Photogrammetry and Remote Sensing* 80 (June 2013), pp. 21–38. DOI: 10.1016/j.isprsjprs.2013.02.003.

[4] G. P. Anderson. *AFGL atmospheric constituent profiles (0-120km)*. 1986.

[5] Jay Anderson. “Meteorological changes during a solar eclipse”. In: *Weather* 54.7 (July 1999), pp. 207–215. DOI: 10.1002/j.1477-8696.1999.tb06465.x.

[6] Roger Angel. “Feasibility of cooling the Earth with a cloud of small spacecraft near the inner Lagrange point (L1)”. In: *Proceedings of the National Academy of Science* 103.46 (Nov. 2006), pp. 17184–17189. DOI: 10.1073/pnas.0608163103.

[7] K. L. Aplin, C. J. Scott, and S. L. Gray. “Atmospheric changes from solar eclipses”. In: *Philosophical Transactions of the Royal Society of London Series A* 374.2077, 20150217 (Sept. 2016), p. 20150217. DOI: 10.1098/rsta.2015.0217. arXiv: 1603.02987.

[8] Prasanta Kumar Bal et al. “Effects of global warming and solar geoengineering on precipitation seasonality”. In: *Environmental Research Letters* 14.3, 034011 (Mar. 2019), p. 034011. DOI: 10.1088/1748-9326/aafc7d.

[9] A. M. Bass and R. J. Paur. “The ultraviolet cross-sections of ozone. I. The measurements. II - Results and temperature dependence”. In: *Atmospheric ozone; Proceedings of the Quadrennial*. Ed. by C. S. Zerefos and A. Ghazi. Jan. 1985, pp. 606–616.

[10] Steffen Beirle et al. “Pinpointing nitrogen oxide emissions from space”. In: *Science Advances* 5.11 (Nov. 2019), eaax9800. DOI: 10.1126/sciadv.aax9800.

[11] Nikos Benas et al. “The MSG-SEVIRI-based cloud property data record CLAAS-2”. In: *Earth System Science Data* 9.2 (July 2017), pp. 415–434. DOI: 10.5194/essd-9-415-2017.

A

[12] Germar Bernhard and Boyan Petkov. “Measurements of spectral irradiance during the solar eclipse of 21 August 2017: reassessment of the effect of solar limb darkening and of changes in total ozone”. In: *Atmospheric Chemistry & Physics* 19.7 (Apr. 2019), pp. 4703–4719. DOI: 10.5194/acp-19-4703-2019.

[13] S. Bley and H. Deneke. “A threshold-based cloud mask for the high-resolution visible channel of Meteosat Second Generation SEVIRI”. In: *Atmospheric Measurement Techniques* 6 (10 Oct. 2013), pp. 2713–2723. DOI: 10.5194/amt-6-2713-2013.

[14] Peter N. Blossey et al. “Marine low cloud sensitivity to an idealized climate change: The CGILS LES intercomparison”. In: *Journal of Advances in Modeling Earth Systems* 5.2 (June 2013), pp. 234–258. DOI: 10.1002/jame.20025.

[15] Ping Bo, Su Fenzhen, and Meng Yunshan. “A Cloud and Cloud Shadow Detection Method Based on Fuzzy c-Means Algorithm”. In: *IEEE Journal of Selected Topics in Applied Earth Observations and Remote Sensing* 13 (Jan. 2020), pp. 1714–1727. DOI: 10.1109/JSTARS.2020.2987844.

[16] Rumen D. Bojkov. “The ozone variations during the solar eclipse of 20 May 1966”. In: *Tellus* 20.3 (1968), pp. 417–421. DOI: 10.3402/tellusa.v20i3.10020. eprint: https://doi.org/10.3402/tellusa.v20i3.10020. URL: https://doi.org/10.3402/tellusa.v20i3.10020.

[17] H. Bovensmann et al. “SCIAMACHY: Mission Objectives and Measurement Modes”. In: *Journal of Atmospheric Sciences* 56.2 (Jan. 1999), pp. 127–150. DOI: 10.1175/1520-0469(1999)056\textless{}0127:SMOAMM\textgreater{}2.0.CO;2.

[18] Michael S. Buban et al. “Observations and Numerical Simulation of the Effects of the 21 August 2017 North American Total Solar Eclipse on Surface Conditions and Atmospheric Boundary-Layer Evolution”. In: *Boundary-Layer Meteorology* 171.2 (May 2019), pp. 257–270. DOI: 10.1007/s10546-018-00421-4.

[19] John P. Burrows et al. “The Global Ozone Monitoring Experiment (GOME): Mission Concept and First Scientific Results.” In: *Journal of Atmospheric Sciences* 56.2 (Jan. 1999), pp. 151–175. DOI: 10.1175/1520-0469(1999)056\textless{}0151:TGOMEG\textgreater{}2.0.CO;2.

[20] D. S. Candra, S. Phinn, and P. Scarth. “Cloud and Cloud Shadow Masking Using Multi-Temporal Cloud Masking Algorithm in Tropical Environmental”. In: *ISPRS - International Archives of the Photogrammetry, Remote Sensing and Spatial Information Sciences* 49B2 (June 2016), pp. 95–100. DOI: 10.5194/isprs-archives-XLI-B2-95-2016.

[21] Danang Surya Candra, Stuart Phinn, and Peter Scarth. “Automated Cloud and Cloud-Shadow Masking for Landsat 8 Using Multitemporal Images in a Variety of Environments”. In: *Remote Sensing* 11.17 (Sept. 2019), p. 2060. DOI: 10.3390/rs11172060.

[22] D. Chakrabarty et al. “Further evidence of total ozone variation during the solar eclipse of 1995”. In: *Journal of Geophysical Research* 106 (Feb. 2001), pp. 3213–3218. DOI: 10.1029/2000JD900522.

[23] D. K. Chakrabarty, N. C. Shah, and K. V. Pandya. "Fluctuation in ozone column over Ahmedabad during the solar eclipse of 24 October 1995". In: *Geophysical Research Letters* 24.23 (1997), pp. 3001–3003. DOI: 10.1029/97GL03016. eprint: https://agupubs.onlinelibrary.wiley.com/doi/pdf/10.1029/97GL03016. URL: https://agupubs.onlinelibrary.wiley.com/doi/abs/10.1029/97GL03016.

[24] Subrahmanyan Chandrasekhar. *Radiative transfer*. New York: Dover Publications, 1960.

[25] William Chauvenet. *A manual of spherical and practical astronomy*. J.B. Lippincott, Philadelphia, 1863.

[26] L. P. Chitta, H. N. Smitha, and S. K. Solanki. "Solar Photosphere". In: Oxford Research Encyclopedia of Physics, 2020, 1, p. 1. DOI: 10.1093/acrefore/9780190871994.013.26.

[27] P. A. Clark. "Numerical simulations of the impact of the 20 March 2015 eclipse on UK weather". In: *Philosophical Transactions of the Royal Society of London Series A* 374.2077, 20150218 (Sept. 2016), p. 20150218. DOI: 10.1098/rsta.2015.0218.

[28] *Clouds and Climate: Climate Science's Greatest Challenge*. Cambridge University Press, 2020. DOI: 10.1017/9781107447738.

[29] Paul J. Crutzen. "Albedo Enhancement by Stratospheric Sulfur Injections: A Contribution to Resolve a Policy Dilemma?" In: *Climatic Change* 77.3-4 (Sept. 2006), pp. 211–220. DOI: 10.1007/s10584-006-9101-y.

[30] M. de Graaf et al. "Absorbing Aerosol Index: Sensitivity analysis, application to GOME and comparison with TOMS". In: *Journal of Geophysical Research (Atmospheres)* 110.D1, D01201 (Jan. 2005), p. D01201. DOI: 10.1029/2004JD005178.

[31] Martin de Graaf. *TROPOMI ATBD of the Aerosol Optical Thickness. Doc. No. S5P-KNMI-L2-0033-RP, Issue 3.0.0, Royal Netherlands Meteorological Institute (KNMI)*. https://data-portal.s5p-pal.com/product-docs/aot/s5p_aot_atbd_v3.0.0_2022-02-10_signed.pdf. [Online; accessed 18-January-2024]. 2022.

[32] W. A. de Rooij and C. C. A. H. van der Stap. "Expansion of Mie scattering matrices in generalized spherical functions". In: *Astronomy and Astrophysics* 131.2 (Feb. 1984), pp. 237–248.

[33] H. M. Deneke and R. A. Roebeling. "Downscaling of METEOSAT SEVIRI 0.6 and 0.8 μm channel radiances utilizing the high-resolution visible channel". In: *Atmospheric Chemistry and Physics* 10 (20 2010), pp. 9761–9772. ISSN: 16807316. DOI: 10.5194/acp-10-9761-2010.

[34] Hartwig Deneke et al. "Increasing the spatial resolution of cloud property retrievals from Meteosat SEVIRI by use of its high-resolution visible channel: Implementation and examples". In: *Atmospheric Measurement Techniques* 14 (7 July 2021), pp. 5107–5126. ISSN: 18678548. DOI: 10.5194/amt-14-5107-2021.

A

[35] Tim Deutschmann et al. “The Monte Carlo atmospheric radiative transfer model McArtim: Introduction and validation of Jacobians and 3D features”. In: *Journal of Quantitative Spectroscopy and Radiative Transfer* 112 (Apr. 2011), pp. 1119–1137. DOI: 10.1016/j.jqsrt.2010.12.009.

[36] James T. Early. “Space-based solar shield to offset greenhouse effect”. In: *Journal of the British Interplanetary Society* 42 (Dec. 1989), pp. 567–569.

[37] F. D. Eaton et al. “Solar Eclipse Effects Observed in the Planetary Boundary Layer Over a Desert”. In: *Boundary-Layer Meteorology* 83.2 (Jan. 1997), pp. 331–346. DOI: 10.1023/A:1000219210055.

[38] C. Emde and B. Mayer. “Simulation of solar radiation during a total eclipse: a challenge for radiative transfer”. In: *Atmospheric Chemistry & Physics* 7.9 (May 2007), pp. 2259–2270.

[39] Fred Espenak and Jean Meeus. *Five millennium canon of solar eclipses : -1999 to +3000 (2000 BCE to 3000 CE)*. NASA Technical Publication TP-2006-214141, 2006.

[40] Alberto Fernández et al. *Learning from Imbalanced Data Sets*. Cham, Switzerland: Springer International Publishing, Springer Nature Switzerland AG, Jan. 2018. ISBN: 978-3-319-98073-7. DOI: 10.1007/978-3-319-98074-4.

[41] D. Founda et al. “The effect of the total solar eclipse of 29 March 2006 on meteorological variables in Greece”. In: *Atmospheric Chemistry & Physics* 7.21 (Nov. 2007), pp. 5543–5553. DOI: 10.5194/acp-7-5543-2007.

[42] Sandra C. Freitas et al. “Quantifying the Uncertainty of Land Surface Temperature Retrievals From SEVIRI/Meteosat”. In: *IEEE Transactions on Geoscience and Remote Sensing* 48.1 (Jan. 2010), pp. 523–534. DOI: 10.1109/TGRS.2009.2027697.

[43] Christer Fuglesang and María García de Herreros Miciano. “Realistic sunshade system at L_1 for global temperature control”. In: *Acta Astronautica* 186 (Sept. 2021), pp. 269–279. DOI: 10.1016/j.actaastro.2021.04.035.

[44] Stanley David Gedzelman. “Sky color near the horizon during a total solar eclipse”. In: *Appl. Opt.* 14.12 (Dec. 1975), pp. 2831–2837. DOI: 10.1364/AO.14.002831. URL: http://ao.osa.org/abstract.cfm?URI=ao-14-12-2831.

[45] Stanley David Gedzelman. “Solar eclipse skies and limb reddening”. In: *Appl. Opt.* 59.21 (July 2020), F78–F84. DOI: 10.1364/AO.396964. URL: http://ao.osa.org/abstract.cfm?URI=ao-59-21-F78.

[46] Aristeidis K. Georgoulias et al. “Detection of NO_2 pollution plumes from individual ships with the TROPOMI/S5P satellite sensor”. In: *Environmental Research Letters* 15.12, 124037 (Dec. 2020), p. 124037. DOI: 10.1088/1748-9326/abc445.

[47] Jordan J. Gerth. “Shining light on sky cover during a total solar eclipse”. In: *Journal of Applied Remote Sensing* 12, 020501 (Apr. 2018), p. 020501. DOI: 10.1117/1.JRS.12.020501.

[48] M. Gil et al. “Behavior of NO_2 and O_3 columns during the eclipse of February 26, 1998, as measured by visible spectroscopy”. In: *Journal of Geophysical Research* 105.D3 (Feb. 2000), pp. 3583–3593. DOI: 10.1029/1999JD900973.

[49] Elizabeth Good. "Satellite observations of surface temperature during the March 2015 total solar eclipse". In: *Philosophical Transactions of the Royal Society of London Series A* 374.2077, 20150219 (Sept. 2016), p. 20150219. DOI: 10.1098/rsta.2015.0219.

[50] Nicholas R. Goodwin et al. "Cloud and cloud shadow screening across Queensland, Australia: An automated method for Landsat TM/ETM+ time series". In: *Remote Sensing of Environment* 134 (July 2013), pp. 50–65. DOI: 10.1016/j.rse.2013.02.019.

[51] W. W. Grabowski et al. "Daytime convective development over land: A model intercomparison based on LBA observations". In: *Quarterly Journal of the Royal Meteorological Society* 132.615 (Jan. 2006), pp. 317–344. DOI: 10.1256/qj.04.147.

[52] P. Gross and A. Hense. "Effects of a Total Solar Eclipse on the Mesoscale Atmospheric Circulation over Europe - A Model Experiment". In: *Meteorology and Atmospheric Physics* 71 (Jan. 1999), pp. 229–242. DOI: 10.1007/s007030050057.

[53] J. F. de Haan, P. B. Bosma, and J. W. Hovenier. "The adding method for multiple scattering calculations of polarized light". In: *Astronomy & Astrophysics* 183 (Sept. 1987), pp. 371–391.

[54] Edward Hanna. "Meteorological effects of the solar eclipse of 11 August 1999". In: *Weather* 55.12 (Dec. 2000), pp. 430–446. DOI: 10.1002/j.1477-8696.2000.tb06481.x.

[55] J. E. Hansen and L. D. Travis. "Light scattering in planetary atmospheres". In: *Space Science Reviews* 16.4 (Oct. 1974), pp. 527–610. DOI: 10.1007/BF00168069.

[56] R. Giles Harrison and Edward Hanna. "The solar eclipse: a natural meteorological experiment". In: *Philosophical Transactions of the Royal Society of London Series A* 374.2077, 20150225 (Sept. 2016), p. 20150225. DOI: 10.1098/rsta.2015.0225.

[57] D. F. Heath et al. "The solar backscatter ultraviolet and total ozone mapping spectrometer (SBUV/TOMS) for Nimbus G." In: *Optical Engineering* 14 (Aug. 1975), pp. 323–331. DOI: 10.1117/12.7971839.

[58] R. H. Heiblum, I. Koren, and G. Feingold. "On the link between Amazonian forest properties and shallow cumulus cloud fields". In: *Atmospheric Chemistry & Physics* 14.12 (June 2014), pp. 6063–6074. DOI: 10.5194/acp-14-6063-2014.

[59] J. R. Herman. "The response of stratospheric constituents to a solar eclipse, sunrise, and sunset". In: *Journal of Geophysical Research: Oceans* 84.C7 (1979), pp. 3701–3710. DOI: https://doi.org/10.1029/JC084iC07p03701. eprint: https://agupubs.onlinelibrary.wiley.com/doi/pdf/10.1029/JC084iC07p03701. URL: https://agupubs.onlinelibrary.wiley.com/doi/abs/10.1029/JC084iC07p03701.

A

[60] J. R. Herman et al. “Global distribution of UV-absorbing aerosols from Nimbus 7/TOMS data”. In: *Journal of Geophysical Research: Atmospheres* 102.D14 (1997), pp. 16911–16922. DOI: 10.1029/96JD03680. eprint: https://agupubs.onlinelibrary.wiley.com/doi/pdf/10.1029/96JD03680. URL: https://agupubs.onlinelibrary.wiley.com/doi/abs/10.1029/96JD03680.

[61] H. Hersbach et al. *ERA5 hourly data on pressure levels from 1979 to present*. Copernicus Climate Change Service (C3S) Climate Data Store (CDS). (Accessed on 12-Oct-2021), Jan. 2018. DOI: 10.24381/cds.bd0915c6.

[62] Hans Hersbach et al. “The ERA5 global reanalysis”. In: *Quarterly Journal of the Royal Meteorological Society* 146.730 (2020), pp. 1999–2049. DOI: https://doi.org/10.1002/qj.3803. URL: https://rmets.onlinelibrary.wiley.com/doi/abs/10.1002/qj.3803.

[63] T. Heus et al. “Formulation of the Dutch Atmospheric Large-Eddy Simulation (DALES) and overview of its applications”. In: *Geoscientific Model Development* 3.2 (2010), pp. 415–444. DOI: 10.5194/gmd-3-415-2010. URL: https://gmd.copernicus.org/articles/3/415/2010/.

[64] Q. Hu et al. “The characterization of Taklamakan dust properties using a multi-wavelength Raman polarization lidar in Kashi, China”. In: *Atmospheric Chemistry and Physics Discussions* 2020 (2020), pp. 1–30. DOI: 10.5194/acp-2020-375. URL: https://acp.copernicus.org/preprints/acp-2020-375/.

[65] Chengquan Huang et al. “Automated masking of cloud and cloud shadow for forest change analysis using Landsat images”. In: *International Journal of Remote Sensing* 31.20 (2010), pp. 5449–5464. DOI: 10.1080/01431160903369642. eprint: https://doi.org/10.1080/01431160903369642. URL: https://doi.org/10.1080/01431160903369642.

[66] M. Hughes and Daniel Hayes. “Automated Detection of Cloud and Cloud Shadow in Single-Date Landsat Imagery Using Neural Networks and Spatial Post-Processing”. In: *Remote Sensing* 6.6 (May 2014), pp. 4907–4926. DOI: 10.3390/rs6064907.

[67] Keith D. Hutchison et al. “A Geometry-Based Approach to Identifying Cloud Shadows in the VIIRS Cloud Mask Algorithm for NPOESS”. In: *Journal of Atmospheric and Oceanic Technology* 26.7 (Jan. 2009), p. 1388. DOI: 10.1175/2009JTECHA1198.1.

[68] Michael J. Iacono et al. “Radiative forcing by long-lived greenhouse gases: Calculations with the AER radiative transfer models”. In: *Journal of Geophysical Research (Atmospheres)* 113.D13, D13103 (July 2008), p. D13103. DOI: 10.1029/2008JD009944.

[69] Elsy Ibrahim et al. “Cloud and Cloud-Shadow Detection for Applications in Mapping Small-Scale Mining in Colombia Using Sentinel-2 Imagery”. In: *Remote Sensing* 13.4 (Feb. 2021), p. 736. DOI: 10.3390/rs13040736.

[70] Peter J. Irvine et al. “An overview of the Earth system science of solar geoengineering”. In: *WIREs Climate Change* 7.6 (2016), pp. 815–833. DOI: https://doi.org/10.1002/wcc.423. URL: https://wires.onlinelibrary.wiley.com/doi/abs/10.1002/wcc.423.

[71] Peter J. Irvine et al. “Key factors governing uncertainty in the response to sunshade geoengineering from a comparison of the GeoMIP ensemble and a perturbed parameter ensemble”. In: *Journal of Geophysical Research (Atmospheres)* 119.13 (July 2014), pp. 7946–7962. DOI: 10.1002/2013JD020716.

[72] Hiren Jethva, Omar Torres, and Changwoo Ahn. “A 12-year long global record of optical depth of absorbing aerosols above the clouds derived from the OMI/OMACA algorithm”. In: *Atmospheric Measurement Techniques* 11.10 (Oct. 2018), pp. 5837–5864. DOI: 10.5194/amt-11-5837-2018.

[73] Andreas Kazantzidis et al. “Attenuation of global ultraviolet and visible irradiance over Greece during the total solar eclipse of 29 March 2006”. In: *Atmospheric Chemistry and Physics* 7 (Dec. 2007). DOI: 10.5194/acpd-7-13475-2007.

[74] David W. Keith. “Geoengineering”. In: *Nature* 409.6818 (Jan. 2001), p. 420. DOI: https://doi.org/10.1038/35053208.

[75] J. Kemp et al. “The optical polarization of the Sun, measured at a sensitivity of parts in ten million”. In: *Nature* 328 (July 1987). DOI: 10.1038/328092a0.

[76] Gaëlle Kerdraon and Emmanuel Fontaine. *Algorithm Theoretical Basis Document for the Cloud Product Processors of the NWC/GEO (GEO-CMA-v5.1 (NWC-009), GEO-CT-v4.1 (NWC-016), GEO-CTTH-v4.1 (NWC-017) and GEO-CMIC-v2.1 (NWC-021)*. Technical Report NWC/CDOP3/GEO/MFL/SCI/ATBD/Cloud, Issue 1, Rev 0.1. Météo-France / Centre d’études en Météorologie Satellitaire, Oct. 2021.

[77] Q. L. Kleipool et al. “Earth surface reflectance climatology from 3 years of OMI data”. In: *Journal of Geophysical Research: Atmospheres* 113.D18 (2008). DOI: https://doi.org/10.1029/2008JD010290. eprint: https://agupubs.onlinelibrary.wiley.com/doi/pdf/10.1029/2008JD010290. URL: https://agupubs.onlinelibrary.wiley.com/doi/abs/10.1029/2008JD010290.

[78] R. B. A. Koelemeijer et al. “A fast method for retrieval of cloud parameters using oxygen A band measurements from the Global Ozone Monitoring Experiment”. In: *Journal of Geophysical Research* 106.D4 (Feb. 2001), pp. 3475–3490. DOI: 10.1029/2000JD900657.

[79] Peter Koepke, Joachim Reuder, and Jan Schween. “Spectral variation of the solar radiation during an eclipse”. In: *Meteorologische Zeitschrift* 10.3 (May 2001), pp. 179–186. DOI: 10.1127/0941-2948/2001/0010-0179.

[80] Maurits L. Kooreman et al. “Effects of clouds on the UV Absorbing Aerosol Index from TROPOMI”. In: *Atmospheric Measurement Techniques* 13.12 (Nov. 2020), pp. 6407–6426. DOI: 10.5194/amt-13-6407-2020.

[81] Takanobu Kosugi. “Role of sunshades in space as a climate control option”. In: *Acta Astronautica* 67.1 (July 2010), pp. 241–253. DOI: 10.1016/j.actaastro.2010.02.009.

[82] Ben Kravitz et al. “Climate model response from the Geoengineering Model Intercomparison Project (GeoMIP)”. In: *Journal of Geophysical Research (Atmospheres)* 118.15 (Aug. 2013), pp. 8320–8332. DOI: 10.1002/jgrd.50646.

A

[83] Ben Kravitz et al. “Comparing different generations of idealized solar geoengineering simulations in the Geoengineering Model Intercomparison Project (GeoMIP)”. In: *Atmospheric Chemistry & Physics* 21.6 (Mar. 2021), pp. 4231–4247. DOI: 10.5194/acp-21-4231-2021.

[84] Ben Kravitz et al. “The Geoengineering Model Intercomparison Project (GeoMIP)”. In: *Atmospheric Science Letters* 12.2 (Apr. 2011), pp. 162–167. DOI: 10.1002/asl.316.

[85] Jochen Landgraf et al. “The TANGO mission: A satellite tandem to measure major sources of anthropogenic greenhouse gas emissions”. In: *EGU General Assembly Conference Abstracts*. EGU General Assembly Conference Abstracts. May 2020, 19643, p. 19643.

[86] Mark G. Lawrence. “The Relationship between Relative Humidity and the Dewpoint Temperature in Moist Air: A Simple Conversion and Applications.” In: *Bulletin of the American Meteorological Society* 86.2 (Feb. 2005), pp. 225–233. DOI: 10.1175/BAMS-86-2-225.

[87] Walker Raymond Lee et al. “High Latitude Stratospheric Aerosol Geoengineering Can Be More Effective if Injection Is Limited to Spring”. In: *Geophysical Research Letters* 48.9, e92696 (May 2021), e92696. DOI: 10.1029/2021GL092696.

[88] T. M. Lenton and N. E. Vaughan. “The radiative forcing potential of different climate geoengineering options”. In: *Atmospheric Chemistry & Physics* 9.15 (Aug. 2009), pp. 5539–5561. DOI: 10.5194/acp-9-5539-200910.5194/acpd-9-2559-2009.

[89] P. F. Levelt et al. “The Ozone Monitoring Instrument”. In: *IEEE Transactions on Geoscience and Remote Sensing* 44.5 (May 2006), pp. 1093–1101. DOI: 10.1109/TGRS.2006.872333.

[90] Sanmei Li, Donglian Sun, and Yunyue Yu. “Automatic cloud-shadow removal from flood/standing water maps using MSG/SEVIRI imagery”. In: *International Journal of Remote Sensing* 34.15 (Aug. 2013), pp. 5487–5502. DOI: 10.1080/01431161.2013.792969.

[91] Erwin Loots et al. *Algorithm theoretical basis document for the TROPOMI L01b data processor. Doc. No. S5P-KNMI-L01B-0009-SD, Issue 8.0.0, Royal Netherlands Meteorological Institute (KNMI)*. http://www.tropomi.eu/sites/default/files/files/S5P-KNMI-L01B-0009-SD-algorithm_theoretical_basis_document-8.0.0-20170601_0.pdf. [Online; accessed 13-August-2020]. 2017.

[92] A. Lorente et al. “Quantification of nitrogen oxides emissions from build-up of pollution over Paris with TROPOMI”. In: *Scientific Reports* 9, 20033 (Dec. 2019), p. 20033. DOI: 10.1038/s41598-019-56428-5.

[93] Antje Ludewig et al. “In-flight calibration results of the TROPOMI payload on board the Sentinel-5 Precursor satellite”. English. In: *Atmospheric Measurement Techniques* 13.7 (July 2020), pp. 3561–3580. ISSN: 1867-1381. DOI: https://doi.org/10.5194/amt-13-3561-2020. URL: https://amt.copernicus.org/articles/13/3561/2020/ (visited on 09/24/2020).

[94] D. J. Lunt et al. ""Sunshade World": A fully coupled GCM evaluation of the climatic impacts of geoengineering". In: *Geophysical Research Letters* 35.12, L12710 (June 2008), p. L12710. DOI: 10.1029/2008GL033674.

[95] Y. Luo, A. Trishchenko, and K. Khlopenkov. "Developing clear-sky, cloud and cloud shadow mask for producing clear-sky composites at 250-meter spatial resolution for the seven MODIS land bands over Canada and North America". In: *Remote Sensing of Environment* 112.12 (Dec. 2008), pp. 4167–4185. DOI: 10.1016/j.rse.2008.06.010.

[96] G. I. Marchuk, G. A. Mikhailov, and M. A. Nazaraliev. *The Monte Carlo methods in atmospheric optics*. 1980.

[97] Alexander Marshak and Anthony Davis. *3D Radiative Transfer in Cloudy Atmospheres*. 2005.

[98] Matthias Mauder et al. "Atmospheric Response to a Partial Solar Eclipse over a Cotton Field in Central California". In: *Journal of Applied Meteorology and Climatology* 46.11 (Nov. 2007), pp. 1792–1803. DOI: 10.1175/2007JAMC1495.1.

[99] M. Mautner. "A Space-Based Solar Screen Against Climatic Warming". In: *Bulletin of the American Astronomical Society*. Vol. 21. June 1989, p. 993.

[100] B. Mayer. "Radiative transfer in the cloudy atmosphere". In: *European Physical Journal Web of Conferences*. Vol. 1. European Physical Journal Web of Conferences. Feb. 2009, p. 75. DOI: 10.1140/epjconf/e2009-00912-1.

[101] Jean Meeus. *Elements of solar eclipses, 1951-2200*. Willman-Bell Inc., Virginia, 1989.

[102] J. F. Meirink, R. A. Roebeling, and P. Stammes. "Inter-calibration of polar imager solar channels using SEVIRI". In: *Atmospheric Measurement Techniques* 6.9 (Sept. 2013), pp. 2495–2508. DOI: 10.5194/amt-6-2495-2013.

[103] Forrest M. Mims and Eric R. Mims. "Fluctuations in column ozone during the total solar eclipse of July 11, 1991". In: *Geophysical Research Letters* 20.5 (1993), pp. 367–370. DOI: 10.1029/93GL00493. eprint: https://agupubs.onlinelibrary.wiley.com/doi/pdf/10.1029/93GL00493. URL: https://agupubs.onlinelibrary.wiley.com/doi/abs/10.1029/93GL00493.

[104] A. Montornès et al. "Implementation of Bessel's method for solar eclipses prediction in the WRF-ARW model". In: *Atmospheric Chemistry and Physics* 16.9 (2016), pp. 5949–5967. DOI: 10.5194/acp-16-5949-2016. URL: https://acp.copernicus.org/articles/16/5949/2016/.

[105] A. Morel and S. Maritorena. "Bio-optical properties of oceanic waters: A reappraisal". In: *Journal of Geophysics Research* 106 (Apr. 2001), pp. 7163–7180. DOI: 10.1029/2000JC000319.

[106] Rosemary Munro et al. "The GOME-2 instrument on the Metop series of satellites: instrument design, calibration, and level 1 data processing - an overview". In: *Atmospheric Measurement Techniques* 9.3 (Mar. 2016), pp. 1279–1301. DOI: 10.5194/amt-9-1279-2016.

A

[107] Teruyuki Nakajima and Michael D. King. “Determination of the optical thickness and effective particle radius of clouds from reflected solar radiation measurements. I - Theory”. In: *Journal of Atmospheric Sciences* 47 (Aug. 1990), pp. 1878–1893. DOI: 10.1175/1520-0469(1990)047<1878:DOTOTA>2.0.CO;2.

[108] Swadhin Nanda et al. “A neural network radiative transfer model approach applied to the Tropospheric Monitoring Instrument aerosol height algorithm”. In: *Atmospheric Measurement Techniques* 12.12 (Dec. 2019), pp. 6619–6634. DOI: 10.5194/amt-12-6619-2019.

[109] Paul Ockenfuß et al. “Accurate 3-D radiative transfer simulation of spectral solar irradiance during the total solar eclipse of 21 August 2017”. In: *Atmospheric Chemistry & Physics* 20.4 (Feb. 2020), pp. 1961–1976. DOI: 10.5194/acp-20-1961-2020.

[110] Sudhanshu Pandey et al. “Satellite observations reveal extreme methane leakage from a natural gas well blowout”. In: *Proceedings of the National Academy of Science* 116.52 (Dec. 2019), pp. 26376–26381. DOI: 10.1073/pnas.1908712116.

[111] Eija Parmes et al. “Automatic Cloud and Shadow Detection in Optical Satellite Imagery Without Using Thermal Bands—Application to Suomi NPP VIIRS Images over Fennoscandia”. In: *Remote Sensing* 9.8 (Aug. 2017), p. 806. DOI: 10.3390/rs9080806.

[112] Jerome Pearson, John Oldson, and Eugene Levin. “Earth rings for planetary environment control”. In: *Acta Astronautica* 58.1 (Jan. 2006), pp. 44–57. DOI: 10.1016/j.actaastro.2005.03.071.

[113] Marcos A. Peñaloza-Murillo and Jay M. Pasachoff. “Cloudiness and Solar Radiation During the Longest Total Solar Eclipse of the 21st Century at Tianhuangping (Zhejiang), China”. In: *Journal of Geophysical Research (Atmospheres)* 123.23 (Dec. 2018), pp. 13, 443–13, 461. DOI: 10.1029/2018JD029253.

[114] M. Penning de Vries and T. Wagner. “Modelled and measured effects of clouds on UV Aerosol Indices on a local, regional, and global scale”. In: *Atmospheric Chemistry & Physics* 11.24 (Dec. 2011), pp. 12715–12735. DOI: 10.5194/acp-11-12715-201110.5194/acpd-10-24135-2010.

[115] M. J. M. Penning de Vries, S. Beirle, and T. Wagner. “UV Aerosol Indices from SCIAMACHY: introducing the SCattering Index (SCI)”. In: *Atmospheric Chemistry and Physics* 9.24 (2009), pp. 9555–9567. DOI: 10.5194/acp-9-9555-2009. URL: https://acp.copernicus.org/articles/9/9555/2009/.

[116] Abelardo Pérez Albiñana et al. “Sentinel-5: the new generation European operational atmospheric chemistry mission in polar orbit”. In: *Society of Photo-Optical Instrumentation Engineers (SPIE) Conference Series*. Vol. 10403. Society of Photo-Optical Instrumentation Engineers (SPIE) Conference Series. Aug. 2017, 104030P, 104030P. DOI: 10.1117/12.2268875.

[117] M. P. Petrov and S. Alitto. *Takla Makan Desert*. 2019. URL: https://www.britannica.com/place/Takla-Makan-Desert (visited on 10/03/2020).

[118] A. K. Pierce and C. D. Slaughter. “Solar limb darkening. I: lambda lambda (3033 - 7297).” In: *Solar Physics* 51.1 (Feb. 1977), pp. 25–41. DOI: 10.1007/BF00240442.

[119] A. K. Pierce and C. D. Slaughter. “Solar limb darkening. I: lambda lambda (3033 - 7297).” In: *Solar Physics* 51.1 (Jan. 1977), pp. 25–41. DOI: 10.1007/BF00240442.

[120] A. K. Pierce, C. D. Slaughter, and D. Weinberger. “Solar limb darkening in the interval 7404 - 24018 Å, II.” In: *Solar Physics* 52.1 (Apr. 1977), pp. 179–189. DOI: 10.1007/BF00935800.

[121] A. K. Pierce, C. D. Slaughter, and D. Weinberger. “Solar limb darkening in the interval 7404 - 24018 Å, II.” In: *Solar Physics* 52.1 (Apr. 1977), pp. 179–189. DOI: 10.1007/BF00935800.

[122] Ulrich Platt and Jochen Stutz. *Differential Optical Absorption Spectroscopy*. Springer Nature Switzerland AG, Cham, 2008. DOI: 10.1007/978-3-540-75776-4.

[123] Shi Qiu, Zhe Zhu, and Binbin He. “Fmask 4.0: Improved cloud and cloud shadow detection in Landsats 4-8 and Sentinel-2 imagery”. In: *Remote Sensing of Environment* 231 (Sept. 2019), p. 111205. DOI: 10.1016/j.rse.2019.05.024.

[124] Robert M. Rabin and David W. Martin. “Satellite observations of shallow cumulus coverage over the central United States: An exploration of land use impact on cloud cover”. In: *Journal of Geophysical Research* 101.D3 (Mar. 1996), pp. 7149–7155. DOI: 10.1029/95JD02891.

[125] V. Ramanathan et al. “Cloud-Radiative Forcing and Climate: Results from the Earth Radiation Budget Experiment”. In: *Science* 243.4887 (Jan. 1989), pp. 57–63. DOI: 10.1126/science.243.4887.57.

[126] Philip J. Rasch et al. “An overview of geoengineering of climate using stratospheric sulphate aerosols”. In: *Philosophical Transactions of the Royal Society of London Series A* 366.1882 (Nov. 2008), pp. 4007–4037. DOI: 10.1098/rsta.2008.0131.

[127] Fabian Romahn et al. *Sentinel-5 precursor/TROPOMI 1 Level 2 Product User Manual O3 Tropospheric Column. Doc. No. S5P-L2-DLR-PUM-400C, Issue 02.03.00, Royal Netherlands Meteorological Institute (KNMI)*. https://sentinel.esa.int/documents/247904/2474726/Sentinel-5P-Level-2-Product-User-Manual-Ozone-Tropospheric-Column. [Online; accessed 13-September-2021]. 2021.

[128] William B. Rossow. “Measuring Cloud Properties from Space: A Review.” In: *Journal of Climate* 2.3 (Mar. 1989), pp. 201–213. DOI: 10.1175/1520-0442(1989)002<0201:MCPFSA>2.0.CO;2.

[129] Rick D. Russotto and Thomas P. Ackerman. “Changes in clouds and thermodynamics under solar geoengineering and implications for required solar reduction”. In: *Atmospheric Chemistry & Physics* 18.16 (Aug. 2018), pp. 11905–11925. DOI: 10.5194/acp-18-11905-2018.

[130] Joan-Pau Sánchez and Colin R. McInnes. “Optimal Sunshade Configurations for Space-Based Geoengineering near the Sun-Earth L1 Point”. In: *PLoS ONE* 10.8 (Aug. 2015), e0136648. DOI: 10.1371/journal.pone.0136648.

A

[131] A. F. J. Sanders et al. “Evaluation of the operational Aerosol Layer Height retrieval algorithm for Sentinel-5 Precursor: application to O_2 A band observations from GOME-2A”. In: *Atmospheric Measurement Techniques* 8.11 (Nov. 2015), pp. 4947–4977. DOI: 10.5194/amt-8-4947-201510.5194/amtd-8-6045-2015.

[132] Stéphane Saux Picart et al. “A Sea Surface Temperature data record (2004-2012) from Meteosat Second Generation satellites”. In: *Remote Sensing of Environment* 240 (Apr. 2020), p. 111687. DOI: 10.1016/j.rse.2020.111687.

[133] S. Saux-Picart. *Algorithm Theoretical Basis Document for MSG/SEVIRI Sea Surface Temperature data record, version 1.3*. Technical Report SAF/OSI/CDOP2/MF/SCI/MA/256. Ocean and Sea Ice Satellite Application Facility (OSI SAF), 2018. DOI: https://doi.org/10.15770/EUM_SAF_OSI_0004.

[134] C. Schaaf and Z. Wang. *MCD43C3 MODIS/Terra+Aqua BRDF/Albedo Albedo Daily L3 Global 0.05Deg CMG V006 Data set*. NASA EOSDIS Land Processes DAAC, accessed 2023-06-24 https://doi.org/10.5067/MODIS/MCD43C3.006, 2015.

[135] Johannes Schmetz et al. “An Introduction to Meteosat Second Generation (MSG).” In: *Bulletin of the American Meteorological Society* 83.7 (July 2002), pp. 977–992. DOI: 10.1175/1520-0477(2002)083<0977:AITMSG>2.3.CO;2.

[136] H. Schmidt et al. “Solar irradiance reduction to counteract radiative forcing from a quadrupling of CO_2: climate responses simulated by four earth system models”. In: *Earth System Dynamics* 3.1 (June 2012), pp. 63–78. DOI: 10.5194/esd-3-63-2012.

[137] Oliver Schneising et al. “Remote sensing of methane leakage from natural gas and petroleum systems revisited”. In: *Atmospheric Chemistry & Physics* 20.15 (Aug. 2020), pp. 9169–9182. DOI: 10.5194/acp-20-9169-2020.

[138] P. Kenneth Seidelmann. *Explanatory Supplement to the Astronomical Almanac*. U.S. Naval Observatory, Washington, D.C., University Science Books, California, 1992.

[139] Glenn E. Shaw. “Sky Brightness and Polarization During the 1973 African Eclipse”. In: *Appl. Opt.* 14.2 (Feb. 1975), pp. 388–394. DOI: 10.1364/AO.14.000388. URL: http://ao.osa.org/abstract.cfm?URI=ao-14-2-388.

[140] J.G. Shepherd. *Geoengineering the climate: science, governance and uncertainty*. Project Report. Sept. 2009. URL: https://eprints.soton.ac.uk/156647/.

[141] Richard Siddans. *S5P-NPP Cloud Processor ATBD. Doc. No. S5P-NPPC-RAL-ATBD-0001, Issue 1.0.0, RAL Space*. https://sentinels.copernicus.eu/documents/247904/2476257/Sentinel-5P-NPP-ATBD-NPP-Clouds. [Online; accessed 10-November-2021]. 2016.

[142] A. P. Siebesma. “Shallow Cumulus Convection”. In: *Buoyant Convection in Geophysical Flows*. Ed. by E. J. Plate et al. Dordrecht: Springer Netherlands, 1998, pp. 441–486. ISBN: 978-94-011-5058-3. DOI: 10.1007/978-94-011-5058-3_19. URL: https://doi.org/10.1007/978-94-011-5058-3_19.

[143] A. Pier Siebesma, Pedro M. M. Soares, and João Teixeira. "A Combined Eddy-Diffusivity Mass-Flux Approach for the Convective Boundary Layer". In: *Journal of Atmospheric Sciences* 64.4 (Jan. 2007), p. 1230. DOI: 10.1175/JAS3888.1.

[144] Bernd Sierk et al. "The Copernicus CO2M mission for monitoring anthropogenic carbon dioxide emissions from space". In: vol. 11852. Society of Photo-Optical Instrumentation Engineers (SPIE) Conference Series. June 2021, 118523M, p. 118523M. DOI: 10.1117/12.2599613.

[145] J. J. Simpson and J. R. Stitt. "A procedure for the detection and removal of cloud shadow from AVHRR data over land". In: *IEEE Transactions on Geoscience and Remote Sensing* 36.3 (May 1998), pp. 880–897. DOI: 10.1109/36.673680.

[146] James J. Simpson, Zhonghai Jin, and James R. Stitt. "Cloud shadow detection under arbitrary viewing and illumination conditions". In: *IEEE Trans. Geosci. Remote. Sens.* 38 (2000), pp. 972–976.

[147] F. Spada, M. C. Krol, and P. Stammes. "McSCIA: application of the Equivalence Theorem in a Monte Carlo radiative transfer model for spherical shell atmospheres". In: *Atmospheric Chemistry & Physics* 6.12 (Oct. 2006), pp. 4823–4842. DOI: 10.5194/acp-6-4823-2006.

[148] D. M. Stam et al. "A fast method for simulating observations of polarized light emerging from the atmosphere applied to the oxygen-A band." In: *Journal of Quantitative Spectroscopy and Radiative Transfer* 64 (Jan. 2000), pp. 131–149. DOI: 10.1016/S0022-4073(99)00009-6.

[149] Piet Stammes. "Spectral radiance modelling in the UV-visible range". In: *IRS 2000: Current Problems in Atmospheric Radiation, edited by: Smith, W.L. and Timofeyev, Y.M., A. Deepak Publishing, Hampton, Virginia* (2001), pp. 385–388.

[150] Deborah Stein Zweers, Arnoud Apituley, and Pepijn Veefkind. *Algorithm theoretical basis document for the TROPOMI UV Aerosol Index. Doc. No. S5P-KNMI-L2-0008-RP, Issue 1.1, Royal Netherlands Meteorological Institute (KNMI).* http://www.tropomi.eu/sites/default/files/files/S5P-KNMI-L2-0008-RP-TROPOMI_ATBD_UVAI-1.1.0-20180615_signed.pdf. [Online; accessed 14-September-2020]. 2018.

[151] J. O. Stenflo. "Polarization of the Sun's continuous spectrum". In: *Astronomy and Astrophysics* 429.2 (2005), pp. 713–730. DOI: 10.1051/0004-6361:20041667. URL: https://doi.org/10.1051/0004-6361:20041667.

[152] J. O. Stenflo and C. U. Keller. "The second solar spectrum. A new window for diagnostics of the Sun." In: *Astronomy and Astrophysics* 321 (May 1997), pp. 927–934.

[153] M. S. Stengel et al. "CLAAS: the CM SAF cloud property data set using SEVIRI". In: *Atmospheric Chemistry & Physics* 14.8 (Apr. 2014), pp. 4297–4311. DOI: 10.5194/acp-14-4297-2014.

[154] G. L. Stephens. "Radiation Profiles in Extended Water Clouds. II: Parameterization Schemes." In: *Journal of Atmospheric Sciences* 35.11 (Nov. 1978), pp. 2123–2132. DOI: 10.1175/1520-0469(1978)035<2123:RPIEWC>2.0.CO;2.

A

[155] Roland B. Stull. *An introduction to boundary layer meteorology*. Dordrecht, Boston and London: Kluwer Academic Publishers, 1988. DOI: 10.1007/978-94-009-3027-8.

[156] Lin Sun et al. "A cloud shadow detection method combined with cloud height iteration and spectral analysis for Landsat 8 OLI data". In: *ISPRS Journal of Photogrammetry and Remote Sensing* 138 (Apr. 2018), pp. 193–207. DOI: 10.1016/j.isprsjprs.2018.02.016.

[157] N. Theys et al. "Global monitoring of volcanic SO_2 degassing with unprecedented resolution from TROPOMI onboard Sentinel-5 Precursor". In: *Scientific Reports* 9, 2643 (Feb. 2019), p. 2643. DOI: 10.1038/s41598-019-39279-y.

[158] Simone Tilmes et al. "Sensitivity of Aerosol Distribution and Climate Response to Stratospheric SO_2 Injection Locations". In: *Journal of Geophysical Research (Atmospheres)* 122.23 (Dec. 2017), pp. 12, 591–12, 615. DOI: 10.1002/2017JD026888.

[159] L. G. Tilstra. *TROPOMI ATBD of the directionally dependent surface Lambertian-equivalent reflectivity, KNMI Report S5P-KNMI-L3-0301-RP, Issue 1.2.0*. https://www.temis.nl/surface/albedo/tropomi_ler.php. [Online; accessed 7-February-2022]. May 2022.

[160] L. G. Tilstra et al. "A directional surface reflectance climatology determined from TROPOMI observations". In: *Atmospheric Measurement Techniques* 17.7 (2024), pp. 2235–2256. DOI: 10.5194/amt-17-2235-2024. URL: https://amt.copernicus.org/articles/17/2235/2024/.

[161] L. G. Tilstra et al. "Directionally dependent Lambertian-equivalent reflectivity (DLER) of the Earth's surface measured by the GOME-2 satellite instruments". In: *Atmospheric Measurement Techniques* 14.6 (2021), pp. 4219–4238. DOI: 10.5194/amt-14-4219-2021. URL: https://amt.copernicus.org/articles/14/4219/2021/.

[162] L. G. Tilstra et al. "In-orbit Earth reflectance validation of TROPOMI on board the Sentinel-5 Precursor satellite". In: *Atmospheric Measurement Techniques* 13.8 (2020), pp. 4479–4497. DOI: 10.5194/amt-13-4479-2020. URL: https://amt.copernicus.org/articles/13/4479/2020/.

[163] L. G. Tilstra et al. "Surface reflectivity climatologies from UV to NIR determined from Earth observations by GOME-2 and SCIAMACHY". In: *Journal of Geophysical Research (Atmospheres)* 122.7 (Apr. 2017), pp. 4084–4111. DOI: 10.1002/2016JD025940.

[164] W. Torge and J. Müller. *Geodesy*. De Gruyter, Berlin, 2012. ISBN: 9783110207187.

[165] O. Torres et al. "Derivation of aerosol properties from satellite measurements of backscattered ultraviolet radiation: Theoretical basis". In: *Journal of Geophysical Research: Atmospheres* 103.D14 (1998), pp. 17099–17110. DOI: 10.1029/98JD00900. eprint: https://agupubs.onlinelibrary.wiley.com/doi/pdf/10.1029/98JD00900. URL: https://agupubs.onlinelibrary.wiley.com/doi/abs/10.1029/98JD00900.

[166] Omar Torres, Hiren Jethva, and P. K. Bhartia. "Retrieval of Aerosol Optical Depth above Clouds from OMI Observations: Sensitivity Analysis and Case Studies". In: *Journal of the Atmospheric Sciences* 69.3 (Mar. 2012), pp. 1037–1053. DOI: 10.1175/JAS-D-11-0130.1.

[167] Omar Torres et al. "Impact of the ozone monitoring instrument row anomaly on the long-term record of aerosol products". In: *Atmospheric Measurement Techniques* 11.5 (May 2018), pp. 2701–2715. DOI: 10.5194/amt-11-2701-2018.

[168] V. Trees, P. Wang, and P. Stammes. "Restoring the top-of-atmosphere reflectance during solar eclipses: a proof of concept with the UV absorbing aerosol index measured by TROPOMI". In: *Atmospheric Chemistry & Physics* 21.11 (June 2021), pp. 8593–8614. DOI: 10.5194/acp-21-8593-2021.

[169] V. J. H. Trees et al. "DARCLOS: a cloud shadow detection algorithm for TROPOMI". In: *Atmospheric Measurement Techniques* 15.10 (2022), pp. 3121–3140. DOI: 10.5194/amt-15-3121-2022. URL: https://amt.copernicus.org/articles/15/3121/2022/.

[170] Victor J. H. Trees et al. "Cancellation Of Cloud Shadow Effects In The Absorbing Aerosol Index Retrieval Algorithm Of Tropomi". In: *Atmospheric Measurement Techniques* 18 (Jan. 2025), pp. 73–91. DOI: 10.5194/amt-18-73-2025.

[171] Victor J. H. Trees et al. "Clouds dissipate quickly during solar eclipses as the land surface cools". In: *Communications Earth and Environment* 5.1, 71 (Feb. 2024), p. 71. DOI: 10.1038/s43247-024-01213-0. arXiv: 2402.08510 [physics.ao-ph].

[172] I. Trigo et al. *Algorithm theoretical basis document for land surface temperature (LST)*. Technical Report SAF/LAND/IM/ATBD_MLST/1.2, Issue 2. Land surface analysis satellite application facility (LSA-SAF), 2017.

[173] Olaf Tuinder et al. *Algorithm theoretical basis document for the NRT, Offline and Data Record Absorbing Aerosol Index Products. Doc. No. ACSAF/KNMI/ATBD/002, Issue 2.61, Royal Netherlands Meteorological Institute (KNMI)*. https://acsaf.org/docs/atbd/Algorithm_Theoretical_Basis_Document_NAR_NAP_ARS_ARP_Sep_2019.pdf. [Online; accessed 8-October-2020]. 2019.

[174] Ronald van der A et al. "Connecting the dots: NOx emissions along a West Siberian natural gas pipeline." In: *Npj Climate and Atmospheric Science* 3 (2020), p. 16. DOI: 10.1038/s41612-020-0119-z.

[175] J.H.G.M. van Geffen et al. *TROPOMI ATBD of the total and tropospheric NO_2 data products. Doc. No. S5P-KNMI-L2-0005-RP, Issue 2.2.0, Royal Netherlands Meteorological Institute (KNMI)*. https://sentinel.esa.int/documents/247904/2476257/Sentinel-5P-TROPOMI-ATBD-NO2-data-products. [Online; accessed 18-August-2021]. 2021.

[176] D. J. Varon et al. "Satellite Discovery of Anomalously Large Methane Point Sources From Oil/Gas Production". In: *Geophysical Research Letters* 46.22 (Nov. 2019), pp. 13, 507–13, 516. DOI: 10.1029/2019GL083798.

[177] J. P. Veefkind et al. “TROPOMI on the ESA Sentinel-5 Precursor: A GMES mission for global observations of the atmospheric composition for climate, air quality and ozone layer applications”. In: *Remote Sensing of Environment* 120 (May 2012), pp. 70–83. DOI: 10.1016/j.rse.2011.09.027.

[178] T. Vincenty. “Direct and Inverse Solutions of Geodesics on the Ellipsoid with Applications of Nested Equations”. In: *Survey Review* 23.176 (1975), pp. 88–93. DOI: 10.1179/sre.1975.23.176.88. eprint: https://doi.org/10.1179/sre.1975.23.176.88. URL: https://doi.org/10.1179/sre.1975.23.176.88.

[179] J. G. Virgin and C. G. Fletcher. “On the Linearity of External Forcing Response in Solar Geoengineering Experiments”. In: *Geophysical Research Letters* 49.15, e00200 (Aug. 2022), e00200. DOI: 10.1029/2022GL100200.

[180] Daniele Visioni et al. “Seasonal Injection Strategies for Stratospheric Aerosol Geoengineering”. In: *Geophysical Research Letters* 46.13 (July 2019), pp. 7790–7799. DOI: 10.1029/2019GL083680.

[181] Max Waldmeier. *Ergebnisse und probleme der sonnenforschung, von dr. M. Waldmeier mit 102 figuren.* Lpz Akademische Verlagsgesellschaft Becker & Erler, 1941.

[182] Zhengming Wan and J. Dozier. “A generalized split-window algorithm for retrieving land-surface temperature from space”. In: *IEEE Transactions on Geoscience and Remote Sensing* 34.4 (July 1996), pp. 892–905. DOI: 10.1109/36.508406.

[183] P. Wang et al. “FRESCO+: an improved O_2 A-band cloud retrieval algorithm for tropospheric trace gas retrievals”. In: *Atmospheric Chemistry & Physics* 8.21 (Nov. 2008), pp. 6565–6576.

[184] Tianxing Wang et al. “Detection and Removal of Clouds and Associated Shadows in Satellite Imagery Based on Simulated Radiance Fields”. In: *Journal of Geophysical Research (Atmospheres)* 124.13 (July 2019), pp. 7207–7225. DOI: 10.1029/2018JD029960.

[185] Guoyong Wen et al. “Reduction of Spectral Radiance Reflectance During the Annular Solar Eclipse of 21 June 2020 Observed by EPIC”. In: *Frontiers in Remote Sensing* 3 (2022). ISSN: 2673-6187. DOI: 10.3389/frsen.2022.777314. URL: https://www.frontiersin.org/articles/10.3389/frsen.2022.777314.

[186] Peter Winkler et al. “Development of meteorological parameters and total ozone during the total solar eclipse of August 11, 1999”. In: *Meteorologische Zeitschrift* 10 (July 2001), pp. 193–199. DOI: 10.1127/0941-2948/2001/0010-0193.

[187] Donald Wuebbles and Julius S. Chang. “A theoretical study of stratospheric trace species variations during a solar eclipse”. In: *Geophysical Research Letters* 6.3 (1979), pp. 179–182. DOI: https://doi.org/10.1029/GL006i003p00179. eprint: https://agupubs.onlinelibrary.wiley.com/doi/pdf/10.1029/GL006i003p00179. URL: https://agupubs.onlinelibrary.wiley.com/doi/abs/10.1029/GL006i003p00179.

[188] Lin Yan and David P. Roy. “Spatially and temporally complete Landsat reflectance time series modelling: The fill-and-fit approach”. In: *Remote Sensing of Environment* 241 (May 2020), p. 111718. DOI: 10.1016/j.rse.2020.111718.

[189] C. S. Zerefos et al. “Changes in surface solar UV irradiances and total ozone during the solar eclipse of August 11, 1999”. In: *Journal of Geophysical Research: Atmospheres* 105.D21 (2000), pp. 26463–26473. DOI: 10.1029/2000JD900412. eprint: https://agupubs.onlinelibrary.wiley.com/doi/pdf/10.1029/2000JD900412. URL: https://agupubs.onlinelibrary.wiley.com/doi/abs/10.1029/2000JD900412.

[190] Zhe Zhu, Shixiong Wang, and Curtis E. Woodcock. “Improvement and expansion of the Fmask algorithm: cloud, cloud shadow, and snow detection for Landsats 4-7, 8, and Sentinel 2 images”. In: *Remote Sensing of Environment* 159 (Mar. 2015), pp. 269–277. DOI: 10.1016/j.rse.2014.12.014.

[191] Zhe Zhu and Curtis E. Woodcock. “Automated cloud, cloud shadow, and snow detection in multitemporal Landsat data: An algorithm designed specifically for monitoring land cover change”. In: *Remote Sensing of Environment* 152 (Sept. 2014), pp. 217–234. DOI: 10.1016/j.rse.2014.06.012.

[192] Zhe Zhu and Curtis E. Woodcock. “Object-based cloud and cloud shadow detection in Landsat imagery”. In: *Remote Sensing of Environment* 118 (Mar. 2012), pp. 83–94. DOI: 10.1016/j.rse.2011.10.028.

[193] Zhe Zhu et al. “Cloud and Cloud Shadow Detection for Landsat Images: The Fundamental Basis for Analyzing Landsat Time Series, Remote Sensing Time Series Image Processing”. In: CRC Press, Boca Raton, May 2018, pp. 3–24. ISBN: 9781315166636. DOI: 10.1201/9781315166636-1.

Curriculum Vitæ

Victor Jacq Hugo Trees

Research Experience

2024–Present	Postdoc at Delft University of Technology *Capturing Venus in total flux and polarisation from the UV to the NIR.*
2024	Postdoc (4 months) at Delft University of Technology *Moonshot: simulating the Earth as an exoplanet as seen from the Moon.*
2020–2024	PhD student at Delft University of Technology / Royal Netherlands Meteorological Institute (KNMI) *Shadows: Impact of cloud shadows and solar eclipses on satellite data.*
2018–2019	PhD student (10 months) at University of Oxford *Simulating planetary phase curves of hot Jupiter-like exoplanets.*
2017–2018	Intern (6 months), Royal Netherlands Meteorological Institute (KNMI) *Analyzing trends in OMI reflectance data (2005–2006).*

Education

2016–2018	MSc Aerospace Engineering, Delft University of Technology MSc track Spaceflight. Specialization in Planetary Atmospheres and Exoplanets. Distinction: Cum Laude. Thesis: 'Transfer of Polarized Light in an (Exo)planetary Atmosphere-Ocean System.' Final grade: 9.5.
2011–2016	BSc Aerospace Engineering, Delft University of Technology Minor: Spaceflight
2010–2011	Orientation year Courses in BSc Medicine (University of Amsterdam) and BSc Applied Mathematics (Delft University of Technology)
2004–2010	Pre-University Education (VWO), Sint Laurens College Rotterdam Profile program: Nature and Technology (Natuur en Techniek)

TEACHING ACTIVITIES

2024	Daily MSc. thesis supervisor of student Aurora Cagnoni (Mar–Jul): 'Investigating an observation strategy for the Earth as an exoplanet from the Moon', Geoscience and Remote Sensing.
2023/2024	Group supervisor, AESB1440, Methodology of Geophysics and Remote Sensing
2023/2024	Daily MSc. thesis supervisor of student Jelle Schrijver (Mar 2023–Feb 2024): 'The impact of solar eclipses on NO_2 in the Earth's atmosphere', Geoscience and Remote Sensing.
2022	MSc. thesis graduation committee member of Gytha Mettepenningen: 'The relation between clouds and surface water on exoplanets', Aerospace Engineering.
2022/2023	Teaching assistant, UD1052, Can we cool the Earth?
2021/2022	Teaching assistant, CIE4708, Water in the Atmosphere
2021/2022	Teaching assistant, CIE4601, Physics of the Earth and Atmosphere
2020/2021	Teaching assistant, CIE4601, Physics of the Earth and Atmosphere

TALKS

SCIENTIFIC TALKS

- Conference talk: 'Impact of solar eclipses on clouds', International Radiation Symposium (IRS), Hangzhou, China, June 2024.
- Conference talk: 'Cancellation of cloud shadow effects in the absorbing aerosol index of TROPOMI data', International Radiation Symposium (IRS), Hangzhou, China, June 2024.
- Conference poster: 'Searching for cloud shadow effects in TROPOMI NO_2 data with the cloud shadow detection algorithm DARCLOS', TROPOMI 5-year anniversary, Taormina, Italy, 10–14 October 2022.
- Public talk: 'Detecting cloud shadows in TROPOMI data with DARCLOS', International Radiation Symposium (IRS), Thessaloniki, Greece, 4–8 July 2022.
- Conference poster: 'DARCLOS: a cloud shadow detection algorithm for TROPOMI', ESA Living Planet Symposium, Bonn, 23–27 May 2022.
- Online talk: 'DARCLOS: a cloud shadow detection algorithm for TROPOMI', ESA ATMOS conference, 26 November 2021.
- Conference pitch: 'Restoring the top-of-atmosphere reflectance during solar eclipses: a proof of concept with the UV Absorbing Aerosol Index measured by TROPOMI', EGU meeting, 28 April 2021.
- Conference poster: 'Restoring Top of Atmosphere Reflectance Spectra during Partial and Annular Solar Eclipses: a Proof of Concept with the Absorbing Aerosol Index Measured by the TROPOMI/S5P Instrument', AGU Fall Meeting, 7 December 2020.

- Presentation: 'Restoring the top-of-atmosphere reflectance during solar eclipses: a proof of concept with the UV Absorbing Aerosol Index measured by TROPOMI', OMI-TROPOMI workshop, 26–29 October 2020.

PUBLIC TALKS

- YouTube interview: 'How Do Solar Eclipses Affect Clouds? Scientist Victor Trees Answers', SETI Institute, 9 April 2024.
  https://www.youtube.com/watch?v=wWf9aI9E1TM

- Evening lecture (2×45 min): 'Zoeken naar oceanen op exoplaneten', Weer- en Sterrekundevereniging EuroSter, Rotterdam, 16 December 2022.

- Evening lecture (2×45 min): 'Luchtkwaliteitmetingen vanuit de ruimte en zonsverduisteringen', Weer- en Sterrekundevereniging EuroSter, Rotterdam, 16 September 2022.

- Evening lecture (2×45 min): 'Luchtkwaliteitmetingen vanuit de ruimte en zonsverduisteringen', Leidse Weer- en Sterrekundige Kring, Leiden Observatory, 15 February 2022.
  https://lwsk.nl/?page_id=12

IN THE MEDIA AND RESEARCH HIGHLIGHTS

TOPIC: IMPACT OF SOLAR ECLIPSES ON CLOUDS (2024)

- **NRC**: 'Eclips doet stapelwolken verdwijnen'
  https://www.nrc.nl/nieuws/2024/02/26/eclips-doet-stapelwolken-verdwijnen-a4191311

- **The New York Times**: 'Solar Eclipse Could Make Some Clouds Perform a Disappearing Act'
  https://www.nytimes.com/2024/04/08/science/solar-eclipse-clouds-totality.html

- **CNN**: 'Why some clouds vanish during solar eclipses'
  https://edition.cnn.com/2024/03/30/world/clouds-vanish-solar-eclipse-scn/index.html

- **USA Today**: 'The solar eclipse may drive away cumulus clouds. Here's why that worries some scientists.'
  https://eu.usatoday.com/story/news/nation/2024/02/26/solar-eclipse-cumulus-cloud-impact/72744512007/

- **Forbes**: 'Why Cloud Could Disappear As the Total Solar Eclipse Begins'
  https://www.forbes.com/sites/jamiecartereurope/2024/04/08/clouds-may-vanish-during-april-8s-total-solar-eclipse-say-scientists/?sh=15cce2782ada

- **BBC Sky at Night Magazine**: 'Eclipses clear the clouds! Research suggests solar eclipses have an effect on weather and cloud cover'
  https://www.skyatnightmagazine.com/news/solar-eclipses-affect-weather-clouds
- **AGU EOS**: 'Low-Level Clouds Disappear During a Solar Eclipse'
  https://eos.org/articles/low-level-clouds-disappear-during-a-solar-eclipse
- **TU Delft**: 'Wolken verdwijnen als sneeuw voor de zon tijdens zonsverduistering'
  https://www.tudelft.nl/2024/citg/wolken-verdwijnen-als-sneeuw-voor-de-zon-tijdens-zonsverduistering
- **KNMI**: 'Dim het zonlicht en wolken lossen op'
  https://www.knmi.nl/over-het-knmi/nieuws/dim-het-zonlicht-en-wolken-lossen-op

TOPIC: DETECTING LIQUID WATER OCEANS ON EXOPLANETS (2019)

- **Nature Astronomy, 3, 474 (2019)**: 'Ocean detection by polarization colors' — Research highlight by Luca Maltagliati
  https://www.nature.com/articles/s41550-019-0817-9
- **TU Delft**: 'De kleur van trillend licht verraadt oceanen op exoplaneten'
  https://www.tudelft.nl/2019/tu-delft/de-kleur-van-trillend-licht-verraadt-oceanen-op-exoplaneten

List of Publications

10. **V.J.H. Trees, P. Wang, P. Stammes, L.G. Tilstra, D.P. Donovan, and A.P. Siebesma**, *Cancellation of cloud shadow effects in the absorbing aerosol index retrieval algorithm of TROPOMI*, Atmospheric Measurement Techniques **18**, 73–91 (2025).

9. **V.J.H. Trees, S.R. de Roode, J.I. Wiltink, J.F. Meirink, P. Wang, P. Stammes, and A.P. Siebesma**, *Clouds dissipate quickly during solar eclipses as the land surface cools*, Nature Communications Earth & Environment **5**, 71 (2024).

8. **L.G. Tilstra, M. de Graaf, V.J.H. Trees, P. Litvinov, O. Dubovik, and P. Stammes**, *A directional surface reflectance climatology determined from TROPOMI observations*, Atmospheric Measurement Techniques 17.7 (2024), pp. 2235–2256.

7. **S.R. Vaughan, T.D. Gebhard, K. Bott, S.L. Casewell, N.B. Cowan, D.S. Doelman, M. Kenworthy, J. Mazoyer, M.A. Millar-Blanchaer, V.J.H. Trees, D.M. Stam, O. Absil, L. Altinier, P. Baudoz, R. Belikov, A. Bidot, J.L. Birkby, M.J. Bonse, B. Brandl, A. Carlotti, E. Choquet, D. van Dam, N. Desai, K. Fogarty, J. Fowler, K. van Gorkom, Y. Gutierrez, O. Guyon, S.Y. Haffert, O. Herscovici-Schiller, A. Hours, R. Juanola-Parramon, E. Kleisioti, L. König, M. van Kooten, M. Krasteva, I. Laginja, R. Landman, L. Leboulleux, D. Mouillet, M. N'Diaye, E.H. Por, L. Pueyo, and F. Snik**, *Chasing rainbows and ocean glints: Inner working angle constraints for the Habitable Worlds Observatory*, Monthly Notices of the Royal Astronomical Society **524**(4), 5477–5485 (2023).

6. **V.J.H. Trees and D.M. Stam**, *Ocean signatures in the total flux and polarization spectra of Earth-like exoplanets*, Astronomy & Astrophysics **664**, A172 (2022).

5. **V.J.H. Trees, P. Wang, P. Stammes, L.G. Tilstra, D.P. Donovan, and A.P. Siebesma**, *DARCLOS: a cloud shadow detection algorithm for TROPOMI*, Atmospheric Measurement Techniques **15**, 3121–3140 (2022).

4. **V.J.H. Trees, P. Wang, and P. Stammes**, *Restoring the top-of-atmospheric reflectance during solar eclipses: a proof of concept with the UV Absorbing Aerosol Index measured by TROPOMI*, Atmospheric Chemistry & Physics **21**, 8593–8614 (2021).

3. **A. Groot, L. Rossi, V.J.H. Trees, J.C.Y. Cheung and D.M. Stam**, *Colors of an Earth-like exoplanet: temporal flux and polarization signals of the Earth*, Astronomy & Astrophysics **640**, A121 (2020).

2. **M.L. Kooreman, P. Stammes, V. Trees, M. Sneep, L.G. Tilstra, M. de Graaf, D.C. Stein Zweers, P. Wang, O.N.E. Tuinder, and J.P. Veefkind**, *Effect of clouds on the UV Absorbing Aerosol Index from TROPOMI*, Atmospheric Measurement Techniques **13**, 6407–6426 (2020).

1. **V.J.H. Trees and D.M. Stam**, *Blue, white, and red ocean planets: simulations of orbital variations in flux and polarization colors*, Astronomy & Astrophysics **626**, A129 (2019).